Characterizing the diffuse neutrino flux with the future KM3NeT/ARCA detector

Charakterisierung des diffusen Neutrinoflusses
mit dem zukünftigen KM3NeT/ARCA-Neutrinoteleskop

Der Naturwissenschaftlichen Fakultät
der Friedrich-Alexander-Universität Erlangen-Nürnberg
zur Erlangung des Doktorgrades Dr. rer. nat.

vorgelegt von
Thomas Gerhard Georg Heid
aus Roth

Als Dissertation genehmigt von der Naturwissenschaftlichen Fakultät
der Friedrich-Alexander-Universität Erlangen-Nürnberg

Tag der mündlichen Prüfung:	13.12.2018
Vorsitzender des Promotionsorgans:	Prof. Dr. Georg Kreimer
Gutachter:	Prof. Dr. Gisela Anton Dr. Paschal Coyle

Contents

Chapter 1

Introduction

During 100 years after Victor Hess discovered the cosmic rays in 1912 [1], the measurements done with numerous experiments increased the knowledge about features of the cosmic ray flux. The observable energy interval has been extended up to highest energies of 10^{20} eV [2]. Nevertheless, more and more questions have arisen. The origin of cosmic-ray particles is not clear up to now. As the cosmic-ray particles, discovered by Hess, are charged particles, they are deflected by magnetic fields on their journey to the Earth. Therefore, their path and origin are hidden. However, there are two unique messengers which are not deflected by magnetic fields. They point back to the place of their creation. Firstly, there are the γ-ray photons, which can be observed by experiments like H.E.S.S. [3]. Sky maps are full of sources found by these experiments, but the production mechanism is not yet fully understood as γ-rays can be produced by electro-magnetic as well as hadronic processes. Another messenger combines the benefits of the straight path from the source to the observer and is produced in hadronic processes only, therefore it can resolve the "electromagnetic-versus-hadronic" puzzle.

The particle sought is the neutrino, which was first postulated by Pauli in 1930 [4]. Neutrinos do not interact via strong force nor electro-magnetic force, so the weak interaction is the only production and detection mechanism. The neutrino can traverse dense regions in astrophysical objects, which is not possible at the same extent for γ-rays due to a much shorter interaction length. Neutrinos will enable mankind to look into objects which were unreachable up to now. Though neutrinos are perfect probes to study the universe, they are not easy to detect. The interaction cross section is very small. Additionally, the flux in the interesting energy interval of galactic and extra-galactic sources is very low on Earth, of the order of 10 interacting neutrinos above 1 PeV per year in cubic-kilometer sized detectors. Only a few years ago, this new "light" from the sky pushed the young field of neutrino astronomy when the astrophysical neutrino flux was detected by the IceCube collaboration [5]. In the course thereof cubic-kilometer-sized detectors are planned and built or were built. Another collaboration facing this challenge is KM3NeT (km3-Neutrino Telescope), a European collaboration for neutrino research facilities [6]. Its experiment ARCA (Astroparticle Research with Cosmics in the Abyss) is optimized for galactic neutrino point-like sources. It is located deep in the Mediterranean Sea near Sicily and is still growing. However, as the neutrino flux is so small, up to now no point-like source was detected. Even if single neutrino sources are too weak to be detected, the diffuse flux emitted collectively by all sources is strong enough as seen with the discovery of IceCube [5]. Nevertheless, most characteristic quantities are still hidden behind the sparse data. Most analyses aim at measuring the total neutrino flux or one single-flavor flux. The expectation of the ratio between different neutrino flavors, the so-called neutrino flavor composition, has not been unraveled up to now. Analyses, like the IceCube analysis from 2015 [7], show a wide range of possible values.

This work is one step towards a better understanding of neutrino sources via solving the question of neutrino flavor composition. The degree to which ARCA can characterize the neutrino flux depends

significantly on the possibility to separate neutrinos according to their flavor. Furthermore, the confidence in the omnipresent background of atmospheric particles and its rejection directly influences the view on the flavor composition. In this thesis, these two conditions are examined and optimized to work out the first estimate on the sensitivity of ARCA to the neutrino flavor composition. For this purpose, a new method to separate events into several classes of event topologies is developed. The subsamples are further used to evaluate the sensitivity of KM3NeT/ARCA to the neutrino flavor composition. This is done with techniques of spectral fitting.

This thesis starts with a brief introduction to neutrino astronomy. Chapter 2 summarizes the physics of neutrinos, starting from their production at astrophysical sites, proceeding with the neutrino's journey being subject to neutrino oscillations and ending with the interaction of neutrinos inside the detector. The detection principle and its implementation are outlined in Chapter 3. Standard simulation algorithms necessary for the event identification and flavor composition analysis are introduced in Chapter 4. A systematic study of atmospheric particles as the main background to KM3NeT experiments is described in Chapter 5. A new method of event identification in KM3NeT/ARCA is introduced and applied in Chapter 6. In Chapter 7, the ingredients introduced before are used to calculate the sensitivity of ARCA to the neutrino flavor composition. Finally, Chapter 8 summarizes the contribution of this work to the field of neutrino astronomy and points to future improvements.

Chapter 2

Neutrino physics

2.1 Neutrino properties

In 1930, Pauli postulated the neutrino (ν) for the first time [4]. The existence was proven in the Cowen-Reines neutrino experiment in 1956 [8], which detected the electron neutrino (ν_e). Only 6 years later, the muon neutrino (ν_μ) was discovered in a beam experiment, in which pions decayed to muons (μ) and neutrinos [9]. In 1975, when the τ was discovered [10], the tau neutrino (ν_τ) was predicted consequentially. Only in the year 2000 the tau neutrino (ν_τ) was directly observed in the DONUT experiment [11]. The three neutrino flavors and the three charged leptons are ordered in the standard model of elementary particles in three generations. Each charged lepton is associated with a neutrino, because within the weak interactions a neutrino can create a charged lepton and vice versa. Neutrinos are fermions with a spin of one half. As they are electrically neutral and have no color charge in the sense of strong interaction, they interact only via the weak force [12]. The standard model does not provide a mass term for neutrinos. However, the observation of neutrino oscillations [13] (see Chapter 2.3) enforces a non-zero mass. Kinematics of the Tritium decay constrain the neutrino mass to be smaller than 2 eV [12]. For each of the charged leptons there exists an antiparticle. However, up to now it is not clear if the neutrino is its own antiparticle, namely a Majorana particle, or if not, a Dirac particle. The neutrino-less double beta decay is a type of experiment, which can answer this question [14]. NEXO will be one implementation of such an experiment [15]. Further details of neutrino interactions are discussed below.

2.2 Neutrino production

High-energy cosmic rays arrive on Earth. It is assumed that the production sites of these particles also generate neutrinos [16]. One production mechanism is called bottom-up scenario, in which particles are accelerated to high energies. In contrast, there is the top-down scenario, where ultra-heavy particles decay to lighter ones with given kinetic energy.
Enrico Fermi described the process of stochastic acceleration of charged particles in shock fronts [17], for the first time. Inhomogeneities in magnetic fields move particles back and forth over the shock front. Each transition delivers on average an additional amount of energy to the particle. Finally, the particle can escape the region of acceleration. This mechanism provides a characteristic energy to each acceleration site according to the size of the site. At energies above $\sim 10^{19}$ eV the escaped protons can interact with the photons of the cosmic microwave background. This effect is called the **G**reisen-**Z**atsepin-**K**uzmin (GZK) cutoff, which becomes important, if the travel path is longer than 50 Mpc [18]. An other possibility for the particle is to interact in a shock front with the surrounding matter producing secondary particles traveling through space. The resulting particles can carry a huge amount of kinetic energy. The confirmation of the GZK cutoff [19] favors the bottom-up scenario [16],

so the top-down scenario is not further considered here.
As for KM3NeT the production of neutrinos is most important, this part concentrates on these. If the particles interact with matter, mostly pions and kaons are created. At low energies the pions dominate over kaons, but for high energies kaons also contribute.
The following processes can be found in astrophysical objects as well as in the Earth's atmosphere. The pion decays further in the process

$$\pi^{\mp} \rightarrow \ell^{\mp} + \nu_{\ell}(\bar{\nu}_{\ell}) \tag{2.1}$$

where $\ell = \mathrm{e}, \mu$ [20].
The process produces no ν_{τ} as leptons with smaller mass are only allowed. A ν_{τ} is only created in decays of charmed particles. As the lifetime of charmed mesons is very short, the additional component is called the prompt component. This is not regarded in detail here as it is expected to be negligible [21]. More information can be found in Chapter 5 describing the prompt neutrino component of atmospheric neutrino flux. Although the electron can be produced, this branch is suppressed as the decay width depends on the mass of resulting leptons. The electron production is suppressed by a factor of $1.23 \cdot 10^{-4}$ [12] with respect to the decay to muons [20, 22].
The muon decays further via

$$\mu^{\mp} \rightarrow \mathrm{e}^{\mp} + \nu_{\mathrm{e}}(\overline{\nu}_{\mathrm{e}}) + \overline{\nu}_{\mu}(\nu_{\mu}), \tag{2.2}$$

which creates additional $\nu_{\mathrm{e}}(\overline{\nu}_{\mathrm{e}})$ and $\nu_{\mu}(\overline{\nu}_{\mu})$. Finally there is a total flavor composition of 1:2:0 for ν_{e}:ν_{μ}:ν_{τ}.
The last mentioned step is only possible if the muon decays. If the surrounding media is so dense that the interaction length becomes much shorter than the decay length, no additional neutrinos are created. This so-called muon-damped scenario leads to a composition of 0:1:0, therefore only muon neutrinos are produced.
Otherwise, there is the possibility to create only ν_{e}. Hereto, neutrons decay via the classical β-decay [20]:

$$\mathrm{n} \rightarrow \mathrm{p} + \mathrm{e}^{-} + \overline{\nu}_{\mathrm{e}}. \tag{2.3}$$

The most favored flavor composition is 1:2:0. The other scenarios are disfavored as most likely neutrons interact before they decay. However, the density of the astrophysical sources is assumed not being sufficient enough to lead to the muon-damped scenario. Moreover, the ratio can be energy-dependent [23] or more tau neutrinos than commonly assumed can be produced [21].

2.2.1 Neutrinos from astrophysical sources

Commonly, the sources for high-energy cosmic rays are split into two populations. Firstly, there are the objects inside the Galaxy, which dominate up to the so-called knee in the cosmic-ray spectrum slightly above 10^{15} eV. For example, these are supernovae remnants (SNR), X-ray binaries or pulsars. Secondly, there are production sites located extra-galactic, i.e. outside of our Galaxy. Here, especially active galactic nuclei and Gamma Ray Bursts have to be mentioned. For each component one candidate is highlighted, for more candidates see reference [16].
A supernova remnant is a source of high-energy neutrinos, commonly observed as galactic. When a dying star collapses, the falling shell rebounces at the inner core. Afterwards a shock front is moving outwards through the inter-stellar media. Particles can be accelerated via the Fermi acceleration as described, above. The neutrino yield can be derived from cosmic-ray observations assuming a hadronic production. For detailed calculations see reference [16].
One of the extra-galactic source candidates is the active galactic nucleus. It is a massive black hole in the center of a galaxy. The nucleus is activex, when it accretes matter from a disc of dust around the black hole. A jet is formed perpendicular to the disc and moving outwards. Again, a shock front is the source region of high-energy particles.

The observed cosmic ray flux obeys a nearly perfect power law. Only minor modifications like the *knee* and the *ankle* are observed. As the neutrinos are originated in the same processes, the shape is to be very similar.
In this work, two different ways of modeling the flux are evaluated. Firstly, the flux is treated as a simple power law. Secondly, assuming the particles are only accelerated to a maximum energy, the flux needs to be modeled with a cut off.
The benchmark flux per flavor in the power law model is defined as

$$\Phi(E_\nu) = 2.3 \cdot 10^{-18} \left(E_\nu/100\,\mathrm{TeV}\right)^{-2.5} \mathrm{GeV}^{-1}\mathrm{s}^{-1}\mathrm{cm}^{-2}\mathrm{sr}^{-1}, \tag{2.4}$$

where E_ν is the energy of the neutrino. This flux is based on the combined flavor analysis [7] performed by the IceCube collaboration. The multiple datasets with different neutrino contributions were fit simultaneously. However, there are still large uncertainties associated with these values. The $1\,\sigma$ confidence level for the normalization gives a 20% variation. The spectral index can vary from 2.41 to 2.59 in the $1\,\sigma$ range. Therefore, larger or smaller normalization or varying spectral indexes are treated as nuisance parameters in the flavor composition analysis (see Chapter 7).
The benchmark flux with cutoff is given by:

$$\Phi(E_\nu) = 1.0 \cdot 10^{-8} \left(E_\nu/GeV\right)^{-2} \exp(-E_\nu/3\,\mathrm{PeV})\,\mathrm{GeV}^{-1}\mathrm{s}^{-1}\mathrm{cm}^{-2}\mathrm{sr}^{-1}. \tag{2.5}$$

The cutoff is defined at 3 PeV introduced in the exponential decay term. The normalization was reported when the spectral index is fixed to a value of -2. This flux is leaned on recent IceCube measurements with up-going neutrinos [24].
Figure 2.1 shows the two models side by side. The measurement of IceCube relies on the neutrino flux in the range from 10^4 GeV to 10^7 GeV. As the normalization of both fluxes has to be equal in the region of measurement, the spectral index has to be different. In particular the flux with cutoff has to be less steep. Without the change in the spectral index, the observed neutrino flux canx not be modeled.

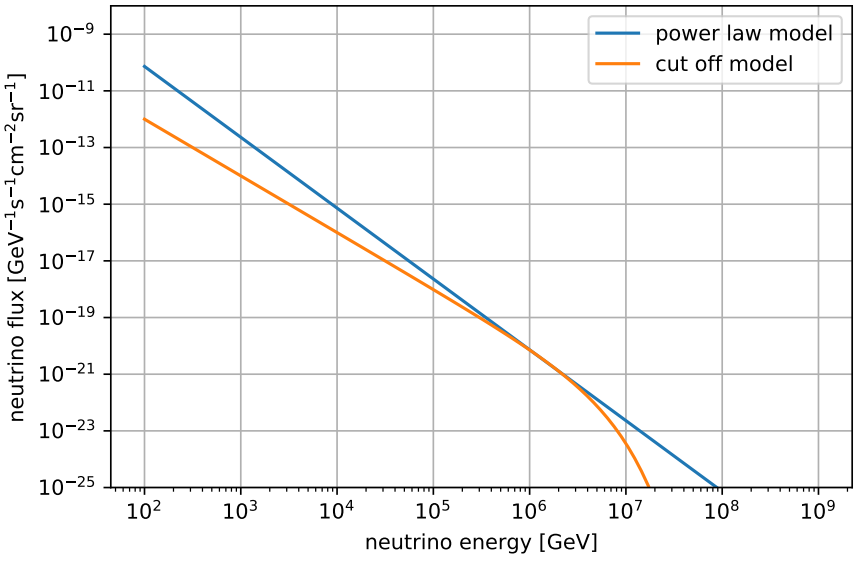

Figure 2.1: The two different models used to model the astrophysical neutrino flux based on current measurements from IceCube [7, 24]. Given is a power law of spectral index with cut off at 3 PeV and a spectral index of -2 (orange) and additionally a power-law model without cutoff and a spectral index of -2.5 (blue).

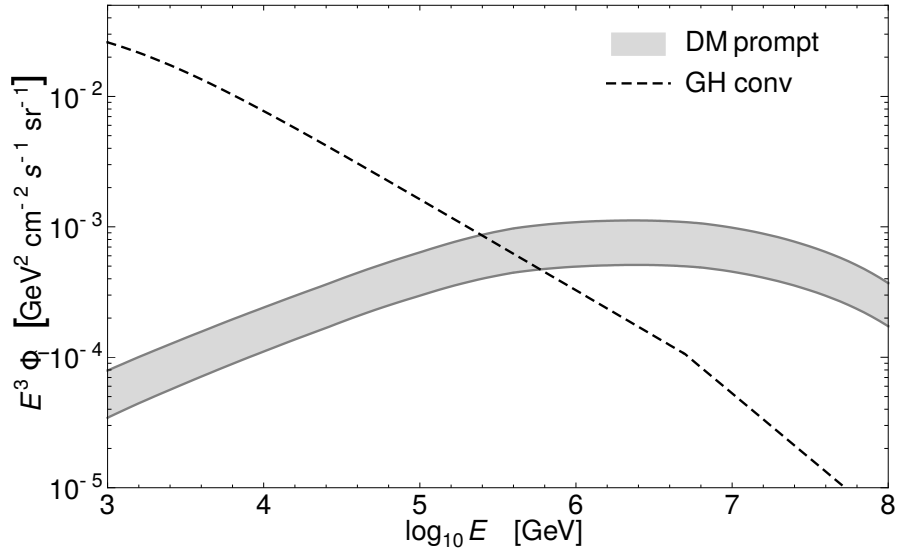

Figure 2.2: Prompt and conventional $\nu_\mu + \overline{\nu}_\mu$ fluxes in the zenith direction. The shaded band indicates the theoretical uncertainty of the prompt flux calculated in [25]. The conventional flux is shown as dashed line with the model of Gaisser and Honda [26]. Figure is adapted from [25]

2.2.2 Neutrinos produced in the Earth's atmosphere

The main background of KM3NeT/ARCA are neutrinos produced in the Earth's atmosphere. As described above, the same processes, which start with accelerated particles like protons, are responsible for the atmospheric neutrinos. In contrast to the astrophysical neutrino production, most of the high-energy muons can survive the path to the detector.
As the path length of atmospheric neutrinos is not long and the energy is high, these neutrinos measured with ARCA are not affected by oscillation. In contrast to ORCA, the oscillation is a fundamental property.
There are two components in the atmospheric neutrino flux. On the one hand, there is the so-called conventional component. These neutrinos are produced by the decay of pions and kaons. In this work, the Honda model is used [27]. The model is based on the DPMJET-III model [28], which was adapted in such a way that the muon flux predicted by the model matches atmospheric muon measurements. The simulation takes the Earth's magnetic field into account. The atmosphere is simulated with the US-standard atmosphere as the authors state that the influence on neutrinos is negligible. Furthermore, the azimuth is averaged from the grounds of the small effect of the Earth's magnetic effect on the high-energy particles. For energies above a few GeV, this is correct, otherwise the muons become deflected by the magnetic field. In Chapter 5.3, the independence to the azimuth is shown for the muon flux in ARCA. One important quantity for measurements is the ratio between electron neutrinos and muon neutrinos. The uncertainty hereon is quoted with 3% at high energies [27]. Consequently, in further analyses this is a subdominant effect and will be neglected as other uncertainties are much larger.
The used model was compared to other interaction models. All models coincide in a range of 25% at 1 TeV. The model is based on a cosmic ray spectrum with a spectral index of -2.71 above 100 GeV. In former analyses, this was simply extrapolated to even larger energies. However, the cosmic ray spectrum shows further features. Therefore, the conventional flux is corrected towardss the H3a cosmic ray flux. In this way the knee is incorporated [29]. The correction is also applied to the second, the prompt component.
To built up the prompt component, in the very first collisions heavier mesons are produced, like D-mesons with a charm quark. They have shorter life times. This flux dominates above 10^5 GeV. In this work, the model of Enberg et al. is used [25]. It was shown that the shape of the spectrum was

independent from the input parameters of the simulation, so only the normalization will vary up to a factor of 2. Figure 2.2 shows the uncertainties in prompt component in comparison to the conventional neutrino flux.
The prompt component can contain ν_τ, but this channel is highly suppressed with respect to the other channels. Further studies have shown that the τ-production can be neglected for current neutrino telescopes [30].

2.3 Neutrino Oscillation

Early neutrino experiments showed a deficit in neutrinos arriving from the sun [31]. For the first time the Homestake experiment encountered this deficit in the 1960es. The experiment was only sensitive to ν_e, because it uses inverse beta-decay $\nu_e + {}^{37}\mathrm{Cl} \rightarrow {}^{37}\mathrm{Ar} + e^-$ for detection. Later it was shown that there is an effect during neutrino propagation: the neutrino oscillation.
Pontecorvo predicted neutrino oscillations even in advance [32]. The standard explanation was derived in the 1970es. It is based on a plane wave description and the propagation of mass eigenstates (ν_k), which are linear superpositions of flavor eigenstates (ν_l). An explanation according to Barger [14] is used here. The different eigenstates are connected via the PMNS-matrix U (**P**ontecorvo–**M**aki–**N**akagawa–**S**akata):

$$\nu_\ell = \sum_k U_{\ell k} |\nu_k\rangle \tag{2.6}$$

with $\ell \in \{e, \mu, \tau\}$ and k as the index of massive neutrino. U is the PMNK matrix given as:

$$U = \begin{bmatrix} 1 & 0 & 0 \\ 0 & c_{23} & s_{23} \\ 0 & -s_{23} & c_{23} \end{bmatrix} \begin{bmatrix} c_{13} & 0 & s_{13}\exp(-i\delta) \\ 0 & 1 & 0 \\ -s_{13}\exp(i\delta) & 0 & c_{13} \end{bmatrix} \begin{bmatrix} c_{12} & s_{12} & 0 \\ -s_{12} & c_{12} & 0 \\ 0 & 0 & 1 \end{bmatrix}, \tag{2.7}$$

where s_{ij} and c_{ij} indicate $\sin(\Theta_{ij})$ and $\cos(\Theta_{ij})$, respectively, with the mixing angles Θ. δ represents the CP-violating phase. For Majoranna type neutrinos further corrections are needed, which are neglected here.
Neutrinos are produced in flavor eigenstates. However, the propagation is driven by the mass eigenstates. The detection shows the flavor state again. As the propagation is in mass eigenstates, the final flavor state is not necessarily the same as the initial state.
For this derivation, it is assumed that there are three flavors of neutrinos. The calculations of additional sterile neutrinos would be similar except with matrices of higher dimension [12]. Additionally, the flavor content measured by experiments like KM3NeT or IceCube might be changed [33].
The solution of the Schrödinger equation for the propagation $i\mathrm{d}\Psi/\mathrm{d}t$ leads to the oscillation probability which is proportional to $\sin^2(\Delta m^2 L/4E)$ (full derivation in [20]). This last term averages for large-distanced astrophysical objects to 1/2. The full oscillation probabilities are given by [20]

$$P_{\ell\ell} = \sum_k |U_{\ell i}|^4 \tag{2.8}$$

and

$$P_{\ell\ell'} = \sum_k |U_{\ell i}|^2 |U_{\ell' i}|^2. \tag{2.9}$$

With given matrix elements one can consider the described production scenarios and derive the flavor composition on Earth. Further approximations are done with the so-called tribimaximal mixing, with ($\Theta_{23} = \pi/4$) and $U_{e3} = 0$.
Figure 2.3a shows the compositions on Earth for the three scenarios described in Chapter 2.2. The most favored scenario of pion decay leads to a equipartition composition on Earth. The scenarios are

mechanism	Source	Earth
pion decay	1:2:0	1:1:1
with muon dumping	0:1:0	4:7:7
neutron decay	1:0:0	5:2:2

(a)

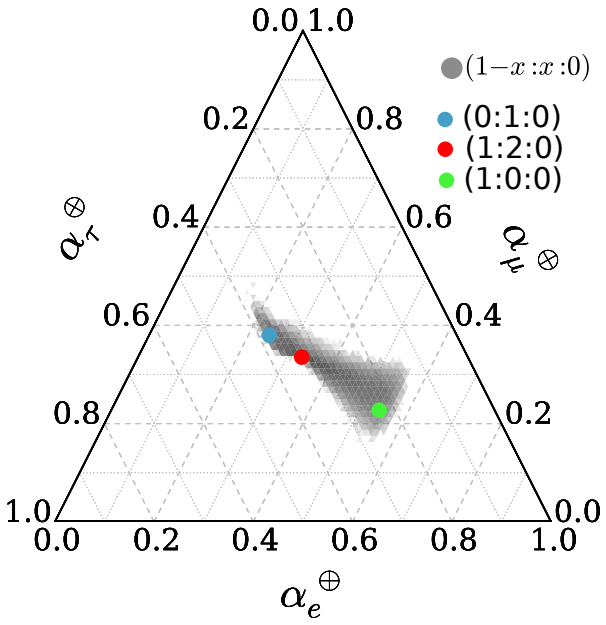

(b)

Figure 2.3: Predicted composition of the neutrino flux on Earth under various production mechanisms, assuming tribimaximal mixing. (a) shows the composition with best fit oscillation parameters for distinct production mechanisms. (b) shows allowed regions of the flavor content on Earth using the results of current oscillation parameter measurements. The intensity of the shaded area is proportional to the probability of the given model values. Figure is based on [35].

also included in Figure 2.3b as colored markers. The three markers lie on a line nearly parallel to the muon axis. Though the scenarios look well distinct, variations can lead to the same outcome on Earth, e.g. if the ν_e-content at source is 1/3, the final composition is 1:1:1 all the time. Additional exotic physics can mimic different source scenarios [34]. Thus, the flavor composition is one jigsaw item to solve the mysteries of neutrino production.
Figure 2.3b draws an even more detailed picture of possible compositions on Earth. Uncertainties of a few percent are attached to oscillation parameters [12]. The effect on the final composition on Earth is shown in this figure [35]. The uncertainties lead to a washed out shape, but the tendency perpendicular to the muon axis is preserved. While developing the event identification (see Chapter 7), one sees that the area of uncertainties in flavor composition is perpendicular to the physics shown here, e.g. it is an elongated shape oriented perpendicular to the ν_μ-axis.

2.4 Neutrino interaction

Building a neutrino detector requires a profound understanding of neutrino interactions. First of all, the number of neutrinos interacting in a detector is important in order to calculate the sensitivity to physical quantities. Therefore, the cross section of neutrinos with targets in the detector is discussed here.
Following Figure 2.4 from bottom to top, the least dominant process is the scattering of neutrinos on electrons via the exchange of a Z-boson. This process is suppressed due to the low mass of the electron particles by almost four orders of magnitude compared to the other shown interaction channels. There is one notable exception. The $\overline{\nu}_e$ can undergo a resonance with the production of an intermediate W-boson in the $\overline{\nu}_e$ e^--interaction, which is called the Glashow resonance [36]. This process is by far the most prominent interaction and takes place for 6.3 PeV [37].

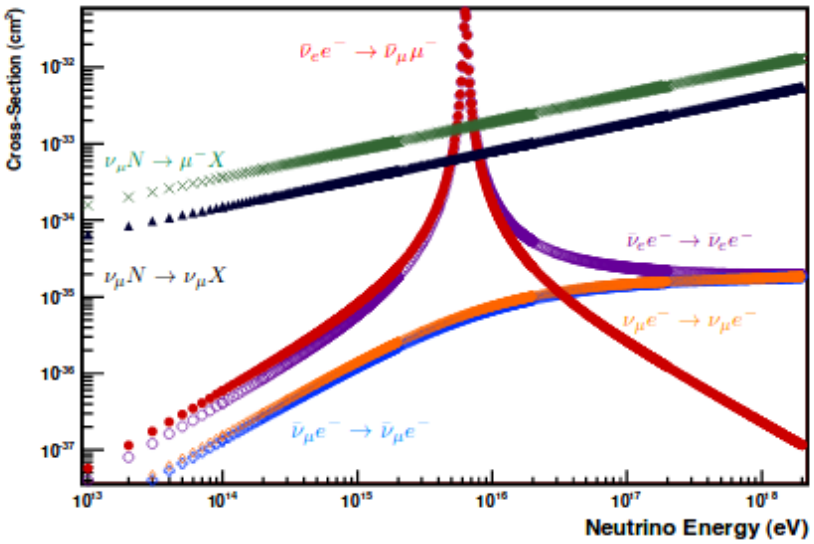

Figure 2.4: Neutrino cross section with respect to the neutrino energy. If not stated otherwise, the ν_μ can be replaced by any other neutrino flavor, which will give a similar cross section. N stands for a nucleus and X for secondary particles producing a cascade. Figure taken from [37].

Furthermore, the interactions of neutrinos with nuclei (N) are important. The neutral current (NC) is the interaction with the second highest cross section. Here the neutrino scatters at the nucleon, where the energy is transferred to the nucleon initiating a hadronic cascade. The neutrino leaves the interaction vertex unchanged.
The charged current (CC) is the largest source of interaction. Its cross section is twice the cross section of NC. The difference can be derived from the difference in the exchange boson [37]. Here the neutrino interacts with the nucleon and the neutrino changes to the corresponding lepton. For energies above a few GeV, the deep inelastic scattering dominates [37]. In this case the neutrino interacts directly inelastically with one of the partons inside the nucleon [20][37].
To describe the interaction in more detail, the Bjorken y variable is defined:

$$y = \frac{E_\nu - E_\ell}{E_\nu}. \tag{2.10}$$

Bjorken y is the energy transfer to the hadronic system. The higher the value, the more the hadronic cascade dominates the event.
The predictive power of cross section is important for the interpretation of experiments. The cross sections are extrapolations starting from available beam measurements.
The design of a neutrino telescope has to be optimized to the distribution of particles and the light yield. Furthermore the knowledge of the event topology, e.g. the particle and light distribution, is fundamental to the analysis. First of all, this is relevant for the reconstruction of energy and direction. Besides, the topology helps to identify the type of interaction. Therefore, the relevant topologies are described in the following with their consequences on reconstruction and identification.
The neutrino cannot be detected directly. For this purpose, the figure visible in the detector is based on the light emitted by secondary particles in the neutrino interaction, hence the charged secondary particles are considered, because they can emit Cerenkov radiation. A charged particle moving faster than light in the surrounding medium emits a characteristic optical radiation by polarization effects in the medium. The angle Θ_C between particle's direction and the Cherenkov radiation is given by:

$$\cos\Theta_C = \frac{1}{n\beta} \tag{2.11}$$

with n as the refraction index and β as the velocity of the particle in units of the speed of light. This leads to a rotational symmetric Cherenkov cone which moves with the particle. The Cerenkov angle Θ_C is given with 42° for the water in KM3NeT. [38]

2.4.1 Interactions of neutrinos of all kinds of flavor in the neutral current

The products of neutral current (NC) interactions are particles with low interaction length in the order of a few tens of centimeters. Therefore, the elongation of the particle cascade is at the order of a few meters up to twenty meters. All photons, which can be detected, are emitted at this small space. In contrast to the size of KM3NeT with vertical distance of 36 m and horizontal spacing of 90 m, the emission looks like a point source. Nevertheless, there are particles like the pion which can decay to muons. These muons can leave the region of the cascade vertex. This effect is by far below a one percent level as seen in the simulations.
Each particle on its own produces a Cherenkov-cone. However, as there are a lot of particles scattering in different directions, the light emission is no longer peaked. Thus nearby the interaction vertex, the probability to detect photons is uniformly distributed in all directions. However, as the photon sensors move apart from the interaction vertex, the probability of detecting light is higher under the Cherenkov angle. Figure 2.5 shows the increasing visibility of the Cherenkov peak with increasing distance. This makes it possible to reconstruct the direction. The reconstruction accuracy reached with KM3NeT is below 2° for these cascades [6].
The energy reconstruction of those events is based on the detected amount of light emitted by the charged particles in the cascade. Herein a drawback is already found: the neutrino carries energy out of the detector, which cannot be measured anymore. The energy lost for the measurement is fixed by the Bjorken y variable. Figure 2.6 shows that the mean value of the Bjorken y variable is energy-dependent. Furthermore, no difference in charged-current and neutral-current is visible. In the low-energy interval, there is a difference between neutrino and antineutrino. This can lead to an identification of them on a statistical base. Concluding every reconstruction can only give a lower estimate of the incoming neutrino energy, as the Bjorken y distribution shows a clear hint for outgoing energy.

2.4.2 Interaction of ν_e in the charged current

Like the neutral current events described above, ν_e in the charged current (CC) produces only particles with a small interaction length. Thus, the cascade looks like a point-like source. In contrast to NC events, the neutrino changes to an electron. The electron initiates an additional cascade, so that there are two cascades at once: an electro-magnetic cascade and the hadronic cascade originated from the disrupted nuclei. Both cascades overlap and look like one cascade. Finally, all energy is deposited inside the detector and no invisible particle leaves. For KM3NeT, the ν_e-CC event is the best case in sense of energy estimation. The standard deviation in the energy reconstruction is approximately 5% [6].

2.4.3 Interaction of ν_μ in the charged current

In the past, the by far most investigated channel of neutrino interaction in neutrino astronomy was the ν_μ-CC channel. The most beneficial part of this channel is the leaving muon. As muon looses only a small fraction of its energy on its path, it can travel easily out of the detector. Furthermore, if a neutrino interacts outside the instrumented volume of the detector, the muon can nevertheless travel to the detector and cause a signal. While the directional information is washed out in cascade topologies, it can be derived from the outgoing muon in case of this event type. The long leaver arm helps a lot to fix the direction. The difference in direction of a leaving muon and an incoming neutrino

is below 0.1 degree above a few TeV and decreases to values below the reconstruction accuracy for higher energy [6]. The performance of reconstruction algorithms in KM3NeT reaches 0.1°. For the energy reconstruction, the energy of the muon is used. This again results in a lower bound for the initial neutrino energy. The standard deviation of $log_{10}(E_{reco}/E_{\mu})$ is above 0.3.

2.4.4 Interactions of ν_τ in the charged current

Presumably the channel with the most different final states is the ν_τ interaction via charged current. Figure 2.7 shows the signatures which can be detected. There is the classical double bang, which was first described in 1995 [40]. The term ”bang” is used as synonym of cascade here. The position of the interaction of the neutrino determines the first bang. The second bang is either an electromagnetic

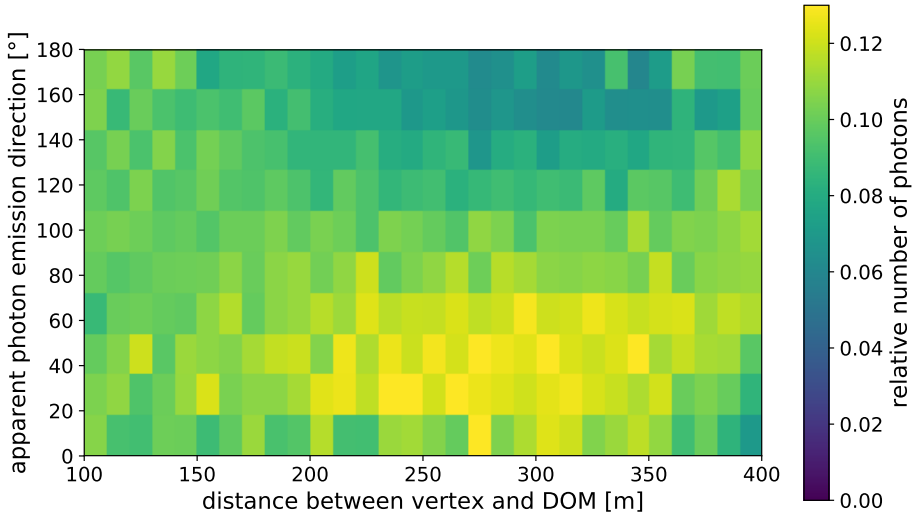

Figure 2.5: Solid angle-corrected distribution of detected hits. Each bin in distance is normalized to one. Unweighted triggered ν_e-NC events are used according the simulated spectrum from $1 \cdot 10^3$ GeV to $1 \cdot 10^8$ GeV.

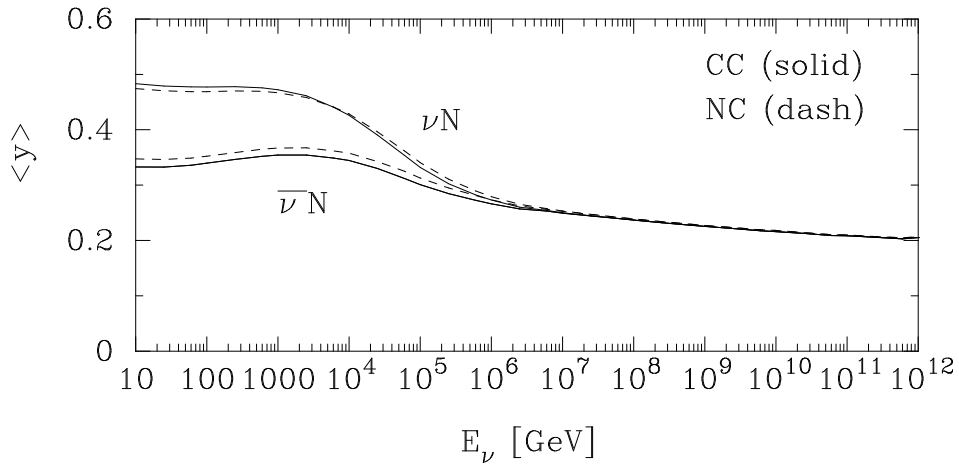

Figure 2.6: Mean value of the Bjorken y variable for charged-current (solid lines) and neutral-current (dashed lines) interactions as a function of the incident neutrino energy. Figure taken from [39]

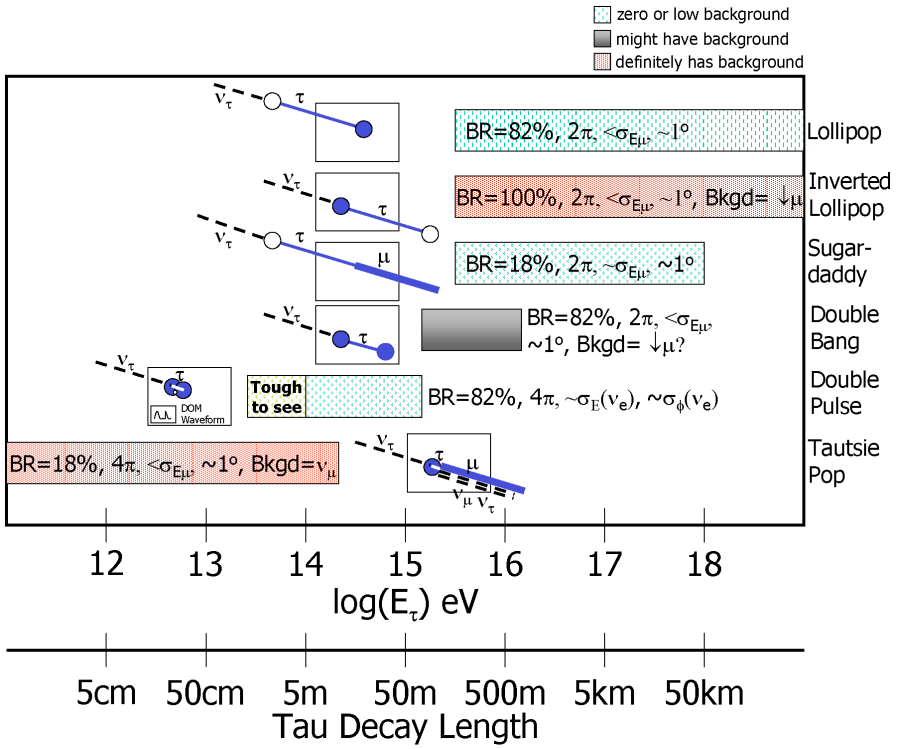

Figure 2.7: Summary of ν_τ-interaction channels shown as a function of energy and approximate tau decay length. The branching ratio and possible background is given, too. Figure taken from [42]

cascade (branching ratio $\sim$ 17% of the τ decay) or a hadronic cascade ($\sim$ 67%) [12]. In total, this channel composes a 84% branching ratio [12]. However, not all bangs will be detected as two bangs as either the first or the second event can lie outside the detector. These are treated as one of the other ν_τ-CC topologies. The crossover from double bang to other classes depends on the detector geometry and the interaction vertex of the ν_τ. Considering a mean decay length of a τ (τ decay path length of 5m/100TeV), ARCA can host τ double bang with at most 10^7 GeV due to the limiting size. With a looser definition of containment, the threshold can be set slightly higher. The main background will be atmospheric muons with multiple catastrophic energy losses, which mimic the cascades. A tailored tau double bang reconstruction is in development for KM3NeT.

Beside this fully contained topology, there are multiple semi-contained event topologies. One of the partially contained topologies is the lollipop event, where the first interaction vertex is not inside the detector. The tauon travels into the detector and interacts leading to the second cascade. Hence there is a track of the tau and afterwards a cascade. This inverse structure can only be mimicked by a muon which is stopped inside the detector.

The other way around forms a similar image but the timing is reversed. The event is called the inverted lollipop. The interacting neutrino initiates a cascade and the tauon leaves inside the detector. The final interaction of the τ is outside the instrumented volume and the detector is not able to see them.

In contrast to a second bang, the tau can decay to a muon with a branching ratio of 17% [12]. The decay produced further a ν_τ via $\tau \rightarrow \nu_\tau + \mu + \overline{\nu}_\mu$. The lighter muon can give a brighter trace in the detector than the much heavier mother particle [41]. A dedicated reconstruction of muon traces could enable to see the jump in brightness [42].

Finally, there is the tautsie pop. Its topology is characterized by the decay of the τ to a μ. Here the decay length is too short to be resolved. It looks like a ν_μ-CC event, but not all energy transferred to the tau is also transferred to the muon as the neutrino consumes energy which is invisible for the detector. However, on a statistical basis, this topology will change the spectrum of reconstructed energy. Events of higher energy are shifted towards lower energies.

Chapter 3

KM3NeT: A worker for neutrino astronomy

After the prediction of neutrinos in 1930, it took quite a while until the possibility of neutrino astronomy was conceived. First, detectors in large mines were proposed, but in the early 1960es Markov [43] suggested to instrument large natural volumes of water or ice. The detection principle is the same for all neutrino telescopes either in water or in ice, but the technical implementation has to be chosen differently. As the interaction cross section is small and the flux for high energy astrophysical neutrinos is small, too, a large volume has to be chosen. Naturally available media are favorable with respect to cost.
In the interaction, secondary, electrically charged particles, are produced. They produce Cherenkov light as described in Chapter 2. With this knowledge the kinematic parameters of particles can be reconstructed. The light yield is in the order of hundreds or thousands of photons. Therefore, the sensors have to be sensitive for single photons for this purpose **p**hoto **m**ultiplier **t**ubes (PMT) with a nanosecond resolution are chosen.
The historical review given below follows [44]. The first instrument in water was DUMAND starting in 1975, a not successful experiment. Nevertheless, the idea was pursued further and AMANDA operating in ice was active from 1997 to 2009. The successor is IceCube, which still operates at the geographic south pole. For the future, IceCube Gen2 is planned, which is ten times the size of IceCube.
The Baikal neutrino telescope was the first underwater construction which was able to reconstruct muon tracks and measure the atmospheric neutrino flux. In the Mediterranean Sea a few experiments were implemented, namely the NEMO and the NESTOR project, pursued by Italy. ANTARES, which has operated since 12 years, has contributed significantly to the development of neutrino astronomy besides IceCube. All these water Cherenkov telescopes helped to enable KM3NeT.

3.1 KM3NeT

In the previous chapters, the physics of neutrinos was introduced. The KM3NeT collaboration, consisting of institutes distributed all over Europe and some more countries (see Figure 3.1a), is taking the challenge to build up a neutrino research infrastructure with two planned neutrino detectors. One of these is tailored to the **O**scillation **R**esearch with **C**osmics in the **A**byss (ORCA) at the French coast near Toulon. This work mostly deals with the other initiative: the **A**stroparticle **R**esearch with **C**osmics in the **A**byss (ARCA). Figure 3.1b shows where ARCA is located, near Portopalo at Sicily, Italy with the exact coordinates of 36°16′N and 16°6′E . The position is chosen because the detection of neutrino has special requirements. A dominant background is the atmospheric muon flux (see Chapter 5), which makes a shield necessary against the muon flux. As many other experiments located deep in the rock, KM3NeT is built under a huge column of water. The detector anchors at a ground depth of 3.5 km. The top level of ARCA is at 1.9 km depth. The shield suppresses the muon rate from 500 kHz at the sea surface to 1 kHz at the top border of the detector.

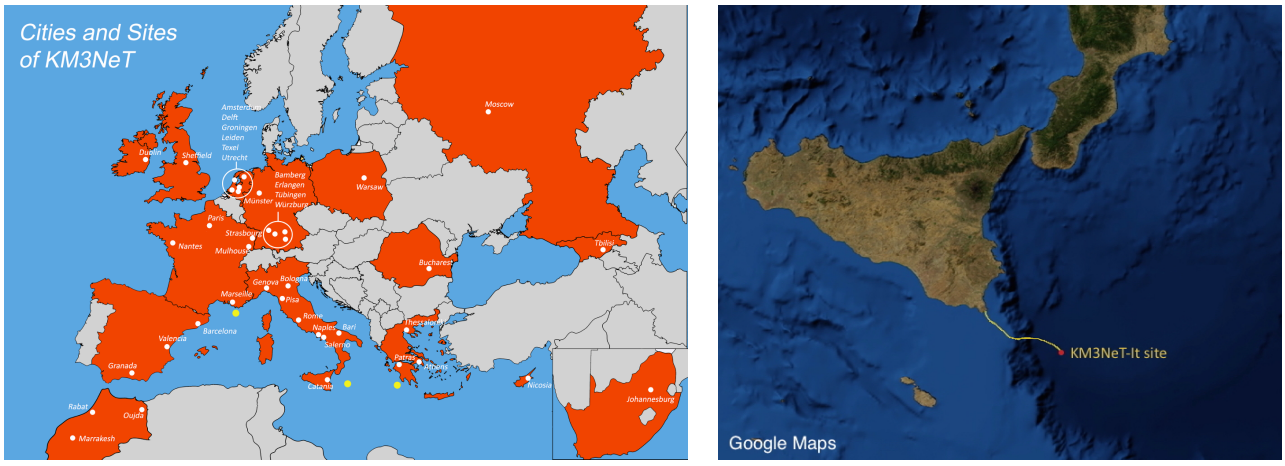

(a) (b)

Figure 3.1: Important locations for the KM3NeT collaboration. (a) Cities hosting collaborating institutes and the three possible sites for instrumentation [45]. (b) Location of KM3NeT/ARCA site 100 km offshore from Porto Paolo, Sicily, Italy. The detector is placed in a depth of 3500 km [6].

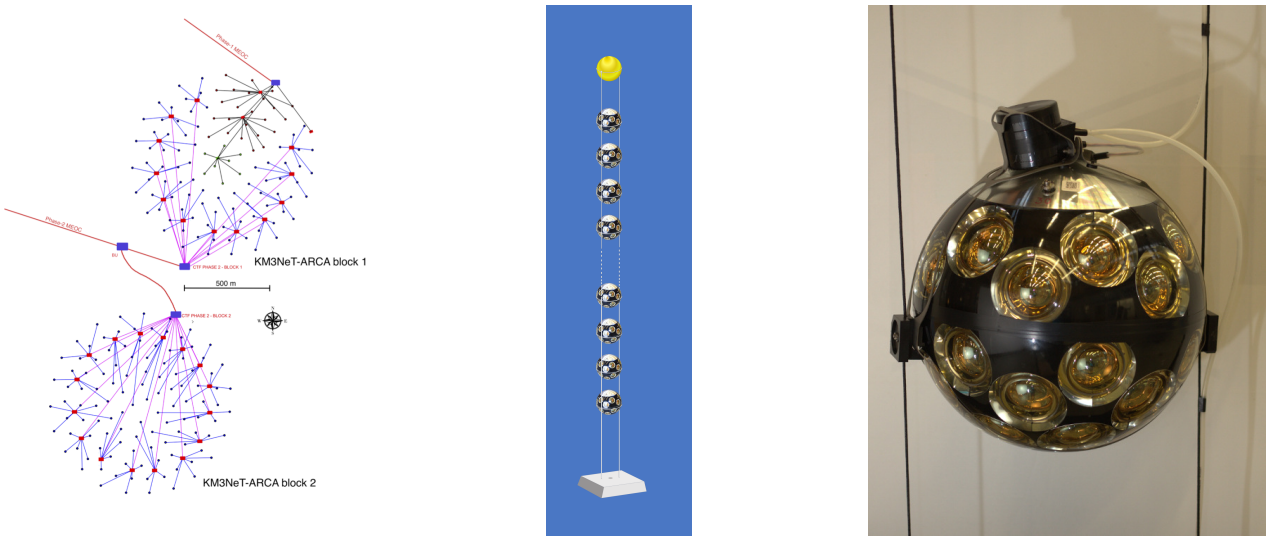

(a) (b) (c)

Figure 3.2: Technical details of the KM3NeT detector. (a) the footprint with connections for data transfer and power supply. (b) One detection unit equipped with Digital Optical Modules. (c) Digital Optical Module attached to the Dyneema ropes. Images from [6]

The detail structure of ARCA is a three dimensional spatial grid of photo sensors. The photo sensors are PMTs to achieve single photon detection. The PMTs are arranged in the **D**igital **O**ptical **M**odules (DOM) in a way to achieve a 4π coverage as shown in Figure 3.2c. Each DOM is a 17 inch glass sphere. 18 of them attached to two ropes comprise one **D**etection **U**nit (DU). Although the DOMs already give uplift, the DU is straightened by a buoy at the top end and an anchor at the see bottom. In total, one DU is about 700 m high and is equipped with 18 DOMs in a equidistant of 36 m. Figure 3.2b shows one detection unit. The DU itself is modular so the detector can be built with numerous units. In KM3NeT one detection block consists of 115 DUs. Figure 3.2a shows the planned ARCA in its entire extent, consisting of two blocks. The total instrumented volume with two building blocks is 1 km^3.

As the environment of KM3NeT/ARCA is defined, one can see the main background to the neutrino detection. First of all, there is the atmospheric muon background, which will be characterized later. Secondly, life is present in the deep sea. Plankton and other animals produce light which is visible in bursts and a background which is constant on a time scale of hours up to several days [46]. The third type of background is the ^{40}K-decay. The small quantity of radio active ions dissolved in the salty water bombards the detector constantly with single photons [6]. This stream of photons hides neutrino events, but its constant flux can be used to calibrate the detector [47].

3.2 Future prospects of neutrino astronomy

With the detection of the first astrophysical neutrinos the neutrino astronomy has started into a promising future. Future detectors will get closer to the physical boundaries. The reconstruction of high energy cascades benefits from a large volume as it is most reliable if the cascade is contained inside the detector. Additionally, a larger monitored volume increases the event rates. At some point, the resolution meets intrinsic limits and cannot be improved anymore. A split of the detector into smaller units like in KM3NeT makes the deployment and the maintenance of the telescope easier.
Beside KM3NeT, there is another water **C**herenkov telescope currently being built up, the **G**igaton **V**olume **D**etector (GVD) in the Lake Baikal [48]. The instrumented volume will be 1.5 km^3.
Further improvements towards higher energies and more effective volume can be achieved with the IceCube Gen2 detector, which is in the design phase. The instrumented volume is planned up to 10 km^3 [49].
Apart from water Cherenkov detectors, there are other detection strategies which can be used for neutrino astronomy. On Earth there is another transparent medium available in huge amounts, the atmosphere. Air cascade experiments are supposed to measure neutrinos interacting in the upper atmosphere [50]. The events are measured in two different ways, detection of Cherenkov/fluorescence light like it is done with Auger or coherent radio emission, first predicted by Askaryan [51] and further suggested for particle detectors in 1965 [52].
Efforts have been already made with RICE [53], ANITA [54] and with AURA within IceCube [55]. Future prospects are expected from the Askaryan Radio Array (ARA). With an instrumented area of 200 km^2 it can monitor more than 10 km^3 of ice [56]. Even larger would be ARIANNA [57], planned to cover an area of 1000 km^2. These telescopes would see around 10 to 100 events per year at the very highest energies to give a clear signal to the astrophysical neutrino flux.
Beside high-energy extensions, detectors for energies below 100 GeV are planned in addition. Their names are DeepCore in IceCube and ORCA in KM3NeT and PINGU in IceCube.

Chapter 4

Detector Simulation

Monte Carlo simulations are used to estimate the expected detector response. The simulation has to treat the interaction, the propagation and the generation of Cherenkov light as well as the response of the detector, including noise. Most of the software packages used were initially developed from the ANTARES Collaboration. The KM3NeT Collaboration adopted the packages to the new needs.

First of all, the software simulates the neutrino flux of particles through the detector. Therefore, the propagation of particles through the Earth is simulated. Afterwards the interaction of neutrinos and secondary particles is treated in rock and seawater.

For the simulation, the so-called *can* needs to be defined. The *can* is defined as the instrumented volume enlarged by three times the absorption length of light in water. This way ensures that all events, which the detector can potentially reconstruct as enough light reaches the detector, are simulated. For neutrino events with short range products (e.g. cascade-like events), the generation takes place in this volume. Muons are generated in a larger volume and are propagated to the *can* as they are characterized by a larger free path length. MUSIC [58] is used for the propagation of muons through rock and water. τ leptons are propagated as minimizing ionization particles by a dedicated simulation software. Both neutral current and charged current interactions are simulated. Furthermore, all three neutrino types are simulated. [6]

Particles which move inside the *can* are subject to further software, treating the interaction inside the detector. The particles propagated to the *can* are simulated with GEANT [59] within the *can* volume. For the ν_τ channel, only decays with two or three products are simulated. Here TAUOLA [60] is used. These interactions represent up to three quarters of the total branching [12]. The channel, in which the τ decays further to the muon, is kept with the branching ratio of 17%, but the rest is renormalized to a total of 100%. Hadronic and mixed hadronic/electromagnetic cascades are treated the same as electromagnetic cascades, but the energy is changed according to the particle's type and energy is used. [6]

The next step is the Cherenkov light production. Photons are emitted and recorded at the position of PMTs according to tabulated values. Additional photons caused by the ^{40}K background are added with a rate of 5 kHz. Coincidence hits are considered, too.

The PMT simulation is treated based on lab measurements, which include the absorption and quantum efficiency for photons on the way through the PMT. The measured hits are characterized by the timing when the electrical signal is above a predefined threshold. First, there is the start time when the electrical signal raised to the threshold. Secondly, the time in which the electrical signal is above a predefined threshold, the so-called **t**ime **o**ver **t**hreshold (ToT). The transit time, the time the signal takes for the processing in the PMT, is smeared by a 2 ns Gaussian smearing. The ToT has a maximal value of 40 simultaneous photons and its readout is cut at 255 ns. One photon results in typically 27 ns of ToT. [6]

The last step is the triggering. KM3NeT as well as ANTARES follow the all-data-to-shore principle. Thus each hit detected by an PMT is transferred to the shore station, where trigger algorithms are

channel	generated events	triggered events	spectrum	lifetime
atmospheric muons > 10 TeV	$25 \cdot 10^6$	$7 \cdot 10^6$	MUPAGE	$88.1 \pm 3 \cdot 10^{-2}$d
atmospheric muons > 50 TeV	$8 \cdot 10^6$	$2.5 \cdot 10^6$	MUPAGE	$1112 \pm 8 \cdot 10^{-2}$d
ν-NC	$500 \cdot 10^3$	$75 \cdot 10^3$	-1.4	–
ν_e-CC	$500 \cdot 10^3$	$120 \cdot 10^3$	-1.4	–
ν_μ-CC	$10 \cdot 10^9$	$145 \cdot 10^3$	-1.4	–
ν_τ (ν_τ)-CC to cascade	$600 \cdot 10^3$	$100 \cdot 10^3$	-1	–
ν_τ (ν_τ)-CC to muon	$1 \cdot 10^6$	$80 \cdot 10^3$	-1	–

Table 4.1: Number of generated events and triggered events of the full simulation available for this work. For the neutrino production, the generation spectrum is given but no lifetime as this depends on the spectrum. For atmospheric muons, which are produced with MUPAGE, the lifetime is given. The trigger conditions are the standard conditions as described in [6]

performed online. Hits are called triggered hits, if there are two hits on one DOM within a small time window. The time window is chosen to be 10 ns. There have to be 5 of such hits, which are causally connected within a spherical geometry for cascades and in a cylindrical geometry for tracks. The trigger conditions were optimized, so that most random background is rejected. As atmospheric muon background causes most of the events, the trigger rate is further optimized in a way that the remaining atmospheric muon rate can be handled by the computer farm on shore.
Particle propagation dominates the computational cost for simulation. The cost increases with energy as more secondary particles and consequently more Cherenkov photons are produced. [6]
The KM3NeT collaboration compared the simulation to a deployed prototype detection unit. The similarity showed the reliability of the Monte Carlo simulation. [61]

The atmospheric muon flux at the surface of the *can* is estimated with MUPAGE [62, 63]. The parametric simulation is a very fast way of simulating atmospheric particles. However, MUPAGE is only dedicated to the simulation of muons, so neither neutrinos or the connection between neutrinos and muons are simulated. The reference [62] states that 10^7 Events were generated within one hour on a 2xIntel Xeon Quad Core with 2.33 GHz. A corresponding full Monte Carlo simulation takes in the order of weeks. MUPAGE was developed on the basis of a full cascade simulation called HEMAS [64]. Particle distributions obtained from this full Monte Carlo are the basis to the parameterization [63]. Finally, the muon flux was optimized to fit various experiments. In past days, the reduced computing power was an enormous disadvantage. Nowadays the possibilities of grid computing and CPUs with higher computing power make it possible to produce large amounts of air shower events. Furthermore the particle composition of the primary cosmic-ray flux was given in the HEMAS simulation. After the muon generation, the same steps as described above are used to simulate the detector response.
CORSIKA [65] is used for the correlation of atmospheric neutrinos with atmospheric muons. A detailed description and the physical discussion can be found in Chapter 5 describing studies on CORSIKA.

Table 4.1 shows the number of simulated and triggered events. The simulation of atmospheric muons is separated into two productions. The first production provides events with a bundle energy of at least 10 TeV. Due to the steep production spectrum, which follows the expected spectrum, the number of high-energy events is very small. The second production fills this lack. The production is optimized for events with at least 50 TeV bundle energy. The last column shows the lifetime, the time it takes to see the simulated amount of events with KM3NeT. Even though the number of simulated events in the low-energy range is larger than the other production, the lifetime is about 100 times lower due to the steep spectrum with a spectral index of around -2.7.

effect	variation
change in absorption length	±10%
change in scattering length	±10%
effective area of PMTs	±10%
failure of DOMs	10% DOMs randomly off
failure of DUs	1 DU missing

Table 4.2: Available simulations to evaluate the impact of systematic uncertainties.

The neutrino production is simulated with a spectral index of $\gamma = -1.4$ for all flavors, except the ν_τ, where $\gamma = -1$ is used. Compared to the expected spectral index of -2.0 to -2.5, this provides more simulated high-energy events relative to the low-energy events. $\gamma = -1$ for the ν_τ production was used as the number of high-energy events and the variety was not sufficient for the analysis. Especially the number of τ double-bang events was not large enough for the development of reconstruction and identification algorithms. As the spectral index of the neutrino flux differs from the one given here, no lifetime is stated in Table 4.1.
Most of the physics constants necessary for analyses are only known up to some degree of certainty. Simulations are done with underlying truth, which is reasonable off the standard values. Deviations from the standard values are treated in additional simulations. Table 4.2 shows the systematic effects which are reproduced in simulation. One example is the simulation with an increased absorption length by 10%. For KM3NeT, this would mean that more photons can find their way to a PMT than are detected. The events look brighter than in the reference configuration.
Also the scattering length influences the detector performance. The higher the scattering length, the more prominent is the Cherenkov cone as the light is not deflected. If the scattering length is lower like in ice, the Cherenkov cone is washed out. However, ice comes with a larger absorption length and more light can be detected, which can improve reconstruction. Further possibilities would be to investigate aging effects, which can lead to the failure of parts of the detector. Additionally, an incorrect calibrated detector will harm the results in reconstruction.
There is a difference in systematics. On the one hand, there are systematics, which one does not know beforehand, but can be measured simultaneously to the experiment. For example, the absorption length will be measured with high accuracy in operation, but now it is not known up to the needed certainty. For these effects, one have to see the influence of the performance to the detector. On the other hand, there are systematics, which are not known now and they will be not measured within the data-taking. Here one has to mention some oscillation parameters of neutrinos. ARCA is not geared towards this type of measurement and one has to look to other experiments to get better values in future. Besides the final results carries their uncertainties.

Chapter 5

Atmospheric muons and neutrinos in KM3NeT

The major background for astrophysical neutrinos in KM3NeT are atmospheric neutrinos and muons. In current KM3NeT analyses, the atmospheric neutrino contribution is simulated according to the models described in Chapter 2.2.2 [6]. Changing the spectrum is easily done by re-weighting each event. For example this was applied for the described knee correction. Atmospheric muons are simulated with MUPAGE separately (see Chapter 4). In MUPAGE a fixed cosmic-ray spectrum is used to model the final spectrum [62]. The muon flux cannot be re-weighted in an easy way to other cosmic ray flux models. Another drawback of these two individual productions are the circumstances that there is a connection between them. In the interaction of cosmic-ray particles, muons and neutrinos are produced. Moreover, both types of particles reach the detector simultaneously. However, current simulation treats them independently.
For validating the currently used particle fluxes and getting an idea of systematic errors on the fluxes, an alternative approach is used here. CORSIKA [65] is used with multiple high-energy interaction models to see the differences between them, which will be treated as uncertainties in the end. Finally, the simulation can be used to reject atmospheric neutrinos. Even though neutrinos behave the same whether they arrive from the atmosphere or from extra-terrestrial sources, atmospheric neutrinos can be accompanied by atmospheric muons [66, 67]. This so-called self-veto effect can only be used if neutrinos and muons are generated simultaneously in the simulation.
This section will introduce the reason of atmospheric particles - the cosmic ray flux. Thereafter the atmospheric cascade simulation is developed. The last part is dedicated to the comparison of different interaction models, which lead to the uncertainties KM3NeT is facing with.

5.1 Cosmic Rays

The first step towards the flux of particles generated in the atmosphere is the cosmic ray flux. Several flux models are available. Here a few of them are described to show the differences. The compilation cannot be complete at this point, only spectra which are needed for this work or spectra which seem to be most up-to-date are described and used here.

Poly-gonato The first model to be described here is the poly-gonato model [68]. The model was developed in 2002. Even if it seems to be quite old, it is used for the development of MUPAGE. It is essential to understand the model for the comparison between MUPAGE and the CORSIKA simulation done in the following.
The name is an allusion to the knee visible in the all-particle spectrum. The name is based on Greek and means ”multiple knees”, which are visible in the cosmic-ray flux.

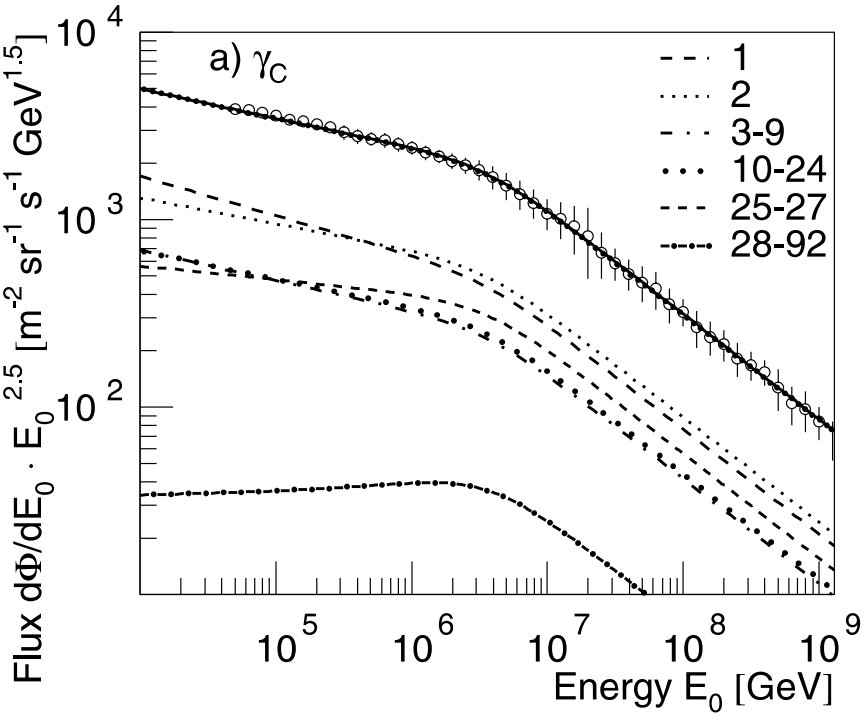

Figure 5.1: All-particle energy spectrum. The circles stand for the normalized average flux measured by air shower experiments. The lines represent for the poly-gonato model for the corresponding nuclei. A common spectral index above the knee and a constant cut-off energy is assumed. Each line stands for a nuclei with given ordinal number. Figure taken from [68].

The development started with experiments ranging from low energies below the knee upwards to the energies above the knee. The model starts with direct measurements from each nucleus. As the direct measurement is limited to low energies up to those slightly above the knee, additional information must be considered. These results are extrapolated towards indirect measurements like air shower experiments (e.g. Kaskade Grande etc.).

Figure 5.1 shows the flux parameterized with the poly-gonato model. Different lines show the flux for different nuclei with their ordinal number Z. The particle spectrum is assumed as two power laws with a transit called cut-off at the knee. The two knees visible in the spectrum can be explained in that way, that the first is the beginning of a cutoff region, whereas the second knee is the end of the cut off region at Z=92, the end of stable nuclei. The cut off is interpreted as the end of a galactic component. An individual cutoff could be introduced for each nuclei, but here a constant value is chosen as it gives the best accordance also in the high energy region. Below the knee for each nucleus, an individual spectral index is fitted according to direct measurements. Two possibilities are tested, first, a constant offset between both spectral indices and second, a common spectral index for all nuclei. Both ideas lead to similar good fits and the common spectral index is chosen for this work. The normalization and spectral index for the region behind the knee is derived from fits. The values from intermediate nuclei from He to Iron were taken from Wiebel-Sooth [69].

The fit is performed to many indirect measurements. All indirect measurements depend heavily on interaction models of the cosmic-ray particles with the atmosphere. It was tried to find experiments using the QGSJeT model [70] as this was most up-to-date at that time. The absolute normalization was widely distributed in the range of a factor of two. All particle fluxes were re-normalized so that the lower boundary matches direct measurements. The normalization is kept in the range of experimental uncertainties, at most at 15%.

Hillas-Gaisser Model (H3a and H4a) The Hillas-Gaisser model [71] is also modeled with multiple power laws. However, it assumes three generations each with a rigidity-dependent cutoff. The rigidity is defined as the total energy per electric charge of the nucleus:

$$R = \frac{pc}{Ze}. \tag{5.1}$$

For a characteristic, rigidity the acceleration process reaches a limit as the gyro radius is larger than the size of the accelerator. The gyro radius is defined as $r = R/B$ with the magnetic field strength B and the rigidity R and gives the radius of the closed curved trajectory of the charged particle in magnetic fields in the accelerator region.
The first population is assumed to have origin from supernova remnants. The second population is also of galactic origin but of unknown source. The last population is expected to be of extra-galactic origin. Each population consists of a composition of different nuclei. The nuclei are dovoded into 5 groups according the atomic number: H, He, C N O, Mg-Si and Mn-Fe. In principle there could be more than three compositions. Consequently, for more differentiated production mechanisms, the three-population model has to be considered as a minimum requirement only [72].
The total flux of one component is given by:

$$\Phi_i(E) = \sum_{j=1}^{3} a_{ij} E^{-\gamma_{ij}} \cdot \exp\left(-\frac{E}{Z_i R_{c,j}}\right), \tag{5.2}$$

where a is the normalization of each population. E is the energy per nucleus and γ the spectral index. This flux is given in units of $\mathrm{d}N/\mathrm{d}\ln E$. The subscript i stands for the different components (1 to 5). The subscript j iterates over the populations.
The values for the first population are derived from direct measurements of CREAM [73, 74]. The other populations are fitted to indirect measurements as shown in Figure 5.2. The complete table is issued in [71].

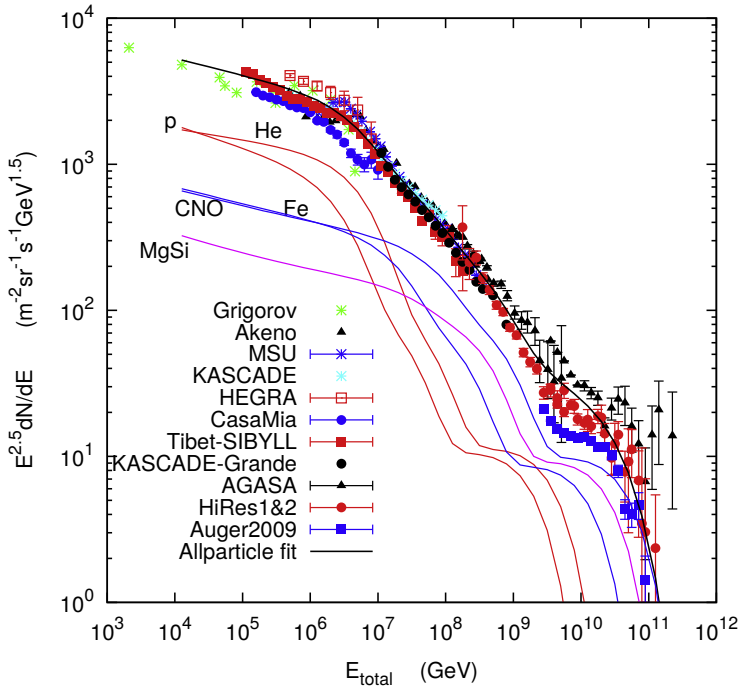

Figure 5.2: The cosmic ray flux model as supposed by H3a for the total nucleus energy. It is composed by three population and five nuclei groups. Dots stand for indirect measurements. Figure taken from [71].

In contrast to the poly-gonato model, this model is extended up the the ankle at 10^{11} GeV. At low energies, the light nuclei dominate the spectrum. Above 10^8 GeV, iron takes the leading contribution. Again due to the rigidity depending cutoff, the proton starts with the knee at the lowest energies and iron concludes the knee at around 10^8 GeV. In addition to the three-population model, one can build a four population model. The differences between these two models are very small. Relevant differences can be shown in the high energy regions.
As the flux does not stop with the cut-off at the first knee, it is higher for large energies than for the poly-gonato model. In this way more features of the spectrum can be modeled. Finally, more recent and more numerous indirect measurements were used for the fit.
In the following, this model is referred as H3a. The third population can be treated as proton only, then it is called H4a.

Gaisser-Stanislav-Tilav model (GST3 and GST4) The Gaisser-Stanislav-Tilav model (GST) [72] is technically the same as the previous one. There are multiple generations in number three (GST3) or four (GST4) composed by grouped nuclei. Though the new model is still the minimum requirement for three populations to model the different features in the cosmic ray flux, the new one was introduced after a hardening of the cosmic-ray spectrum was observed [75]. A harder spectrum can be achieved with a lower cutoff for the first population. Thus the first cutoff is shifted from 4 PeV to 120 TeV. Other rigidity cutoffs are shifted accordingly.
In literature it is stated that the flux composition of high-energy flux is extremely difficult to measure for the very high energy events. First of all this is because of the ”large fluctuations from cascade to cascade, which tend to smear out differences arising from different mixtures” [72]. It seems to be hard to find a way to model the mass composition followed by the all-particle flux. Here the first and second population represents all groups of nuclei, as it is given by the direct measurements. However the third population is composed with protons and iron only. This model is called GST3. Figure 5.3 shows the GST3 model in comparison to measurements. Although the match is very good with regard to to energy, the composition does not fit for high-energy particles as shown in Figure 5.4 with the green line. Similar to the H4a, a GST4 is defined with an additional population after the third one. However, in GST a fourth population is introduced, which consists only of protons and a cutoff at rigidity of 40 EeV. Without this modification there was a disagreement found in the measured atomic mass. GST3 showed a steeply increasing value for the atomic mass while measurements of HiRes, Auger and Telescope Array show a settling behavior at $\ln A = 1$ above 10^9 GeV. The differences between the models in the logarithm of atomic mass number is shown in Figure 5.4.

Figure 5.5 shows the all-particle spectrum of the described models at once. Up to 10^4 GeV, the GST models are lower than the other models. The difference is about a factor of two. For higher energies the GST and Hillas-Gaisser models reach the same level. The poly-gonato falls back as it is modeled only up to the end of the knee region in the spectrum. The other spectra provide similar values for particles with the highest energies. They vary in a band of factor three at most. All models describe the knee at 10^6 GeV.
These models can be compared to the atmospheric models used in KM3NeT up to now. In this work models are only compared in terms of atmospheric muons. Another work dedicated to the flux of neutrinos is ongoing in the KM3NeT collaboration.

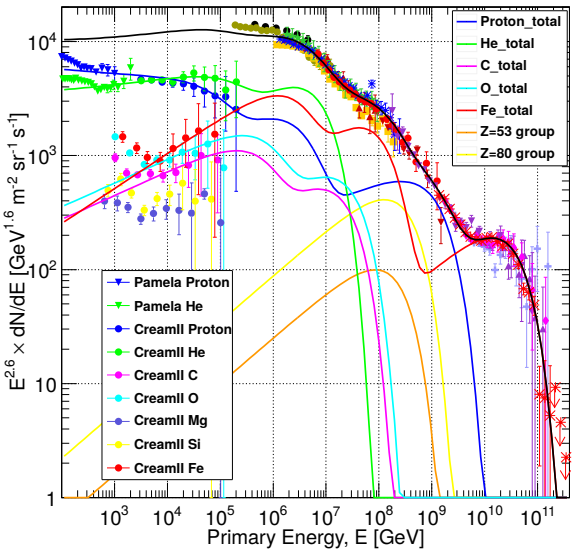

Figure 5.3: GST3 model drawn together with indirect cosmic ray measurements and direct measurements. Solid black line is the total flux. Individual nuclei are drawn, too. Figure taken from [72].

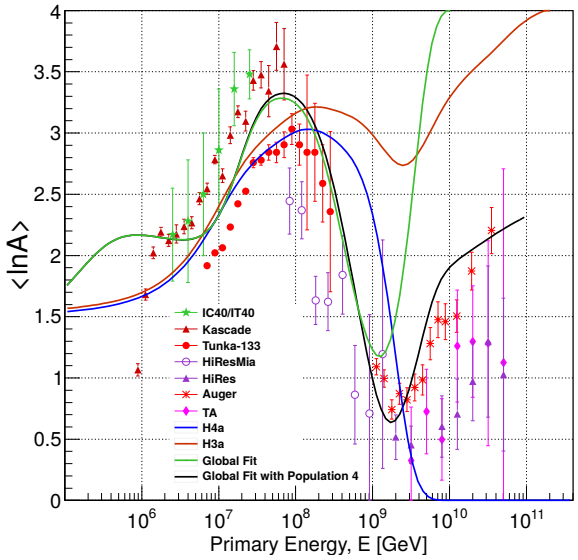

Figure 5.4: Mean atomic mass of cosmic ray. The different models as solid lines. The air shower measurements with markers. Figure taken from [72].

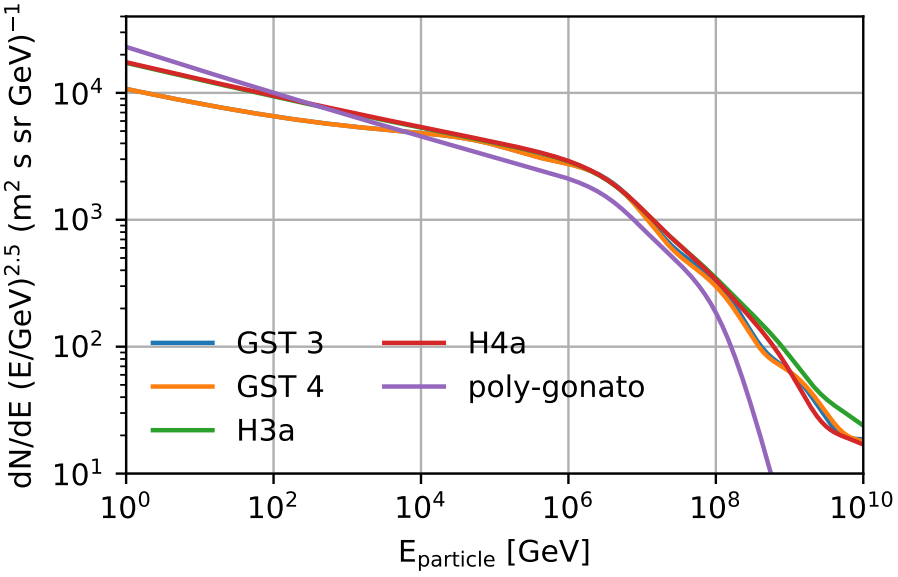

Figure 5.5: All-particle spectrum for described models in this work plotted for total particle energy. GST: Gaisser-Stanislav-Tilav [72], H3a/H4a Hillas-Gaisser [71] and poly-gonato [68]. Figure adopted from [76]

.

5.2 Simulation

Chapter 4 already showed the standard simulation of atmospheric particles in KM3NeT/ARCA. This chapter focuses on an alternative to the usually used MUPAGE simulation package [62, 63].
There are two principles simulating these particles. Firstly, there is a parametric simulation, which is done with MUPAGE [62, 63]. Secondly, a full cascade simulation is possible, by using CORSIKA [65]. The parametric simulation is a very fast way of simulating atmospheric particles. However, MUPAGE is only dedicated to the simulation of muons, so neither neutrinos or the connection between neutrinos and muons are simulated. In the past, the reduced computing power was an enormous disadvantage. Nowadays the possibilities of grid computing and CPUs with higher computing power make it possible to produce large amounts of air shower events. Furthermore the particle composition of the primary cosmic-ray flux was fixed in the HEMAS simulation. The composition cannot be changed.
MUPAGE is extensively used in ANTARES [77] and MACRO [78]. This leads to huge knowledge available. CORSIKA was used in the past for single analysis in KM3NeT, but not for big production. Thus new methods to include simulated events have to be invented. Other experiments like Auger [79] or Kaskade Grande [80] have a huge experience with CORSIKA, resulting in a large enough community to understand the problems inherent in the simulation program.
New possibilities, like higher resolution in the neutrino telescopes enables the physicist to use the connection between neutrinos and muons to access new physics. Therefore, it is necessary to take the step from MUPAGE to a full Monte Carlo simulation. In the following, the parameters to run the CORSIKA and MUPAGE are explained in detail. The list of parameters, which is shown here, is not complete, as only those are chosen which are non-standard or have an increased impact to the simulations. A complete list is given in the Appendix A.

5.2.1 CORSIKA

CORSIKA can be adopted to the experiment's need in two ways. Firstly, there are the compilation parameters, which are given when compiling the CORSIKA software. Secondly, there are options which are given on run time.

Magnetic Field A magnetic field deflects charged particles due to the Lorentz force. There are models available which provide the strength and direction at each site. Here two models are compared. Firstly, there is the World Magnetic Model (WMM) [81]. Secondly there is the International Geomagnetic Reference Field (IGRF) [82].
The field properties are calculated for the ARCA site at 36°16' N 16°06' E. Table 5.1 shows the comparison of the two different models. The magnetic field is taken at the 9th of February in 2015. The values do not differ a lot. The Earth's magnetic field depends on space and time. In the region of interest around the Mediterranean Sea, the magnetic field is smooth, so there are no changes on small distances. The seasonal variations are below 30 nT and can be neglected in analyses.
Further considerations could be made relative to¡F3¿ short term variations as induced by solar flares. Table 5.2 compares the magnetic fields at the ARCA and the ORCA site. The total field is very similar up to a level of 4%. Nevertheless, the inclination is different by 7°. The inclination is the angle between horizon and the field direction. The difference is expected as ORCA is closer to the magnetic pole than ARCA, so the B-field is more horizontal at the ARCA site. The direction of the magnetic field plays a role as particles moving with the same direction as the magnetic fields are not deflected in contrast to particles moving perpendicular to the magnetic field, because the Lorentz force is given by $F = v \times B$.
However, when calculating the gyro radius of a muon with a few GeV, one sees a maximum deflection of 1 m at the Earth's surface, when the particle starts at 20 km height. As the reconstruction does not

Model	Magnetic field North direction [μT]	Magnetic field Upwards direction [μT]	Magnetic Declination [°]
World Magnetic Model [81]	27.67 ± 0.14	34.96 ± 0.17	3.02
International Geomagnetic Reference Model [82]	27.65	34.96	3.02

Table 5.1: Properties of Earth's magnetic field calculated with different models at the ARCA site (36°16' N 16°06' E). Values are calculated for the 9th of February 2015. Only the WWM returns confidence intervals.

detector	total field [μT]	declination [°]	inclination [°]
ORCA	46.3	1.67	58.56
ARCA	44.7	3.2	51.55

Table 5.2: The magnetic field at 17th of May in 2017 at two different sites of KM3NeT with the World Magnetic Model 2015-2020[81]. The small differences with respect to Table 5.1 comes mostly as a different date was chosen.

give such high precision in the reconstruction of the neutrino and muon path, the magnetic field will not influence the results at that very moment.
The magnetic field can be changed at runtime. The declination is not important for CORSIKA as the north direction used by CORSIKA is fixed to the magnetic field.

Atmosphere The atmospheric air showers are heavily dependent on the surrounding media as shown for example in [83]. However, if the atmospheric profile for one site is known as good as currently possible, uncertainties in interaction depth and deposit energy are less than 5% [83]. In CORSIKA, several models are implemented, for example the US-Standard atmosphere, which serves as a kind of reference to other atmosphere models. The atmospheric model which is located closest to KM3NeT sites is the atmosphere above Karlsruhe, developed for KASKADE. However, the climate changes a lot from Germany to Southern Italy or France, so this work develops a new atmospheric model for KM3NeT neutrino facility sites.
There are empiric atmospheric models on the market. They are based on multiple measurements from satellites, ground based station or balloon experiments. In the following, the NRLMSISE-00 model is used [84]. A software, which generates an atmosphere according to the model, is freely available. First of all this model is based on total mass density measurements from satellites. Additionally, the temperature is gained from radar measurements. The model produces a list of atomic composition, total mass density and the temperature. The data is given for each day of a year. For this analysis, the values are averaged over one month.
Otherwise one can have measurements based on radio probes in the atmosphere. In Auger, a rapid atmospheric monitoring system is installed to get live information about the atmosphere, when it is necessary [85]. For the exact status of the atmosphere at certain dates, it might be useful to have an accurate measurement. This can be the case when some extremely rare event was observed. However, for the current preparation phase of KM3NeT, a model is sufficient.
It is important to know that deviations in atmospheric values above around 60 km in height are negligible for atmospheric air shower. Figure 5.6 shows that more than 99% of primary particles interact below 60 km. The heaviest nuclei and therefore the particles with the shortest interaction length are chosen.
For each month, the mean values are calculated up to an altitude of 130 km with five steps per kilometer. Figure 5.7 shows the density profile of the atmosphere for the ARCA site for every month.

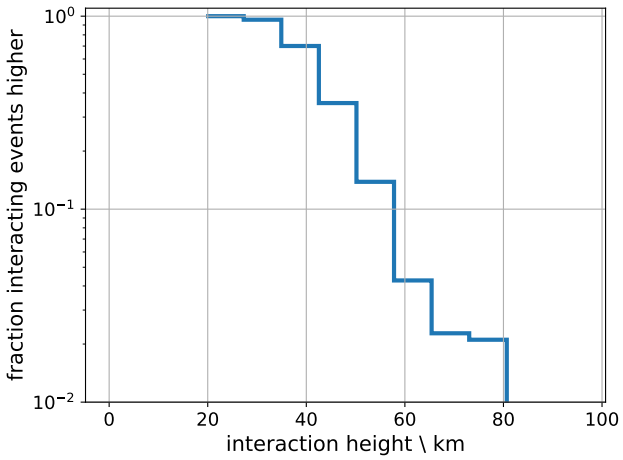

Figure 5.6: Cumulative distribution of the height of first interaction in the atmosphere for iron-nuclei-induced cascades. Showers are simulated with CORSIKA 7.5000 combined with Sibyll2.3 [86] high energy hadronic model. The ARCA mean atmosphere is used. H3a [71] cosmic ray flux is used for weighting.

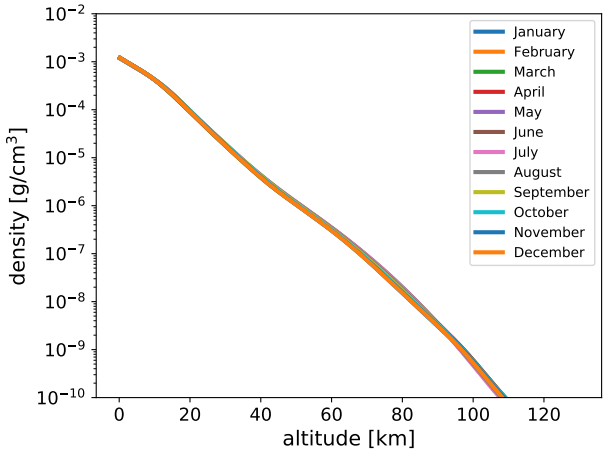

Figure 5.7: density of the model atmosphere derived with NRLMSISE-00 for the ARCA site

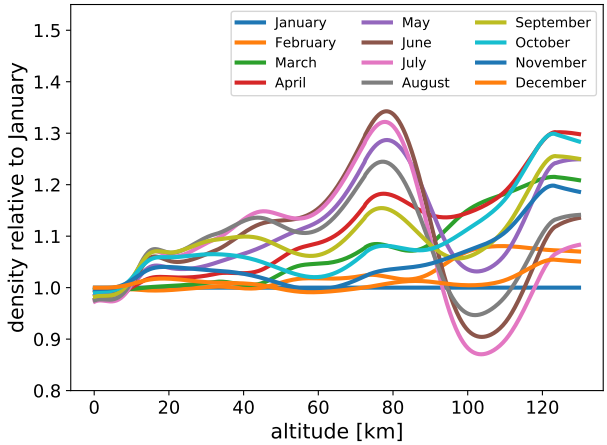

Figure 5.8: density of the model atmosphere derived with NRLMSISE-00 for ARCA site compared to the values of January.

The shape follows a power law. However, there are some deviations corresponding to different atmospheric layers. This power-law behavior suggests the way CORSIKA models atmospheres. CORSIKA will create five layers, each with a exponential behavior. Figure 5.8 shows a more detailed view on the differences over the year. The density at ground level is higher in the winter than in the summer due to colder climate and fewer high pressure regions. The interaction region for air showers shows a contrary behavior. The atmosphere in the summer is denser than the atmosphere in the winter [87].
Finally, the atmospheric depth is most important for particle physics considerations. The atmospheric depth is the cumulative density for a particle that traverses the atmosphere from the zenith. Figure 5.9 shows the variation of the atmospheric depth at the ARCA site over the year. The figure shows again the dip in the upper atmosphere around 100 km where the atmosphere is less deep in the summer months due to upper wind bands [87].
Figure 5.10 shows the variation of the depth for the ORCA site. The shapes are very similar to the ARCA site as both climates are of the Mediterranean type. The variation between summer and winter is larger at the ORCA site in the South of France, compared to the ARCA site which is near Sicily and right inside the subtropical zone [87]. ORCA is located at the top border of the subtropical zone

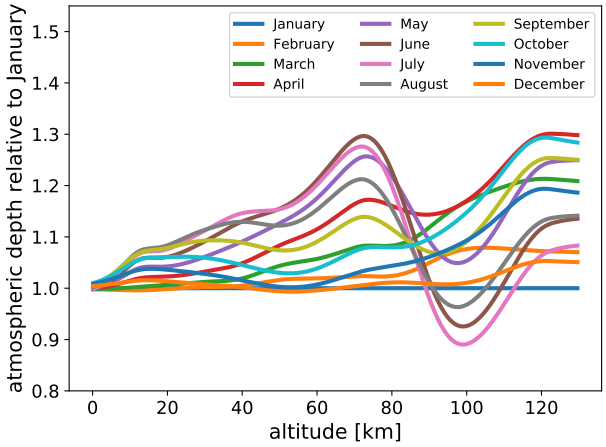

Figure 5.9: depth of the model atmosphere derived with NRLMSISE-00 for ARCA site compared to the values of January.

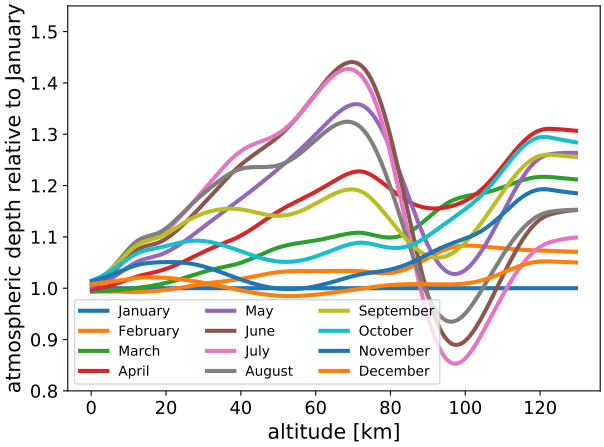

Figure 5.10: depth of the model atmosphere derived with NRLMSISE-00 for ORCA site compared to the values of January.

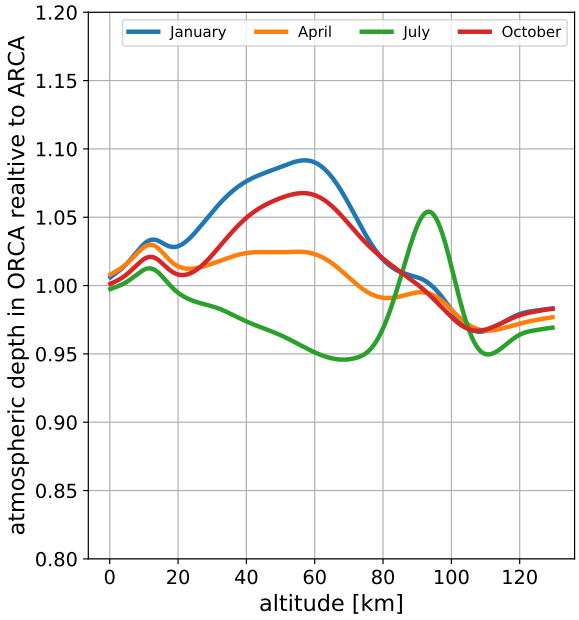

Figure 5.11: Atmospheric depth compared between the ARCA site and ORCA site for each month individually.

and thus has a subtropical summer but a rainy and more central European type winter. The difference between the two sites is illustrated in Figure 5.11. Again, the most dramatic change happens in the upper atmosphere during the summer months. During all seasons, the ORCA-atmosphere is deeper than the one of the ARCA site unless in the summer, when the situation is reversed.
A larger atmospheric depth means that the particles will interact in a higher altitude. In this way, less muons should survive the journey down to the detector.

As soon as the atmospheric data is given, a fit has to be performed. CORSIKA uses a five layer fit [65]. Beginning from the ground, the first four layers are approximated by an exponential function of the shape

$$x = a_i + b_i \exp(-h/c_i) \tag{5.3}$$

where a, b and c are layer-dependent variables, which have to be fitted. h is the height above sea level

and x is the atmospheric depth.
The fifth layer is a linear approximation.

$$x = a_i - h/c_i \tag{5.4}$$

This layer is not very accurate, which is visible in the fits below. Nevertheless, as most of the atmospheric interaction takes place in the atmosphere below 60 km, this is sufficient.
CORSIKA uses the Bernlohr package [88] to perform the fit automatically on a wide range. However, setting the boundaries of the layers is a challenge for the fit algorithm and is therefore better done by hand. The resulting models are shown in the figures 5.12 to 5.15. The complete set of fitted values are in the Appendix A.3.
The true and the fitted graph lie on top of each other. These points are the defined layer boundaries. The overall shape looks promising and the total values for different months are reasonable. The deviation between truth and fit is within a few percent up to 70 km, which is satisfying for the atmospheric particle simulations. In the case of ORCA, the best way is to let the fit overshoot the values of the reality, thus achieving the best overall fit within a 3% deviation from the truth.

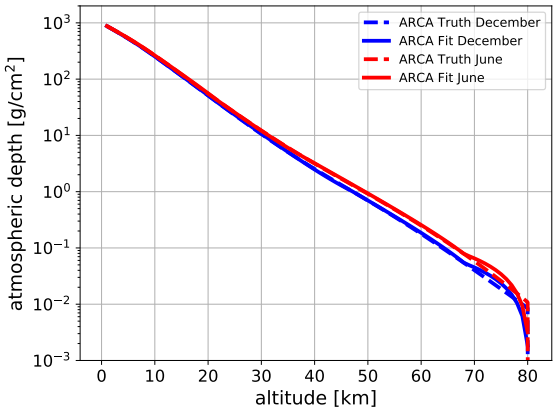

Figure 5.12: The atmospheric depth of the atmosphere at ORCA site. Model atmosphere divided by the fitted one by bernlohr package with adapted layer boundaries.

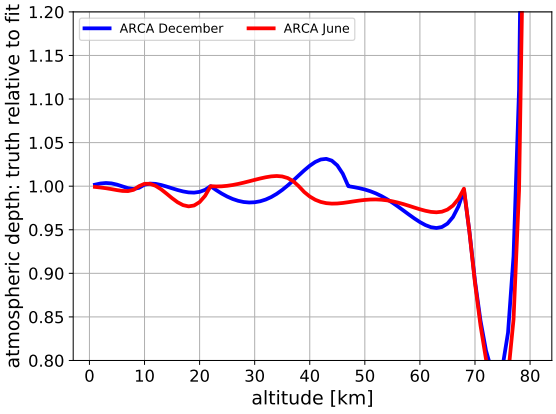

Figure 5.13: The atmospheric depth of the atmosphere at ORCA site. Model atmosphere divided by the fitted one by bernlohr package with adapted layer boundaries.

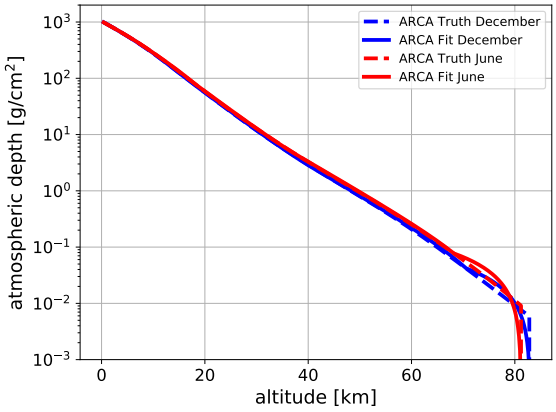

Figure 5.14: The atmospheric depth of the atmosphere at ARCA site. Model atmosphere divided by the fitted one by bernlohr package with adapted layer boundaries.

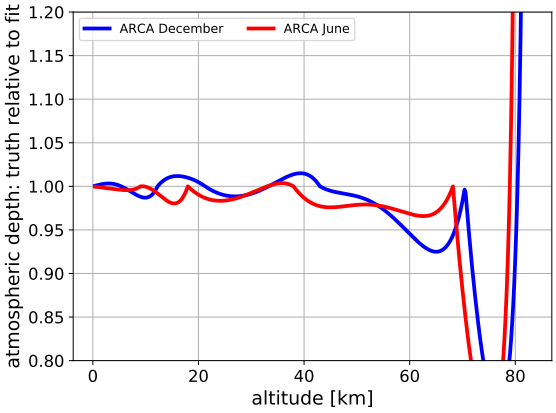

Figure 5.15: The atmospheric depth of the atmosphere at ARCA site. Model atmosphere divided by the fitted one by bernlohr package with adapted layer boundaries.

According to [89], the most dominant influence to the muon flux is the density profile at the path through the atmosphere. The density profile can vary with different frequencies. Firstly there is the seasonal variation, which is observed by other neutrino telescopes looking at muon fluxes. Secondly, there are much shorter frequencies caused by tides. Furthermore, there are much shorter frequencies which can be assigned to tidal frequencies. For the tidal frequency, a variation in the order of 0.5% was found [89]. This effect is much smaller than the uncertainties in the neutrino detector and is therefore currently expected to be negligible by KM3NeT.

Detector geometry Different detectors have different detection areas exposed to a particle flux. Especially with varying zenith angle, a different area is exposed by the particle flux. With the detector geometry one alters the way, the flux is simulated according to the zenith angle. There are three different detector geometries available to run with CORSIKA. The first is the flat surface detector geometry, suitable for flat detectors geometries like AUGER, where the detection units are in a flat arrangement. The second geometry is the vertical string detector, which might be suitable for neutrino detectors. However, as the geometry of KM3NeT is more like a sphere, the third option can also be used. It is much easier to reweight the events produced for spherical geometries to any different geometry than using any shaped geometry For this reason, the volume detector geometry is used in this work.

ESLOPE As described in Chapter 5.1, the flux of cosmic rays is very well described by a power law. In particle physics, one always tries to mimic the lifetime of the experiment within the simulations. Thus the fraction between high energy and low energy events is the same in simulation and experiment. However, the total number is often not as interesting as the actual variance between the simulated events. After a large number of simulated low-energy events, the parameter space and the topological appearance of these cascades is exhausted, but there is only a small number of simulated high-energy air showers. This low statistics is usually not sufficient to make high precision statements. The solution is to produce more high-energy than low-energy cascades. This is expressed in the energy slope (CORSIKA parameter: ESLOPE) of the generation spectrum. In current productions, KM3NeT collaboration chose the slope of -1 in comparison to the spectral index of -2.7 of the cosmic ray flux.
However, the self-veto analysis (see Chapter 5.4) shows that in addition, a high number of low-energy events is needed. A large number of events with low energy is rejected by triggering and other cuts against atmospheric background, so there is a cutoff with low statistics on the low-energy side of selected events, too.

ERANGE Atmospheric particles should be simulated from a lower limit range given by the minimum energy which enables the muon to reach the detector. For KM3NeT/ARCA, the lower boundary was chosen to be 1 TeV. In case the simulation is used for other detectors like ORCA, the range has to be adapted. ORCA is mounted in more shallow water and therefore less energy is lost on the way down to the detector. Additionally, the energy threshold to detect an atmospheric muon or neutrino is lower. ARCA is optimized for TeV neutrinos, whereas ORCA is tailored to neutrinos of a few GeV.
The upper bound is given by the assumption made on the extension of the spectrum. The upper bound is given from the physics goals of how far one wants to go width your spectrum. In ARCA, energies up to 1 EeV give a signal with reasonable strength, so the upper bound is given by this value. It is assumed that cascades with more energy will be rejected anyway and give no background at all to the measurement. However, for the measurement of the prompt component of the muon flux this might be of interest.

ECUTS The ECUTS parameter gives the lower thresholds for particles in CORSIKA. Particles with less energy than the threshold are not propagated to the Earth's surface. The argumentation regarding the ECUTS parameters is similar as described before for ERANGE. The lower bound should comprise particles not visible for the detector. Like for muons this threshold is set at 1 TeV. Additionally, CORSIKA asks for the energy threshold of other particles. It is set to 1 TeV, because neutrinos and muons can only be created from particles with the given energy. For other detectors like ORCA, the threshold has to be set lower.

Interaction models CORSIKA separates the hadronic interaction models into two different energy regions. In the low-energy region, which is used for particles with energies less than 80 GeV, the KM3NeT collaboration decided for GHEISHA 2002d (**G**amma **H**adron **E**lectron **I**nteraction **SH**ower code) [90]. However, the energy threshold is too low to reach the detector, so that the model will never be used for particles reaching the ARCA detector.
The choice of the high-energy interaction model fixes the final particle distributions. CORSIKA provides several interaction models. Some of them are no longer maintained and updated. They are not used for KM3NeT. There are the QGSJET models, which were updated after the latest LHC measurements to QGSJETII-4 [91, 92]. The old version QGSJET 01C [70] is still available, because it can simulate the charmed component, which is no longer available in the latest versions.
Otherwise, there is the EPOS-LHC model (**E**nergy conserving quantum mechanical multi-scattering approach, based on **P**artons, **O**ff-shell remnants and **S**plitting parton ladders). The EPOS-LHC model [93] is optimized to recent results from the Large Hadron Collider (LHC). For simplicity this model is called only EPOS in the following.
Both models, QGSJET and EPOS, are based on Gribov-Regge multiple scattering, perturbative QCD and string fragmentation. They are tuned to fit the cross sections of TOTEM [94]. Thus the models are based on measurements up to 7 TeV. In previous versions, EPOS and QGSJET predicted different particle densities above $E_{cms} = 1.8\,\text{TeV}$. In latest versions, they coincide to higher energies up to 7 TeV [95].
Furthermore, KM3NeT collaboration uses Sibyll2.3 [86]. Also this model is tuned to the latest results from LHC experiments. The most important part for the simulation of air showers is the muon multiplicity. The smaller the fraction of neutral pions, the higher the number of muons due to the decay of the charged particles. This fraction increases with the modification, so that the number of muons is getting closer to EPOS and QGSJET [86]. Figure 5.16 shows the average number of muons produced by different interaction models. Reference [86] stats that the number of muons increased by a factor of 1.3. Therefore, it gets closer to the other models in both cases, iron and protons. Furthermore, Sibyll enables the production of charmed particles since version 2.3 [96].
In the following, the variations of these models are used to estimate the systematic uncertainties in following analysis.

Propagate muons from sea level to the detector: corant and propa

CORSIKA is an air shower simulation, so it propagates the particles at most up to the sea level. From the sea level on, one has to use other software. Two more packages are used here. Both were already available within the KM3NeT collaboration, but further adaptation has been done within this thesis.
The first software called corant (**cor**sika to **ant**ares) is used to transform the binary output format of CORSIKA to the ascii format used in ANTARES and KM3NeT. Not every particle is interesting for KM3NeT, so a selection on neutrinos and muons is made. A new feature in corant is that the mother and grand mother particles can be transferred to the final format. In previous versions, they were discarded. Therefore, the particle tag is extended with three additional items, which are simply attached to the particle at the end. The syntax is shown here:

```
neutrino id x y z dx dy dz t E PID charmed? mother grandmother.
```

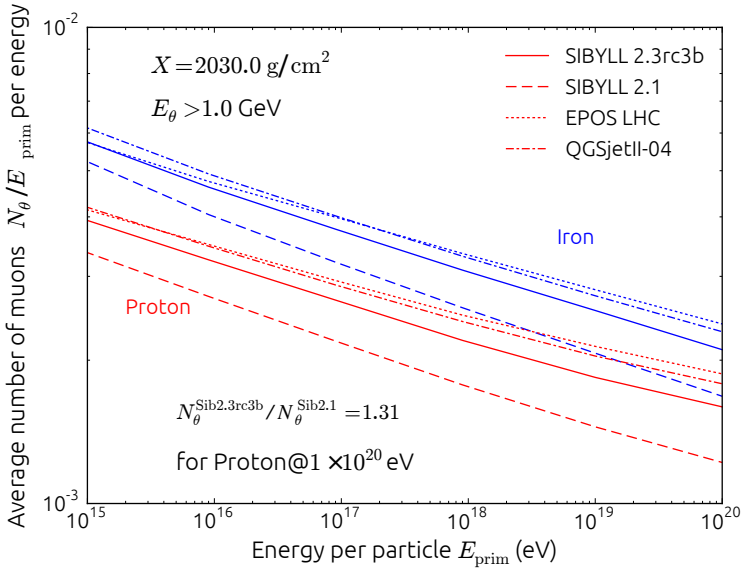

Figure 5.16: The average number of muons for different model prediction in air showers at a atmospheric depth of 1000 g cm^{-2}. Sibyll 2.1 is compared to the new version Sibyll 2.3 and the EPOS LHC and QGSJETII-04, which are tuned to LHC results. Figure taken from [86]

It starts with the tag "neutrino" followed by a counter called id. Afterwards the particle is described by the position, direction, interaction time, energy and the particle type. In this new version, an integer is chosen to state if the particle was created by a particle of the charmed component (0 or 1). The second and third item stand for the particle identifier of the mother and grandmother particle. The particle ids are taken from the definition of CORSIKA. Now both, neutrino and muons are written to the output files.
Additionally, a transformation of the coordinate system is introduced. CORSIKA is oriented in the magnetic field, whereas KM3NeT is oriented in the geographic coordinate system.
The last task of corant is to prepare the weights used later in the analysis. For this purpose, the geometry is evaluated. Finally, a weight is prepared according to the generation spectrum and can be used in the usual way. This means that weighting all events with $w2 \cdot \Phi$ provides the number of events expected in one second whereas Φ is the cosmic-ray flux as described in Chapter 5.1. However, the size of the detector is not yet fixed. The size has to be introduced before using the weights.
The last step from the sea surface down to the detector is done with propa. Propa takes all muons and propagates them with MUSIC [58] down to the detector. In this work, additionally to the propagation of muons, the propagation of neutrinos is implemented. The neutrinos are propagated on a straight line from the sea surface to the detector level. Interactions on the way are not taken into account. These are very small due to the small interaction cross sections. For further analysis, the primary particle track is propagated to the *can* surface. This is called the cascade axis. In the step of propa, the detector geometry is introduced for the first time. Thus the weights are finalized.
Both software packages are available in the KM3NeT software repository.

5.3 Comparison of simulations

In the following, the different simulation packages are compared to each other. The sampling area of the CORSIKA simulation is a sphere, with radius of 950 m. The size is chosen to get a similar effective area as KM3NeT would give. This will be the reference area to which the other simulation options are normalized. With MUPAGE a simulation is performed according to the data cards, which can be seen in the Appendix A.4. Overall 10 million events are generated this is a factor ten more

than the CORSIKA simulation. The detector is shrunk to a plane with a large radius of 10 000 m. The radius is enlarged so that only a small fraction of cascade will miss the detector. This would disturb the wished results by reducing the particles in one cascade. In this way, the sampling areas are different, therefore each event has to be re-weighted. The incoming particle cascade sees a projected area of the detector, which depends on the zenith angle. It is given by:

$$A_{\text{production}} = \pi \cdot r_{\text{can}}^2 \cdot \cos\Theta \tag{5.5}$$

with r_{can} as the radius of the can, Θ the zenith angle of the particle cascade. If the detector would have a vertical extension, further terms have to be added to consider the mantel of the can. The final re-weighting term is given with

$$w = \frac{A_{\text{sampling}}}{A_{\text{production}}} \tag{5.6}$$

with A_{sampling} the sampling area given above with the radius of 950 m.
For cross checks the last partner is the formalism given in [62] to describe the particle distributions. The formulas are implemented in an independent software, so no part of MUPAGE is used. MUPAGE gives raise to various quantities. The multiplicity, energy distribution and the radial distance between particle and cascade axis can be calculated. Most of these quantities are given in differential form, in order to obtain the absolute number of events per second one has to integrate.
In the following the comparison of MUPAGE simulation to the mupage formalism, a dedicated depth is given. In this way it is shown that the simulation and the re-weighting is done in the correct way.
Figure 5.17 illustrates four different comparisons between the simulation and MUPAGE formalism. Figure 5.17a shows the multiplicity of muon bundles. The figure shows the steep decrease of event frequency with increasing multiplicity. Over 90% of all events consist only of one or two muons. Both methods coincide well for a large range of values. Slight deviations above a multiplicity of 25 can be ascribed to low statistics of the simulation in that region.
Figure 5.17b shows the energy distribution of single muons. As in the previous figure, the total number is the same for simulation and formalism. The shape fits, too. One sees the sharp end of the simulation. This raises from the end of statistics in that region.
The third comparison shows the radial distance of muons to the cascade axis. Here one can see a shift from high distances to lower distances, which leads to a different slope. The reason can be assumed in sampling techniques, which are not correctly considered in the implementation of MUPAGE equations.
The last comparison shows a very good agreement in the muon energy distribution of muon bundles with a multiplicity of two.
Concluding, it is shown that the MUPAGE simulation is suited to describe the particle flux at the level of the can's surface.

Muon Multiplicity

The multiplicity of muon bundles is the first quantity described here. The multiplicity also gives the first hint if the overall normalization is equal between different models. For this comparison, the events are weighted according the GST4 cosmic ray flux. Figure 5.18 shows four histograms comparing the yield from different points roif view. All histograms show the x-axis of multiplicity. Each bin consists of exactly one value of multiplicity. Figure 5.18a shows that the dominant part of muon bundles are single muons. The number falls steep. However, the slope flattens with raising multiplicity. This flattening is caused by the different nuclei contributing to the total spectrum. Starting from the low multiplicity, the light nuclei dominate as the initial cosmic ray flux is dominated by light particles. The higher the atomic mass number of the primary particle, the more secondary particles can be produced. Therefore, also more muons are produced. The other nuclei range somewhere in between these two extremes.

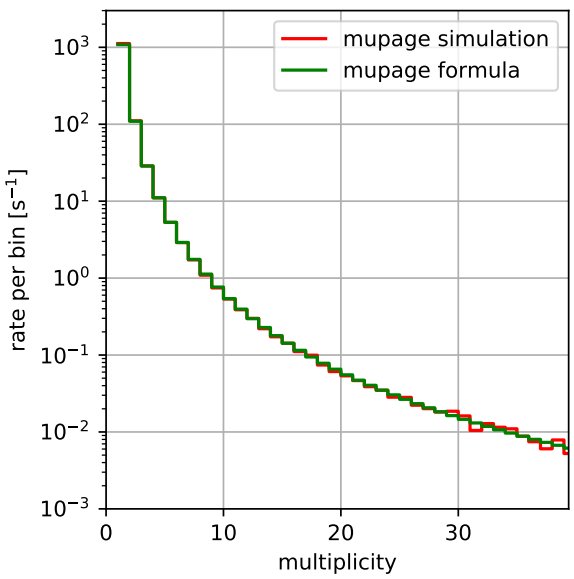

(a) multiplicity

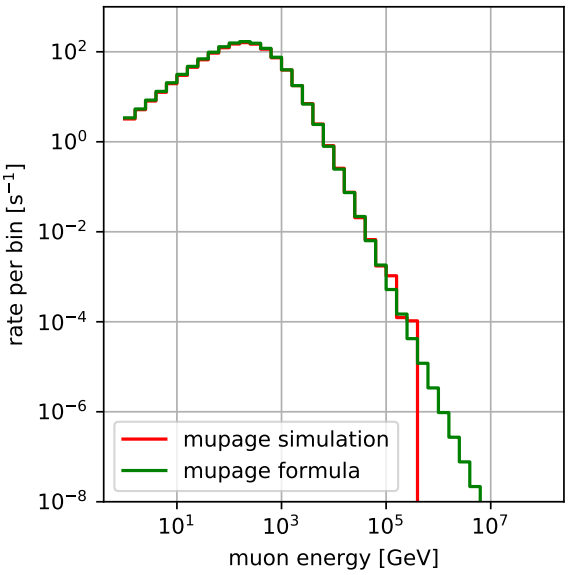

(b) energy of single muons

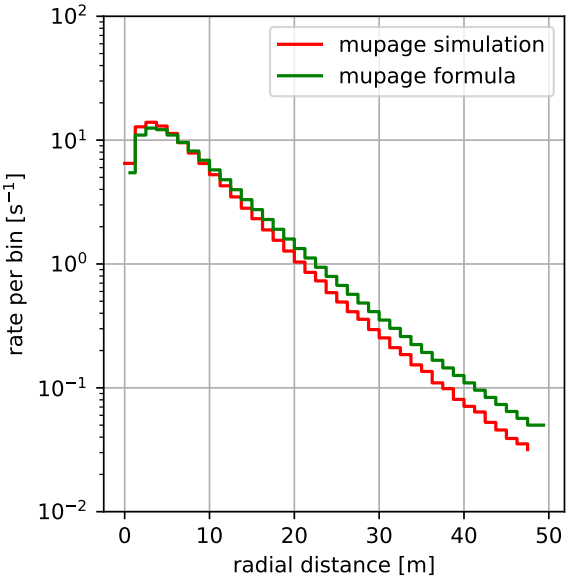

(c) distance of muons to cascade axis (M=2)

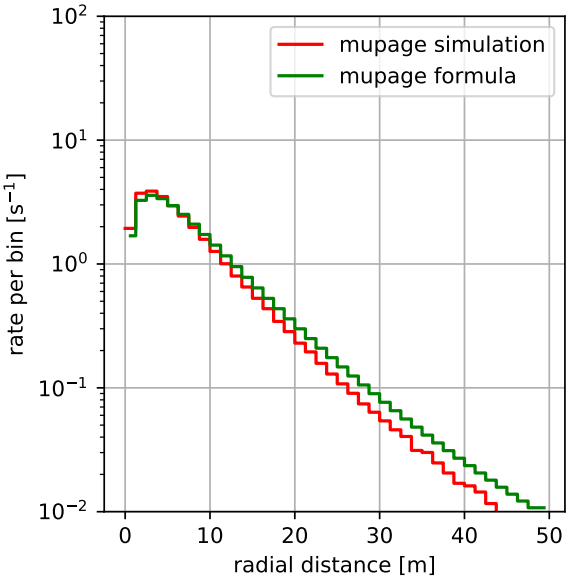

(d) distance of muons to cascade axis (M=3)

Figure 5.17: Distribution of muons at depth 2580 m. Muons are sampled on an area $A_{\text{sampling}} = 950\,\text{m} \cdot 950\,\text{m} \cdot \pi$. The zenith range from 0° to 85° is considered. Dashed line is computed by formalism [62] and solid line shows the results from full MUPAGE simulation

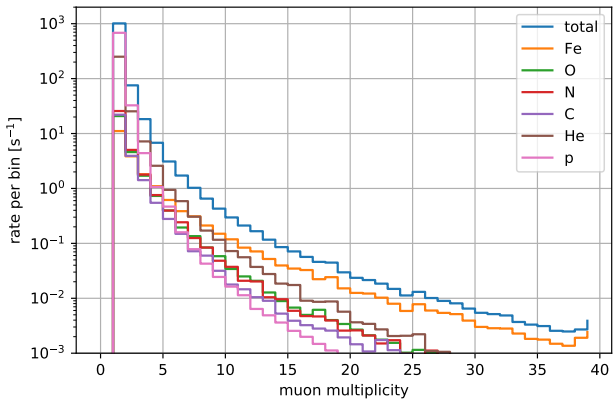

(a) Multiplicity simulated with EPOS splitted into different nuclei

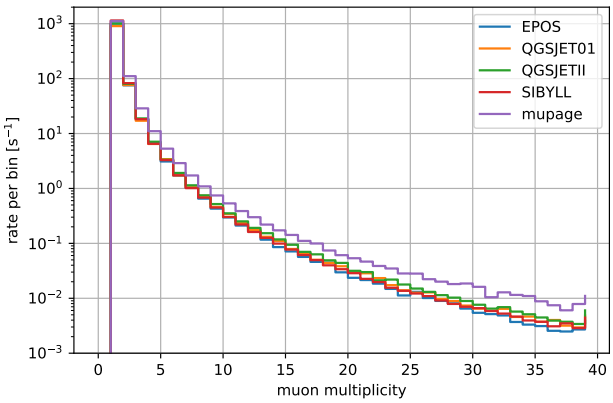

(b) Total multiplicity for multiple interaction models

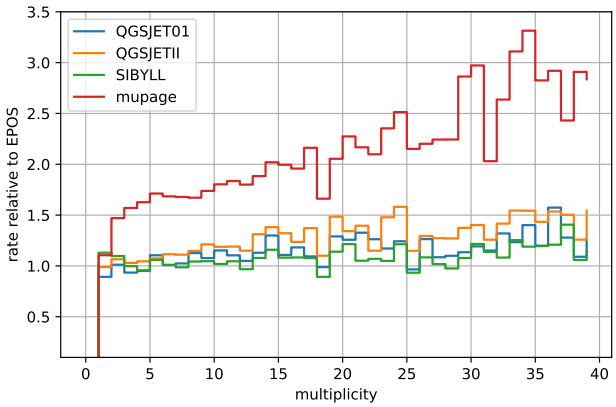

(c) Multiplicity for multiple interaction models

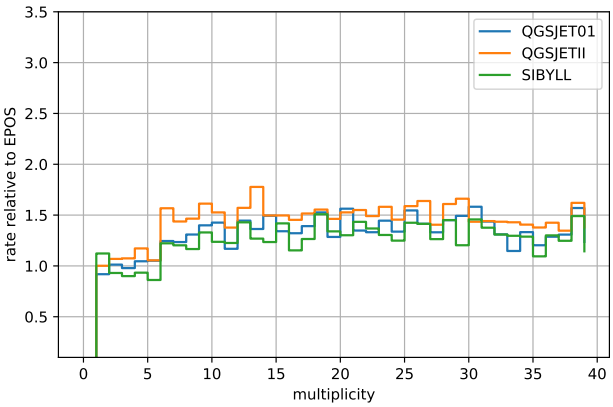

(d) Multiplicity of events induced by proton primaries for multiple interaction models

Figure 5.18: Muon multiplicity simulated by CORSIKA or MUPAGE. The events are weighted according the GST4 cosmic ray flux model

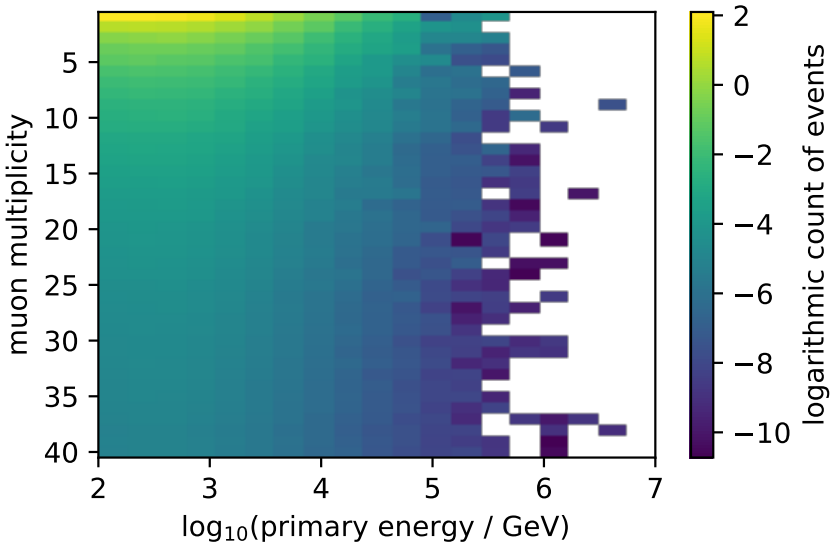

Figure 5.19: Distribution of events weighted with GST4 with respect to the primary energy and multiplicity. The interaction model is EPOS and the primary particles are protons.

Figure 5.18b shows the total flux resolved in multiplicity. The flux is shown for the introduced interaction models. Additionally, flux produced by MUPAGE is shown. MUPAGE does provide more muons on all values as the other interaction models. Figure 5.18c enables a closer look at the differences. At a multiplicity of one, the values are comparable. Afterwards the flux deviates of each other. MUPAGE provides 10% more muons than other interaction models would expect. However, it is known that the interaction models underestimate the muon yield in experiments. The other experiments lie nearly on top of each other. Here one can see that the muon yield of the new version of QGSJET provides more muons, which was intended in the development.

It can be shown that the deviations between the interaction models do not arise from one nucleus but from the sum of all models. The interaction of protons of the cosmic ray flux is shown in Figure 5.18d. Similar shapes as in the previous figure can be seen.

The small variations with multiplicity are due to small statistics in small bins. No physical reason can be found here.

Closing the considerations on muon multiplicity, a correlation between multiplicity and primary particle energy was looked for, but as Figure 5.19, made of protons interaction with EPOS, shows, no correlation was found. Other primary particles showed no correlation, too.

Figure 5.20 demonstrates the predicted muon flux resolved in multiplicity weighted with different cosmic-ray fluxes. MUPAGE does not provide the change of the primary flux. It sticks to the underlying poly-gonato flux. For this reason the poly-gonato flux is shown here in addition. As before, MUPAGE shows the highest flux independent from the assumed cosmic-ray flux. The H3a/H4a and GST models lead to similar muon fluxes, where the H3a/H4a gives slightly higher fluxes all over the spectrum. The poly-gonato shows a steep falling spectrum. It starts with almost the same values with respect to the other models, but looses the contact with raising multiplicity. The shape looks like spectra of light nuclei, so the iron component might not be as strong as in the other components. In the definition of poly-gonato, one can see that the iron component is much weaker here. The effect for the flux induced by primary particles can be seen in Figure 5.20d. For other nuclei, the poly-gonato model lies much closer to the GST model (see Figure 5.20b and 5.20c). The described earlier end of the energy spectrum can not be seen in this figures.

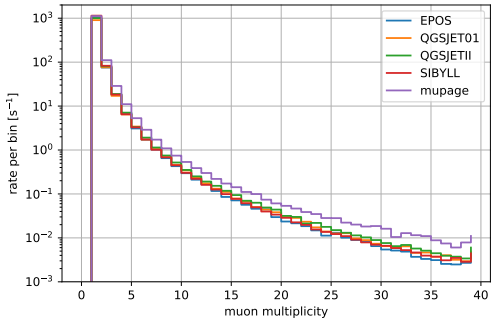

(a) Total flux

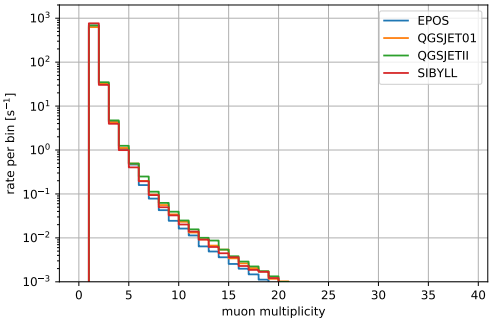

(b) Flux induced by proton primaries

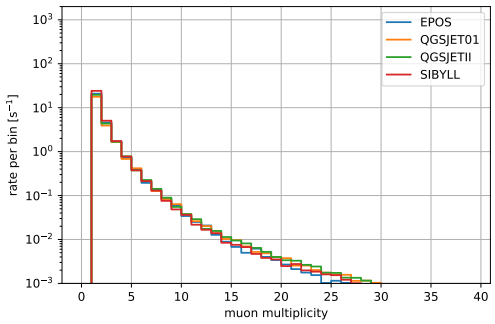

(c) Flux induced by oxigen primaries

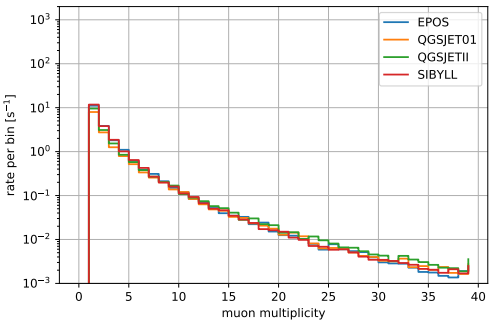

(d) Flux induced by iron primaries

Figure 5.20: Muon multiplicity simulated by CORSIKA or MUPAGE. The events are weighted according to the different cosmic ray flux model.

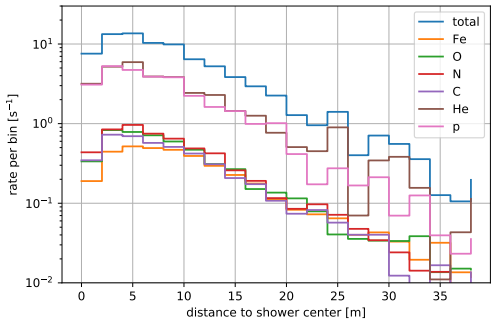

(a) SIBYLL

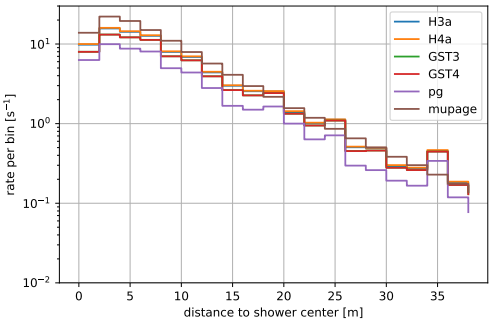

(b) Different interaction models

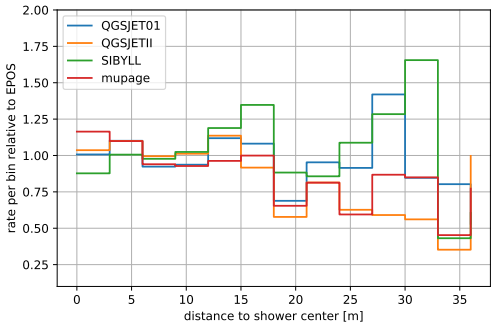

(c) Different interaction models

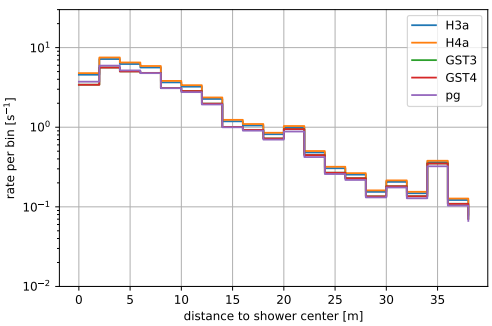

(d) Flux induced by proton primaries

Figure 5.21: Lateral distribution of muons simulated by CORSIKA or MUPAGE for muon bundles with multiplicity of 2. The events are weighted according to the GST4 cosmic ray flux model.

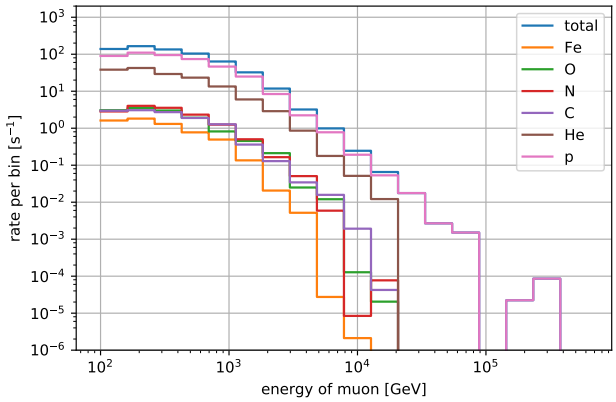

(a) Multiplicity = 1, EPOS-LHC

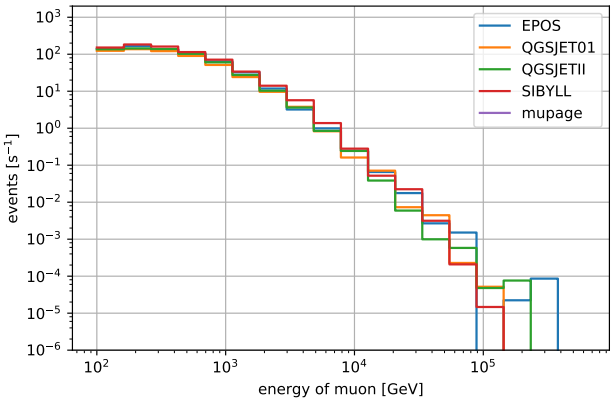

(b) Multiplicity = 1

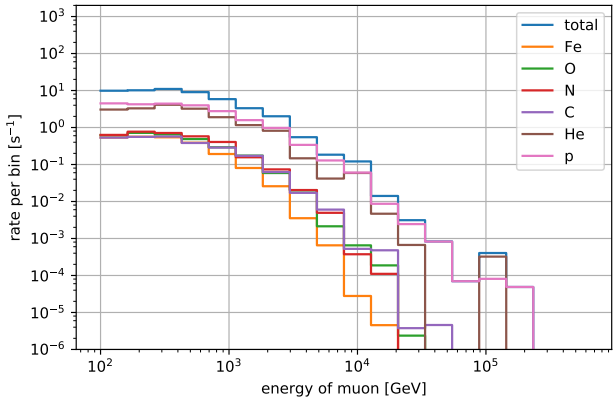

(c) Multiplicity = 2, EPOS-LHC

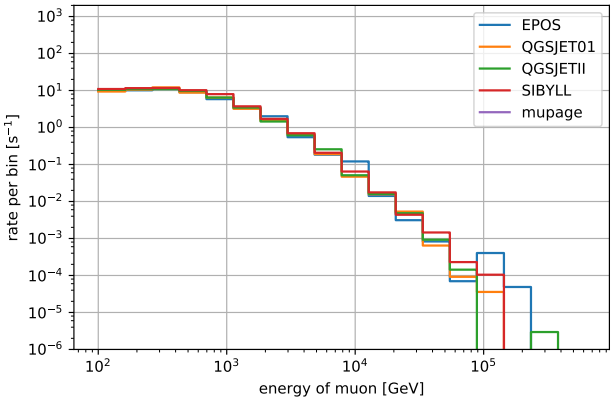

(d) Multiplicity = 2

Figure 5.22: Energy distribution of muons in simulation

Lateral distribution of muons bundles

Muon bundles are not like a single muon with one distinct muon moving through the detector, but there are multiple muons. As in the last section described, the number can rise very high. Reconstructions are based on the time residuals to a track hypothesis. If there are two muons moving side by side, they produce photons at different positions. If they are far apart, the photons from the first muon cannot fit the track hypothesis of the second one anymore. Thus the radial distribution is discussed here. First, the composition by different nuclei is shown in Figure 5.21a. The figure shows that the shape shifts from the light nuclei to the heavy ones. The heavy particles induce cascades with larger lateral spread.

Figure 5.21b and 5.21c show the difference between the different interaction models and to the MUPAGE simulation. No differences can be seen in this compilation. In literature no hint on different treatment on high transverse momentum could be found either. To complete the picture and ensure that some effects can only be found in single nuclei Figure 5.21d shows the picture for protons. Also in this case no differences can be seen.

One can recognize in the comparison of interaction models that they are close together. All variations are below 5%. The same analysis can be shown for other values of multiplicity. However, different multiplicity shows the same behavior.

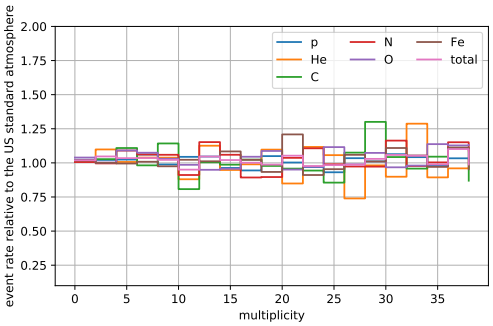

(a) Multiplicity

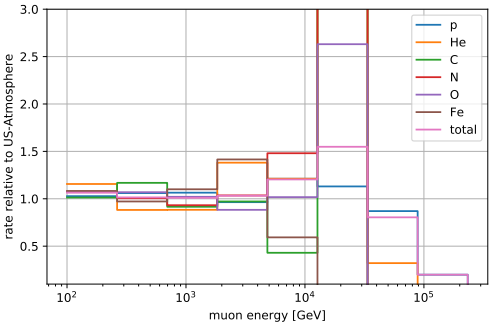

(b) Energy of single muons

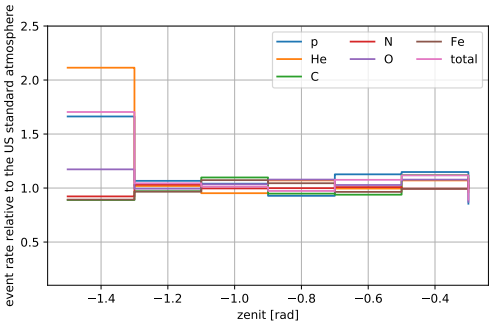

(c) Zenith

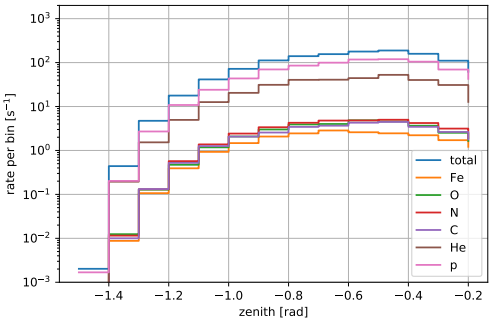

(d) Zenith for standard Sibyll production

Figure 5.23: Comparison between the ARCA atmosphere and the US standard atmosphere in the Sibyll production. In all comparison plots, the flux of Sybill ARCA production is divided by the flux of the Sibyll US standard atmosphere production.

Energy distribution of single muons

The muon flux shown in Figure 5.22a is dominated by muons induced by protons. Other nuclei contribute according to their relevance in the cosmic ray flux. For the flux of muon bundles with multiplicity of 2, the dominance of protons is reduced. The yield of bundles of protons and He nuclei are on equal scale. One can find the reason in the higher mass number, which was already shown in the discussion of the multiplicity dependence of muon bundles. With higher multiplicity the histogram changes its order continously. However, the shape remains mostly the same as one can see also in these plots. No shape difference can be seen here. At an energy above $1 \cdot 10^4$ GeV, no more events of heavy particle can be shown due to a lack of statistics. Consequently no statement on the behavior at this region can be made. However, it is expected that heavier nuclei would take over the others as the higher the energy, the less protons are expected but they are replaced by heavier nuclei. The right side of Figure 5.22 shows the variation of the energy spectrum with changing the interaction model. The variation between models is increasing with increasing muon energy. However, a trend between the models cannot be seen. The total variance changes from below 2% at 100 GeV to 30% as $1 \cdot 10^5$ GeV.

Comparison of ARCA atmosphere to US standard atmosphere

Figure 5.23 shows the difference of Sibyll production with the US standard atmosphere with respect to the self-defined ARCA atmosphere. First of all, the multiplicity (see Figure 5.23a) shows no deviation between the two models. In all nuclei the lines lie at one, which stands for equal number of muons in both models. The other quantities, which are shown here, show slightly different behavior. One can think there is some correlation between the tested quantity and the result in the flux. However, the fluctuation from bin to bin only reflects the lack of statistics. Figure 5.23b shows the

energy distribution of single muons. The fluctuation is large, so a trend cannot be seen at this moment. Other quantities like the lateral spread, interaction height or other energy distributions show also no differences between atmospheric models as far as the number of simulated events offers the possibility for this. The distribution in zenith angle shows a slightly better scenario. Figure 5.23c illustrates a deviation of the values for proton-induced cascades in high zenith angle, so i.e. around -1.4. Nevertheless, in that region, the number of surviving events is very small, which can be seen in Figure 5.23d. Thus the zenith angle was the only quantity tested, which showed some tendency of difference. Therefore their might be a hint that the standard atmosphere provides less muon bundles induced by protons in height zenith angles. In this case simulations with standard atmosphere show a pessimistic assumption.
However, it is not proven that other models would react on different atmospheric models in the same way.

More comparisons can be seen in the appendix. The conclusion of this comparison show that the tested interaction models have an equivalence in the range of a few percent in the very low energy range. Here ORCA is suited. In the energy range where ARCA is operating, the models differ in the the range of 10%. One has to keep in mind that the statistics in this region are very low. As the simulation was indicated to be a one percent simulation, the low statistic was expected. However, for detailed studies of the prompt component, more statistic is needed and planned for CORSIKA. The main uncertainties arise from the interaction models. Other ingredients like atmosphere showed a minor impact. One further import effect has the cosmic ray flux. This influences the flux in a direct way, which could be seen with the impact of the poly-gonato flux. As the differences in the current cosmic ray fluxes are above the knee, one cannot see them here.
One additional item to test here was MUPAGE. It was shown that the multiplicity is not given in the spectral shape. Moreover, the total flux is approximately 10% higher than the flux expected by CORSIKA simulations. Besides, the muons are produced closer to the cascade axis, which can be a consequence of newer interaction models, which treat the transverse momentum more accurately.

5.4 Atmospheric neutrino self-veto

The CORSIKA simulation provides neutrinos and muons from the same event simultaneously. The major source of background to KM3NeT are particles originated from cosmic-ray interactions in the upper atmosphere. Here a method is presented to suppress neutrinos originating from the atmosphere, making use of the fact that muons accompany many down-going atmospheric neutrinos [66] [67]. This leads to event topologies that can be distinguished from those of unaccompanied neutrinos, i.e. cosmic neutrinos. Consequently, this causes a suppression of the atmospheric neutrino background. The method described here was already published in [97].
The simulation used for this is a CORSIKA simulation based on version 7.4001. For high-energy hadronic interactions, QGSJET01 [70] is used. One restriction is that charmed particles are only produced in their ground states (D+, D-, D0).
The primary composition is assumed according to Ref. [69]. It describes the differential flux of primaries from protons up to iron for energies below the knee of the cosmic ray spectrum at around 5 PeV. Above the knee and up to the ankle at $5 \cdot 10^6$ PeV, the differential flux is extrapolated by reducing the spectral index by 0.3 for every type of primary. The analysis is based on a production of cosmic rays for zenith angles between 0° and 87 °C. The events are produced in nine energy regions, ranging from 10 TeV up to 10 EeV. The corresponding event statistics and effective lifetimes are summarized in Table 5.3.
Figure 5.24 shows the neutrino spectrum simulated within the standard production (see Chapter 2) and the spectrum produced by the CORSIKA simulation. It can be seen that the spectra differ at

Shower's primary energy range	Number of cascades	Lifetime (seconds)
10 - 50 TeV	$61.2 \cdot 10^6$	$1.0 \cdot 10^3$
50 - 200 TeV	$41.0 \cdot 10^6$	$1.0 \cdot 10^4$
200 - 1000 TeV	$20.2 \cdot 10^6$	$5.0 \cdot 10^4$
1 - 5 PeV	$2.8 \cdot 10^6$	$1.0 \cdot 10^5$
5 - 20 PeV	$1.6 \cdot 10^6$	$1.0 \cdot 10^6$
20 - 100 PeV	$1.1 \cdot 10^6$	$1.0 \cdot 10^7$
100 - 500 PeV	$4.9 \cdot 10^5$	$1.0 \cdot 10^8$
500 - 2000 PeV	$2.2 \cdot 10^5$	$1.0 \cdot 10^9$
2000 - 10000 PeV	$1.5 \cdot 10^5$	$1.0 \cdot 10^{10}$

Table 5.3: CORSIKA production statistics for self-veto analysis

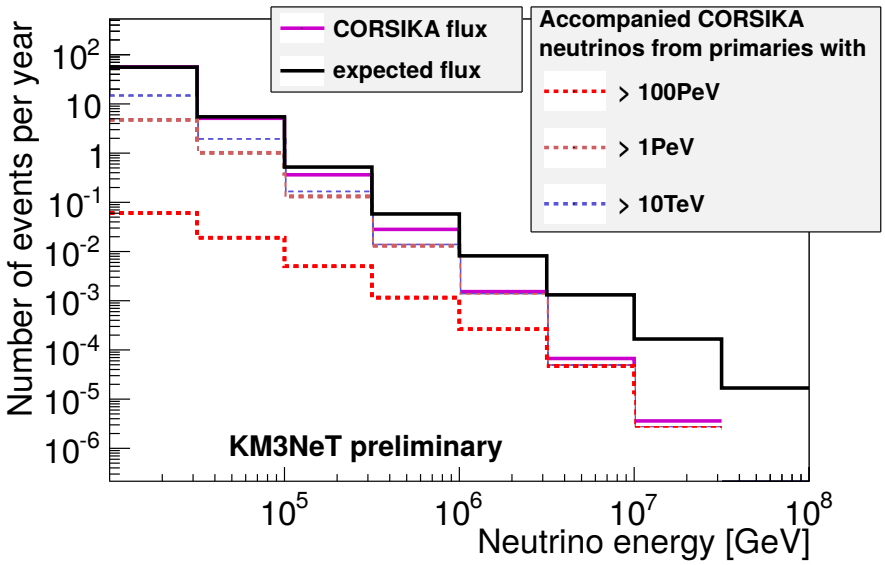

Figure 5.24: Contributions of different regions of primary cosmic ray energy to the neutrino flux from the CORSIKA simulation compared to the Honda parameterization for the atmospheric neutrino flux applied to the standard production. All fluxes shown for ν_μ of neutral current at trigger level. Empty bins show a lack of statistics.

energies above $1 \cdot 10^6$ GeV, where the CORSIKA simulation underestimates the neutrino yield by up to a factor of ten with respect to the standard production. This underestimation is corrected for via the re-weighting procedure described later on. Primary cosmic particles produce atmospheric neutrinos in different energy regions. In our analysis not every region is of same interest, as events for the analysis are not selected uniformly over the energy range. Figure 5.24 also differentiates the contributions of different primary energy regions. The diagram shows the simulated flux per year. The primary cosmic-ray spectrum follows a power law with an index of -2.7, resulting in a neutrino spectrum with an index of -3.7. The most interesting region begins at neutrino energies of 100 PeV, where the current analysis obtains the highest sensitivity [6]. Cosmic rays of energy 1 PeV to 100 PeV have the largest influence in this neutrino energy region. For current investigations, it is important that these primary particles are simulated with high statistics.
As shown in Figure 5.24, the expected neutrino spectrum and the simulated neutrino spectrum are different. The aim of re-weighting is to combine the standard neutrino production (as described in Chapter 4) and the CORSIKA production so that the overall neutrino flux corresponds to the expected neutrino flux described above and accurately reflects the fraction of accompanied and unaccompanied events. The spectrum depends on the zenith angle, neutrino energy and flavor, so the reweighting has to be a function of these parameters. In the following steps, all calculations are made with steps of the size of half a magnitude in neutrino energy and nine in zenith angle, as the current number of simulated events, in the order of 10^8, does not allow a finer binning. Furthermore, the re-weighting must be applied separately for each neutrino flavor and interaction type (NC and CC) as event rate and event topology are different. In total, eight (two flavors, two particle/antiparticle and charged current/ neutral current) weighting tables are produced. The final sample of events can be obtained by adding the re-weighted number of CORSIKA events to the re-weighted number of single events. This number will be equal to the expected number at the detector site. The unaccompanied neutrino flux, for which the standard neutrino production is used, is re-weighted by a factor of $W_G(< 1)$ according to the fraction of unaccompanied events in the CORSIKA production. This leads to

$$W_G(\Theta, E, \ell, I) = \frac{F_U(\Theta, E, \ell, I)}{F_C(\Theta, E, \ell, I)} \tag{5.7}$$

where F_U is the flux of unaccompanied events simulated by CORSIKA and F_C is the total flux of CORSIKA events. The accompanied neutrino flux simulated with the CORSIKA production implicitly includes the fraction of accompanied events in its weight, since only these events are considered. However, this production has to be re-weighted so that the total flux of the CORSIKA production is at the level of the standard production. The weight for CORSIKA events is therefore given by

$$W_C(\Theta, E, \ell, I) = \frac{F_G(\Theta, E, \ell, I)}{F_C(\Theta, E, \ell, I)} \tag{5.8}$$

where F_G is the flux expected by the standard atmospheric neutrino production. The only component on which the calculation of weights depends and which is subject to significant uncertainties is the expected atmospheric neutrino flux. Weights must be recalculated if it is changed.
Figures 5.25a and 5.25b show the final weights used with the appropriate productions. Only weights for anti-electron neutrinos are shown. Further weights can be found in the Appendix B. Figure 5.25a shows the additional weight to the standard neutrino production. High-zenith angles are dominated by neutrino events with no accompanied muons, so the weight is approximately one. At large zenith angles mostly all muons get absorbed during propagation through the water above the detector. The higher the neutrino energy, the higher the probability that muons accompany the neutrino to the detector. In this histogram, empty bins indicate ranges where no neutrino reaches the detector unaccompanied. As the standard production is the reference, neutrino flux weights cannot become larger than one, unlike the weights of the CORSIKA production. Figure 5.25b shows the weight W_C one has to apply to the CORSIKA production. The weights are rather constant along the zenith angle.

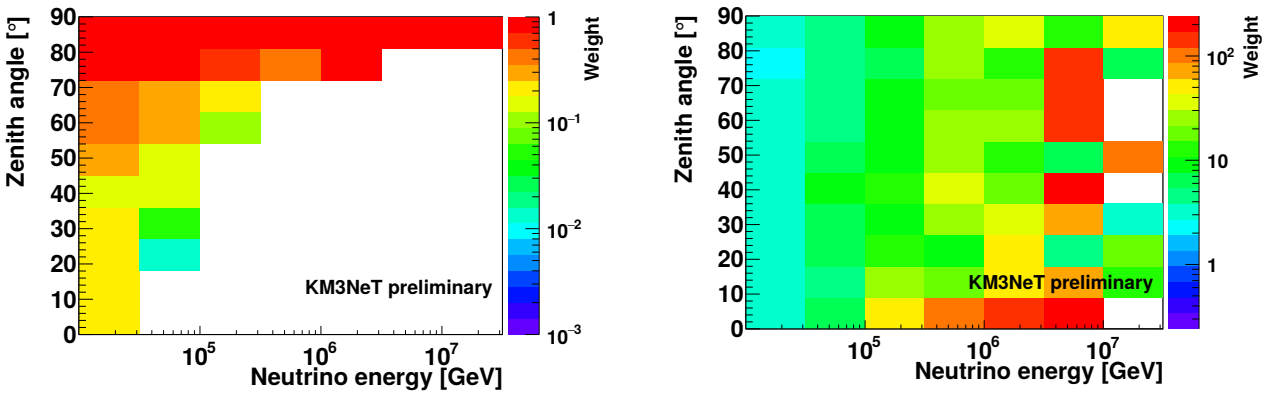

(a) (b)

Figure 5.25: Weights for using the standard (a) and the CORSIKA (b) production for $\overline{\nu}_e$-CC

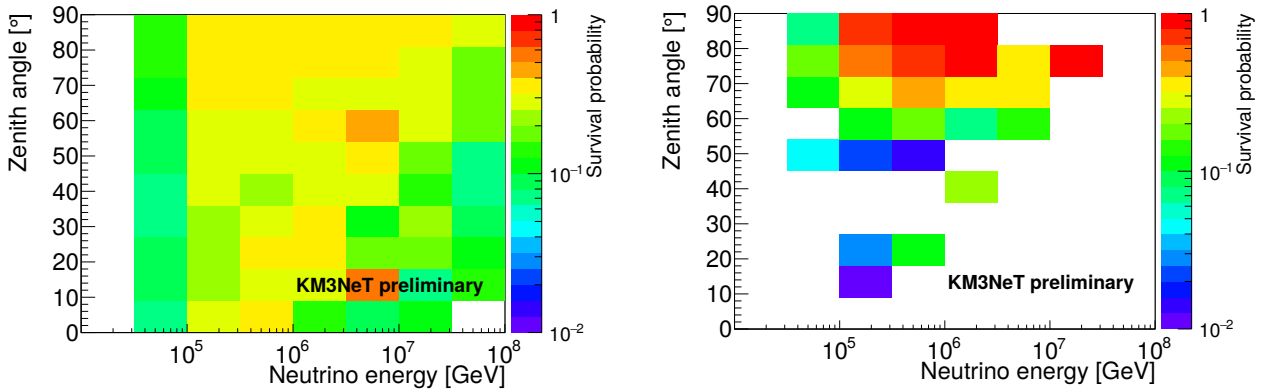

(a) single neutrinos (b) with accompanying muons

Figure 5.26: Probability of neutrino events in $\overline{\nu}_\mu$-CC surviving the final cuts. (a) single neutrinos. (b) additional survival probability for accompanied neutrinos

The trend to larger weights at high energies reflects the afore-mentioned underestimation of neutrinos inside the CORSIKA simulation. Large fluctuations above an energy of $1 \cdot 10^6$ GeV show a lack of statistics. Furthermore, above $1 \cdot 10^7$ GeV the production is so sparse as it is almost unusable. For the current analysis, this is not a significant drawback, because the used energy ranges are mostly between $1 \cdot 10^5$ GeV and $1 \cdot 10^6$ GeV (although in this region there are small fluctuations).

The CORSIKA weights are applied to the sensitivity calculation for the diffuse neutrino flux in KM3NeT. In the following, a short overview of the cut-and-count analysis is given. More details can be found in [6]. The analysis looks for high-energy events which are consistent with a cascade-like topology. The analysis is based on a multi-step rejection of atmospheric background. A boosted decision tree is used to distinguish against atmospheric muon events. Accompanying muons will thus cause neutrino cascade events to be rejected on the basis that the event no longer looks cascade-like. The final sensitivity calculation is done with a cut-and-count method as described in [98].

Figures 5.26a shows the probability that an atmospheric neutrino which is not accompanied by muons survives in the analysis described above. One can see the survival probability is very low at energies below $1 \cdot 10^5$ GeV as this analysis tries to increase the sensitivity to the high-energy signal. The maximum probability of survival of around 50% reflects that events are simulated all over the can. Many of them are too distant from the detector to be used in the analysis. Figure 5.26b shows the additional probability to survive (1-chance of being rejected) if the neutrino is accompanied by muons.

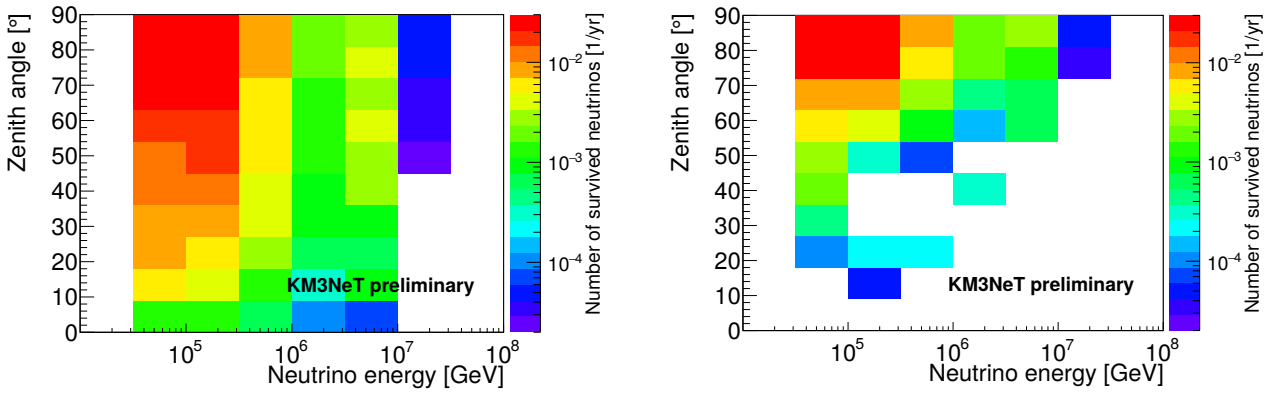

(a) without use of CORSIKA

(b) with use of CORSIKA

Figure 5.27: Number of surviving atmospheric neutrinos after selection for the cut-and-count analysis for diffuse neutrino flux in KM3NeT in $\overline{\nu}_e$-CC

Events near the horizontal cannot be rejected as many of the muons do not reach the detector. Thus the event topology is dominated by neutrinos. By contrast, the sample of low zenith angles consists mostly of events dominated by muons. Empty bins symbolize that there were no events left before or all events are rejected. Zenith angles up to 50 degrees are suppressed completely.
Figures 5.27a and 5.27b show the distribution of expected down-going atmospheric neutrinos as a function of energy, both with and without the self-veto effect. Figure 5.27 reflects the behavior of Figure 5.26. Low-energy events are rejected with high probability. Low zenith angles behave the same way due to the self-veto effect. However, the upper left region between $1 \cdot 10^{4.5}$ GeV and $1 \cdot 10^{6}$ GeV and at high zenith angles cannot be suppressed as well as other regions.
Applying the cut-and-count method without rejecting CORSIKA events, 1.5 events per year are left after the final selection in a sample with all neutrino flavors. Applying the new weights and combining CORSIKA events and standard neutrinosi, the selection leaves 0.7 events per year in this zenith angle region. The total number of surviving upcoming neutrino events is 1.5 in this analysis. The analysis is supposed to reject atmospheric muons, so more down-going events are rejected. The number of up-going and down-going neutrinos are equal although Earth absorption causes a reduction of up-going events.
As proof of concept, the application to the diffuse flux search shows that the amount of atmospheric neutrinos could be reduced from 1.5 expected down-going atmospheric neutrinos to 0.7 atmospheric neutrinos. In this analysis, it was shown for the first time that a full CORSIKA simulation was used through the complete chain. Furthermore the method can reduce the number of atmospheric neutrinos by a significant amount, here a factor of two was achieved.

Chapter 6

Event Identification

Previous chapters described the events which can be observed with KM3NeT/ARCA. There are the astrophysical neutrino events in their full variety, the corresponding atmospheric neutrino events and at last the atmospheric muon events. The underlying physics for events might be different, however, the separation based on the topology is not easy. Nevertheless, there are events which look very different, e.g. neutrino cascade events and atmospheric muon bundles. Otherwise, there are event topologies which look the same, e.g. a ν_μ interaction in charged current resulting to a muon which travels through the detector. This event looks identical to a single muon produced in the atmosphere.
To answer physics questions, one has to separate different event types on the basis of their underlying physics, which were described in Chapter 2. However, this is not easily possible as we saw in the previous examples. Additionally, one has to keep in mind that it is not possible to decide without doubt which neutrino flavor induced one specific event. However, if there are a lot of events, one can make statements in statistical sense.
The question to answer here is whether it is possible to find criteria to separate different event topologies. If these criteria were found, how well could we separate the events and would one do better.

6.1 Definitions towards the goodness of classification

A classification helps to solve the disorder of event topologies. The classifier gives an answer. In most cases it is an integer indicating to which class an event belongs with the highest probability. This result might be correct or faulty. In total, a value to quantify the correctness, averaged over all possible inputs, is needed.
Assuming the event classes are defined, each event corresponds to one class. There are several classification outcomes, which are summarized in Table 6.1, the so-called confusion matrix.

		predicted class	
		this class	other class
actual class	is this class	true positive (TP)	false negative (FN)
	is other class	false positive (FP)	true negative (TN)

Table 6.1: confusion matrix for the result when the algorithm classifies an event into classes.

An event can be classified correctly, which is then named a true positive result (TP). Without any doubt, this is the best outcome. The same event could be classified as a different class and is then a false negative event (FN). This leads to a loss of events. In physics analyses, this leads to a reduced sensitivity of this class. However, this event will pass to some other class. If we want to use this other class in further analyses, the contamination of this class has to be considered. The former example seen from the other side is called a false positive event (FP). This means an event of any other class

is classified as the class one considers. In physics analyses, this can lead to an overestimate of the physical flux or artifacts in spectra. The last cell in the confusion matrix collects the result of an event, which is of another class and is also classified as another class. This is a true negative event (TN). Similar to the true positive event, the event is correctly classified.
To sum it up, the first ojective should be to increase the true positive and true negative event rate. This is true for the main goal of analyses, in which each of the classes should be used for the analysis. However, if the analysis would only use one of the classes, one could drop the requirement for a high true positive rate in the class not needed. Doing so, the false positive rate is reduced. Otherwise it would disturb the analysis. For example, a class containing down-going tracks will always be dominated by atmospheric muons. Hence this class can be considered as worthless for astrophysical neutrino physics and can receive more false classified events. However, as the atmospheric muon contribution is that large with respect to the target neutrinos, the true positive rate has to be very high. Later on it will be shown that a one step approach cannot achieve this, but a two step approach with a dedicated atmospheric muon rejection after the classification can manage this task.
This theoretical part showed thoughts on quantifying the performance of a classifier. In the process of developing the methods, further decisions, which are described at time, are made.

6.2 Calculation of features

A classifier works on the basis of numerical values, so-called features. Either there is any kind of human decision on the cut value or a machine tries to learn where to cut. The experiment provides a distribution of hits in time and space. Therefore, features are calculated on the basis of the distribution of hits in the detector.
In the following, the features used for the classification task are described. In this chapter, not all channels are plotted for the reason of clarity and comprehensibility. In most cases, two extreme cases are plotted. Other cases lie in between.
All events in KM3NeT are contaminated by photons from ^{40}K decay. Mostly these hits are one-photon-hits. If the events are prepared with a cut for hits with higher ToT than 25 ns, most of these hits are vanished, but the physics event is still pronounced. Applying this cut, the calculation of features does not become more time-consuming. Nevertheless, the discrimination power increases.

6.2.1 Spacial distribution

Tensor of inertia The shape of hits in the detector can be described by the tensor of inertia. Originally known from classical mechanics, the tensor provides information about the distribution of mass with respect to a given coordinate system [99]. Here the mass corresponds to the number of hits detected at a certain position corresponding to the PMT. Thus the tensor of inertia is defined as follows:

$$I = \sum_i \begin{bmatrix} y_i^2 + z_i^2 & -x_i y_i & -x_i z_i \\ -y_i x_i & x_i^2 + z_i^2 & -y_i z_i \\ -z_i x_i & -z_i y_i & x_i^2 + y_i^2 \end{bmatrix} \tag{6.1}$$

where x, y and z are the coordinates of the PMTs inside the detector. The sum ranges over each hit symbolized by i. The coordinate system defined for KM3NeT is used. It was tested to use the ToT of each hit as mass equivalent, but as the simulation of the ToT is not trustworthy at the moment, it was discarded.
The tensor can be transformed to a coordinate system, in which the tensor is diagonal. This transformation is done via the eigenvalues by using them for the event identification. Ordered by size, the *small inertia*, *middle inertia* and *big inertia* eigenvalues are defined. These three features are shown in figures 6.1a to 6.1c. The ν_e and ν_μ charged current channel is shown for comparison. The *small*

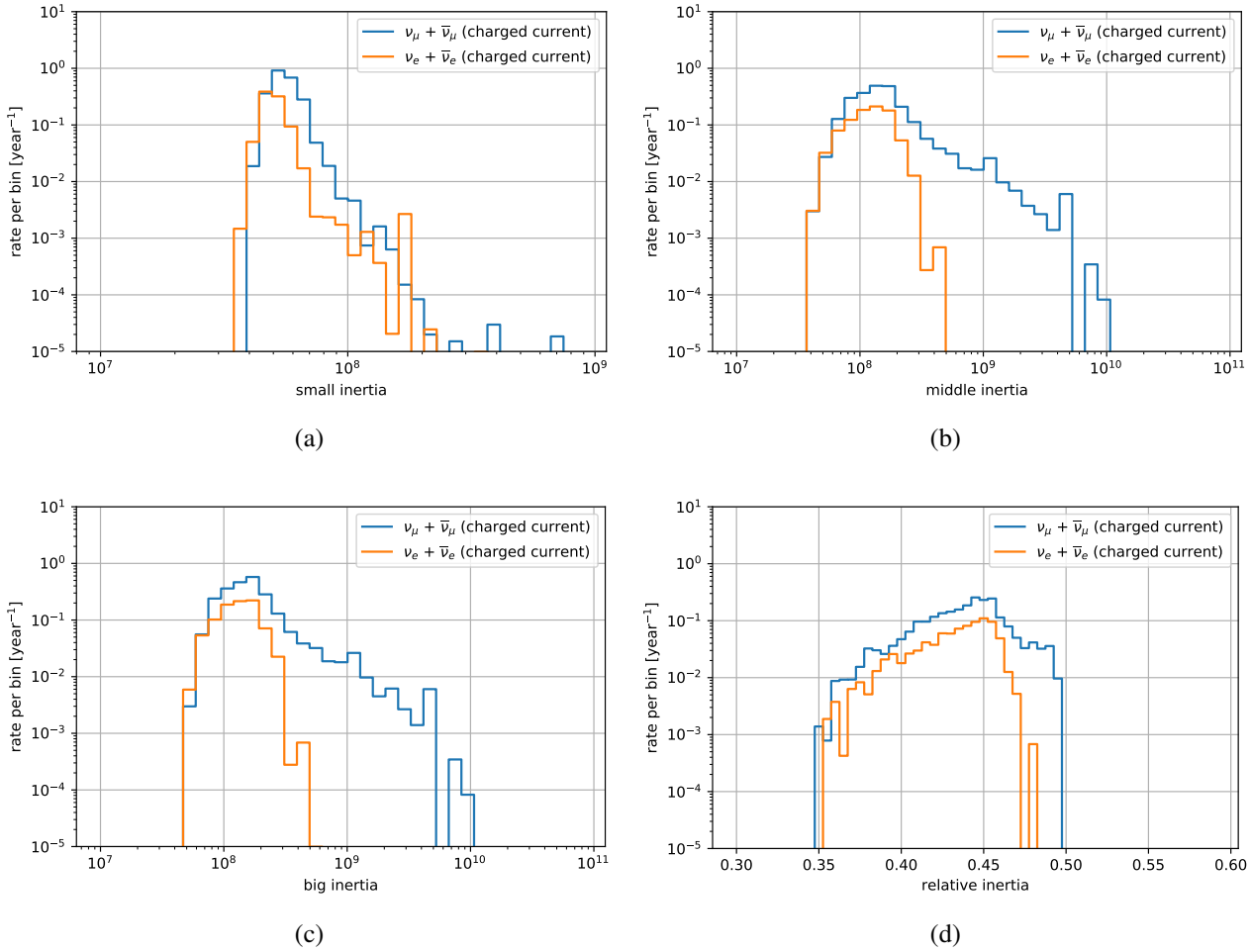

(a) (b) (c) (d)

Figure 6.1: Distribution of features related to the tensor of inertia. All simulated events are used. A pre-processing cut on ToT for each hit is made at a value of 26 ns

inertia is very similar in both shown neutrino flavors. For both flavors, the *middle inertia* and the *big inertia* is similar except for the fact that the *middle inertia* is smaller by definition. However, both are highly correlated and even per event almost identical. A track event is more distributed over the detector so the eigenvalues of the tensor of inertia are larger. Especially the a track event is more elongated, than the cascade, so the *middle inertia* and *large inertia* is larger for the track events.
Additionally, the *relative inertia* is defined, which gives the relative size of the big inertia compared to the sum of the others:

$$\text{relative inertia} = \frac{\text{big inertia}}{\sum \text{inertia}} \tag{6.2}$$

For cascades, a clear cut initiated above 0.45 in Figure 6.1d is seen. As tracks are more elongated, they follow a wider path to larger values.

6.2.2 Time residual distribution

The hits are detected distributed over time. With the high temporal resolution of KM3NeT of 1 ns and high scattering length of photons, the arrival time can be perfectly used to calculate the time of emission. Besides the actual time distribution within an event, the time residual distribution is useful to classify an event. A time residual is the difference between the measured time when a photon arrives and the expected time. The expected time is the time, which the photon takes from the source to the observing PMT. Here a direct path with the speed of light is assumed. The time residual is

defined as follows:

$$\Delta t = t_{\text{travel}} - t_{\text{expected}} \tag{6.3}$$

where

$$t_{\text{travel}} = t_{\text{PMT}} - t_{\text{vertex}} \tag{6.4}$$

and

$$t_{\text{expected}} = \|x_{\text{PMT}} - x_{\text{vertex}}\| \cdot c \tag{6.5}$$

with c the speed of light in the surrounding medium. Hits with negative values are early hits, they arrive earlier than expected. Late hits show values above zero.
Therefore, the starting point and the end point of the photon's journey have to be found, both with time and position. The starting point is not known, at first. However, there are reconstruction algorithms [6], which give an estimate. Every photon is assumed to start at this point. If no reconstructed vertex is available, the center of gravity of selected photons is chosen. Thus the time residuals are calculated with respect to a cascade hypothesis. In order to calculate the time residual with respect to a track hypothesis each photon has to be projected under the Cherenkov angle to the reconstructed trajectory. The end point is given by the detection of the photon.
In the following, only hits with a ToT above 25 ns are chosen. In this way, most of the background is rejected, but enough information about the event is restored.

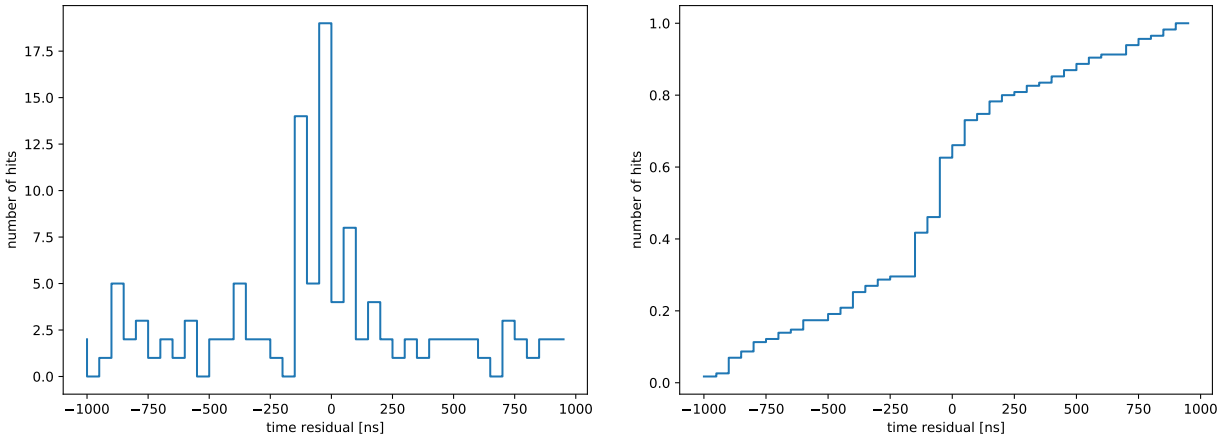

Figure 6.2: Time residual distribution of one $\overline{\nu}_e$-CC event with 10 TeV. Left side: the normal distribution. Right side: cumulative distribution from low time residuals to high values and normalized to a maximum value of one.

The left panel of Figure 6.2 shows a time residual distribution of a $\overline{\nu}_e$–CC event with 10 TeV. The distribution starts at the negative values of time residual with a flat distribution. These are background hits, which are not rejected by the ToT-cut. Around $\Delta t = 0$, a sudden peak is visible. This rise indicates the neutrino interaction, when a lot of photons are produced. Most of these reach their target PMT at a direct path and therefore the time residual is approximately zero. There are some hits above the baseline which have a negative time residual. This can be a hint that the reconstruction did not work perfectly and the vertex was shifted to later times. This could be observed in reconstruction algorithms as most frequently the cascade maximum, which is shifted by a few meters in the direction of movement, is reconstructed. Even if the reconstruction worked perfectly, photons could have arrived earlier than expected. A photon, which seems to travel faster than light, has to be emitted apart from the initial interaction vertex. A secondary particle moves from the vertex and at some time the particle emits the photon. At the first part of this journey the photon travels faster than light as it is "back-packed" to the particle.
The peak expires already after a few tenth of nanoseconds. This is a clear hint that most of the photons are not scattered. More scattering would cause a larger tail of the time residual distribution.

The right panel of Figure 6.2 shows the cumulative distribution of the left one. Furthermore, it is normalized to a maximum value of one. The graph rises all over its range because it is accumulative. In the the first section, the slope is constant as only background hits contribute. Background hits are uniformly distributed over time. Around zero there is a sudden jump, corresponding to the peak in the left figure. Figure 6.3 shows the time residual distribution for a atmospheric muon event in a normal and cumulative way. At around $\Delta t = 0$, a peak is visible. At this point, the cascade reconstruction fits a vertex, which indicates that there must be some accumulation of hits. However, other regions show peaks, too. There is no clear baseline at the beginning of the event and at the end the baseline is missing. Compared to the $\overline{\nu}_e$-CC event, the graph shows a more uniform behavior with a constant slope interrupted by numerous small jumps.

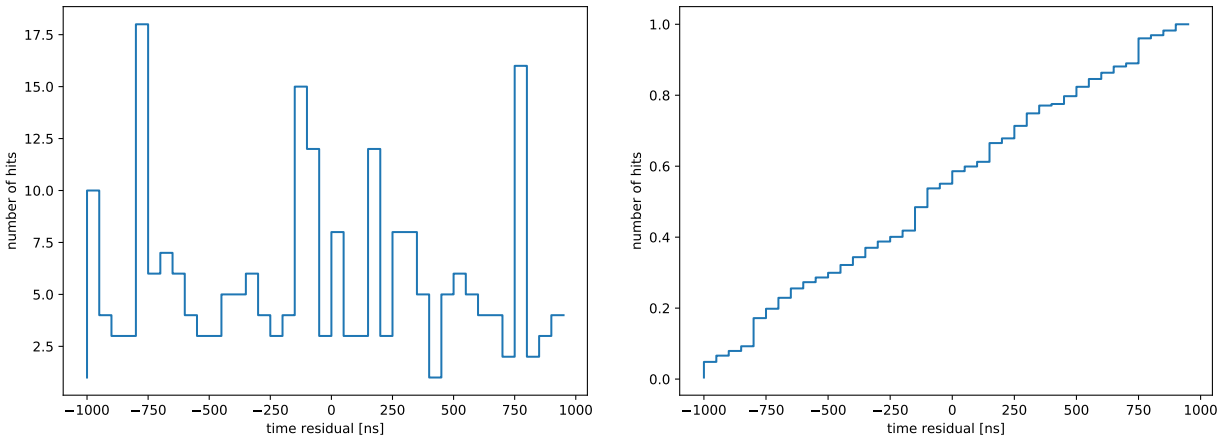

Figure 6.3: Time residual distribution of one ν_μ-CC event with 285 TeV. Left the normal distribution. Right: cumulative distribution from low time residuals to high values.

The distribution can be characterized by several numeric values, which can be used for the classification task.

Mean and Median At first the position of the time residual distribution is described with the *mean*. Similar information comes from the *median* value, but it focuses more on a big peak and outlier influence less. Figure 6.4a shows the distribution of the *mean* value. The *mean* value is calculated on the set of hits resulting in a time residual between −1000 ns and 1000 ns. For ν_μ it is slightly shifted to smaller values, because the photons arrive too early as they travel piggyback on the muon, which moves faster than the speed of light in the surrounding medium. The *median* value of the time residual is peaked for the cascade events nearby zero, whereas the distribution for track events is broadened as the track events do not give a distinct peak around zero. The median is based on the complete sample of time residual values, e.g. hits with values far off the hypothesis are used. Thus, larger values are possible than for the mean. Figure 6.4b shows the distribution for ν_e and ν_μ in the charged current.

Width of distribution Besides the location of a distribution, the spread is used to describe it. In this way, the root-mean-square (RMS) is calculated in the following way:

$$RMS = \sqrt{\frac{1}{N}\sum \left(\Delta t_i - \langle \Delta t \rangle\right)^2} \tag{6.6}$$

The RMS shows larger values for tracks of cascades as the track produces hits with a large variety of time residual values. The hits do not fit to the cascade hypothesis. Figure 6.4c) shows the difference between cascades and tracks. The effect shown here can be increased when all hits are used, not only those in the 2000 ns time window.

The width of the time residual can also be expressed as the difference between the 15% and 85% quantile. In Figure 6.4d, showing the distribution, the two samples are separated more clearly than in the RMS, where some effects are canceled out due to averaging.

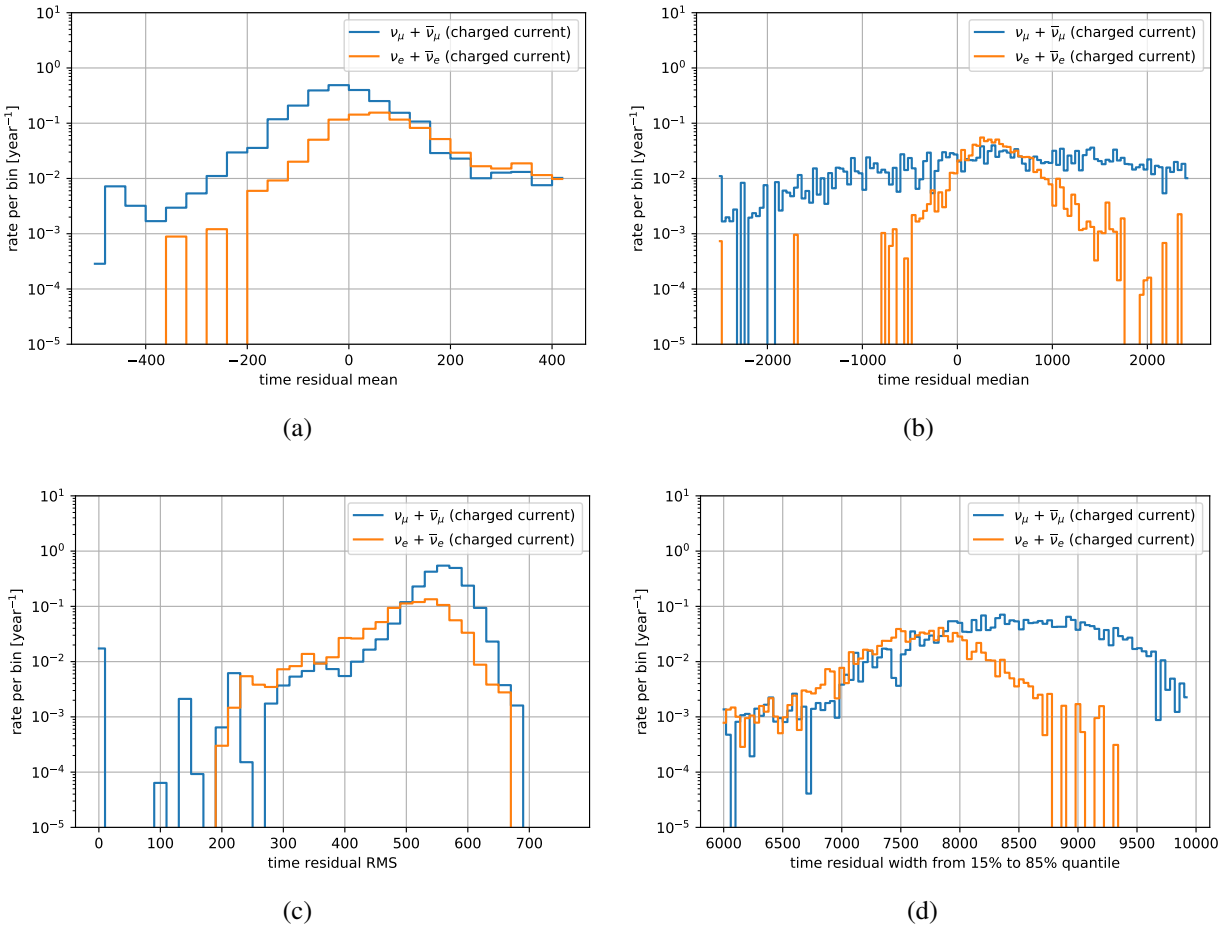

Figure 6.4: Distribution of the features quantifying the time residual distribution given for ν_μ and ν_e interaction in the charged current. Number of events is given per year. Each triggered event is used.

Linear fit to the cumulative distribution The next parameters characterize the shape of the cumulative time residual distribution. A linear function is used to model the behavior of the distribution in certain ranges. The fit gives the *slope* and *y-intercept*. Furthermore, X^2 gives an idea of the fit quality. Track-like signatures show a slope being constant over the whole range, which is shown with the blue lines in Figure 6.5a. Both lines are almost lying upon each other. The distribution for the fit from -1000 to 0 ns is slightly smaller than the other one. The reason for this is that there has to be some step after zero as otherwise there would be no reconstructed vertex. In contrast the cascades (red lines in Figure 6.5a) show a larger shift between both cases. There is a bigger step in the cumulative distribution around zero. Thus, one expects a small slope at the beginning as there are no particles interacting inside the detector. The photons produced by particles give the signal after $\Delta t = 0$. From $\Delta t = 0$, on the slope has to rise, which is shown in Figure 6.5a.
The slope in the lower range shows one more feature. The cascades lead to a smaller slope than the tracks as the particles of the muon event already contribute to the lower range, whereas the cascade particles only contribute to the upper range.
Additionally, the quality of the fit can be used to identify tracks versus cascades. The smaller X^2, the better the fit. Over the complete range the expected behavior for a track is a linear one. The cascades show a linear behavior only at the beginning, when no particle produces photons. At the second range

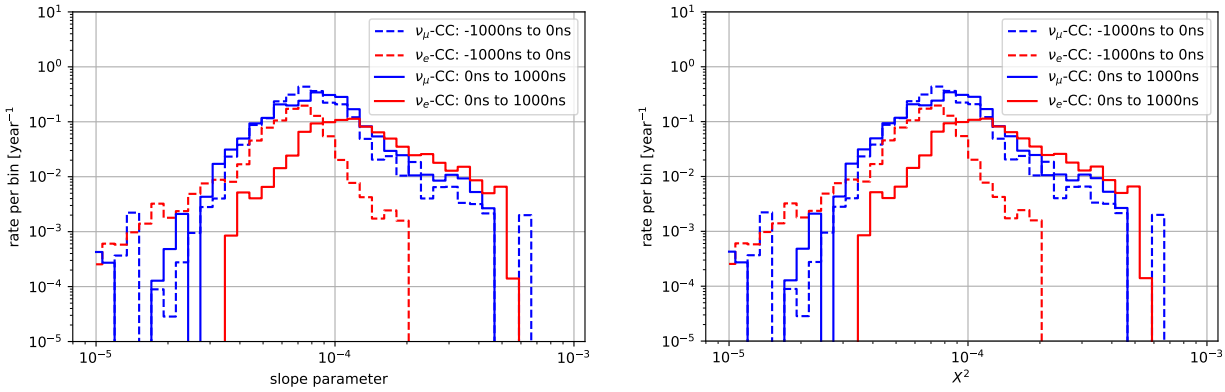

(a) (b)

Figure 6.5: Distribution of slope parameter comparing tracks and cascades as well as the slope of linear fit before (dashed) the reconstructed vertex and after the reconstructed vertex (solid).

above $\Delta t = 0$ the shape is no longer a linear function, as easily seen in Figure 6.3. It is expected that the values for the first range are similar for both cases, whereas the second range shows that the X^2 is smaller for tracks than for cascades. This can be seen in Figure 6.5b. As the track does not vary over the time residual range, both fits are equally good, the values overlap again.
For event identification, more fit intervals are chosen to cover more regions in the time residual space. Furthermore the y-intercept can be used. The full list of parameters calculated is written in Appendix C.1.

G-Parameter and Gold Parameter Besides the RMS and other definition of width, more complex structures are tested here. Two further parameters based on the time residual are calculated: the G-Parameter and the Gold-Parameter. The G-Parameter is defined as follows:

$$g = \frac{1}{N} \sum_N \exp\left(-\frac{(\Delta t - \langle \Delta t \rangle)^2}{\sigma}\right) \tag{6.7}$$

In contrast to referencing to the mean of time residuals, the Gold-Parameter uses directly the time residual:

$$gold = \frac{1}{N} \sum_N \exp\left(-\frac{\Delta t^2}{\sigma}\right) \tag{6.8}$$

In both equations N is the number of hits used, σ is an arbitrarily chosen value to scale the values (here $\sigma = 4.5$).
Hits are only taken into account if they lie in a reasonable range. Here the range is chosen so that the difference between the reconstructed time and the arrival time of the photon is smaller than 500 ns. This leads also to a spacial cut in the detector.
As the gold parameter refers to zero instead of to the mean, the difference between tracks and cascades is larger than for the g-parameter. Previous figures showed that the mean time residual of tracks is smaller than the value for cascades. The distributions of both parameters shown in Figure 6.6a and 6.6b are very similar. While the shape before the maximum is very similar the slope after the maximum gives the discriminative power to this feature.

6.2.3 Output of reconstruction

In addition to the features explicitly developed, there are some quantities which are already calculated by reconstruction algorithms. They are either the reconstructed quantities, like position, direction and

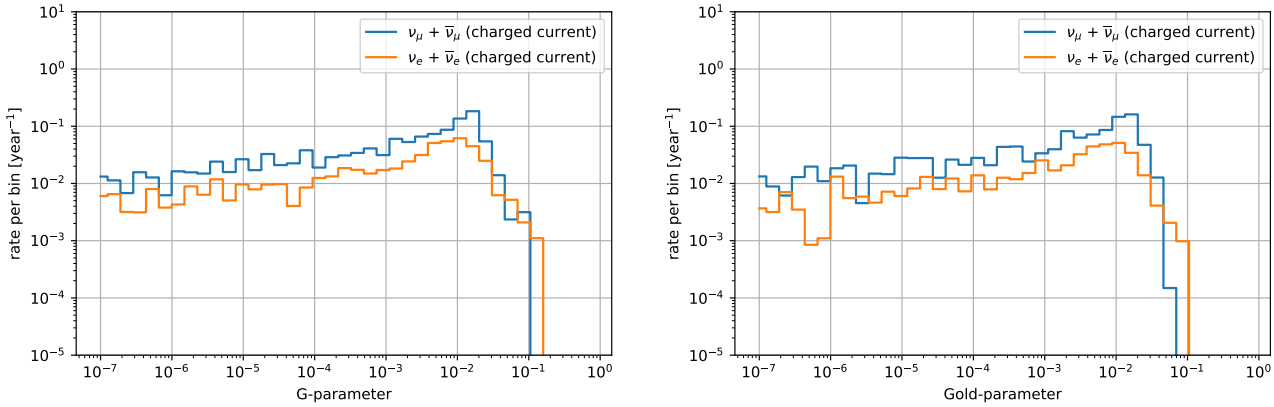

(a) (b)

Figure 6.6: Distribution of the G-Parameter and Gold-parameter given for ν_μ and ν_e interaction in the charged current. The number of events is given per year. All triggered events are included.

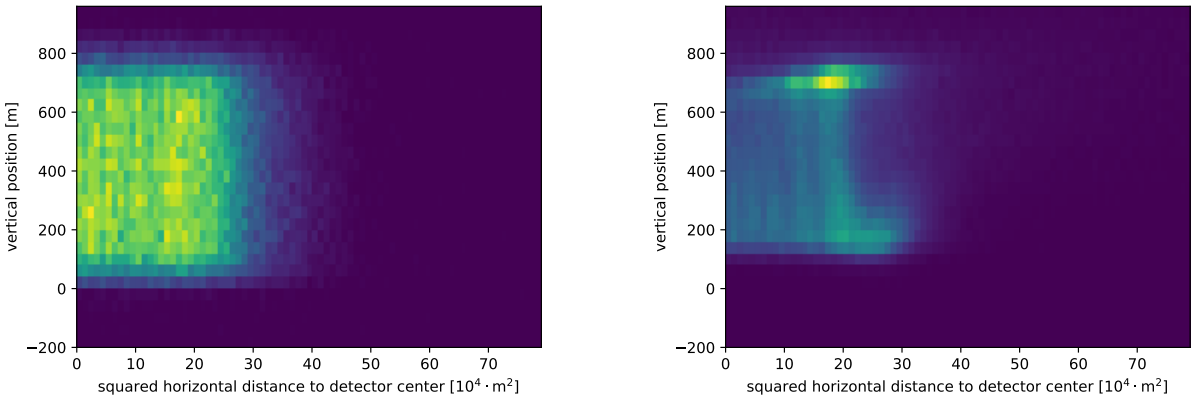

(a) (b)

Figure 6.7: Distribution of reconstructed cascade vertex in the vicinity of the detector. (a) shows $\overline{\nu}_\mu$ and (b) shows atmospheric muons, both without selection cuts and so all triggered events are shown. Events are not weighted. The color indicates the amount of events in each bin (Yellow: many events, Blue: less events)

energy or quality parameters. There are two different kinds of reconstructions available: the cascade reconstruction and the track reconstruction. A double bang reconstruction tailored for ν_τ events is in development, but cannot be used at present.

Reconstructed vertex The vertex gives the location in the detector where the event starts. Most reconstruction algorithms prefer early positions. It means that if a muon starts outside the detector, the algorithm will find a position close to the top. As Figure 6.7 shows, atmospheric muons have vertices close to the upper boundary of the detector. Not all muons are reconstructed in this way, because a muon can have large energy losses everywhere inside the detector. If this so-called catastrophic energy loss happens inside the detector and the cascade is bright enough, the reconstruction can be mislead in a way that the vertex is reconstructed at this position. Furthermore, the density of a reconstructed position at the surface of the detector is higher for atmospheric muons in general as they always enter the instrumented volume. This in mind, in the following, a cut on the reconstructed vertical position and the radius can be performed to reject the atmospheric muon background. Similar conclusions can be drawn from the track reconstruction.

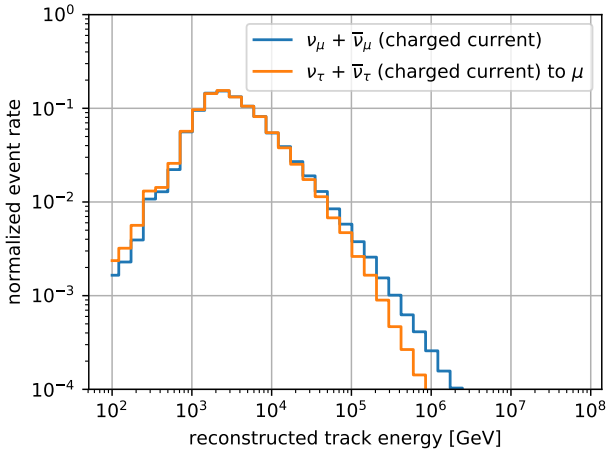

Figure 6.8: Distribution of reconstructed energy for muonic events: ν_μ-CC and ν_τ-CC with $\tau \rightarrow \nu_\tau + \overline{\nu}_\mu + \mu$. Distribution is normalized to 1.

Reconstructed Energy The reconstructed energy on its own does not have a discriminative power as the energy does not say anything about the particle type. However, the spectrum of the reconstructed energy is different for different neutrino flavors. Therefore, the energy spectrum helps to disentangle the event composition in KM3NeT.
One example is the difference in the spectrum between ν_τ and ν_μ, both interacting towards an outgoing muon. In the τ-case, there is the intermediate tau which decays to a muon and a neutrino. The neutrino carries energy which is no longer visible to the detector. The total measured energy is not as high as the one in the muon neutrino case. Alikhanov et al [100] showed that this might open a chance to resolve the contribution of ν_τ. Figure 6.8 shows the spectrum of reconstructed track and cascade energy. The flux of particles is normalized to one. The spectrum of ν_τ is shifted towards lower energies, even if the prepared energy spectrum was the same. This makes the spectrum of reconstructed ν_τ steeper than the spectrum of ν_μ. This is probably not so important for the event identification, but the spectral fit profits from this behavior.

Quality parameters Quality parameters are one major feature of reconstruction algorithms to select well reconstructed events. These parameters give an idea on how good the hits match the fit hypothesis. A cascade does not fit the hypothesis of a track and therefore it has a less good quality than a track would have. For the definition of these quality parameters, the reader is referred to the documentation of the individual reconstruction algorithms [6].

6.3 Definition of classes

As described in Chapter 2, ARCA detects many different event types defined by flavor or interaction channel. Some of them look very different, but some of the interesting physics cases are not distinguishable. There are three different flavors of neutrinos. In the best case, these three flavors would be separated by some algorithm. However, some interactions look the same for different flavors and therefore an algorithm cannot separate them. The best examples here are neutral current interactions. To solve this problem, classes which are more based on the topology than on neutrino flavor are defined. E.g. if some events give a similar topology like the neutral current events, they are defined as the same class. At first this seems contradictory to the objective to identify different neutrino flavors, but in the end, each topological class consists of a well defined sample of events. Therefore, the initial neutrino flux is understood in more detail.
Five classes are defined here with their basic features described in the following:

Class 0: atmospheric muons and down-going tracks The dominant class of events is the atmospheric muon background. KM3NeT/ARCA detects approximately seven orders of magnitude more atmospheric muons than astrophysical neutrinos. When it comes to astrophysics, the need to reject this kind of class is obvious. These events comprise one or more muons traveling through the complete detector. As atmospheric muons arrive only from above, this class is defined as down-going tracks. A neutrino event which starts outside the detector produces a muon, which afterwards moves into the detector and is found there. Therefore, ν_μ-CC events are also defined as a down-going track if the vertex is outside the instrumented volume and the muon moves downwards. Additionally, ν_τ events can be found here. For this purpose, the ν_τ has to interact via the charged current and the τ has to decay to a muon. Finally, a muon travels downwards again.
Three physics cases are combined for this class. As the dominant particle interaction is the atmospheric muon, this class can be seen as a rejection class most frequently.

Class 1: up-going tracks The previous class showed tracks moving downwards. In this class the opposite direction is chosen and therefore ν_μ and ν_τ events belong here. The predominant neutrino flavor is the ν_μ as only about 17% of the τ leptons decay into this channel [12]. In all through-going classes, the initial cascade cannot be observed and therefore the energy of this is not recorded. As stated in the previous chapter, the events might look the same, but the spectral shape in energy will look different so that the composition of this class can be derived from the spectrum.

Class 2: starting track Completing the track events, the class of starting tracks consists of all muonic events starting inside the detector. The direction is neglected in this case, as the start of the muon inside the detector ensures that it is a neutrino event. All other properties are in line with the previous classes.

Class 3: cascade events This class comprises all neutrino flavors. This can be seen as a disadvantage.
In cascade events, neutrinos interact via the neutral current. Additionally, ν_e-CC events look like cascades, however, the physics are slightly different and the secondary particles deposit more energy in the detector. Despite all the drawbacks, cascades are easily distinguished from the atmospheric background. The cascade has a spherical shape instead of the elongated topology of tracks.

Class 4: ν_τ double bang One unique topology is the tau double bang signature with two distinctly visible cascades. If the tau decays after a short path length, both cascades lie on top of one another and cannot be distinguished. However, as the τ travels longer, it becomes more probable that the double bang structure can be resolved. Therefore, a minimal path length for the τ is introduced. If the path length is shorter, the event is defined as a cascade.

At first glance, the definitions seem to be well separated, but for the double bang class a transition was already mentioned: the path length of τ. Such transitions can also be found in other classes. For example, track events put different amount of energy into the initial cascade and the resulting track according to bjorken y. Therefore, a track event can look like a cascade event if the energy deposited into the hadronic cascade overwhelms the track. A definition based on this condition was tested, but not found useful.
It is important to draw lines between the classes for the algorithm. However, finally the results have to be judged with the global knowledge of neutrino physics and not with the boxes arbitrarily chosen here.

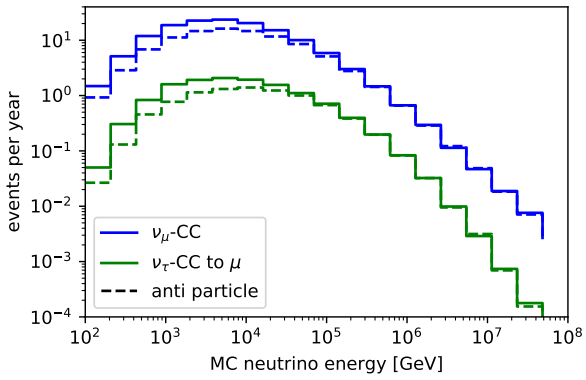

(a) down-going track

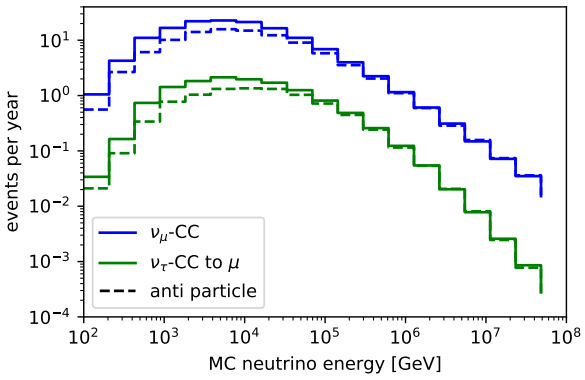

(b) up-going track

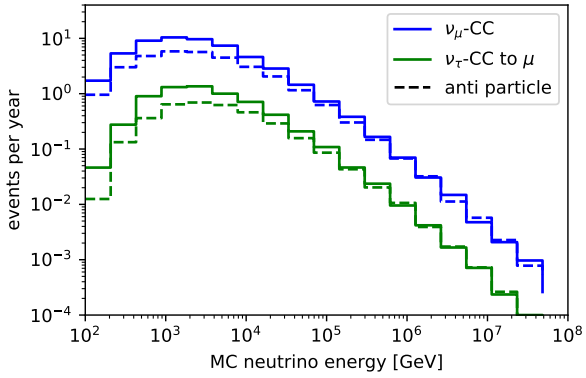

(c) starting track

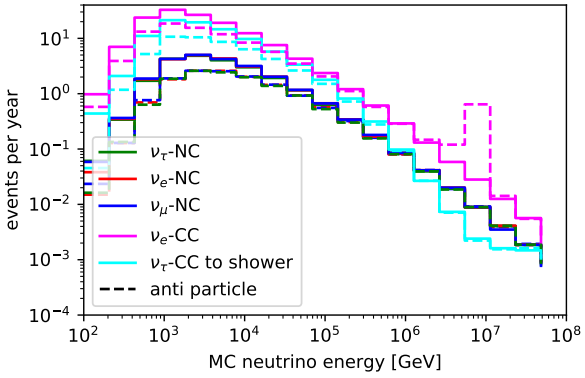

(d) cascade

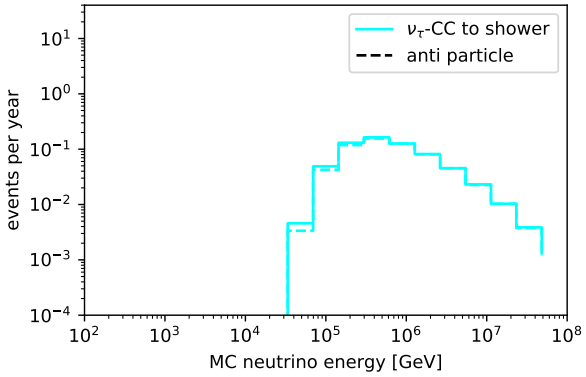

(e) τ double bang

Figure 6.9: Neutrino components of each defined class. Neutrino events are subdivided into charged current and neutral current. Furthermore, the ν_τ channels are divided according to their final state.

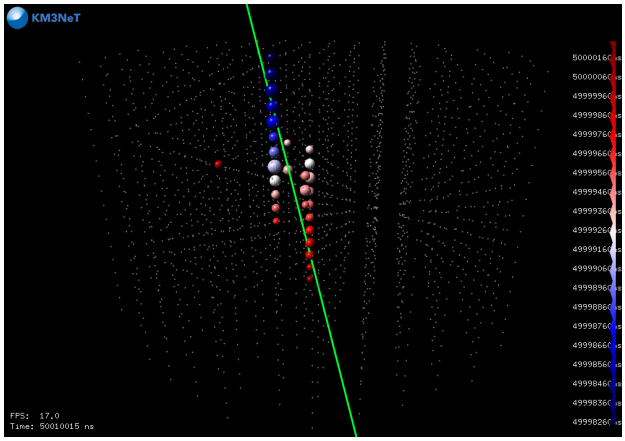

(a) atmospheric muon bundle (E_{bundle}=200 PeV)

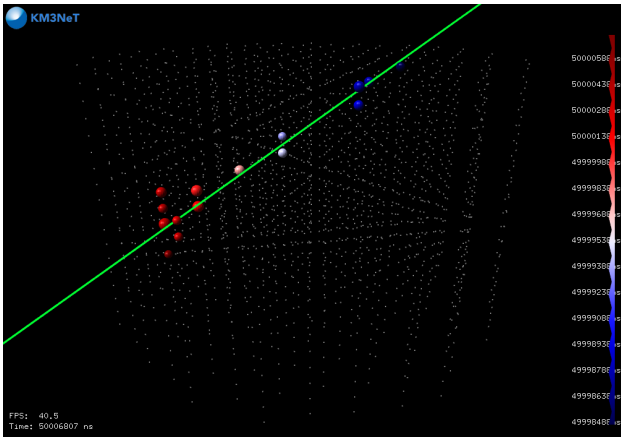

(b) down-going track (ν_μ-CC, E_{ν_μ}=40 TeV, y=0.25)

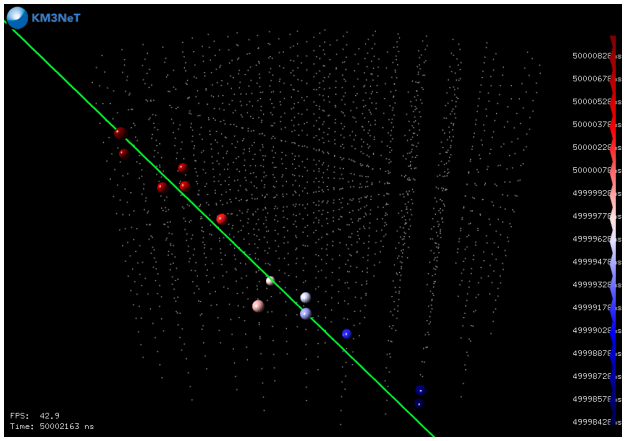

(c) up-going track (ν_μ-CC, E_{ν_μ}=96 TeV, y=0.83)

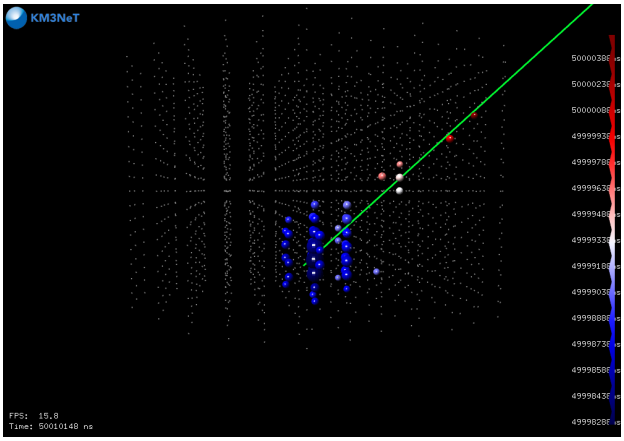

(d) starting track (ν_μ-CC, E_{ν_μ}=91 TeV, y=0.8)

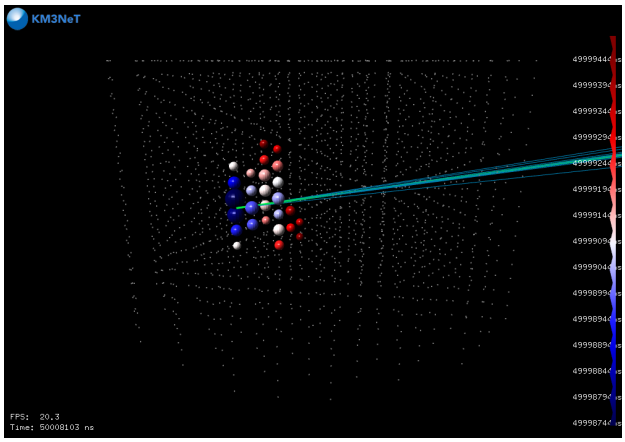

(e) cascade (ν_μ-NC, E_{ν_μ}=1.06 PeV, y=0.6)

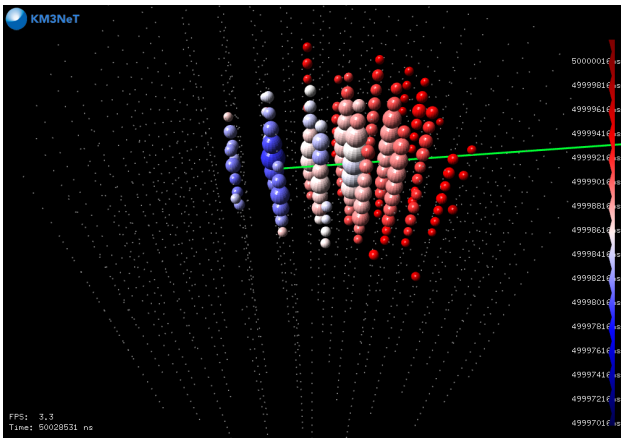

(f) τ double bang (ν_τ-CC to cascade E_{ν_τ}=1.1 PeV, y=0.19, s_τ=161 m)

Figure 6.10: Compilation of event classes defined for KM3NeT. Each small white dot indicates the position of a DOM. The green line is the direction of the initial neutrino starting at the interaction point. blue lines show the direction of secondary particles. Large blobs are hits, the larger the blob the larger the ToT. Color indicates the time of the first hit from blue earls over white to red as late hit times.

6.4 Identification neutrino events with machine learning algorithms

In former analyses, scientists separated the event sample with cuts on pre-calculated quantities which they developed by hand. Accordingly, analysts had to look at every feature and try to follow the behavior, a very time-consuming method.
There are machine learning techniques which can learn the cuts on their own. The machine is fed with appropriate training data and finds correlations between the features and the target class. Two different approaches were used in former KM3NeT analyses.
Firstly, there are tree based algorithms [101]in which an event passes several decisions each on one feature. Thereafter the so-called random decision tree makes a decision, which depends on the final leaf, in which the decision had stopped. It can be viewed as a lot of hand-crafted cuts in the feature space, so that even smaller parts can be rejected or selected. The results for ORCA shown in this thesis are based on a tree-based algorithm.
Secondly, there are artificial neural networks, which were applied in ANTARES for background suppression [102]. In these networks, the correlation between features is used to calculate the target class or quantity via linear transformations. As the features are combined, the way to the target class cannot be followed easily. Both algorithms learn the linear transformation or the position of the cuts on their own.
The main difference between the hand-crafted version and the machine learning algorithms is the speed of the algorithm. All other parts in the process can also be done by hand, if time does no play a role. The basics of machine learning were already developed in the 1970s, but the computing power was not sufficient. As a result, the technology fell asleep until the 2000s when the computing power increased, leading to a renaissance of machine learning.
Neural networks are the state of the art nowadays. One reason for this is that neural network can handle a lot of different input structures from simple independent numeric values over to two dimensional images to videos. Consequently, neural networks based on pre-calculated features are used here for the classification task.

6.4.1 Neural network

The algorithm chosen for this analysis is the neural network, which is inspired by the human brain. The network consists of neurons, synapses, and layers of neurons.
A sketch of the work flow of the neuron is shown in Figure 6.11. A neuron gets information about its environment (red circles) via the synapses (blue arrows). The neuron itself calculates an output on the basis of weights w and input z. The output of a neuron can be written as:

$$\mathrm{x} = w \cdot z, \tag{6.9}$$

where w is a vector with individual weights for each input value, which are the entries of the vector z. Furthermore, an activation function f is used to force the output to a certain range, often from -1 to 1. Additionally, the activation function can damp values far off. For example, a sigmoid function is highly progressive nearby zero but does not change so much for larger values. The final output y of the neuron is:

$$\mathrm{y} = f(w \cdot z). \tag{6.10}$$

Numerous neurons comprise one layer and multiple layers comprise the neural network.
Three layers comprise the neural network used here: an input layer, a hidden layer and an output layer. Figure 6.12 shows the architecture of this simple neural network. The input layer is fed with the data of an event. The data has to be numeric, so each neuron gets a certain number as an input.

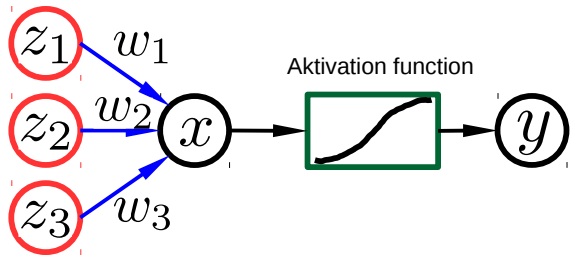

Figure 6.11: sketch of neuron within a neural network. The journey of information to the output is visualized

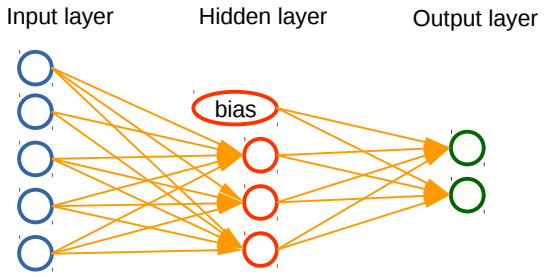

Figure 6.12: sketch of neural network, with three layers. From left to right: input layer, hidden layer, output layer

In my case, the features described in Chapter 6.2 are fed to the neural network. In other applications like image recognition, a neuron can also be a pixel of an image.
The neural network used here is a fully connected network. Every neuron is connected to all neurons of the previous layer. Each layer uses all the information from the previous layer. Within each layer there is one additional neuron without any input, called the bias neuron. It has the ability to introduce some shifts, which can be necessary to achieve a good convergence of the learning process. The hidden layer uses a rectified linear unit (ReLU) as an activation function, which is defined as follows:

$$f(x) = max(0, x). \tag{6.11}$$

For every event, the algorithm proceeds through the network until it reaches the last layer, which is called the output layer. The output of this last layer is the output of the whole neural network.
The last layer consists, in the case of a classifier, of as many neurons as classes are defined. Therefore, five neurons are used in this analysis.
The output neurons use a soft-max function which is defined as follows:

$$f(x) = \frac{\exp(x)}{\sum \exp(x)}. \tag{6.12}$$

This function normalizes the total of all output neurons to one. Thus, the result of each neuron can be interpreted as the safety that the considered event is part of the class for which the neuron is optimized. Even if the value is not regarded as the probability, the class with the largest value has to be favored.
Up to now the classification process of a neural network was described only. Above it was written that the network has weights for each connected pair of neurons. These weights are optimized in a training phase.
In the training the output is associated with variables, which are to be reconstructed by use of the input data. The training algorithm uses back-propagation, which was developed in 1960 [103, 104]. Here the error in the output is calculated. According to the deviation the weights are altered.

6.5 Training process

Events have been processed in a way that they are reconstructed and the additional features (see Chapter 6.2) are calculated. In the following several steps are needed for the training of a neural network. Some of these steps are only applied in the training process, others apply also for the application to unknown data. The application is addressed later on.
First an event selection is applied in a way that only events, which can be well described, are used for the training. Then the features are scaled and completed, which avoids problems in the learning process. Before starting the actual learning process the composition of the training sample must be

defined, which is done in the so-called homogenization process. Afterwards the machine learning algorithm is trained. Every step is implemented as a so-called module and is described in detail in the following.
The training is implemented in the framework of km3pipe [105]. This framework was already used for the calculation of the features. In the training process one cycle does not only provess one event, as the training needs to see multiple events at once. Therefore, one cycle is used to learn only one configuration of the classification. For example, the first cycle uses a learner with 23 hidden neurons, whereas the next cycle uses 45 hidden neurons. Hence different hyper-parameters can be tested in one execution. Further configurations of the data or of the classifier setup which have to be made only once are done only once, while others are done multiple times.

6.5.1 Event selection

The simulation and the reality give a lot of events to KM3NeT, but often these events display only a few hits, caused by neutrinos. Therefore, the events do not bring forth enough information for reconstruction or event identification. Poorly reconstructed events are rejected by using reconstruction algorithms [6]. These cuts are based on reconstruction parameters. However, they only allow one dedicated cut. For this reason in this work another quality cut based on a neural network is applied.
The selection is justified as it can be shown that a training sample containing badly reconstructed events results in a less performing classifier. It shows the probability for an event to be identified correctly. For each line, the classifier is trained with, events fulfill certain quality criteria. However, the fraction of correctly classified events is based on all triggered events. With harder quality cuts (e.g. better reconstructed events), the share of correctly classified events increases. At some point the learning breaks down as the number of remaining events is too low, especially in the high-energy interval. Therefore, one has to find a point with enough statistics in the training process, but also a good performance.
The classifier trained for the quality selection follows the same rules as the classifier described for the event identification upon these very lines. For this reason, only differences are described here.
Two selections are prepared. The first one is prepared to decide on the cascade reconstruction, the second one for track events. For training and evaluation purposes, ν_e-CC events are used for the event selection in cascade reconstruction and ν_μ-CC events are used for the track reconstruction.
A neural network is used to decide whether an event is well reconstructed or not. Therefore, the events are defined into classes of good and bad according to the reconstruction performance. The definition of good and bad is not trivial in this context. If the resulting performance curve shows a preferably flat behavior in the interesting energy interval ($1 \cdot 10^4$ GeV to $1 \cdot 10^6$ GeV), this is good by definition. The efficiency of this selection should not be smaller for this approach in the event that the same reconstruction performance should be reached. This request is well achieved by these algorithms.
Another consideration might be a regression task for the reconstruction error instead of a classification task. This possibility was checked but discarded because the results were not satisfactory.
In addition, the preprocessing is applied as described in Chapter 6.5.2. In the end, the output of the identification consists of safety values to each class, good or bad. The safety of the class for good events is used for the final selection. In the following, only events are used which give a higher safety than a given threshold. The correlation follows the principle: the higher the threshold, the better the performance. Finally, the median moves with a changing threshold of the neural network's output. Beside the median, the quantiles in the final event selection are of interest, as a wide spread of events can defeat a high sensitivity of the experiment. These bands become more narrow with harder cuts. The differences between a low and a high cut value can be seen in figures 6.13 and 6.14.
Finally, the most flat curve is chosen with the angular deviation definition of 3.5° and the energy error is set to 0.9. The given angular resolution, the energy resolution as well as the efficiency of this cut is outlined in Figure 6.13a. Figure 6.13b shows the same performance, but with lower cut values in

case the definition is tailored to a smaller deviation.
For the low definition, one can see that the band for high energy above $1 \cdot 10^8$ GeV is raising faster. Consequently, the high definition was chosen.

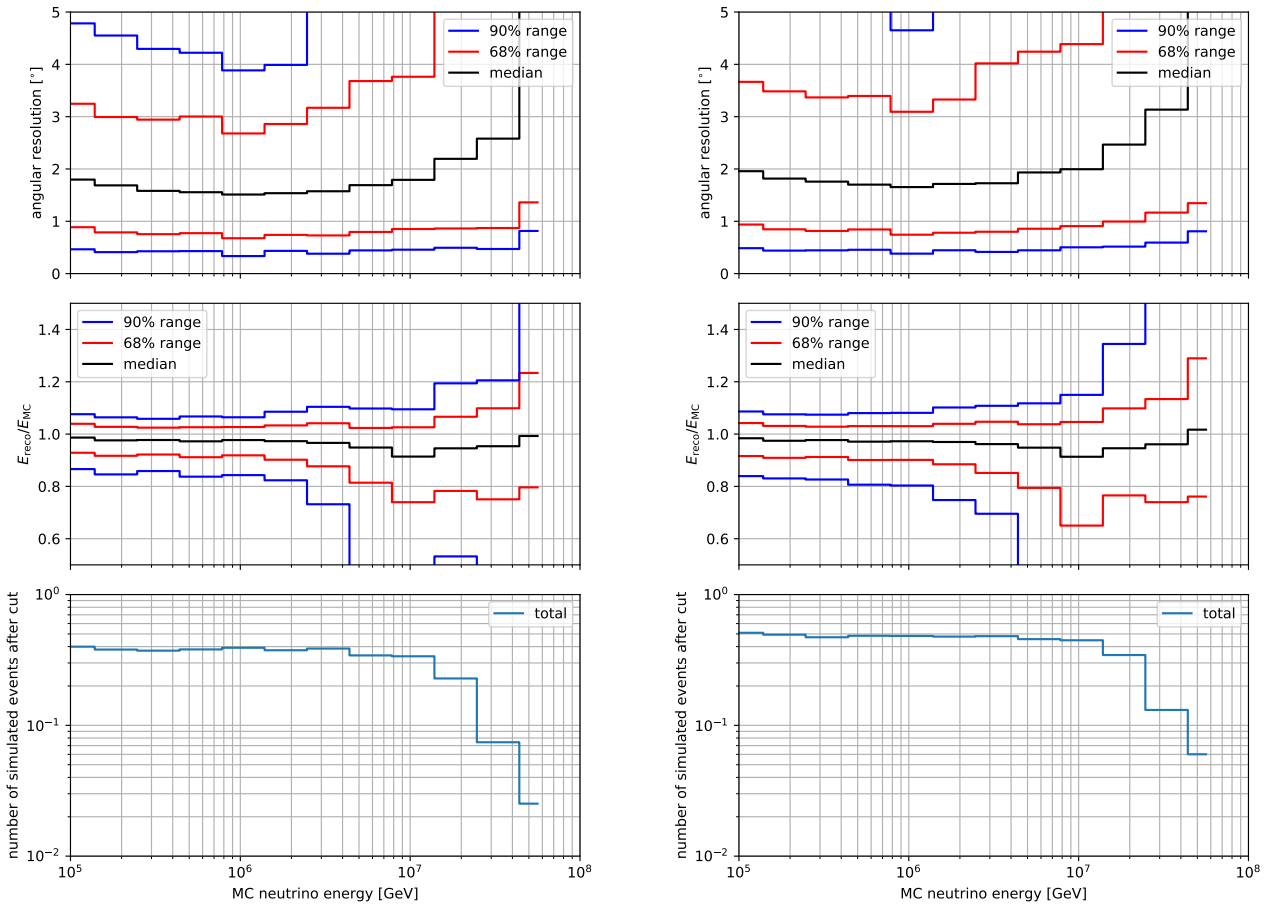

(a) (b)

Figure 6.13: the reconstruction performance for cascade reconstruction with (a) high value definition cut value as 0.8 and (b) low value definition cut value at 0.5

The identical procedure is executed for the track reconstruction. The most important parameter here is the reconstructed direction, which can be below 0.1 degree. This is why the figures only show this number. The energy reconstruction is always dependent on the path length of the muon visible for the detector. If the muon leaves the detector, the energy is no longer visible and the energy is underestimated.
The same as stated for the choice of the definition with respect to the cascades holds for the tracks, too. Figure 6.14a gives the performance of well reconstructed events which are used for training. The median value of directional error is well below 0.1°. This value is reached at an energy of $1 \cdot 10^3$ GeV. Both selections for cascade and track reconstruction are comparable to the performance described in [6].
In the following, only events which either fulfill the quality criteria for tracks or cascades are used for the training process. For this purpose, a value of 0.8 for the cascade reconstruction and of 0.8 for the track reconstruction is chosen.
Applying this cut, the number of events decreases according to the last line of the performance graphs 6.13a and 6.14a. The efficiency is at 40% for both reconstruction algorithms. Figure 6.16 shows the final statistic for the training sample. Therefore, the neural network is fed with enough statistics in the range of interest.

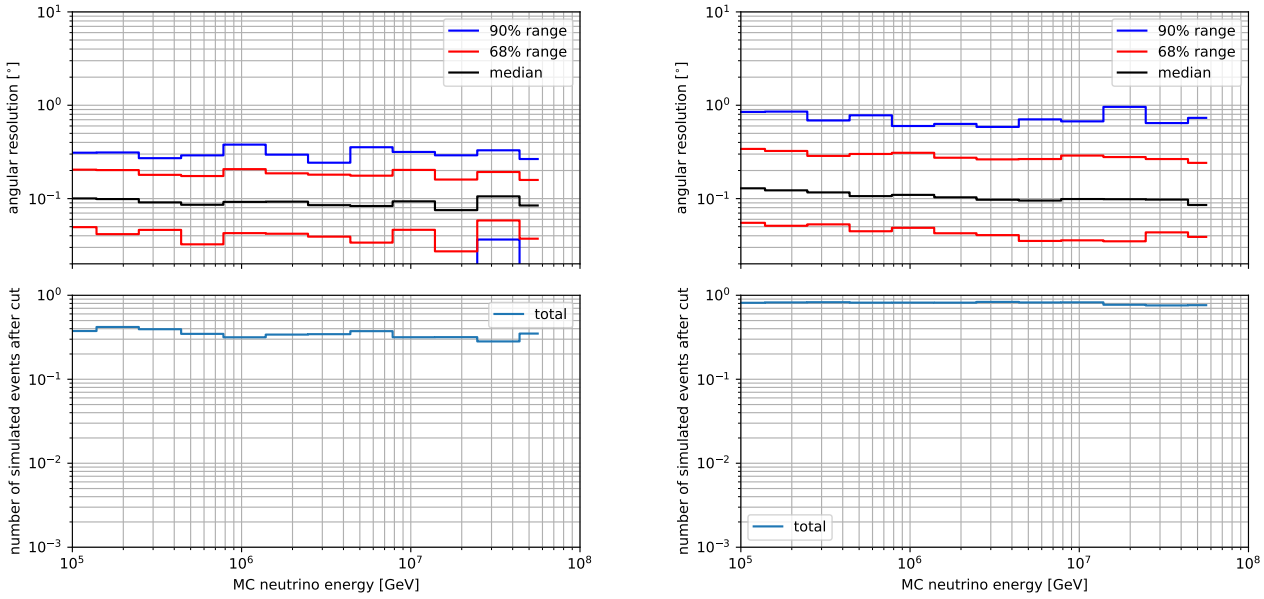

(a) (b)

Figure 6.14: The reconstruction performance for the track reconstruction with (a) high value definition cut value as 0.8 and (b) low value definition cut value at 0.2. The

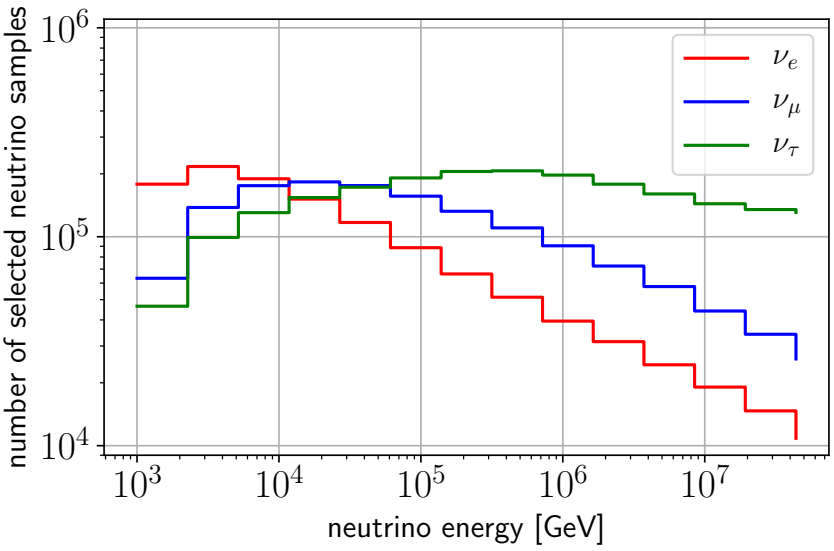

Figure 6.15: Number of MC events for each neutrino flavor, which can be used for training. The number is shown with respect to the MC neutrino energy.

6.5.2 Event preprocessing

Even though machine learning algorithms have the ability to learn a lot by their own, the developer can be a helping hand. This accelerates the convergence to the final weights. In some cases, the convergence cannot be reached without any preprocessing of the data. In this work, three preprocessing steps are performed on each event: imputation, standardization and principle component analysis. These steps are described in the following. Each preprocessing step can be replaced, removed or extended on its own. The methods and classes used are taken from scikit-learn [106]. Each method is developed once and can be applied to other event samples.

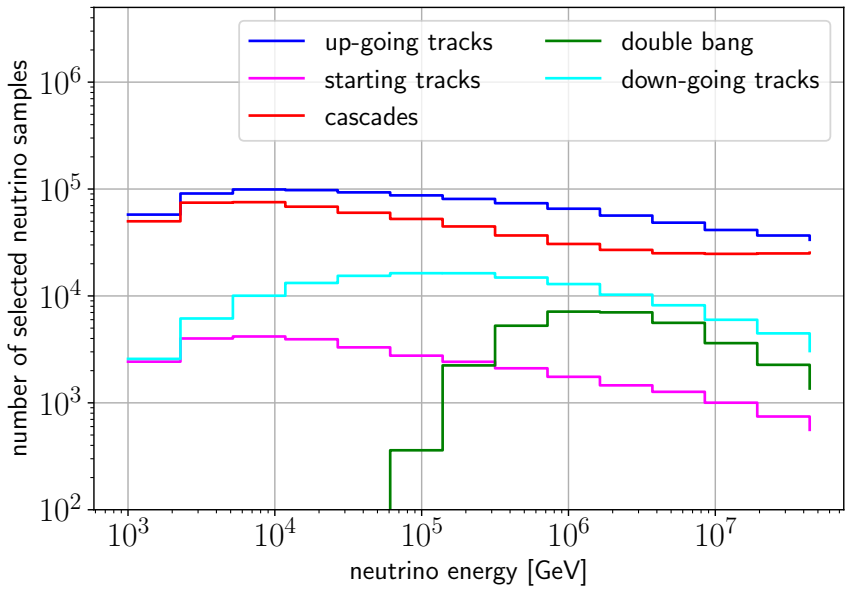

Figure 6.16: Number of MC events for each class which can be used for training. The number is shown with respect to the MC neutrino energy.

Imputation

In data mining processes, data is often not complete [107]. For instance, some features are not calculated at all for a single event, which should not be the case here, as the files are processed by the KM3NeT collaboration on its own. However, some quantities cannot be calculated for the reason that the process stopped at some point. This happens if the event contains not enough hits, so that the algorithms can work with them. In such cases, the algorithm sets some arbitrary value to this feature, in most cases *nan* or infinity. Both cases cannot be treated by machine learning algorithms directly. *nan* is - by definition - not a numerical value, but is absolutely needed. An infinite value is numerical but would defeat the calculation of derivatives inside the algorithms, which leads to useless values for the minimizing process.
The so-called imputation process is applied to remove the missing values. For a missing value, the mean of the unweighted sample for this feature is used. This might seem very rough but the step is necessary to remove values which distract the learner otherwise. Furthermore, the values lie well inside the distribution and so the effect of this value is minimized. Another possibility is the reconstruction of the missing value based on the other features. In the author's view, this leads to an computational overhead, which is not necessary at this moment as the actual value of this feature is not needed. An estimate of this feature does not increase the amount of information.

Standardization

The values of each feature can have very different sizes. A feature with larger values or variance can dominate the learning process over other relevant features. This step reduces the differences in absolute values and shape. Thus, the mean value is removed by a shift of the distribution. Furthermore, the sample is scaled to unit variance. This way ensures that each feature influences the classification equally.
In literature one find that neural networks can handle features with not standardized values. This step was chosen, to easily change the learner and more important the learning rate can be increased [108]. In this work the training time was decreased by a factor of 1.5, which represents a significant reduction of computational power, especially if a lot of hyperparameters have to be tested.

Everyone contributes: PCA

The next step is a **p**rinciple **c**omponent **a**nalysis (PCA), which was first developed by Pearson in 1901 [109]. Therein the feature space is reduced in dimensionality. This is done with linear transformations, which are applied in a way that the features become more decorrelated. Therefore, features, which are highly correlated or contain the same information, can be reduced.
Similar to the previous preprocessing step, the PCA shows the possibility to reduce the computing time in the training. This is possible as the learner has to find a reduced number of weights describing the network. In this work, the dimension of the feature space is reduced from 155 to 55. The reduction of dimensions by a factor of three accelerates the learning process by a factor of two. This is done on the expense of the time the PCA takes, which is only 5% of the time the final learner needs. In the end, the identification performs the same as if without the PCA.
Commonly, the PCA is also looked upon as to improve the classification performance [110]. This could not be reproduced here. An additional advantage is that each learning process can be started with all available features as they are reduced and combined automatically during the PCA. Therefore, feature selection is done without any additional effort.

6.5.3 Balancing the dataset

Earlier it was shown in the context of KM3NeT/ORCA that imbalanced training samples can bias the outcome of the classification. Figure 6.17 displays the fraction of correctly classified events. The classification task is to separate tracks and cascades in ORCA within the energy range up to 40 GeV. Tracks are ν_μ-CC events. Neutral current and ν_e events are defined as cascades. The fraction of correctly classified tracks increases towards the lower energy boundary, whereas the fraction of correctly classified cascades decreases. The reason is shown in Figure 6.18. The training sample has a lot more track events in this energy region than cascade events. This mismatch comes from the reconstruction and triggering in the processing before the event identification starts [6]. This induces the learner to vote for the predominant class in these regions.
There are cases imaginable in which this behavior is desirable. For instance, if missclassification harms one class more than the other way. In KM3NeT however, the aim is to measure ratios between classes, therefore, different classes have to influence the classification equally.

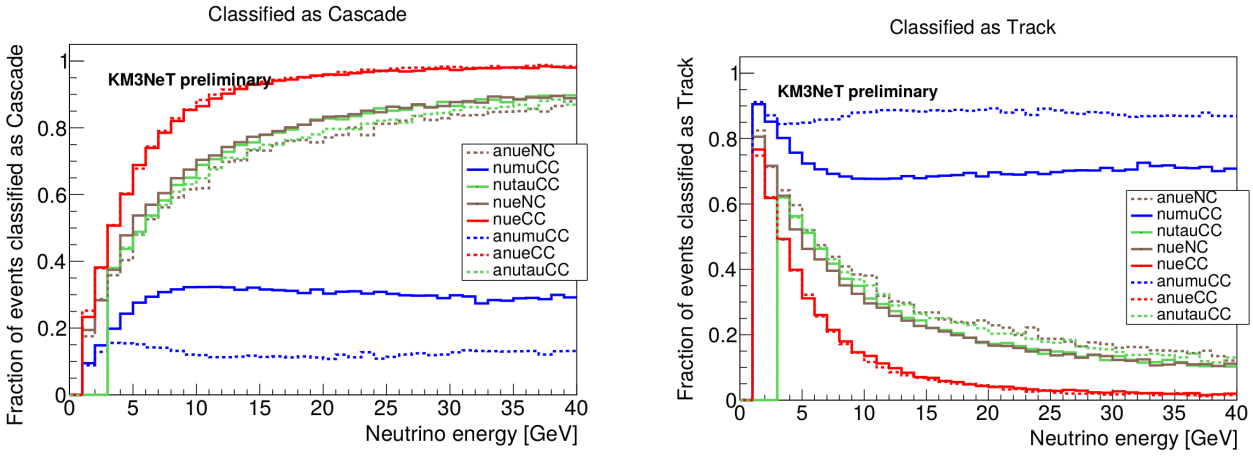

(a) (b)

Figure 6.17: Fraction of correctly classified events in ORCA. A decision is made on track versus cascade. Same figures as already shown in [6].

Finally in this work balanced datasets are used for training. However balancing between classes is not enough as it does not remove imbalances dependent on energy, as seen above. The algorithm

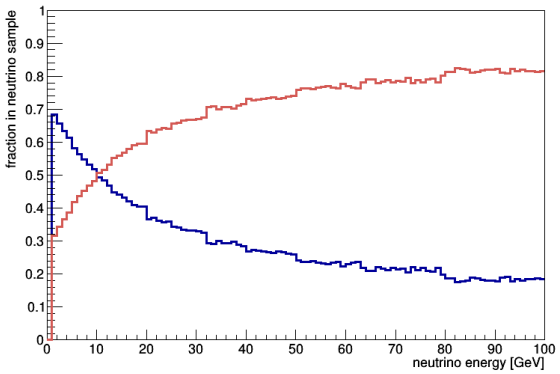

Figure 6.18

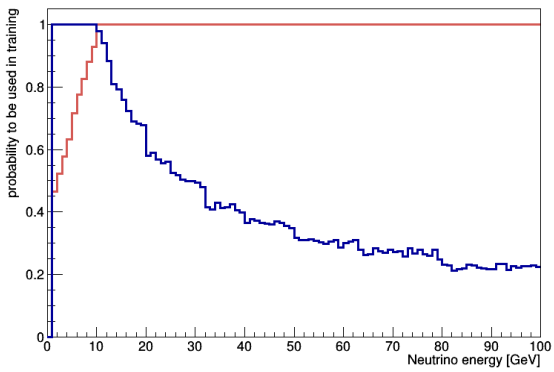

Figure 6.19

finds the imbalance with respect to the underlying Monte Carlo energy. Thus one has to go one step beyond. The dataset is balanced in each class and each energy bin. Therefore, the events are binned in a histogram over the Monte Carlo energy. Similar problems can be seen in racial discrimination of machine learning algorithms [111]. If there are weights applied to the events for the training, they have to be applied here, too. With one histogram per class the final weighting can be calculated, so that the event sample is balanced in the described way. Figure 6.18 shows the weighted samples for the training process. The event yield is very different for both classes. However, Figure 6.19 shows the additional weights so that the sample can be re-weighted and the learner sees a balanced dataset.
In this work, the Monte Carlo energy was used to balance the dataset, but every other quantity could also be used here. The energy was chosen because the final analyses will be based on energy spectra. The homogenization process makes it possible to accomplish any desired outcome, e.g. if one dedicated class should be favored in some part of the feature space, it could be highlighted for the learner with a higher weighting. However, as this seems to be cheating, the present work chooses the conservative approach meaning that all classes are equally pronounced to the learner.
Figure 6.20 shows the fraction of correctly classified events after a training with the balanced dataset. The fraction of low-energy events classified as tracks is reduced. The rest of the histogram is adapted accordingly. For highest energies, the fraction is equal to the values without homogenization.

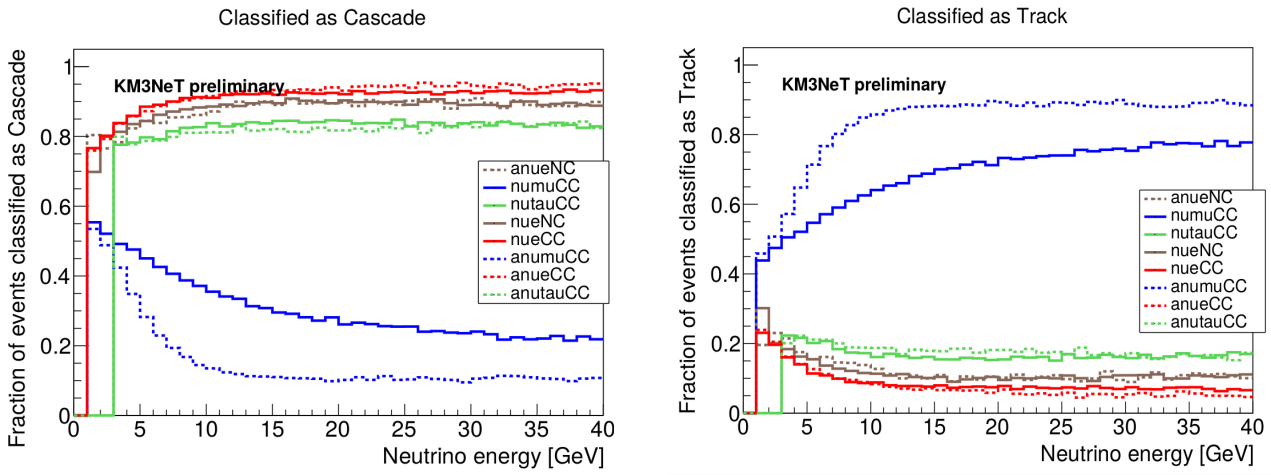

(a) (b)

Figure 6.20: Fraction of correctly classified events in ORCA with homogenization. A decision is made on track versus cascade. The same figures already shown in [6].

6.5.4 Training of the neural network

The final step in the training process is the training of the classifier itself. Herein two different tasks have to be fulfilled: firstly the estimate of the best hyperparameters and secondly the weights describing the linear transformation of the neural network. The latter task is accomplished by the learning process of the classifier. Usually, the learning has to be achieved within many iterations by the scientist itself.

The optimization of hyperparameters is the most tricky part, as there is no clear hint in literature which configuration delivers the best result for a given classification task. Hyperparameters, which have to be set here, are for example the number of hidden neurons, the dimensional reduction with the PCA or the configuration of the initial weights of the neural network. After some reasonable ranges of these parameters are set, the rest of the optimization is done by random hyperparamter optimization. When the hyperparameters are chosen randomly, the training is performed and afterwards the performance can be compared. This means that the training process is repeated with different hyperparameter settings. The advantage with respect to a regular grid search is that one hyperparameter is tested at more different points in the hyper parameter space than usual for regular grid search [112].

In this way, the number of hidden neurons is set to 42. In the range between 30 and 50, there is no variation in the performance, therefore a value in the middle is chosen. Neural networks with less neurons show a decreased classification performance. The more neurons comprise the hidden layer, the longer the learning takes.

The neural network implementation is taken from theanets [113], which is a python package based on theano [114]. Computational intensive calculations are exported to C-based code, which is faster in runtime than pure python code. The network chosen is a feed-forward classifier. The learner tries to minimize a cross-entropy loss, which compares the target values to current training results.

Initial weights have to be chosen for the training. It was shown in previous works, that the initialization cannot be achieved with some regular values, e.g. with some symmetries or even set to one value for all weights [115]. Thus, the weights are chosen according to a Gaussian distribution with a mean of 0.1 and a standard deviation of 0.2. In this way, each individual start of the training is from some other point of the parameter space, which forces the learner to take another track to find the best classification. Other values were tested without any improvement for the convergence or classification output.

One possibility to stop the training process is when a maximum number of iterations is reached. This can be helpful if something is to be tested. However, in the real case the training proceeds until the best result is achieved. Therefore, the training stops if no more progress is made. For this purpose two parameters are defined. At first the improvement is defined, which stands for the amelioration from one iteration to the next. If this threshold is missed, a counter is increased. The maximal value of the counter is the second parameter, the so-called patience, is to be defined. If the counter reaches the value of the patience, the training is stopped. The patience is chosen to be five and the minimum improvement is set to 0. Hence after five iterations in series with no improvement the training will be stopped.

In the training process, there are two types of samples. Firstly, there is the training sample, which is used to train a model. Based thereon, the loss function is minimized. Otherwise, there is the validation sample, which is used to measure the performance on unseen data after the training process. In this way, some events are used for training, whereas the other part is used for evaluation. The samples used for training cannot be used for further analyses as the classification is optimized to this dataset. In general, the classifier has a better performance in case of the training sample than in case of the validation sample. However, there is a cross validation which eliminates this drawback. The complete data sample is split into separate parts. One part is used as validation set and all the others are used for the training process. This is done multiple times until every part was used for validation. In doing so, each single event is used for training and validation, respectively. Thus, a classification result for

each single event comes out, which is never based on a training using the event itself. The number of splits can be chosen randomly. More parts give higher confidence to the performance, but the training time is increasing with each part, because the number of individual neural networks increases. In the following chapter, the splitting is used to see the variance in the trainin as each trained model gives a slightly different decision on each event. Therefore, the overall classification performance can vary. A high variance raises concerns on the classifier.
The training of a set of hyperparameters takes time in the order of 20 min in this case. This makes it possible to train in the magnitude of one hundred different neural networks to obtain the perfect hyperparameter setting.

6.6 Application of trained classifier

The previous chapter showed the way from simulated events to a trained classifier, containing preprocessing steps and the actual neural network. Some parts of the developed training chain are not needed provided that the neural network classifies unknown events. Furthermore, the software tools have to switch to an application mode. The implementation enables the user to use the same modules like in the training process and the application process, except, once the target file name is given, to save the fitted values. In the application task, this input parameter is replaced by the prepared file containing the configuration. An event selection is not needed in advance because the classification can be applied for all kind of events. After all, the preprocessing steps are used as they are trained in previous steps. As the application does not need any weights, the homogenization step is not a prerequisite.
The cross validation step can be applied and for this purpose multiple trained neural networks have to be provided. This possibility enables the evaluation of the stability of the classifier. Thus, error bars on base of the reliability of the neural network can be calculated. The actual output of only one neural network is smeared. If one neural network would be trained so that it always would give cascades, the others would be more normal and so the final result would be more trustworthy. The main step for the classification is the neural network itself. The trained neural network is used in the application module, which has to replace the learner module. Further reading and writing modules remain the same.
This application software can be used for unknown data, in the future for the data out of the sea. At the moment it is utilized for events which are not used in the training process and therefore do not have any classification output.
In the following, results are shown which are a composition of the output of the cross validation and the application software so that each triggered event is used for evaluation.

6.7 Results of event identification

6.7.1 Performance criteria

In the training period, one step is the evaluation of the performance, which is based on the cross entropy. Here the learner maximizes the separation power of the classifier. As this value is not illustrative and the meaning to the final physics analysis is not directly visible, more evaluation methods are introduced here.
The first to be described here is the purity of a class. It is defined for a class called x as

$$\text{purity} = \frac{\text{Number of correctly classified events of class } x}{\text{Number of all events classified as class } x} \tag{6.13}$$

A high purity says, that there are only a few events classified as a class but incorrectly classified. The

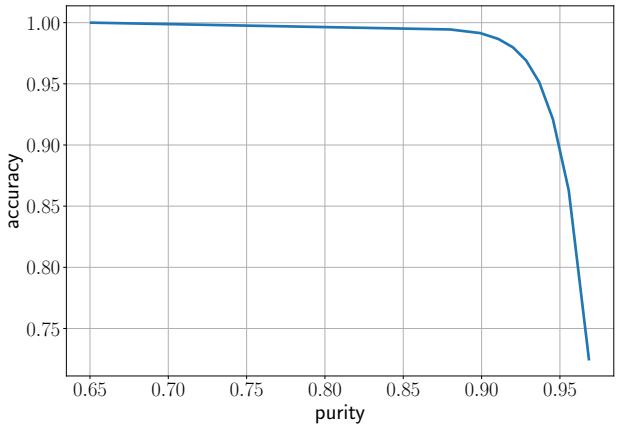

Figure 6.21: Purity versus the accuracy of the cascade event channel in the energy range between $1 \cdot 10^4$ GeV and $1 \cdot 10^5$ GeV. The final configuration of the classifier is used. The pairs are given for different choice of safety for this class. Low safety gives high accuracy, whereas high safety results in a high purity.

opposite direction gives the accuracy, which states the fraction of a defined, correctly classified class:

$$\text{accuracy} = \frac{\text{Number of correctly classified events of class } x}{\text{Number of all events of class} x} \tag{6.14}$$

The higher this value, the more sensitivity can be pulled out from this class if it is used as a standalone parameter. The both described quantities work in the opposite direction. If a classifier is pushed towards higher purity, which means that differently looking events have to be sorted out, also events of the actual class are rejected. Figure 6.21 shows one example of the correlation between purity and accuracy. As the purity increases, the accuracy decreases. Each data point in this figure stands for a different cut value after the classification process. The more the curve fits to the upper right edge of the figure, the better is the classifier. This figure is most often shown when there is a task to reject one class.

This work is focused on the definition of five classes. Therefore, the simple illustration as described before is not directly applicable. In Chapter 7, where shape differences will be used to find the flavor composition of the neutrino flux, the emphasis will be placed on the final composition of the resulting samples and their spectral shapes, respectively. For this purpose the composition, in different views, is shown in the following chapter. It gives an intuitive way of understanding the differences of the various classifiers.

Additionally, a quantity is defined, which gives a measure for the differences in spectral shapes. In history of science, a lot of counting experiments were conducted. They ranged from the radioactive decay to astroparticle physics. There are several methods to calculate the significance of a counting experiment. A widely used approach stems from Li and Ma, developed in 1983 [116]. They described two approaches, the first using strictly the Poissonian variances and the other one being a likelihood approach. The main difference to the application described later is that simulations have shown that the likelihood approach is valid down to lower counts compared with the other approach [116].

A basic principle is the concept of significance. A measurement with one sigma comes to the conclusion that the hypothesis according to which the background produces this result can be rejected by 68%.

In a classical application, in gamma ray astronomy, there is a counting experiment, too. The measurement is carried out in the direction of the source and receives the count N_{on}. Then another direction is observed and the count N_{off} is received. Finally, the significance of the measurement of signal events

is calculated as:

$$S = \frac{N_S}{\sqrt{N_B}} = \frac{N_{\text{on}} - \alpha N_{\text{off}}}{\sqrt{\alpha(N_{\text{on}} + N_{\text{off}})}} \tag{6.15}$$

where α is the ratio between the times of measurement for the off and the on zone. In this work, it is not intended to measure the signal and background but to estimate the strength of one source with regard to the others. With a given background estimate and the signal estimate, one has to eliminate the on-zone and off-zone in the equation.

$$N_{\text{on}} = N_S + N_B \tag{6.16}$$

$$n_{\text{off}} = N_B \tag{6.17}$$

α has the value 1 as the counts are made in the same bin and therefore the size and time of measurement are the same.
Finally, we get:

$$S = \frac{N_S}{\sqrt{N_S + N_B}} \tag{6.18}$$

Algorithms evaluating the strength of single spectra have to evaluate their significance for all the bins and sum them up:

$$T' = \sum_{0}^{N_{bins}} \frac{N_S}{\sqrt{N_S + N_B}} \tag{6.19}$$

This quantity will be called the *Total Performance*.
The result is dominated by high count bins. Therefore, the question arises how one should treat different values in different bins.
In a first approximation, one can normalize the significance of each bin to the number of events in the bin, but on the other hand, a high number of events in a bin has advantages as it contributes to a better fit confidence. Therefore, the normalization with N_{total}^{a} in which a is an arbitrary constant is chosen. The value for it is chosen to be $a = 0.5$. This seems to be the most natural way of normalizing the values. It keeps a satisfying amount of high event numbers as usable but does not neglect the features in low count regions at the same time. Finally, we get the *performance*:

$$T = \sum_{0}^{N_{bins}} \frac{N_S}{N_S + N_B} \tag{6.20}$$

The above mentioned second approach of Li and Ma to calculate significance is not shown here as it is way more complicate and time-consuming and I could not see any benefit regarding the selection of suitable spectra for the spectral fitting process.
This approach was already tested in the diffuse neutrino flux analysis [117]. There is one pointing difference in that analysis compared to the flavor composition task here. In diffuse analysis, we have one signal, the neutrinos, whereas in the new analysis we have three signals, the three different neutrino flavors. Thus for a specific flavor, the significance with respect to the total of the others and its *Total Performance* is calculated.
This chapter made clear that there are several points of view offered for selection to find the best classifier. The next point is to show the results of the finally chosen classifier. Other applications may need a different selection of the classifier.

6.7.2 Event distributions

The figures shown in the following section describe the event distribution after the classification process. Figure 6.22 shows the expected flux of neutrinos in different interaction channels. Here

four interaction channels illustrating the typical behavior are selected. The first figure, 6.22a, displays the flux for $\overline{\nu}_e$-CC channel. The figure visualizes the distribution of this channel into the five classes, firstly as it is defined in advance (dashed line), secondly as the classifier labels the events finally (solid line). The channel is purely defined as cascades. However, there are more labels used by the classifier. Nevertheless, the fraction of $\overline{\nu}_e$-CC events which are not classified as cascades is very small, 5% at most. The peak induced by the Glashow resonance can be seen in the cascade as well as in the other classes. The corresponding bin shows the largest deviation, which indicates that this channel provides the most different variability to the event topology. The shape of the final distribution for double bang events reveals an interesting feature. The shape is similar to the defined shape of real double bang events. It starts between $1 \cdot 10^4$ GeV and $1 \cdot 10^5$ GeV. Furthermore, the shape follows the common decay of the flux. Therefore, the classifier learned that double bang events can be found most frequently in this region. In other channels, like $\overline{\nu}_\mu$-CC shown in Figure 6.22b, the shape is visible, too. However, here it is shifted towards lower energies, which is caused by the reduced energy visible in the initial cascade.

For the ν_μ-CC channel, a small fraction of events was defined as cascades, indicated by the dashed red line. However, it can be shown, that this fraction cannot influence the accuracy or purity in the flavor image. The picture in classes looks different, but this is not important for the flavor composition. The fraction of events classified as cascades remain nearly the same. In total, the fraction of starting events is small with respect to the overall flux. Even though this channel gives a clear signal for neutrinos, the up-going track channel is most important to find astrophysical neutrinos. The figure shows that for low energies, the classified flux is lower than the defined one, whereas above $1 \cdot 10^5$ GeV a higher flux after the classification is observed. Therefore, events staring outside reveal some cascade-like structure on their way through the detector. Additionally, so-called corner clippers yield a cascade-like structure.

Similar to the case of $\overline{\nu}_e$-CC, Figure 6.22c shows the distribution into classes for a cascade like structure. The fraction of correctly classified events is similar. As the total flux of neutral current events is smaller than the flux for $\overline{\nu}_e$-CC events, the total flux is reduced also in this figure.

Finally, Figure 6.22d shows the flux for the ν_τ-CC channel with a decaying τ to a cascade. The definition of double bang leads to a large fraction of cascades and a localized distribution of double bang events. The line illustrating the true spectrum of cascades shows a dip when the double bang events become partners. However, in the final classification, the flux of cascades is overestimated, as some of the double bang events are classified as cascades. Therefore, the dip in cascades vanishes but the number of double bang events decreases. In the very highest energy range, the total flux of double bang and cascade is of similar amplitude. However, it is already at a very small value of around 10^{-2} events per year. For this reason, one would not expect a high enough signal and therefore much contribution of tau double bang events to the final analysis.

Before shedding more light on the internal structure in each channel, Figure 6.23 shows the distribution of classes inside each flavor. The individual flux predictions for flavors show similar features like the individual channels shown before. As the electron neutrino flux consists of cascade events only, it is identical to previous shown histograms.

The flux of muon neutrinos consists of several classes. Firstly, there are the up and down-going neutrinos. The flux of down-going tracks increases with energy with respect to the up-going tracks as for high-energy neutrinos, the absorption by the Earth plays a role. Whatever the case, the fraction of correctly classified events is above 90%. Most of these events are missclassified as cascades. It is shown later on that most of these events are low bjorken y events, thus events with a less bright track but a bright initial cascade.

The last flavor, the tau neutrino, is composed by all target classes. The double bang class is defined as a flux of at most one event per year in one bin, but the final classification gives raise to at most half an event per year. Here, over the complete range, the cascade channel is overestimated because a lot of defined classes can have events which look like a cascade.

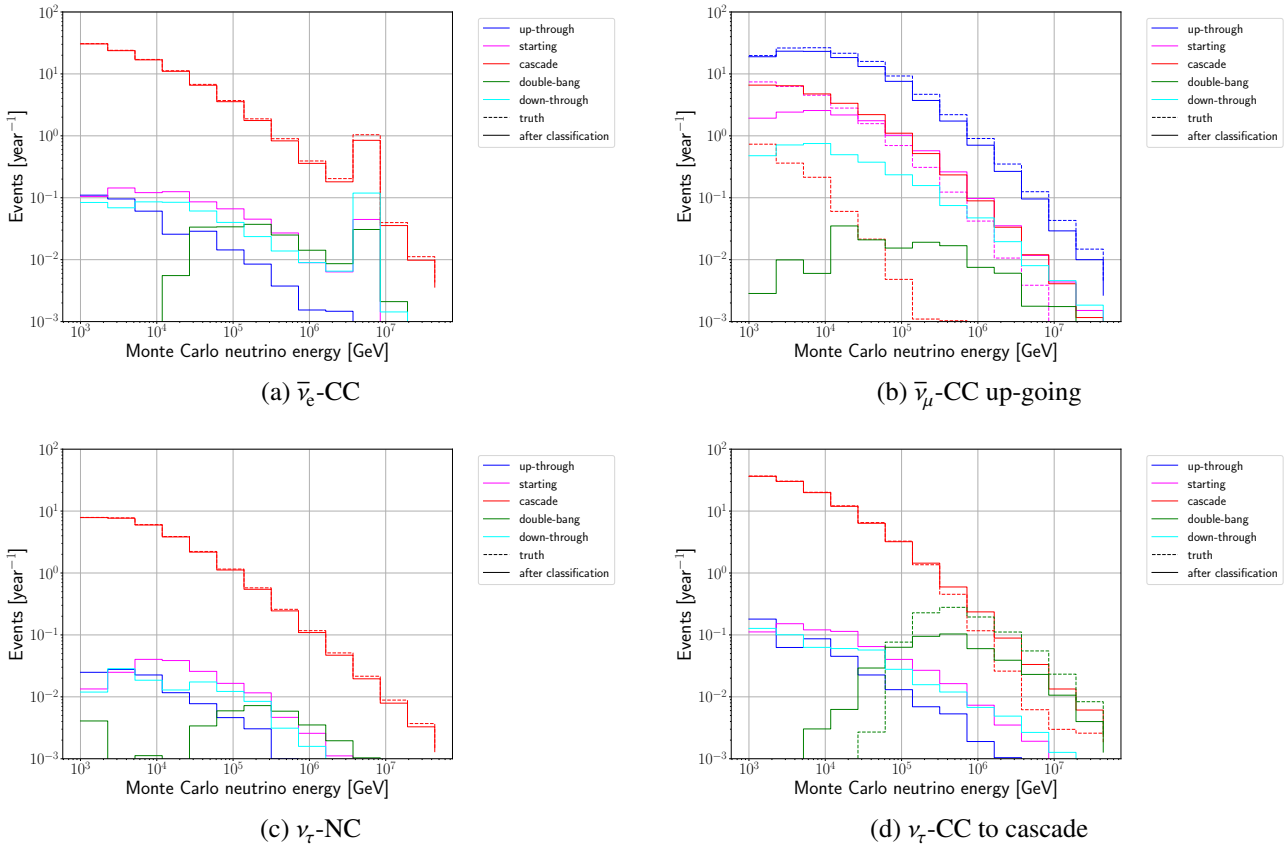

(a) $\overline{\nu}_e$-CC (b) $\overline{\nu}_\mu$-CC up-going

(c) ν_τ-NC (d) ν_τ-CC to cascade

Figure 6.22: Event distribution versus energy for different neutrino channels. The flux is divided into the five target classes. The dashed lines show the distribution as it was defined in advance. The solid lines show the distribution as obtained by the classifier.

The last way to show the expected neutrino flux with respect to the Monte Carlo neutrino energy is the composition of the target class in Figure 6.24. Again, the true composition is shown by dashed lines. The final composition after classification is shown as solid lines.

Up-going tracks, as shown in Figure 6.24a, are defined by tau neutrinos and muon neutrinos. Nevertheless, a small fraction of electron neutrinos finds its way to this class. The number of tau and muon neutrinos is smaller than the one defined. As in the previous argumentation shown, mostly low bjorken y events are classified as cascades and can be found in the cascade channel. The increased flux of muon neutrinos in the cascade class is shown in Figure 6.24c. Tau and the electron neutrino are well reconstructed in this case. The ν_τ spectrum gives some raise to deviation in the high-energy region as the events defined as something different remain at the cascade class.

Figure 6.24b shows the flux of starting tracks. Even though the flux is very similar between defined and classified, the classified flux is higher than the defined one. This will raise problems in the following analysis as track events which are not starting are classified as starting. In the following, this will mainly concern the atmospheric muon background, therefore this class where half of the events are not of this class, will be overwhelmed by atmospheric muons.

Figure 6.24d shows the flux of classified double bang events. With respect to the complicate structure of a double bang event, the fraction of correctly classified events is fine with 50%. However, there are other flavors, which contribute. One can see that the difference in shape is given, therefore in further analyses this can give some signal.

Figure 6.25 shows a detailed view on ν_μ events, which are classified as cascades. As previously mentioned, the more energy of the neutrino is put into the muon, the better it can be recognized. The left figure shows the fraction of events classified as cascades. The uppermost line is the line for high

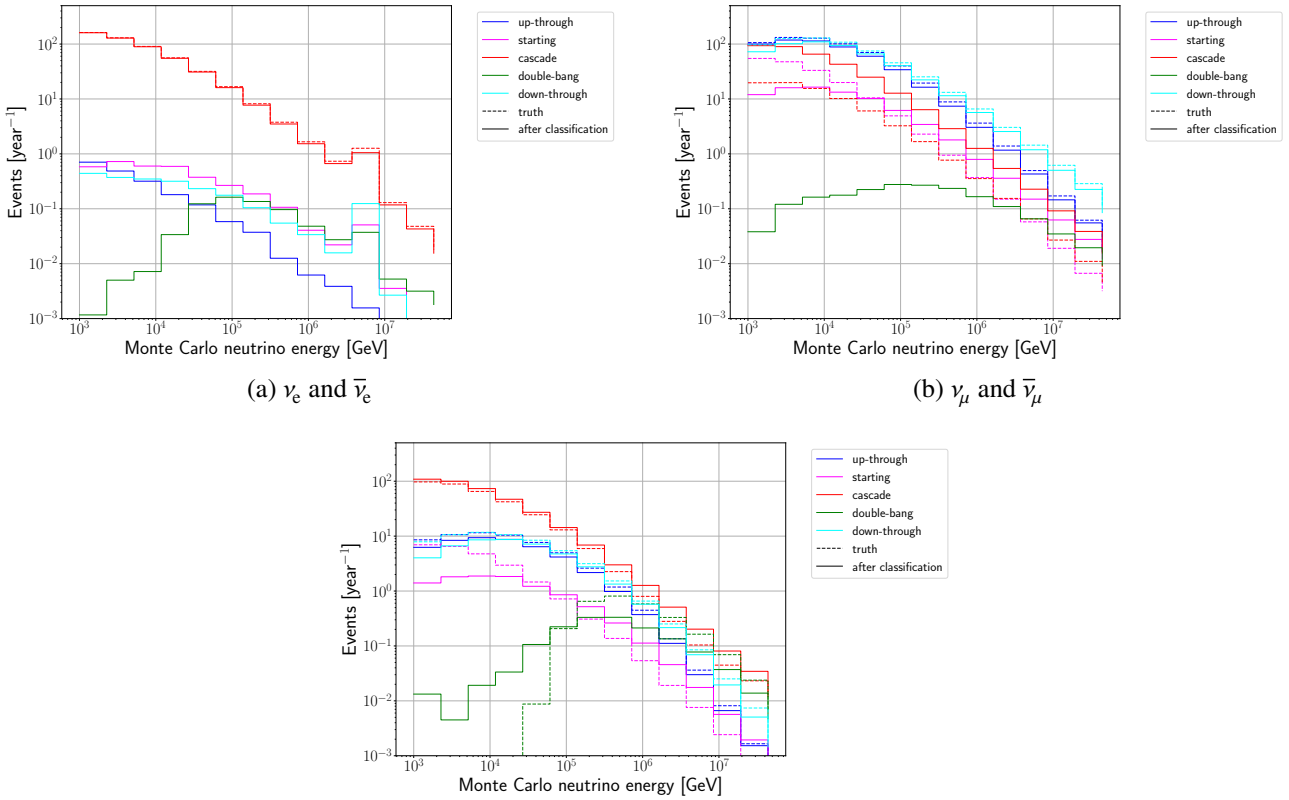

(a) ν_e and $\bar{\nu}_e$

(b) ν_μ and $\bar{\nu}_\mu$

(c) ν_τ and $\bar{\nu}_\tau$

Figure 6.23: Event distribution versus energy for different neutrino flavors. The flux is divided into the five target classes. The dashed lines show the distribution as it was defined previously. The solid lines show the distribution as obtained by the classifier.

cascade energy. There is a clear trend that with higher bjorken y the classification rate drops. The right part of this figure shows the same quantity, but split into intervals of muon energy. Again one can see that the fraction of events decreases with increasing track power. However, the fraction increases with total neutrino energy, which stands for the increasing energy in the initial cascade.
The last figure showed that intrinsic properties of neutrino events can bias the classification to certain results. A similar behavior can be demonstrated for ν_τ. Here Figure 6.26 shows the fraction of events, which are classified to certain event classes. The definition of double bang leads to the definition which decreases in cascades with larger neutrino energy. Nevertheless, when the energy is large enough so that the second bang is outside the instrumented volume, the event is not classified as double bang. The overall shape is the same for the classification fraction, but the numbers are from the definition. One can get a higher coincidence to the definition, but this comes along with a reduction of the purity. Beside the consideration with the neutrino Monte Carlo energy in the left part of Figure 6.26, the fraction of classified events is shown in the right part . The definition at around 14 m can be seen clearly. Above a path length of 100 m more events are classified as double bang than as cascade. Nevertheless, this threshold can be shifted towards a lower threshold, but with the loss in other points. The number of events classified to other classes can be neglected in this case as the cumulative value is below 5%.

6.7.3 Variance of classifier

Up to now the figures have shown the mean value of the expected flux. For sure, the classification introduces new uncertainties. Each time a classification algorithm is trained, the output can be different.

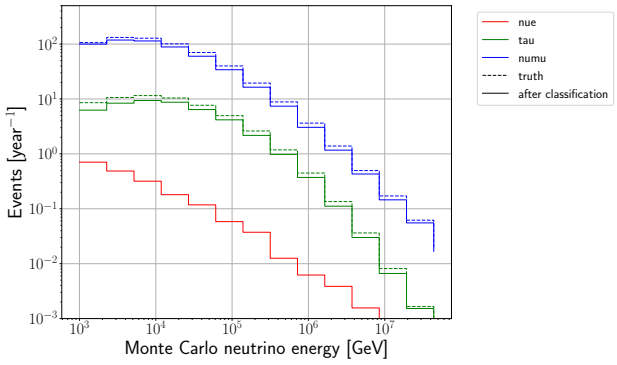

(a) up-going tracks

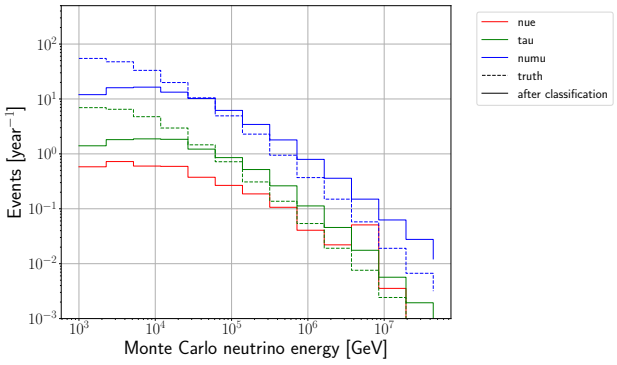

(b) starting tracks

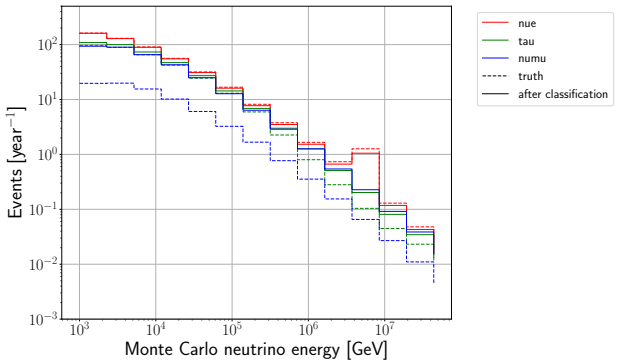

(c) cascades

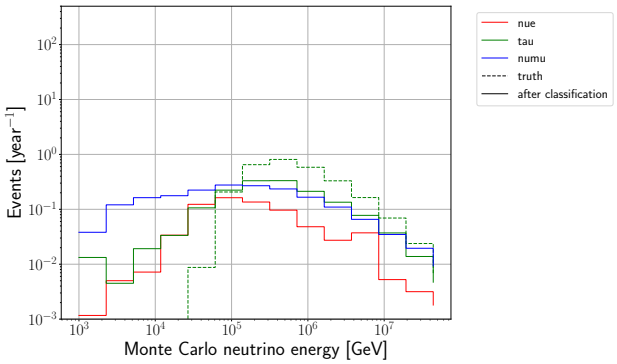

(d) double bang

Figure 6.24: Event distribution versus energy for different event classes. The flux is divided into the three neutrino flavors. The dashed lines show the distribution as it was defined in advance. The solid lines show the distribution, as obtained by the classifier

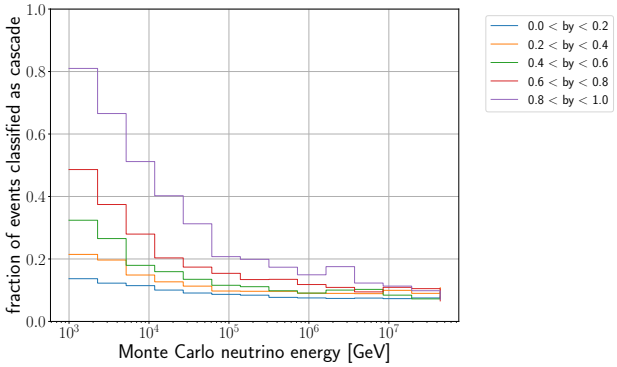

(a)

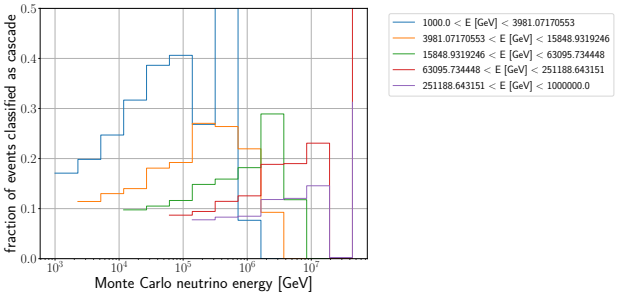

(b)

Figure 6.25: fraction of ν_μ and $\overline{\nu}_\mu$ events which are classified as cascades. Left: split into equidistant intervals of bjorken y. Right: split into equidistant intervals of track energy in logarithmic scale.

This deviation arises from different input samples, but also from the different starting initialization of the neural network.

Here the deviation is calculated with different folds of the cross validation. Each fold is considered as one experiment, so in total there are ten experiments in this case. Finally, the mean and the standard deviation is computed. Figures 6.27 and 6.28 show these standard deviations as relative errors in different views. Additionally to the standard deviation after the classification process, the values in advance are plotted, so the relative errors based in the defined classes. The values in advance arise from the fact that each cross validation fold consists of different events. Thus the composition is

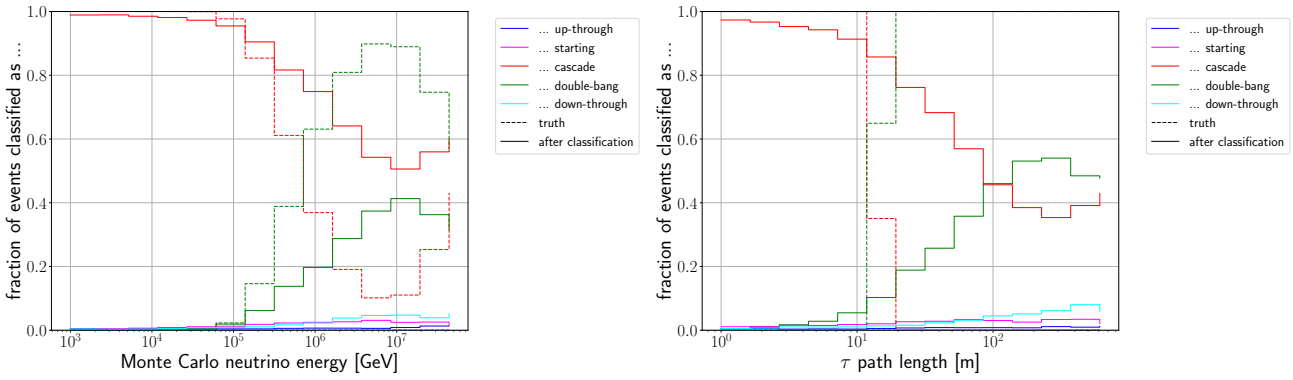

(a) (b)

Figure 6.26: Fraction of ν_τ-CC events in each event class

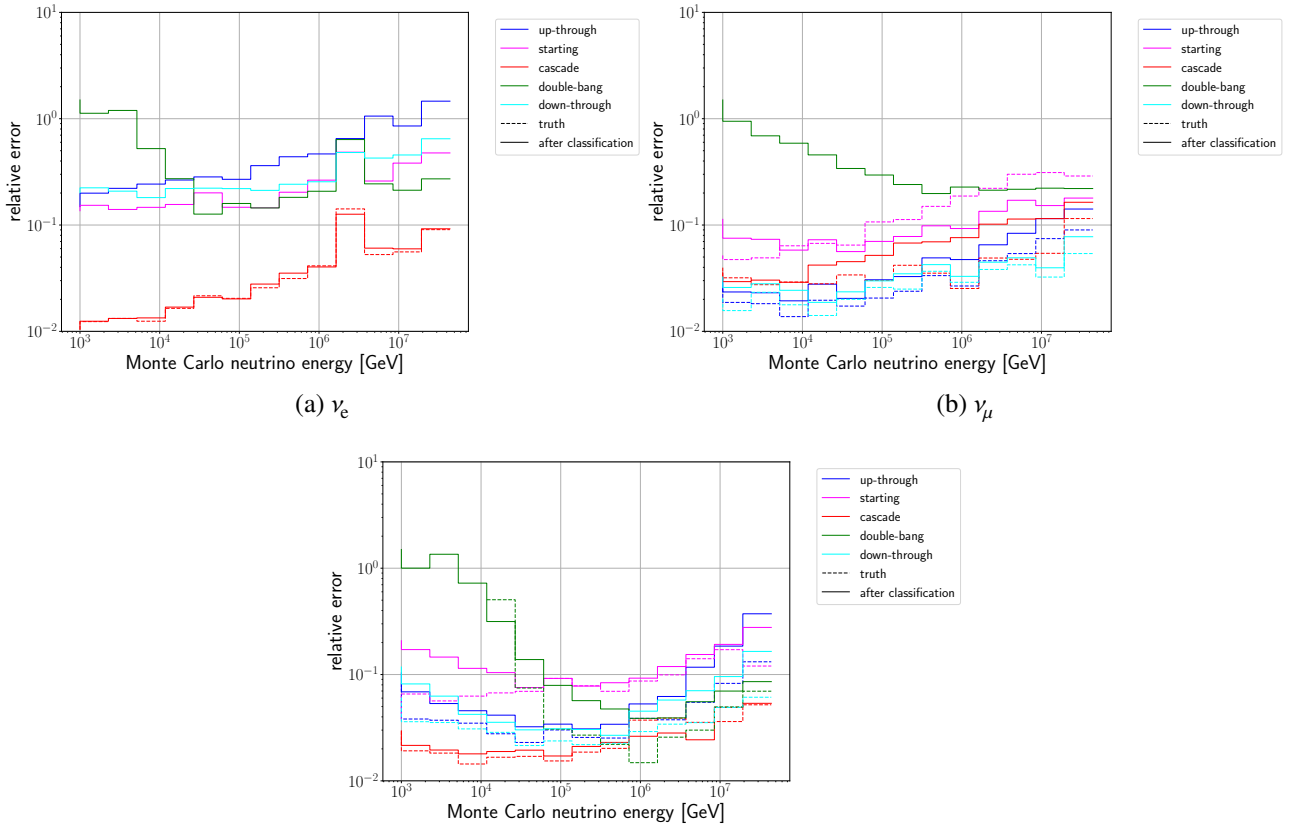

(a) ν_e (b) ν_μ

(c) ν_τ

Figure 6.27: Relative errors on the predicted flux, as described by the defined cross validation samples and the classified cross validation samples

slightly different. Figure 6.27 shows the error for the flux of each neutrino flavor. The ν_e events show an error moving with the statistics - the lower the statistics, the higher the relative error. Therefore, there are large error bars in the high energy region and small error bars in the low energy region. The Glashow Resonance builds up a sharp peak. This value is large as the production spectrum follows a pure power law, but the events are scaled up in this moment. The relative error before and after the classification shows very similar values. Consequently the additional variance is very low. This gives confidence in the classifier. The other target classes are not visible before the classification, but afterwards they are. As seen in the previous chapter, the number of events for these target classes is very small, so the relative errors become larger as the statistics become smaller. However, in absolute

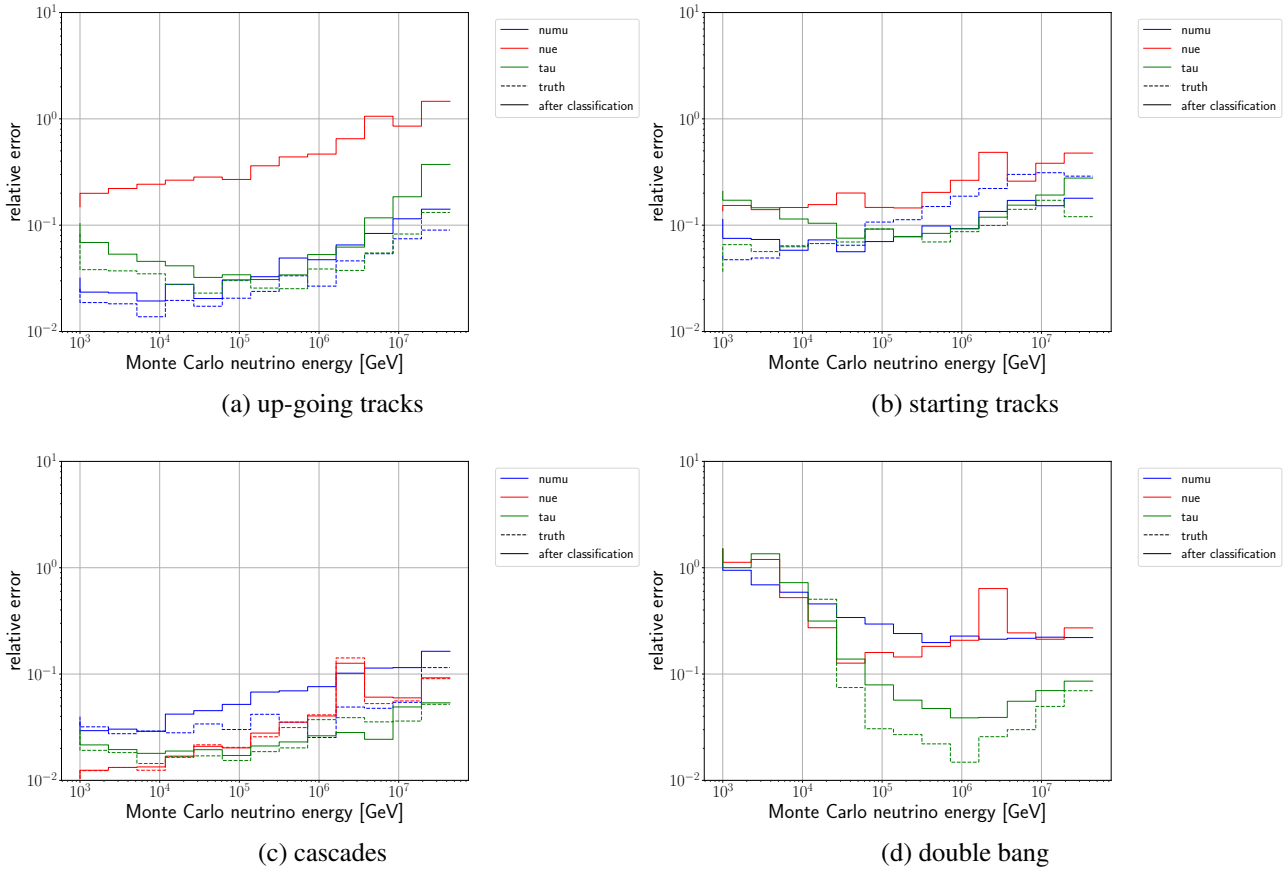

(a) up-going tracks

(b) starting tracks

(c) cascades

(d) double bang

Figure 6.28: Relative errors on the predicted flux, as described by the defined cross validation samples and the classified cross validation samples

values, it is far off the region of the cascade class. The double bang class shows a rise for low-energy events as the number of these events vanishes with lower energy.
Both other flavors show similar behavior for the high energy region. For the low energy region, it reaches a plateau. The plateau is reached below 10%, so it does not concern to much.
Overall the relative error lies below 10%. This value is almost valid for the relative error in advance and this is why a negligible contribution is introduced by the classifier. However, in comparison to the overall uncertainties of neutrino flux, the error here is half the size. The uncertainty, which increases for higher energy, increases for the flux, too.
Figure 6.28 shows the relative error in the expected flux ordered by target classes. Here the difference between error bars before and after classification is very small, too. This confirms the statement that the classifier has a low variance. In energy intervals, where the flux is low, the error bars are larger. Furthermore, $\overline{\nu}_e$ shows the Glashow resonance, with a few events of high weight. Equivalent to $\overline{\nu}_e$ classified to tracks, the error bar is very large for ν_e classified as up-going tracks. As the classification accuracy is high, the final number of events in the final sample is small, so that single events influence a lot.
Figure 6.28d confirms the high confidence in the classifier. Here a small number of events in total at most 0.5 ν_τ are classified into this class, but the error bar becomes larger by only a factor of 3.

6.8 Further Applications

The framework built for the event identification task is not fixed to the task described. In the following, some of the examples which were executed are highlighted representative for more applications.

Especially the problems and expectations are explained in the following.

Rejection of atmospheric neutrinos and atmospheric muons with a neural network

One major business in neutrino astronomy and other astroparticle experiments is the suppression of atmospheric particles. They overwhelm the signal by many orders of magnitude. It is quite an annoying task to reject them purely with neural networks. The learning algorithms always cope very unsatisfactorily with unbalanced tasks. If one class is highly underrepresented it can be up-scaled, but then the number of missclassified atmospheric muons will dominate the signal. So it is convenient to have a precut with hard cuts, manually, against the atmospheric background. After this is done, the balanced dataset can be trained for the rejection of atmospheric muons or neutrinos.
This process is executed for the analysis in ORCA. The first precut against muons leaves muons and neutrinos in the same order of magnitude in the sample. At next, the classification between tracks and cascades is extended to the third class of atmospheric muons. The last step leaves a few-percent contamination of atmospheric muons in the neutrino sample.

6.9 Outlook

This chapter showed the large improvement from hand-driven cuts towards the machine learned cuts. However, the features are still handcrafted. This task takes a large part of the time for the complete development and so it is no wonder that there are attempts to replace the manual features.
The recent development in classification tasks goes into this direction. Therefore, deep neural networks are currently being used in KM3NeT. Experiments like Nova already have published some results with deep neural learning [118]. For these techniques, the complete detector is recorded and integrated in a highly sophisticated way into the neural network. For KM3NeT with its multidimensional data (three dimensional grid and the time), it means the effort to pack the data in a suitable format to the available classifiers. Furthermore, with the increase of computational power in recent years the neutral network becomes deeper. Additional layers and other types of layers can be used. Especially the development of GPU makes it possible to train neural networks with thousands of weights.
There is a danger to arise from this development. The neural network is not as simple to understand as it might look like at first glance. The more complex architecture of the new generation can be miss leaded by artificial information introduced by the simulation. For example, in classical machine learning the scientist has to choose features on which he is sure about. The deep neural network can also learn about some features which are generated by the simulation, even if the features are not physically motivated. All these concerns have to be addressed when using the new deep learning methods. If they are handled correctly, even some new underlying mechanisms with differing events, which the scientist was not aware of in advance, can be found.
Up to now, the machine learning algorithms have proven for tasks with a given output label. As one sees in Chapter 6.3, the definition of labels is not so clear in advance. Thus one can think of an algorithm which separates the neutrino sample into classes by its own, based on the event topology the algorithm sees.

Chapter 7

Flavor Composition

First measurements of a cosmic neutrino flux have been established in the last years [7, 24, 119]. However, measurements of the ratio between the different neutrino flavors have not been conclusive up to now. A lot of mechanisms influence the final flavor composition at the detector, as described in Chapter 2. The neutrino flavor composition at the source is related to the mechanisms acting at the neutrino production site. Additionally, neutrino oscillation plays a significant role in modifying the flavor ratio of the signal at the detector. Furthermore, exotic phenomena such as the presence of sterile neutrinos or non-standard interactions in matter can change the flavor composition at several stages.
Since the discovery of the diffuse neutrino flux with IceCube [5], multiple analyses of the flavor composition have been published. The ratio between recognized cascade-like and track-like events was used to investigate the flavor composition of the signal [120] and to constrain even non-standard physics scenarios such as flavor decay [120, 121]. Further analyses followed these publications and also the release of new event samples by IceCube [122, 123, 124]. The first results on the flavor composition published by the IceCube collaboration were based on the so-called **H**igh **E**nergy **S**tarting **E**vent (HESE) sample [125]. In that work, most of the flavor composition phase space could not be excluded due to the low event statistics. In more recent analyses, multiple neutrino samples are combined to a single likelihood-fitting procedure [7, 126]. Due to the larger dataset, covering an extended lifetime of the detector and a larger statistic of neutrino candidates could be utilized in the analysis because of a better selection of the neutrino samples. Consequently, the allowed parameter space could be constrained in a way that a flux consisting only of electron neutrinos at the source could be excluded with a significance of 3.7σ. The best fit at present suggests an equal amount of ν_e and ν_μ [7]. Other literature recently published showed similar results [127].
In this work, the sensitivity of KM3NeT/ARCA to the flavor composition is evaluated by using pseudo datasets. The future neutrino telescope will record events which can be categorized into different event types according to methods described in Chapter 6. The shown classification results are used as expectations and to produce pseudo experiments which mimic measurements in the deep sea. Therefore, the pseudo experiments can be fitted with the expectations to retrieve a value for the flavor composition. Each of these steps will be explained in the following sections.

7.1 Analysis

Simulated event samples of the standard KM3NeT production, as described in Chapter 4, are used for the following analysis. They represent all neutrino flavors and interaction channels. Neutrino samples are weighted according to the atmospheric flux for the atmospheric component and to the unbroken power-law for the astrophysical component. These fluxes were described in Chapter 2.2. It is not clear whether the spectral index for each neutrino flavor flux is equal. However, in this work the spectral index is assumed to be equal for each neutrino flavor, for reasons of simplicity. Additionally, it is not

expected that the analysis can deliver this information. To achieve this, more observed events with a higher purity would be necessary. Other possibilities to model the flux, such as multiple power-law or spectral cut-offs, are not considered in this work.
Apart from that, each event is reconstructed by dedicated reconstruction algorithms. The output is used for the final spectral fit as well as for event identification and selection. For this reason, the features (see Chapter 6.2) are calculated, too.
There are multiple quantities which can be fitted with this method. The first interesting quantity to be fitted is the normalization factor of the cosmic signal for each neutrino flavor. The atmospheric neutrino flux is the most important remaining background for the measurement. As the systematic uncertainty on its normalization is rather large (of the order of 25%), it is also fitted. It has been verified that different true values of the atmospheric neutrino flux normalization then only have a negligible remaining influence on the results of the spectral fitting procedure.
The spectral index of the astrophysical flux is not known very well up to now. Therefore, also this quantity must be left free in the fit, resulting in an worsening of the flavor composition sensitivity. Chapter 7.2.1 will show that by fixing the spectral index to very hard or very soft values, the spectral fit has a strong tendency to overestimate or underestimate the ν_τ contribution. Fitting the spectral index together with the normalization of the astrophysical flux and the background normalization, successfully avoids this behavior of the fit.

7.1.1 Event selection and identification

The spectral fitting procedure is performed simultaneously on multiple different spectra. These spectra have to be statistically independent from each other, i.e. no event is present in more than one subsample. Event identification algorithms are used to separate the full sample into several subsamples of different event types. For this purpose, the described event identification algorithm is used (see Chapter 6). In precursory analyses, the event selection to separate subsamples was done individually. Afterwards, double-used events were removed from all subsamples except one [126]. The event identification separates the complete sample into five different classes. However, the overwhelming atmospheric muon background reduces the use of some classes. With the reduction of background, the flux in some classes drops to an extremely low count. Even before fitting, the overall flux of the double bang class is very low with a count of one event per year at a maximum, as seen in Chapter 6.7.2. Recent IceCube analyses expect 0.38 events per year [127], which might as well be not sufficient for a spectral analysis. Further on, a background of 0.15 events per year is expected.
Finally, two subsamples are chosen for this analysis. The first to mention is the cascade channel, which consists mostly of neutral current events. Even if it consists of all the neutrino flavors, each component has a different spectral shape, which will finally help to calculate the flavor composition. Therefore, the spectral fit algorithm can retrieve the flavor composition. The up-going track channel, consisting of ν_τ and ν_μ, is chosen as the second channel.
Even though there is the down-going track channel, which is tailored to collect atmospheric muons, there is a huge amount of atmospheric muons in the other samples after event identification. A rejection of atmospheric muons down to a percent-level of residual contamination of the neutrino samples is achieved by cutting on various class-individual and appropriately chosen quantities from the available features.
For the cascade class, the value of the *MEstimator*, which is a time residual-based parameter, is limited. This value was developed to see if a neutrino is well reconstructed. In context of this selection, the value identifies cascades which are badly reconstructed by the track reconstruction. The next cut parameter is some sort of an energy cut. The number of hits used in the cascade reconstruction, being a value correlated to the initial neutrino energy, has to be above 8000, which corresponds to a neutrino energy slightly below 10^6 GeV. Therefore, less energetic atmospheric muons can be rejected. The reconstructed vertex of a track reconstruction points to the earliest light emission along the track

parameter	limits
M-estimator	$\|x\| < 400$
number of hits used for reconstruction	$x > 8000$
reconstructed vertical position in detector	$0 < x < 600$
y-intercept for fit -1000ns to -50ns	$x > 0.25$

Table 7.1: Selection criteria to reject atmospheric muon events in the cascade class

parameter	limits
reconstructed zenith angle	$x > 90°$
reconstructed energy	$x > 10^3$ GeV
likelihood of the reconstruction algorithm	$x < -80$
beta parameter of reconstruction algorithm	$x < -2.7$

Table 7.2: Selection criteria to reject atmospheric muon events in the up-going track class

observed by the detector. For an event entering the detector, the reconstruction tends to deliver the reconstructed vertex at the point of entrance. Thus, there is a cut on the vertical position. The reconstructed vertex has to be below 600 m above sea bed. In this way, some of the upper most layer of the detector are used as veto layers, as they are called in other analyses. Additionally, a cut on the reconstructed horizontal distance to the detector center is used and in doing so, the quality of the remaining events is increased.
In contrast to the quality-driven rejection in the cascade channel, the rejection of atmospheric muons in the track channel is driven by the reconstructed zenith angle. Even though the zenith angle is already present for the neural network, there are still many events with a reconstructed zenith angle below the horizon. Therefore, every event with an arrival direction pointing below the zenith is discarded. Additionally, a cut on the reconstruction quality is set. Similar to the cascade channel, a cut on the reconstructed energy is applied because the spectrum of reconstructed atmospheric muons is steeper than the astrophysical flux. Therefore, above a certain energy threshold the neutrinos will dominate.
The cuts for the cascade and the track channels are very different. The complete list can be seen in the Tables 7.1 and 7.2. Similar analyses use precuts against atmospheric muons and split afterwards into tracks and cascades. However, in the view of this work this does not lead to an optimal selection of the final classes. The final atmospheric muon rejection is based on the remaining events after an identification. The atmospheric muons which are classified as cascades on the one hand and as tracks on the other hand, have a different topology, therefore the final cuts can be optimized to the final sample.
The event rates are shown in Figure 7.1. The flux shown in the figure assumes a flux evenly distributed over the different neutrino flavor. Remaining atmospheric muons with a negligibly small rate are only expected for energies smaller than 10^5 GeV.
The left panel shows events classified as up-going tracks. All components are shown with their expectations. There is a negligible contribution of ν_e from the atmosphere as well as from astrophysical source. The second contribution comes from ν_τ. However, even this contribution is superseded by the ν_μ-contribution by one order of magnitude. Concluding, the flux of astrophysical ν_μ will dominate the spectral fit in this case. However, the astrophysical flux of ν_μ and ν_τ cannot be discriminated in this way as the spectral shape is almost identical. The atmospheric neutrino contribution is surpassed by the astrophysical one above an energy of 10^6 GeV. The neutrino yield above this turnover is in the range up to ten events per year. This fact is important so that the spectral fit algorithm grounds on enough events for the fit process.
The right panel of Figure 7.1 shows the expected flux for an equipartition flavor flux in the cascade

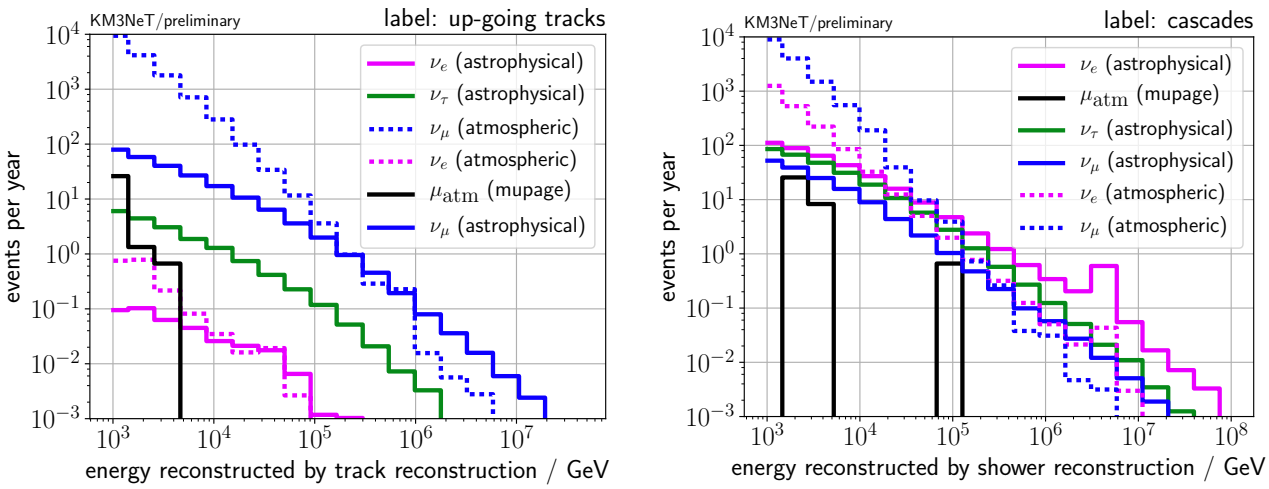

Figure 7.1: Flux of classified events in KM3NeT/ARCA. Left: events classified as up-going tracks. Right: events classified as cascades.

channel. The atmospheric muon background shows similar behavior as in the up-going track class. The flux is negligible in this case. The most dominant source of events are ν_e, with the peak at 6.3 PeV due to the Glashow resonance. The second dominant source are ν_τ.

Unlike in the track channel, the spectra show different slopes: the flux of ν_τ is steeper than the one of ν_e and ν_μ, as energy is carried by leaving ν_τ out off the detector. This difference can lead to a sensitivity for all flavors, without detecting a unique ν_τ signal. The astrophysical flux of ν_μ is a factor five smaller than the ν_e flux. Therefore, ν_e and ν_μ are interchangeable. However, the ν_e shows the unique peak which fixes the total flux.

In conclusion, the expected contributions of different flavors are distributed over the channels as follows: the ν_μ component is fixed with the track channel. Both other neutrino flavors are fixed with the cascade channel, where the ν_e is the dominant source and the spectral shape differs only in the very high energy domain above 10^6 GeV.

Finally, there are spectra for the different neutrino flavor in the astrophysical channel as well as in the atmospheric channel. Further on, there is also the atmospheric muon channel, which is not considered here because the flux is negligible.

7.1.2 Pseudo experiments

The first step in the spectral fitting procedure is the generation of pseudo experiments. A pseudo experiment mimics the outcome of a real experiment. Thereto a truth value of the flavor composition is assumed (ν_e:ν_μ:ν_τ). Every possible value can be chosen here and a experiment lifetime is set. These factors are used to scale the expected event yield. The histograms are binned according to a predefined binning. The binning can be chosen in different ways, which are tested in Chapter 7.2.1.

After fixing the strength and lifetime, the number of events per bin contributing to one component is drawn from a Poissonian distribution implemented in *numpy* [128]. All components are added to result in a simulated spectrum corresponding to a potential experimental measurement with KM3NeT/ARCA. There are two different spectra due to the fact that there are two subsamples used for the spectral fit. As the composition is not known a priori, this step has to be done for every possible flavor composition in the following. In doing so, every true flavor composition is evaluated with the software.

7.1.3 Fit process

The main step of the spectral fitting procedure is the fit itself. Each bin of the distributions will be populated by a few, if not zero, events. Then a Poissonian likelihood fit is applied. The goodness of a fit for underlying Poisson distribution can be given by the likelihood based on [129]:

$$\mathcal{L} = \prod_i \frac{M_i^{D_i}}{D_i!} \exp(-M_i), \tag{7.1}$$

with M as the total of expected events and D as the number of detected events. The cstat statistics used by the minimizing algorithm is set to [130]:

$$C = 2 \sum_i \left[M_i - D_i + D_i(\ln D_i - \ln M_i) \right]. \tag{7.2}$$

Here a logarithm is applied to the likelihood function and the sign is changed so that one has to minimize the log-likelihood. Furthermore the factorial term is approximated by the term $\log(D_i!) = D_i \log(D_i)$.
The fit makes use of the *sherpa* software package [130], developed in the domain of x-ray astronomy. *Sherpa* is a computing library to analyze images, time series or spectra. There is a native and a python interface, which makes it easy to link to other projects. Here the python interface is used. Sherpa is optimized to find different contributions, so-called models, to a measurement. In this work, the different models correspond to the different flavor compositions. Each contribution is implemented so that there are additional parameters, like the spectral index. In this way, the spectral index can be varied. Sherpa provides several minimization algorithms but here the Levenberg algorithm [131] is used.
Above, the reconstructed energy as the quantity of the spectrum was introduced by the way. This choice was made as it gives good results according to the performance measures of Chapter 6. Therefore, the significance of the most dominant source was calculated with respect to the other channels. Furthermore, the shape of the spectrum is explained and considered as trustworthy. There are other quantities to mention, which give similar power to the spectral fit.
It was verified that the fit algorithm does not converge to different results if the fit is performed multiple times and that the start value of the fit does not influence the final result.

7.1.4 Construction of confidence intervals

The final experiment will show only one single outcome. The confidence of such a single experiment is evaluated in the following. Exemplary an experiment with the fit result 1:1:1 is chosen. The method to calculate the confidence intervals is leaned on Feldman and Cousin [132]. In this way, the final confidence intervals will give a range which overlaps the true value with some probability. Figure 7.2 shows the construction of a one-dimensional confidence interval according to Feldman and Cousins. The y-axis shows hypothetical values for the truth of the value of interest. For each value, the central n-sigma interval for the distribution of the experiment's results is calculated. It is drawn as horizontal line, whereby the x-axis shows the experiment's result. When there is a measurement with a result x, the confidence interval is chosen as the overlap of a line parallel to the μ-axis and the calculated distributions of hypothetical experiment's results. The constructed confidence interval covers the n-sigma interval. Here no prior information was used, therefore a probability that one truth is more likely than the other is not taken into account.
In this work, a confidence interval for the flavor composition is to be calculated. This confidence interval is two-dimensional instead of one-dimensional. The interval chosen above is given by the truth values, which contribute the most to the experiment's result. This property is also used in the following. The equivalent to the μ-axis is the flavor composition. Therefore, the flavor composition space

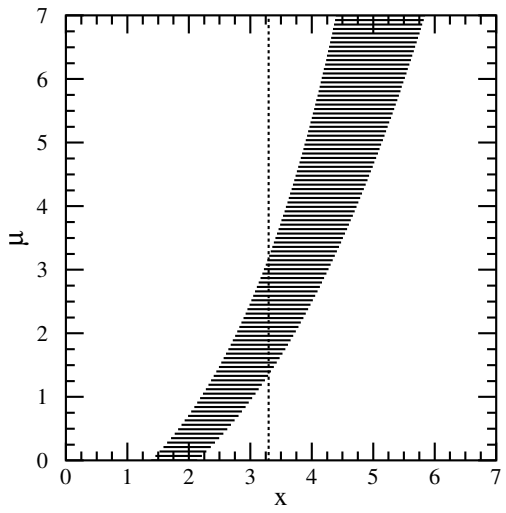

Figure 7.2: Generic confidence belt construction, where x is potential experiment's outcome and μ are the truth values, which lead to a distribution of results in the final experiment. Figure taken from [132].

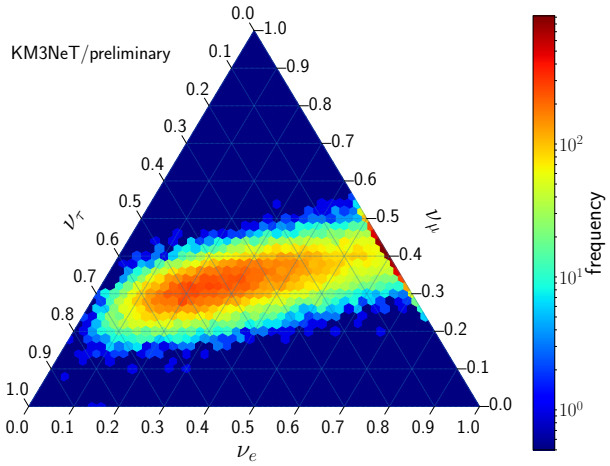

Figure 7.3: Distribution of fit results of spectral fit algorithm for the underlying truth of 1:1:1 (ν_e:ν_μ:ν_τ) and 10 years of lifetime with ARCA. Additionally, the spectral index and the atmospheric neutrino flux was fitted. This distribution is called the fit distribution. The number of pseudo experiments used is in the order of 10^6. The lower end of the color scale is given by the end of the statistics.

is binned into 50 bins for each flavor. For each bin, pseudo experiments were performed according to the procedure described above. The number of pseudo experiments was fixed in a way that the final significance calculations could be done up to 10^{-2}. Finally, 10^{10} pseudo experiments are performed in total. In the end, for each bin in the flavor composition space, a distribution of fit results is found. This distribution is called a fit distribution. One exemplary fit distribution is shown in Figure 7.3.

This distribution is the equivalent of the horizontal bars in Figure 7.2. The figure shows the flavor composition space in a ternary plot. It is printed with the help of the python library *python-ternary* [133]. The three axes show the fraction of the flux of each flavor contribution to the total flux. The color code indicates the number of pseudo experiments with the underlying truth of 1:1:1, which results in the respective bins.

There is an elongated shape from the left bottom to the ν_μ-axis, which arises from the similarity of ν_τ and ν_e. This means that the difference in the flux of ν_τ and ν_e cannot be pinned down as accurately as the flux of ν_μ. For this channel, the relative flux is pinned around 0.3, independent of the other fluxes. This value is close to the expected value of 1/3. The center of the elongated shape is around

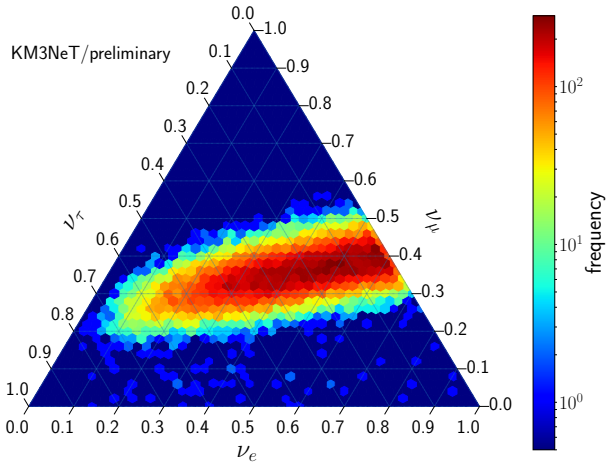

Figure 7.4: Distribution of true flavor composition, which produced pseudo experiments with the outcome 1:1:1 in 10 years of lifetime with ARCA. Additional to the flavor composition, the atmospheric neutrino flux and the spectral index was fitted. This distribution is called the truth distribution. The pseudo experiments used are of the order of 10^6.

0.2:0.3:0.5. Considering that the truth is defined at 1:1:1, this is a clear deviation. It might arise from the different spectral slopes of ν_τ and ν_e. Another feature of Figure 7.3 is the agglomeration of fit results with zero ν_τ contribution. As the ν_τ contribution is never the dominating part in a spectrum, it happens that another neutrino flavor takes over and builds up the complete flux. Similar effects are seen in published analyses, where spectra dedicated to find ν_τ are used. If no ν_τ is observed, in these cases the contribution is fitted to zero, too.
Here the explanation is different. As no dedicated tau neutrino channel is used, the information has to come from the spectral shape. The overall fraction of pseudo experiments with zero ν_τ contribution is given with 15%. Therefore, 15% of real experiments with an underlying truth of 1:1:1 are fitted to that boundary. Furthermore, there is a correlation between a high ν_τ contribution and a lower ν_μ contribution after the fit. Figure 7.1 shows the reason. If a total flux is given and one of two components is decreasing, the other has to increase and vice versa.
Finally, there is one of these figure for each bin in the flavor composition space, which corresponds to all vertical lines inside the Figure 7.2. For the construction of confidence intervals, the truth values, which contribute the most to a given fit's result were sought. For illustration, the fit result of 1:1:1 is chosen here. Figure 7.4 shows the distribution of truth values, which induce pseudo experiments resulting in a fit result of 1:1:1.
In contrast to the Figure 7.3, the center of the distribution is shifted towards lower ν_τ contribution. The reason for this is similar to the shift in the opposite direction upwards. Nevertheless, the key features are reflected in this figure, too. They are the elongated shape, the correlation between ν_τ and ν_μ and the shift along the half-axis.
This distribution can be used to calculate the confidence intervals. A confidence interval gives a range of values surrounding possible truth values, which cannot be rejected with a certain significance. The significance can be given in means of σ, which is related to the width of a Gaussian distribution. $1\,\sigma$ is the interval which hosts approximately a fraction of 68% of the distribution. Further generalization is done with [134]:

$$\Phi = \mathrm{erf}\,(\frac{n}{\sqrt{2}}), \tag{7.3}$$

with n the count if σ and Φ the fraction of complete distribution, called the confidence. *erf* is the error function. The significance is defined as:

$$S = 1 - \Phi. \tag{7.4}$$

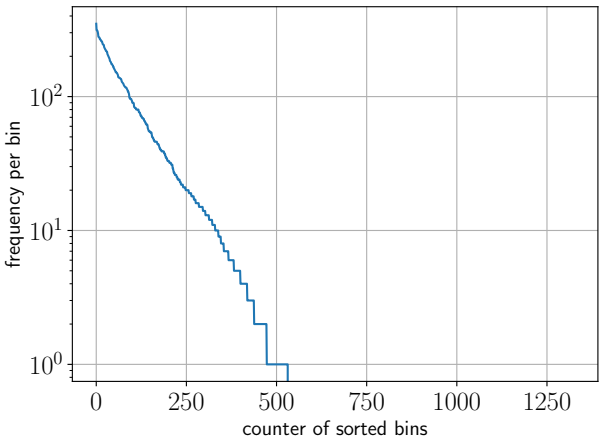

Figure 7.5: Distribution of pseudo experiments with fit result 1:1:1. x-axis shows the bins ordered by frequency.

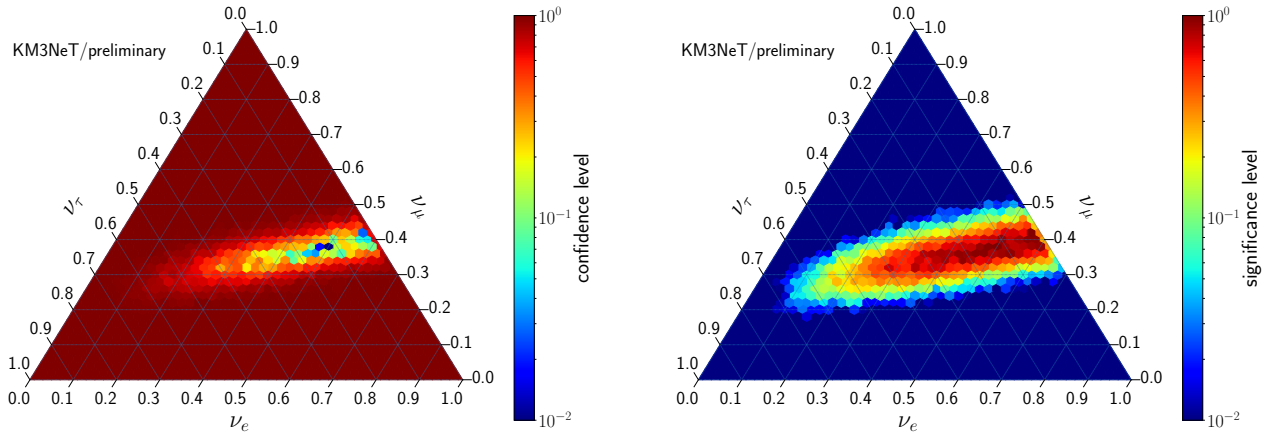

(a) (b)

Figure 7.6: Confidence (a) and significance (b) level of an experiment with the result of 1:1:1 after 10 years of lifetime

The corresponding regions in the histograms shown above were calculated. All bins are ordered descending, starting with the predominant bin in the truth distribution. This one-dimensional distribution is shown in Figure 7.5.
In this one-dimensional representation of the flavor composition space, the one-sided confidence intervals are selected. This interval is transformed to the two dimensional plots shown before by selecting the corresponding bins. Figure 7.6 shows the results. The final confidence belts are not centered around the fit result. As seen above (the fit distribution was shifted towards larger ν_τ contribution), the final confidence belt is shifted towards lower ν_τ contribution. However, as the underlying truth is known on average by the pseudo experiments, the final confidence intervals redo this shift, back to the truth value.
As the spectral fit outcome cannot be used as the best fit value in the end, the center of the confidence level is chosen here.

7.1.5 Fit correction

Figure 7.3 shows the distribution of fit results of pseudo experiments with the underlying truth of 1:1:1. The center of the distribution is not centered around this value. It is centered at around

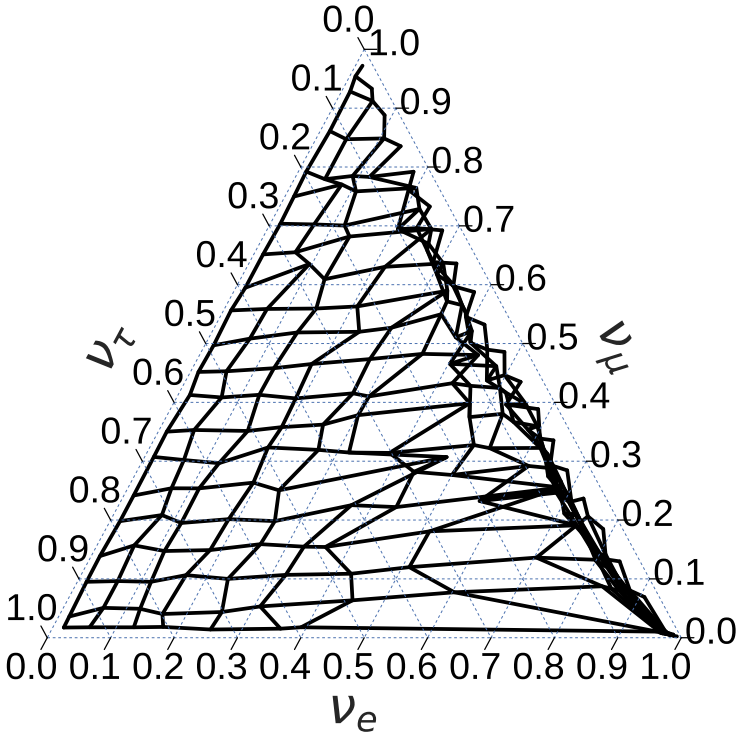

Figure 7.7: Pseudo-four-dimensional plot showing the bias of spectral fit results with respect to the underlying truth. The innner (solid) coordinate system shows the chosen spectral fit result. The outer coordinate system (dotted) shows values of the underlying truth. Solid coordinate system: horizontal lines show the fraction of ν_μ starting from 0.05 with step size of 0.05. The other direction shows the fraction of ν_e in the same binning.

0.25:0.32:0.43. Therefore, the spectral fit is biased.
The Figure 7.6 shown is only one point in the flavor composition space while other regions might be shifted differently. Figure 7.7 shows the map of bias for the spectral fit. It also visualizes an isomerism between two coordinate systems, the fit flavor composition space and the true flavor composition space. It is presented as a pseudo-four-dimensional diagram. The outer coordinate system, drawn as dotted lines, shows the underlying truth of pseudo experiments. In contrast, the inner coordinate system, drawn as solid lines, shows the fit results. The binning is chosen in steps of 0.05. The first grid line for each coordinate is set to 0.05. If the isomorphism would not shift anything, the grid lines would lie on top of each other. However, there is a transformation to be considered.
Assuming the truth is 0.2:0.2:0.6 and the reader wants to find the most probable fit result, he or she would have to go to the point 0.2:0.2:0.6 with respect to the outer coordinate system. The resulting point in the inner coordinate system constitutes the center of the fit distribution. The opposite way is also possible. In doing so, one starts with the fit result in the inner coordinate system and gets the center of the corresponding truth distribution in the outer coordinate system. As described above, the distribution of fit results is not centered around the truth value. This is why the inner coordinate system shows the fit results. The inner coordinate system is not deformed uniformly, which is why the bias depends on the position in flavor composition space.
Figure 7.7 reflects the behavior shown in 7.4. The ν_τ contribution is fitted to higher values than the true value. There is an increasing effect from the left to the right, visible in the increasing coordinate spacing in the inner coordinate system. Finally, the change in the truth near a zero ν_τ contribution

gives a fast change in the fit result. At the very outer end, it is not clear if the change is continuous anymore. This fact induces that if the true flavor composition is in that region, the outcome can vary significantly. This should not harm as the reasonable expectations are suited in the middle of the flavor composition space.
Regarding the ν_μ-axis both coordinate systems match nearly perfect with a slight tendency towards a correlation between increased ν_e contribution and decreasing ν_τ contribution. In such a setting, the ν_μ contribution also increases.
Concluding, the isomorphism shows a continuous behavior in a wide range, especially in the region where standard physical scenarios are expected. This correction map can be used to correct a fit result to the center of corresponding truth distribution. As the correction is included in the construction of confidence intervals anyways, the confidence interval method should be used.

7.2 Results

This section shows first the results for a full spectral fit. After that, studies are described to understand the systematic behavior of the procedure.

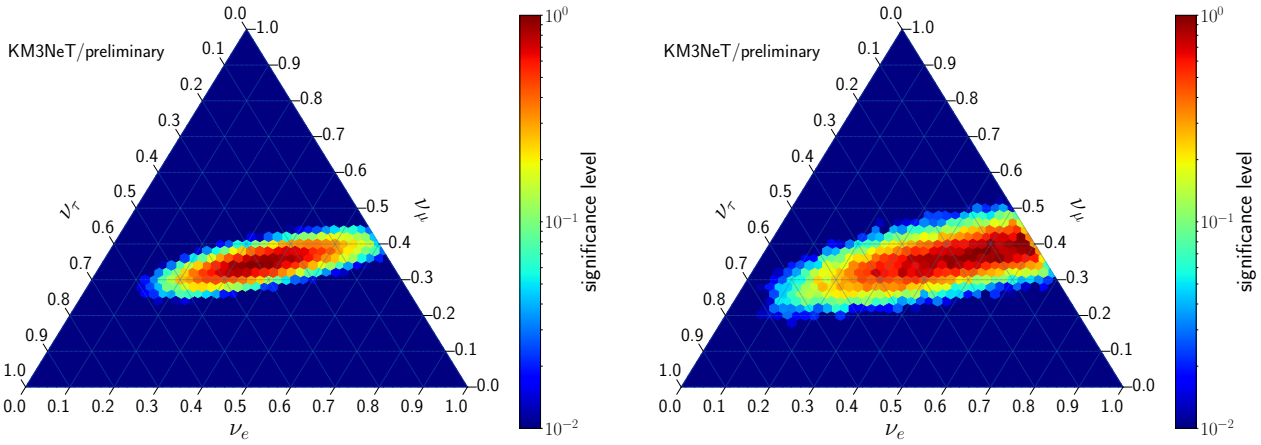

Figure 7.8: The significance level of an experiment with the outcome of of equipartition in the three neutrino flavors. $O(10^8)$ pseudo experiments were generated uniformly in the flavor composition space. The lifetime of KM3NeT/ARCA was set to 10 years. Left: only the astrophysical neutrino flux normalization is fitted. Right: the normalization of the astrophysical, the atmospheric neutrino flux and the spectral index of the astrophysical flux are fitted. Due to the limited number of pseudo experiments, the lower limit of the significance for this evaluation of the KM3NeT/ARCA performance is 10^{-2}. Lower values are rounded to this value.

Figure 7.8 shows the significance levels if the fit results in the outcome of equipartition in the three neutrino flavors. A symmetrical shape around the expected value is observed if the fit is only performed on the normalization of the individual neutrino fluxes. The elongated shape of the ellipse is due to the smaller separation power between the ν_τ and ν_e with respect to the ν_μ content. Therefore, the fraction of ν_μ is given in a range between 0.3 and 0.4. However, the ratio of the other two neutrino flavors can vary to a greater extend. The tilt of the shape with respect to the ν_μ axis results from the ν_τ with a muon leaving the tau decay vertex.
The right plot of Figure 7.8 shows the significance levels obtained in the case that also the spectral index of the astrophysical flux is fitted. Again the fit result 1:1:1 is chosen, but here the experiment's result is 0.5:0.37:0.13. The shape broadens because of the addition of more nuisance parameters in the fit. The overall shape, tilt and elongation, remains the same. However, the ellipse is no longer centered around the expected value, but shifted towards the ν_μ-axis. Experiments with a given truth

are usually fitted with a to high ν_τ contribution. However, the construction of confidence intervals corrects this in this regard.

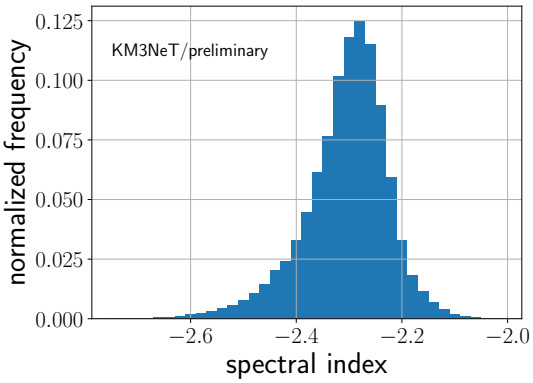

Figure 7.9: Distribution of the fitted spectral index in full fit mode, e.g. normalization and spectral index is fitted. The truth value was -2.3. Experimental outcomes for the true flavor ratio value 1:1:1 are shown.

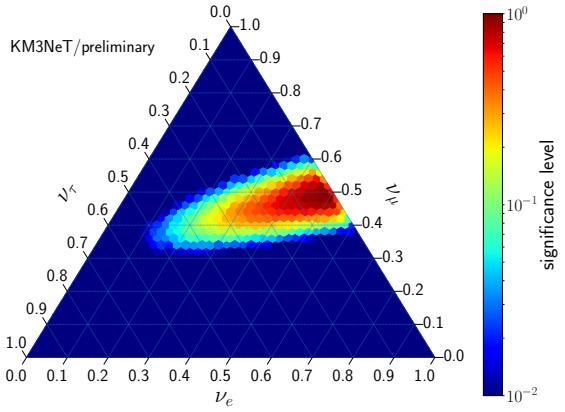

Figure 7.10: The significance levels of an experiment with an outcome of equal distribution between ν_e and ν_μ. $O(10^8)$ pseudo experiments were generated uniformly in flavor composition space. Lifetime was set to 10 years of ARCA measurements. The normalization of the astrophysical and atmospheric neutrino flux and the spectral index of the astrophysical flux are fitted. Due to the limited number of pseudo experiments, the lower limit of the significance for this evaluation of the KM3NeT/ARCA performance is 10^{-2}. Lower values are rounded to that value.

A pseudo experiment assuming a true equipartition in the three neutrino flavors and a true spectral index $\gamma = 2.3$ has been performed. Its outcome is reported in Figure 7.9. The distribution of the fitted spectral index is shown. It is well-centered around the true value. The mean was found at $\gamma_{\text{mean}} = -2.31$, the median even at $\gamma_{\text{median}} = -2.30$. The width of the distribution can be characterized by a standard deviation of 0.088.
Finally, Figure 7.10 shows the significance levels that result when measuring an equal ν_μ and ν_e contribution in absence of ν_τ. This actually corresponds to the best fit in the IceCube analysis even though this result is not yet statistically significant.

7.2.1 Studies on influences to the fit process

There are certain dependencies of the analysis described above. Some of them have already been described as they were necessary for the implementation of the algorithm. However, some of them have not been mentioned yet or there are more details to describe than it was possible in the implementation part. These and their implications will be elucidated in this section.

Influence of binning to the spectral fit

The spectra as shown above have a bin size of 0.125 in the logarithm of energy. The range was defined in the manner that at most 10^{-2} of the events lie below the lower edge and 10^{-7} of the events lie above the largest bin. The values are chosen in this way that the selected quantities used for a spectrum show the tendency to have high statistics at low bins and low statistics in high bins. The binning influences the computing time: the more bins, the more computations needed to calculate

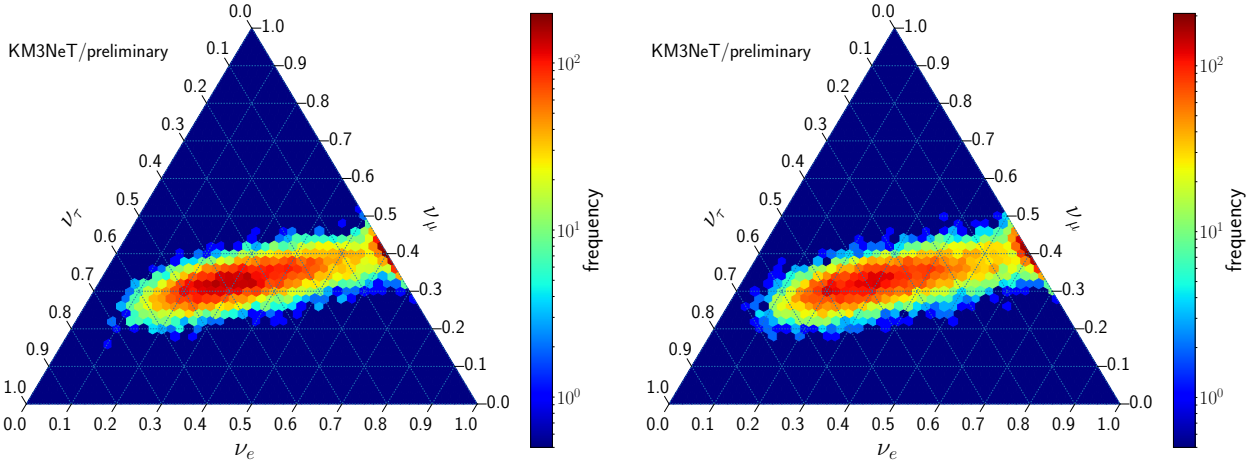

(a) 40 bins (b) 10 bins

Figure 7.11: Two examples of the distribution of outcome in the experiment with the truth 1:1:1. More examples can be found in the appendix. Lifetime: 10 years ARCA. Fit of flavor normalization. The left is performed with a spectrum with 40 bins. The right plot shows the same for 10 bins

the likelihood. Otherwise, sparser binning reduces the information about smaller features. Finer binning causes higher fluctuations in the spectra. This is especially a problem at highest energies above 10^6 GeV with low statistics. A lot of fluctuation will be caught from the fit, as the Poissonian likelihood will find a fit with the least deviations in all bins.
The setting was tested with binning of 40 bins, 20 bins, 14 bins and 10 bins, in the range of 10^3 GeV to 10^8 GeV. As shown in Figure 7.11, the binning does not influence the results. Therefore, one can choose the binning in this setting arbitrarily in the considered ranges. The influence of a larger number of bins on the computation time is not large, therefore the bin size was set to 0.125 the logarithm of energy, e.g. 20 bins are used.

Influence of the spectral index

There are models available for every component, but the spectral index in the astrophysical flux is not fixed yet. Thus, the spectral fit procedure is tested for the case that the spectral index would be fixed, but the assumed spectral index is different to the true spectral index. The experiment is started with a true spectral index of $\gamma = -2.5$, but the fit algorithm assumes a spectral index of -2.3, -2.5 or -2.7. Figure 7.12 shows the difference in the outcome of the fit with the truth of 1:1:1. The region with the most probable outcome moves from the region of high ν_τ contribution to the low tau neutrino region when the assumed spectral index is decreased from -2.3 to -2.7. The reason behind this behavior are the different spectral shapes of the templates used in that case. Primarily the templates of the up-going tracks are dominated by muon neutrinos, which keeps the muon neutrino contribution fixed. However, the templates for the cascade channel show templates with compatible contribution of ν_e and ν_τ. In this way, it is possible to enhance the ν_τ contribution to fulfill the measured spectrum. As the spectrum of the ν_τ contribution is steeper than the one of the other contributions to neutrino flavor, it can mimic a steeper spectrum.
One might think that the true flavor composition can be reproduced by a correction map as seen above. However, as the fit result is highly affected by the spectral index mismatch, the correction map would be affected by the value of the spectral index, too. Moreover, as the spectral index is not known the suitable map cannot be chosen. In conclusion it can be said that the spectral index has to be free floating in the fitting process.
Figure 7.13 shows that there is also an influence of the spectral index provided that it is free floating in the fitting process. Firstly, the region of the most probable outcome is getting bigger. The 1 σ level

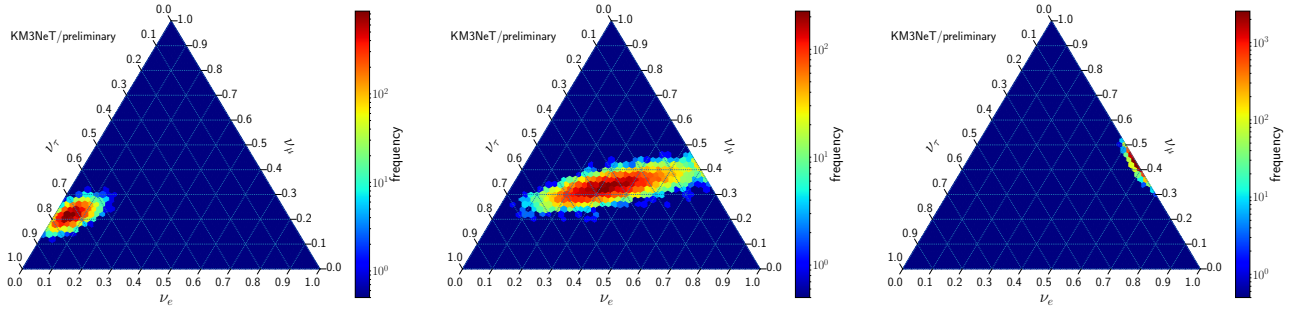

(a) $\gamma = -2.3$ (b) $\gamma = -2.3$ (c) $\gamma = -2.3$

Figure 7.12: Three differently assumed spectral indices in experiments with the same truth of -2.5. The assumed values are from left to right: -2.3, -2.5, -2.7, Lifetime 10 years ARCA, fit of flavor composition and atmospheric flux.

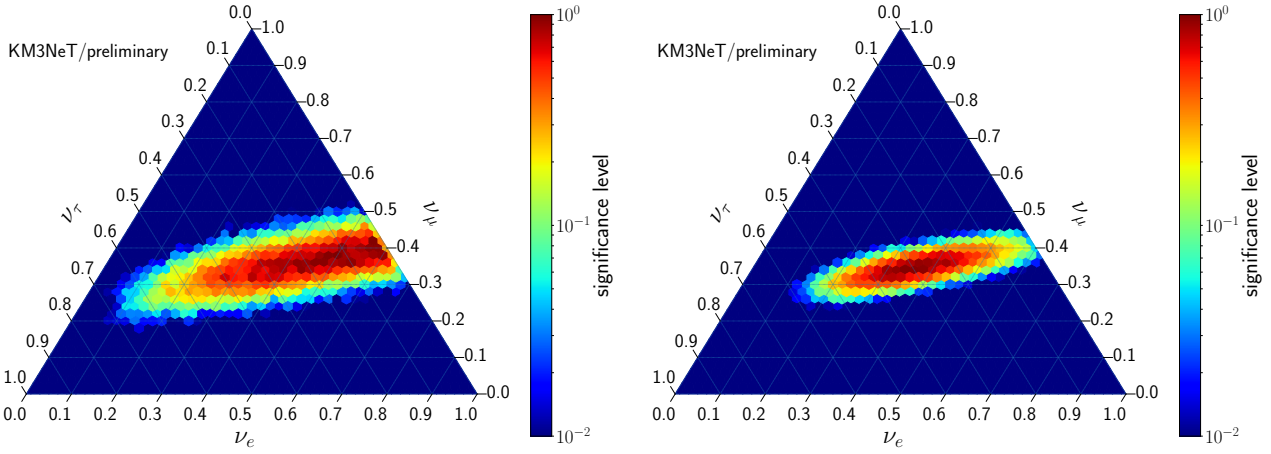

Figure 7.13: Comparison of the full fit (left) and the only normalization fit (right)

moves to the previous 2σ level. Secondly, there is a shift in the spectral fit, which can be corrected as shown above.

7.2.2 Not included in this study

There are problems and systematics involved in this study which could not be resolved but which are mentioned in the following.

Atmospheric neutrino suppression

For this analysis, atmospheric neutrinos are used in their full contribution. However, the suppression potential coming from the self-veto effect caused by accompanying neutrinos was not taken into account here. It was shown in Chapter 5.4 that this improves the sensitivity of the analysis targeting the diffuse neutrino flux. The flavor composition analysis is also influenced by the atmospheric neutrino contribution in a similar manner and this is why the application of a self-veto will improve the sensitivity. This improvement was not implemented here because there is no suitable atmospheric neutrino simulation with accompanied muons at the time being.

Influence of atmospheric muons

In this analysis, the atmospheric muons were assumed to be negligible. However, the statistics in the Monte Carlo simulation is limited. Therefore, one would expect some missreconstructed atmospheric

muons in the final event samples, which were not represented in this analysis. Consequently, new methods will have to be developed in further analyses which estimate the spectrum of the muons for the spectral fit.

7.3 Log-likelihood Ratio Tests

In the previous sections, confidence intervals were constructed based on pseudo experiments and a method adapted from Feldman and Cousins. In the order of 10^8, pseudo experiments were necessary to get smooth distributions shown in the Figures 7.8 to 7.10, which takes a huge amount of computational power. There are other approximating ways to state the confidence. In the following *log-likelihood ratio tests* [135] are used, simply called likelihood ratio test in the following. This method is used in [7] and successors [127, 136, 137] to estimate the performance of the flavor composition determination with IceCube Gen2. The method of likelihood ratio is developed to decide if one alternative hypothesis can be rejected with respect to another, the null hypothesis. Nevertheless, it can also be used to find a region in parameter space which can be rejected significantly. In that case, each point in the parameter space is considered as alternative individually.
As described above, a likelihood is defined, which evaluates the goodness of a fit to given data. The likelihood function defined in Equation (7.1) is used again in the following. Two models (M1 and M2) are ranked according to their likelihood. Therefore, a test statistic, called the likelihood ratio, is defined as:

$$t_s = -2\Delta \ln \mathcal{L} = -2 \ln(\mathcal{L}_1/\mathcal{L}_2), \tag{7.5}$$

with $\mathcal{L}_1$ and $\mathcal{L}_2$ the likelihood of both models. In the limit of large data samples, this test statistic is X^2-distributed [135]. The degree of freedom in the distribution is given by the difference in free parameters between both models. If the sample size is not large enough, the distribution of the test statistic can deviate from the optimal case. In that case, the distribution can be approximated by performing a large number of pseudo experiments, which leads to high computing times, as the method introduced before in Chapter 7.1.4. The confidence of an experiment to reject one model M1 with respect to some other model M2 is given by the cumulative distribution of the X^2-distribution. The likelihood ratio is calculated with:

$$t_s(\mu) = -2 \ln(\mathcal{L}(\hat{\mu}, \hat{\hat{\Theta}})/\mathcal{L}(\mu, \hat{\Theta})), \tag{7.6}$$

where μ is the parameter of interest, in this case it is the flavor composition. $\hat{\mu}$ stands for the best fit result and μ for the flavor composition actually considered. Further Θ gathers all nuisance parameters, which are fitted simultaneous with the parameter of interest. Here $\hat{\Theta}$ are the nuisance parameters under the assumption of some given μ, whereas $\hat{\hat{\Theta}}$ are the nuisance parameter fitted simultaneous with the flavor composition. The nominator is assigned to the likelihood of a full fit, e.g. the flavor composition and nuisance parameter are free floating in the fit process. Thus, $\hat{\mu}$ gives the most probable value for the flavor composition. In the nominator, the flavor composition is fixed and the nuisance parameter are fitted on their own. In this way each point in flavor composition space is evaluated. Figure 7.14 shows three pseudo experiments, for which the event yield is drawn from the expectations with a Poissonian distribution. Each pseudo experiment shows a different most probable value, because the underlying event distribution is different, even if the truth is the same. The shape is given by an ellipse showing the similar low separation power of the event identification between ν_e and ν_μ. The values given in Figure 7.14 can be translated to confidence intervals.
"It is useful to characterize the sensitivity of an experiment by reporting the expected (e.g., mean or median)" [138] confidence region. Therefore, it was shown in [138] that one can calculate the confidence region on the basis of one representative sample, which is called the Asimov dataset. The sample can be simply chosen as the expectation of the event sample [138]. As the expectation contains non-integer values, this cannot be calculated by standard Poissonian likelihood functions as there is

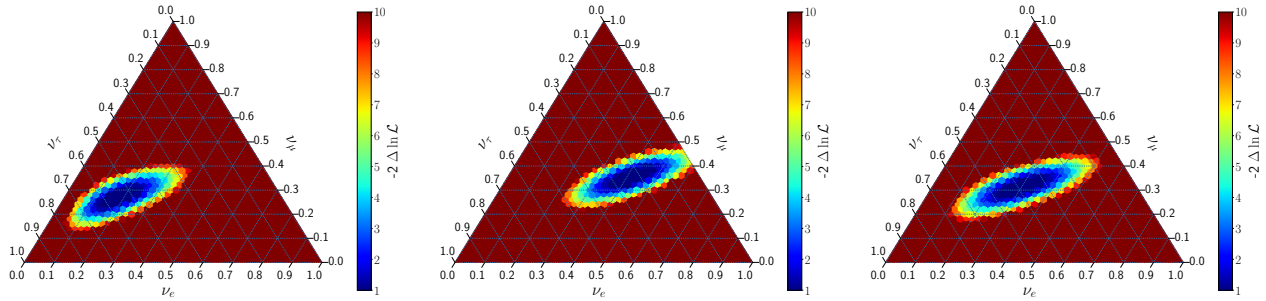

(a) (b) (c)

Figure 7.14: Likelihood ratio for arbitrarily chosen pseudo experiments with the truth off equipartition flavor composition and spectral index of $\gamma = -2.3$.

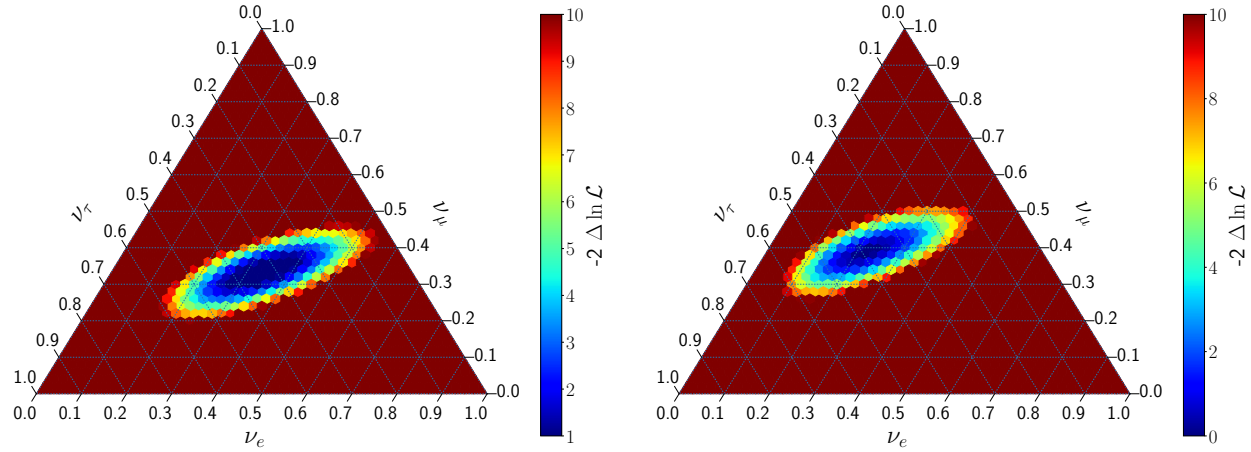

(a) pion decay: 1:1:1 (b) muon damping: 4:7:7

Figure 7.15: Mean likelihood ratio for an experiment of 10 year lifetime and spectral index of $\gamma = -2.3$. (a) for a true flavor composition of 1:1:1 and (b) for 4:7:7 the muon damping scenario

a factorial part. However, the factorial part reduces in the likelihood ratio. Moreover, in the used approximation of the likelihood shown in Equation (7.2) this problematic part does not appear at all. Figure 7.15 shows the likelihood ratio landscape calculated in the described way. The left panel shows the mean likelihood ratio landscape for a truth value of the flavor composition at 1:1:1. The right one shows the confidence region if the true composition is given by the muon damping scenario. The overall elongated shape is similar. The former is centered around the position of 4:7:7. Furthermore, the elongated shape is compressed as the ellipse is closer to the ν_τ-axis, which was already visible in Figure 7.14.

As written above, the test statistic, the likelihood ratio, can be translated to confidence intervals and significance intervals, which are more intuitive to read. Therefore, the cumulative density function of the X^2-distribution is used. Here it has to be assumed that the test statistic is X^2-distributed. As the likelihood functions differ in two dimensions, the X^2-distribution with 2 degrees of freedom has to be chosen [129]. The left panel of Figure 7.16 shows the mean confidence region calculated in the shown way. The right panel shows the significance level of the flavor composition. It is calculated by subtracting the confidence value from one. From here on it is trivial to see the confidence bands in means of σ.

The figure of confidence region has to be read in the following way. A point in the space with for example 68% can be excluded with a confidence of 68%, which means that only in 32% of repeated experiments with a truth of 1:1:1 result in a lower test statistic than achieved in this place. The

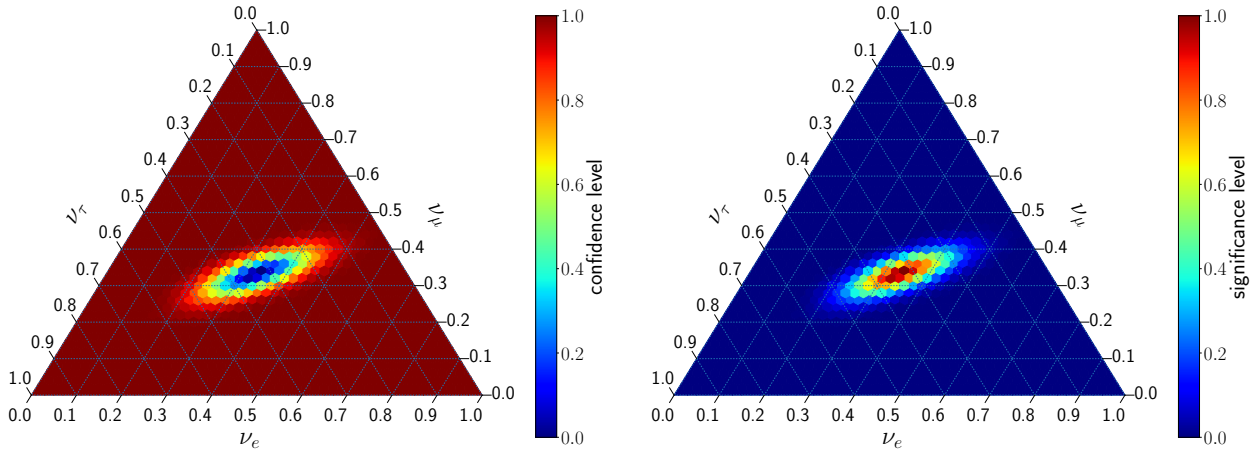

(a) (b)

Figure 7.16: Mean rejection confidence and significance region calculated with the likelihood ratio methods for ARCA in 10 years and assumed equipartition flavor composition.

significance is shown for completeness and as it is common to name exclusion limits in values of significance.
In comparison to figures shown in Chapter 7.1.4 confidence intervals have a slightly different meaning. Confidence intervals constructed by the first method based on Feldman and Cousin say that the truth is covered by the confidence interval with a frequentist's probability of 68%. In the latter case, the area outside of a confidence region of 68% can be excluded to be true with a confidence of 68%. The questions asked in advance are different. Each question is a valid question, but the answer has to be used carefully.

7.4 Comparison to sensitivities for IceCube Gen2

A few analyses have been performed for the IceCube Gen2 Detector [49] to evaluate the sensitivity towards the flavor composition. The final likelihood ratio is calculated in the same way as shown in the previous section. First an estimate is published in [136], which is shown in Figure 7.17a. It is evaluated for 15 years of IceCube Gen2 data. Further details on the calculation are not given in this case. The lines for $1\,\sigma$ and $3\,\sigma$ are shown. Here one sees an extremely narrow band in the ν_μ-extension, but a wider range of possible flavor composition in the ν_τ and ν_e direction. Again the correlation between ν_μ and ν_τ can be seen like for the analysis shown in this thesis. Figure 7.17b shows another analysis, where analytic methods were used to derive the event yield in multiple samples for 10 years of data taking. Four samples are used: Cascades, tracks, Glashow resonance and double bang. Cascades are defined as in this thesis. However, tracks are stated only as ν_μ-CC events in that publication. In this estimate, the elongation is less pronounced, which gives a hint, that more information about ν_τ is used than in [136]. Indeed, the method heavily makes use of the double bang class, which is estimated analytically and a generic threshold for detecting the double bang as two cascades. Both cascades have to be as far apart from each other as two detection units are apart from each other, which implies a threshold of 5.3 PeV. This approach is different to the analysis in this thesis, where the expectations are given by full detector simulation with dedicated cuts to derive final samples.
Figure 7.17c shows the same procedure as Figure 7.17b, except that only cascade and track events are used. In that way the elongation is increased as the double bang event is not used. The confidence intervals showed in Figure 7.16 show a behavior somewhere in between the last two figures.
Both analysis neglect the atmospheric muon background as it is very small in comparison to the

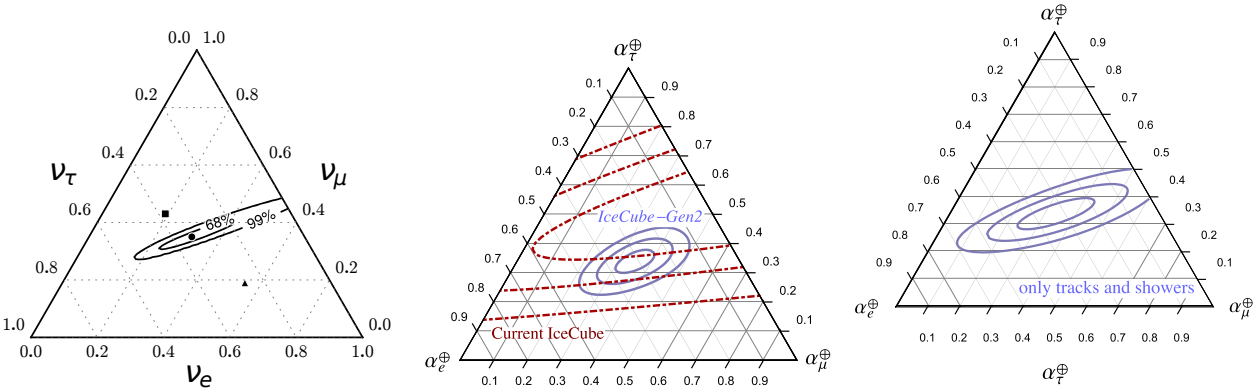

(a) 15 years IceCube Gen2[136] (b) 10 years IceCube Gen2[137] (c) 10 years only cascades and tracks IceCube Gen2[137]

Figure 7.17: Mean confidence intervals for IceCube Gen2 with the assumption of equipartition flavor contribution. Axes show the fraction of each neutrino flavor contributing to the overall astrophysical neutrino flux. (b) and (c) show $1\,\sigma$ to $3\,\sigma$ lines

neutrino flux. Furthermore no particle identification is used in the analysis, which highlights the performance of the flavor composition developed in this thesis, which uses the full particle identification as described in Chapter 6.

7.5 Conclusion

This chapter showed the sensitivity of KM3NeT/ARCA to the flavor composition of the astrophysical neutrino flux. Simulated neutrino and muon events were used. These were categorized according to the algorithms developed in the Chapter 6. Two out of five subsamples could be used for the on-going analysis after a subsample-tailored atmospheric muon rejection. For the other three, either the total neutrino flux was too low or the atmospheric muon contamination thwarted the further use. Each subsample is shown in a histogram according to the best suitable energy reconstruction. An improvement in sensitivity could be achieved here once any other quantity to built up the histogram would be found. Nevertheless, the implemented analysis chain is independent from the chosen quantity. The expected event yield was used as a model for the fit as well as for the basis to draw up random pseudo experiments. The event yield per bin was fitted to an expected neutrino yield. The developed fit chain is based on the *sherpa* package. With a very high number of pseudo experiments the sensitivity can be calculated. Therefore, confidence intervals of the flavor composition were calculated. The method is leaned onto the construction according to Feldman and Cousin. It was shown that the influence of a nuisance parameter, like the spectral index or atmospheric neutrino background, can be fitted simultaneously with the target values. In this way, uncertainties were removed from the analysis. Finally, it was made clear that within a lifetime of 10 years of KM3NeT/ARCA, the $1\,\sigma$ range of the ν_μ fraction can be pinned down to a size of 0.2. The fraction of ν_e and ν_τ show a degeneracy, which decreases slowly with time. The degeneracy is due to the small difference in the topology of ν_τ and ν_e. Remarkably enough, it was shown that the spectral index can be measured with high accuracy.
In addition, a likelihood ratio test was implemented, which is directly comparable to sensitivities shown by IceCube. Here exclusion limits for hypothesis are calculated. It was shown that the sensitivity after ten years of data taking is improved to the sensitivity shown for IceCube Gen2, depending on the actual details of the analysis.

Chapter 8

Conclusion

One of the most important questions in neutrino astronomy is the composition of the neutrino flux with respect to the neutrino flavor, which gives hints to neutrino production mechanisms in distant astrophysical objects. The neutrino flavor composition can be determined by measuring spectra of neutrino properties. This is one goal pursued by KM3NeT/ARCA, a cubic-kilometer water-Cherenkov detector in the Mediterranean Sea. It is currently built by the KM3NeT collaboration. The degree to which ARCA can contribute to this task is significantly depending on the knowledge about atmospheric background and the performance in classifying of events.

The subject of this thesis was to estimate the performance of ARCA with regards to the flavor composition. Key steps at the analysis were developed and evaluated.

Two main developmental results have been achieved. Firstly, the identification of events in topology-based classes was developed to produce independent subsamples of events for the final spectral fit, e.g. no event is used in two different subsamples. The spectral fit itself is the second development, which directly leads to the value of flavor composition. Furthermore, the background estimate of atmospheric muons and neutrinos is one key criterion for the sensitivity to an astrophysical neutrino signal. Therefore, first steps were initiated to estimate the underlying uncertainties in the atmospheric background with a preliminary full particle simulation.

As part of this work, the atmospheric muon background was enlightened in the sense of uncertainties in characteristic quantities, like the muon multiplicity. Therefore, different simulation packages were used and differences between them were treated as systematic uncertainties. At first the commonly used MUPAGE was compared to the newly developed interaction models used in CORSIKA. The KM3NeT collaboration currently builds up the setting of a large production with CORSIKA. In the context of this thesis, values of input parameters were fixed. Worth mentioning here is the modeling of the atmospheric conditions above the KM3NeT sites, which turned out to be quite different for ARCA and ORCA because the climate at the ORCA site is more variable with the seasons. The variation from summer to winter, for the atmospheric depth between 20 km and 40 km, lies around 10% for the ARCA site but at 15% for the ORCA site. Future analyses will correlate this effect to the muon rate reaching the detectors. The comparison of different hadronic interaction models as well as the cosmic-ray flux models showed that they introduce a uncertainty of the order of a few percent. However, the models themselves are stated with uncertainties of up to 20%. The event spectrum of low muon multiplicity simulated with MUPAGE is in good agreement with the one simulated with CORSIKA. The high muon multiplicity bundles are overestimated by MUPAGE with respect to CORSIKA. Otherwise, measurements show that CORSIKA models underestimate the flux. Other physical properties also do not vary with regards to different models and their uncertainties. On the whole, the uncertainty in the interval accessible to this study (up 10^5 GeV) was shown to be in the order of 30% for the energy spectrum.

Another indispensable ingredient for all physics analyses in KM3NeT is the classification of events.

In this thesis, a neural network with five target classes was developed. The classes were motivated by the topology of the light distribution initiated by neutrino events inside KM3NeT. There are three track-like classes. Each depends on the initial neutrino direction and the first interaction vertex. Additionally, there is one cascade class and a so-called double-bang class consisting of high-energy tau neutrinos. One sees the very low count rate of this very rare event topology of double bang, which results in a high contamination from atmospheric background and equal composition of other misidentified events after the classification. Other classes show a by far better classification accuracy. For cascades and up-going tracks, a fraction of correctly classified events above 90% was achieved in the complete considered energy interval. The purity with respect to other neutrinos is as well at a level above 90%.
Finally, an analysis of the sensitivity of ARCA to the neutrino flavor composition was performed. Therefore, the output of the event identification was used to built subsamples consisting of topological similar events. For each subsample, a tailored atmospheric muon rejection was developed and applied. Two classes showed a signal suitable for a fit algorithm based on the spectral shape of the measurements. The spectral fitting algorithm uses the expectations as found by simulation and reconstruction to estimate the different contribution of each component for a measurement. This is done simultaneously for the classes chosen. A method to calculate confidence intervals in this multidimensional space based on Feldman and Cousin was developed. Finally, the sensitivity is estimated by a large number of pseudo experiments. As the uncertainties of the atmospheric neutrino flux and the spectral index have a significant influence, they were fitted simultaneously with the flavor composition. In this way, the influence is reduced. Several hypotheses on the flavor composition were tested. The overall shape of exclusion limits is very similar for all of them. For an assumed equipartition composition, 60% of the flavor composition space can be excluded on a $2\,\sigma$-level after a lifetime of 10 years of ARCA. Compared with IceCube's predictions, this value is a slight improvement. However, in this work, self-veto effects of neutrinos are not included, which is supposed to increase the sensitivity. The confidence region has an elongated shape as well as the range of favored models in flavor composition space. Furthermore, the large half-axes are perpendicular to each other, which makes it possible to reject them, even if the confidence interval is quite large relative to the range of possible models.

Outlook

In the near future, a larger simulation of atmospheric particles will be available, which allows to estimate the uncertainties up to highest energies above 10^6 GeV, where this work lacked statistics. Furthermore, the influence of the prompt component of the atmospheric muon flux could not be evaluated here, but this will be possible with the larger production. This simulation will open the possibility to estimate the self-veto effect on a full simulation basis, which enhances the reliability of the reduction of atmospheric neutrinos in addition to the reduction of atmospheric muons.
This draws the view directly to the next development success of this thesis: the event identification. It was used here for the separation of events into topology-based classes and to find suitable events for the training phase. There are more steps in this and other analyses in which the implemented framework of event identification can be used. As the framework is built up modularly it is an easy way to replace the classes used here by another class definition, for example classes separating single muons from high multiplicity muon bundles. This can help to improve the atmospheric muon background rejection or to get insights into the cosmic-ray flux.
New methods in machine learning arise. In the KM3NeT collaboration, there are already efforts to move from feature-based machine learning algorithms to algorithms which are trained on more "native pictures" of the detector. In doing so, the time-consuming process of implementing the handcrafted features is removed. A deep-learning algorithm will help them to learn on its own. Therefore, the simulation has to be highly trustworthy because otherwise the classifier would use simulation

artifacts, which are not physically reasoned. Such artifacts are found more frequently in the hand-crafted features.
Up to now, only the event classes of cascade and up-going tracks have been used for the final spectral fit. This can be extended with more advanced atmospheric muon rejection to more classes and therefore an enhanced sensitivity to the fitting algorithm, with more astrophysical neutrinos available. The implementation of spectral fitting is independent of the physics input, which is why the framework can be used for all kind of spectral fitting tasks. Currently an analysis is on its way to prove the sensitivity of ARCA to the prompt component in the atmospheric muon neutrino flux. It uses the prompt component and the conventional component as two spectra to fit the overall muon flux.
A few years ago, the neutrino astronomy community founded the Global Neutrino Network (GNN), which enforces a global exchange between neutrino telescopes. It is to facilitate joint analyses as well. In this case, the data of multiple detectors are used simultaneously. The principle is easy: the more detectors, the more data, which gives more sensitivity to the analyses. Finally, systematic uncertainties, which are different for different instruments, can be reduced by this combination. Therefore, the collective effort of GNN towards a global neutrino telescope will open a further window to see the universe in a new light, with neutrinos.

Zusammenfassung

Eine der wichtigsten Fragen der Neutrinoastronomie stellt die Flavourkomposition des Neutrinoflusses dar. Dieses Wissen wird Hinweise auf die Neutrinoproduktionsmechanismen in weit entfernten astrophysikalischen Objekten geben. Das Thema dieser Arbeit war es, die Sensitivität von ARCA gegenüber der Flavourkomposition abzuschätzen und Schlüsselstellen der Analyse zu entwickeln und zu bewerten. Die Neutrinoflavorkomposition kann durch die Messung von Spektren von Neutrinoeigenschaften bestimmt werden. Dies ist ein Ziel von KM3NeT/ARCA, einem Wassertscherenkovdetektor von der Größe eines Kubikkilometers im Mittelmeer. Er wird im Moment von der KM3NeT-Kollaboration gebaut. Das Maß in dem ARCA zu dieser Aufgabe beitragen kann, hängt vom Wissen über den atmospherischen Untergrund zur Messung und der Güte der Eventklassifizierung ab.
Zwei grundlegende Entwicklungen konnten erreicht werden. Zum einen wurde die Identifikation von Ereignissen entwickelt, die auf der Ereignistopologie basiert. Dadurch werden unabhängige Teilmengen von Ereignissen für den finalen spektralen Fit bereitgestellt. Der spektrale Fit selbst ist die zweite Entwicklung, die direkt den Wert der Flavourkomposition berechnet. Des Weiteren ist die Abschätzung des atmosphärischen Neutrino- und Muonflusses ein Schlüsselelement für die Sensitivität gegenüber einem astrophysikalischen Neutrinosignal. Dabei wurden erste Schritte unternommen, um die Unsicherheiten des atmosphärischen Untergrunds mit einer vorläufigen Teilchensimulation abzuschätzen.

Ein Teil dieser Arbeit beleuchtet den atmosphärischen Myonuntergrund im Sinne der Unsicherheiten charakterisierender Variablen, wie es die Myonmultiplizität darstellt. Dafür wurden verschiedene Simulationspakete verwendet und die Unterschiede als systematische Unsicherheiten behandelt. Zuerst galt es, das standardmäßig verwendete MUPAGE mit neueren Interaktionsmodellen in CORSIKA zu vergleichen. Die KM3NeT-Kollaboration setzt im Moment eine große Produktion mit CORSIKA auf. In dieser Arbeit wurden dazu verschiedene Eingabeparameter festgelegt. Zu erwähnen ist ein Modell, das die atmosphärischen Bedingungen über den Detektoren beschreibt. Dabei stellte sich heraus, dass die Bedingungen bei ORCA und ARCA sehr verschieden sind, da das Klima bei ORCA im Jahresverlauf variabler ist. Die jahreszeitlichen Schwankungen in der atmosphärischen Tiefe zwischen 20 km und 40 km Höhe liegen bei rund 10% in der Atmosphäre über dem ARCA-Detektor, aber bei 15% über dem ORCA-Detektor. Zukünftige Analysen werden diesen Effekt mit der Myonrate im Detektor korrelieren. Der Vergleich von verschiedenen Interaktionsmodellen und Modellen der kosmischen Strahlung zeigten, dass sie eine Unsicherheit von einigen Prozent beisteuern, wohingegen die Modelle mit einer Unsicherheit von 20% angegeben werden. Das Spektrum der Myonmultiplizität wie es von MUPAGE simuliert wird, ist bei kleinen Werten in guter Übereinstimmung mit den CORSIKA-Simulationen. Große Multiplizitäten werden allerdings von MUPAGE im Verhältnis zu CORSIKA überschätzt. Auf der anderen Seite zeigen Messungen, dass Modelle in CORSIKA den Fluss von Myonen unterschätzen. Andere physikalische Variablen zeigen ebenfalls wenig Variation mit den Interaktionsmodellen und Modellen kosmischer Flüsse. Im Ganzen wurde gezeigt, dass die Unsicherheiten im in dieser Studie zugänglichen Energieintervall in der Größenordnung von 30% im Energiespektrum sind.
Ein anderer unverzichtbarer Bestandteil aller Physikanalysen in KM3NeT ist die Klassifikation von

Ereignissen. In dieser Arbeit wurde ein neuronales Netzwerk zur Klassifikation in fünf Zielklassen entwickelt. Die Klassen waren durch die Topologie der Lichtverteilung, die durch Neutrinoereignisse in KM3NeT ausgelöst werden, motiviert. Es gibt drei spurenartige Klassen, die jeweils von der anfänglichen Neutrinorichtung und dem ersten Interaktionspunkt abhängig sind. Dazu kommen eine Kaskadenklasse und eine sogenannte „double-bang"-Klasse, bestehend aus hochenergetischen Tauneutrinos. Man sieht die sehr geringe Zählrate dieser sehr seltenen Ereignistopologie des „double-bangs", was zu einer hohen Verunreinigung durch atmosphärischen Untergrund und anderer Klassen nach der Klassifizierung führt. Andere Klassen weisen eine deutlich bessere Klassifizierungsgenauigkeit auf. Für Kaskaden und nach oben weisende Spuren wurde ein Anteil korrekt klassifizierter Ereignisse von über 90% im gesamten betrachteten Energieintervall erreicht. Die Reinheit gegenüber anderen Neutrinos liegt bei ebenfalls über 90%.
Eine weitere wichtige Aufgabe stellte die Analyse der Sensitivität von ARCA gegenüber der Neutrinoflavorkomposition dar. Als Grundlage diente das Ergebnis der Ereignisidentifikation für die Erstellung von Ereignisteilmengen, die aus topologisch ähnlichen Ereignissen bestehen. Für jede Teilmenge wurde eine maßgeschneiderte atmosphärische Myonunterdrückung entwickelt und angewendet. Zwei Klassen zeigten ein Signal, das für einen Fitalgorithmus, der auf der spektralen Form der Messungen basiert, geeignet ist. Der spektrale Fitalgorithmus nutzt die Erwartungen der Ereignisrate relativ zu rekonstruierten Neutrinoenergien, wie sie in der Simulation und Rekonstruktion gefunden wurden, um den unterschiedlichen Beitrag jeder Komponente zu einer Messung abzuschätzen. Dies geschieht gleichzeitig für alle gewählten Klassen. Es wurden Verfahren zur Berechnung von Konfidenzintervallen in diesem mehrdimensionalen Raum auf der Basis von Feldman und Cousin entwickelt. Schließlich wurde die Sensitivität durch eine große Anzahl von Pseudo-Experimenten bestimmt. Da die Unsicherheiten des atmosphärischen Neutrinoflusses und der Spektralindices einen signifikanten Einfluss haben, wurden sie gleichzeitig mit der Flavorzusammensetzung ermittelt. Auf diese Weise wird der Einfluss verringert. Es erfolgte eine Prüfung mehrerer Hypothesen zur Flavorzusammensetzung. Die endgültige Form der Ausschlussgrenzen ist für alle sehr ähnlich. Bei einer angenommenen ausgeglichenen Zusammensetzung überdeckte die $2\,\sigma$-Region 40% des Parameterraums nach einer Lebensdauer von 10 Jahren ARCA. Im Vergleich zu den Prognosen von IceCube ist dieser Wert eine leichte Verbesserung. Jedoch wird in dieser Analyse kein Self-Veto Effekt beachtet, der die Sensitivität von ARCA erhöhen würde. Die Vertrauensregion hat im Raum der möglichen Flavourzusammensetzungen eine längliche Form. Die Palette der bevorzugten Modelle für die Flavourzusammensetzung ist ebenfalls in länglicher Form angeordnet. Allerdings stehen die großen Halbachsen senkrecht zueinander, was es ermöglicht, Modelle zu verwerfen, auch wenn die Konfidenzintervalle im Vergleich zur Verteilung möglicher Modelle relativ groß sind.

Ausblick

In naher Zukunft wird eine größere Simulation der atmosphärischen Teilchen zur Verfügung stehen, die eine Abschätzung der Unsicherheiten bis hin zu den höchsten Energien über 10^6 GeV ermöglicht, bei der es dieser Arbeit an Statistik fehlte. Zudem konnte der Einfluss der prompten Komponente des atmosphärischen Myonflusses nicht ausgewertet werden. Dies wird mit einer größeren Menge an simulierten Daten möglich sein. Diese erweiterte Simulation wird die Möglichkeit einer Abschätzung des Self-Veto Effekts auf einer vollständigen Simulationsbasis eröffnen und damit die Zuverlässigkeit der Reduktion der atmosphärischen Neutrinos zusätzlich zur Reduktion atmosphärischer Myonen erhöhen.
Dies richtet den Blick direkt auf den nächsten Entwicklungserfolg dieser Arbeit, der in zukünftigen Analysen Anwendung finden wird: Die Ereignisidentifikation. Sie wurde hier zur Einteilung von Ereignissen in topologiebasierte Klassen und zur Suche nach geeigneten Ereignissen für die Trainingsphase eingesetzt. In dieser und weiteren Analysen sind zusätzliche Schritte denkbar, in denen das implementierte Framework der Ereignisidentifikation genutzt werden kann. Durch den modularen

Aufbau des Frameworks ist es eine Leichtigkeit, die hier verwendeten Klassen durch eine andere Klassendefinition zu ersetzen, zum Beispiel Klassen, die einzelne Myonen von Myonbündeln mit hoher Multiplizität trennen. Dies kann helfen, die Unterdrückung des atmosphärischen Myonhintergrunds zu verbessern oder Einblicke in den kosmischen Strahlungsfluss zu gewinnen.
Neue Methoden des maschinellen Lernens können der KM3NeT-Kollaboration helfen, von merkmalsbasierten Algorithmen des maschinellen Lernens zu Algorithmen, die auf „native Bilder“ des Detektors trainiert werden, überzugehen. Auf diese Weise entfällt der zeitaufwändige Implementierungsprozess der handgefertigten Features. Die neuen Deep-Learning-Algorithmen helfen dabei, das Features von den Algorithmen selbständig gelernt werden. Damit dies zufriedenstellend funktioniert, muss die Simulation sehr vertrauenswürdig sein, da der Klassifikator sonst Simulationsartefakte verwenden würde, die physikalisch nicht begründet sind. Solche Artefakte werden in handgefertigten Features leichter gefunden.
Bisher werden nur die Ereignisklassen von Kaskaden und aufwärts gerichtete Spuren für den endgültigen spektralen Fit verwendet. Dies kann durch eine erweiterte atmosphärische Myonunterdrückung auf weitere Klassen erweitert werden und damit zu einer erhöhten Sensitivität gegenüber dem Fit-Algorithmus führen, da mehr astrophysikalische Neutrinos zur Verfügung stehen.
Die Implementierung des spektralen Fits ist unabhängig von den physikalischen Größen, weshalb das Framework für alle Arten von spektralen Fits eingesetzt werden kann. Derzeit ist eine Analyse auf dem besten Wege, die Empfindlichkeit von ARCA gegenüber der prompten Komponente im atmosphärischen Myonneutrinofluss zu entwickeln. Sie verwendet die prompte und die konventionelle Komponente als zwei Spektren, um den gesamten Myonfluss zu ermitteln.
Vor einigen Jahren gründete die Gemeinschaft der Neutrinoastronomie das *Global Neutrino Network* (GNN), das den globalen Austausch zwischen Neutrinoteleskopen forciert. Es soll weitere gemeinsame Analysen ermöglichen. Dabei werden die Daten von mehreren Detektoren gleichzeitig genutzt. Das Prinzip ist einfach: Je mehr Detektoren, desto mehr Daten, desto sensitiver sind die Analysen. Systematische Unsicherheiten, die für verschiedene Instrumente unterschiedlich sind, können durch diese Kombination reduziert werden. Daher wird die kollektive Anstrengung von GNN auf dem Weg zu einem globalen Neutrinoteleskop ein weiteres Fenster öffnen, um das Universum in einem neuen Licht zu sehen, mit Neutrinos.

Appendices

Appendix A

Details on atmospheric particle simulation

A.1 Compile options

Neutrino This option enables CORSIKA to create and propagate neutrinos, which we want to see how many of them reach the detector in final.

Taulep Taulep enables the production of charmed particles in the atmosphere if the high energy interaction model fits that.

Curved The atmosphere is curved. If one assumes the atmosphere as a plane shape the travel length through atmosphere becomes to short especially for the high zenith angles.

Upward Also this option is important for highly inclined cascades. In cascades with high zenith angle it can happen that particles move upwards in the atmosphere. The standard code of CORSIKA neglects this particles as they might never reach the observation level. How ever some of them can be rebound to the surface if the shower is highly inclined.

EHistory The history options are used to see the particles which produced the particles arriving at Earth. One will the the most important application here for the prompt particle component.

External Atmosphere An external atmosphere is enabled. One can see the actual used atmosphere below

High energy interaction model Here one of the moels described in the main part can be used: EPOS-LHC, Sibyll or QGSJET

Low energy interaction model The interaction model for particles below 80 GeV in the lab reference system is chosen to be GHEISHA.

Detector geometry The detecor geometry has influence to the zenith angle spectrum of the simulated events. The volume detector model is chosen, as this can be easily reweighted to any other detector geometry. The volume detector model simulates a uniform distribution in the zenith angle.

A.2 Run time options

RUNNR	334	run number
EVTNR	1	number of first cascade event
NSHOW	1	number of cascades to generate
PRMPAR	14	particle type of primary particle (here proton)
ESLOPE	-1	slope of primary energy spectrum
ERANGE	1.E3 5.E9	energy range of primary particle (GeV)
THETAP	0. 87.	range of zenith angle (°)
PHIP	-180. 180.	range of azimuth angle (°)
SEED	0 0 0	seed for 1. random number sequence
SEED	1 0 0	seed for 2. random number sequence
OBSLEV	0.	observation level (cm)
MAGNET	27.67 34.96	magnetic field around the detector in x and z direction (μT)
ECUTS	1.E3 1.E3 1.E3 1.E3	energy cuts for different particle types (GeV)
ATMOD	0	identifier for the chosen atmospheric model
NUADDI	T	enable additional info for neutrinos
MUADDI	T	enable additional info for muons
LONGI	T 10. T T	longit.distr. step size fit out
DIRECT	./	
USER	you	user
DEBUG	F 6 F 1000000	debug flag and log.unit for out
EXIT		terminates input

Table A.1: run options written to the CORSIKA data card. only options which are not default in CORSIKA 7.5700 are shown in this list except some important and chosen values. For details of the different flags one might consult the CORSIKA User Guide [65].

A.3 Atmospheric models

The tables show the parameters which are used in the CORSIKA datacards.

Layer:	1	2	3	4	5
ATMA	-157.857	-28.7524	0.790275	-0.0286999	0.481114
ATMB	1190.44	1171.0	1344.78	445.357	
ATMC	1006100.0	758614.0	636790.0	817384.0	16886800.0
ATMLAY	9.0e5	18.0e5	38.0e5	68.2e5	

Table A.2: Parameters for the ARCA-Summer

Layer:	1	2	3	4	5
ATMA	-116.391	3.5938	0.474803	-0.0246031	0.280225
ATMB	1155.63	1501.57	1271.31	398.512	
ATMC	933697.0	594398.0	636790.0	810924.0	29618400.0
ATMLAY	12.25e5	21.25e5	43.0e5	70.5e5	

Table A.3: Parameters for the ARCA-Winter

Layer:	1	2	3	4	5
ATMA	-158.85	-5.38682	0.889893	-0.0286665	0.50035
ATMB	1145.62	1176.79	1248.92	415.543	
ATMC	998469.0	677398.0	636790.0	823489.0	16090500.0
ATMLAY	9.0e5	22.0e5	38.0e5	68.2e5	

Table A.4: Parameters for ORCA-Summer

Layer:	1	2	3	4	5
ATMA	-132.16	-2.4787	0.298031	-0.0220264	0.348021
ATMB	1120.45	1203.97	1163.28	360.027	
ATMC	933697.0	643957.0	636790.0	804486.0	23109000.0
ATMLAY	9.5e5	22.0e5	47.0e5	68.2e5	

Table A.5: Parameters for ORCA-Winter

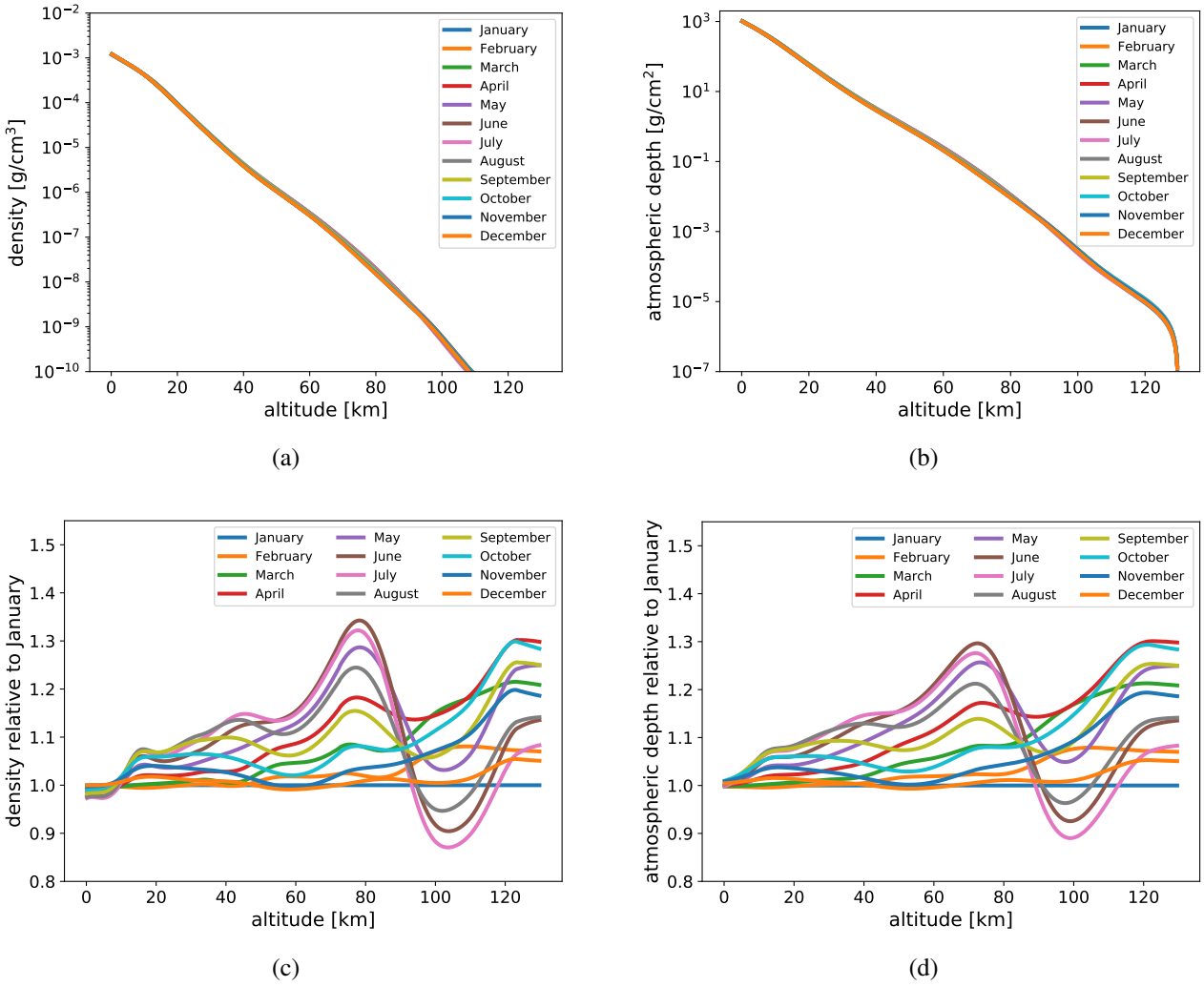

(a) (b)

(c) (d)

Figure A.1: Atmospheric models derived with NRLMSIS-00 for ARCA.

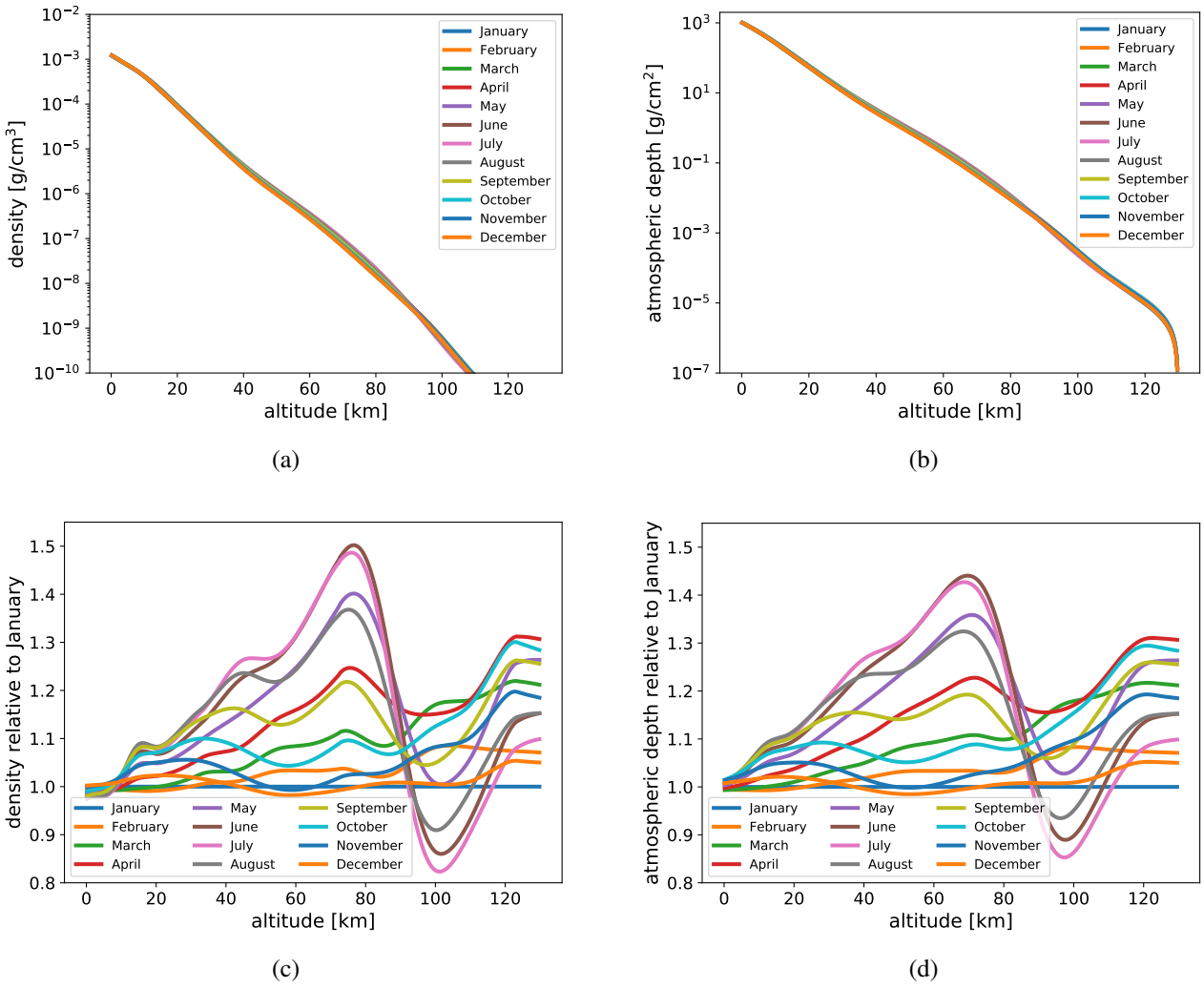

Figure A.2: Atmospheric models derived with NRLMSIS-00 for ORCA.

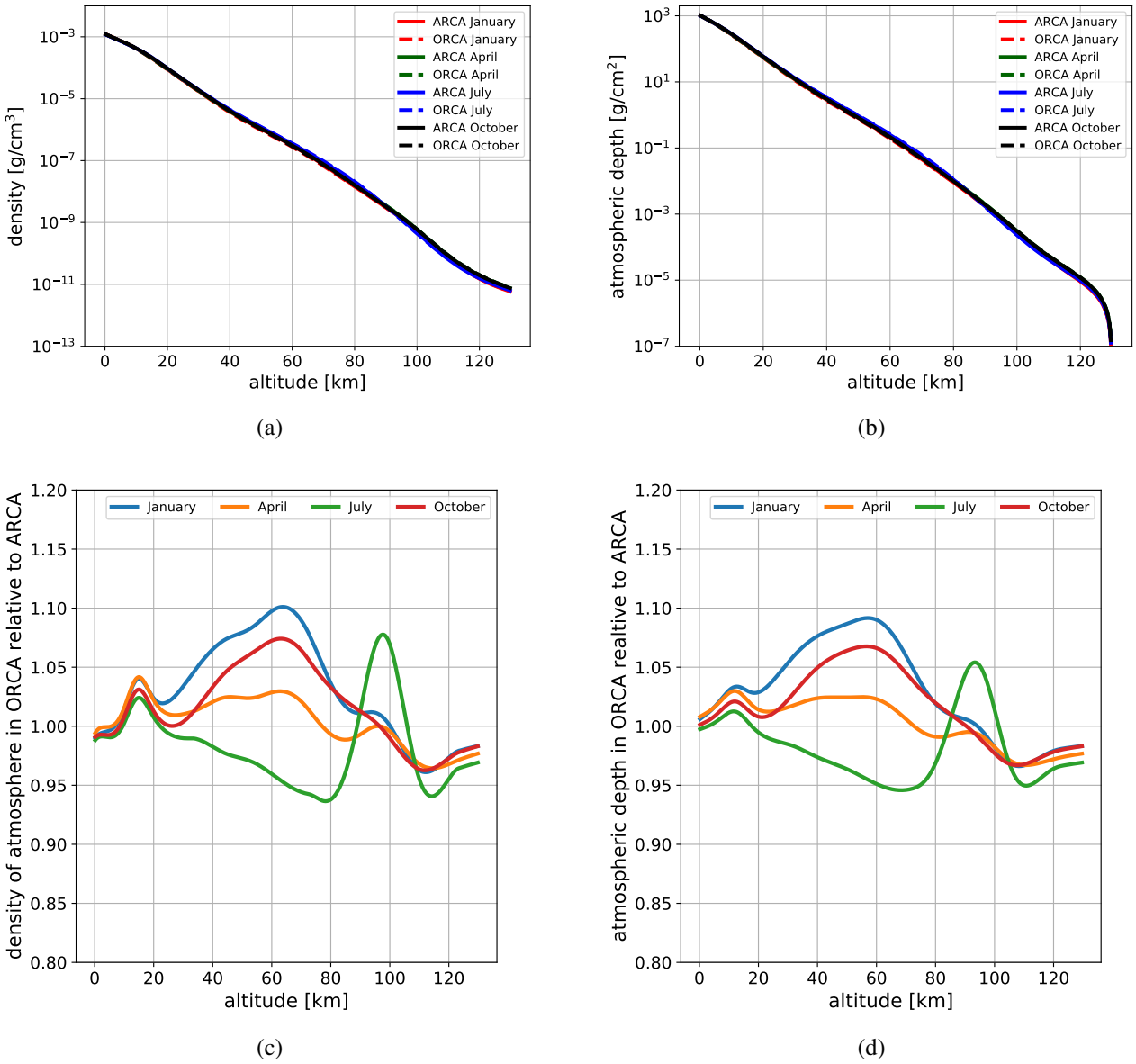

Figure A.3: Atmospheric models derived with NRLMSIS-00 compared for ORCA and ARCA

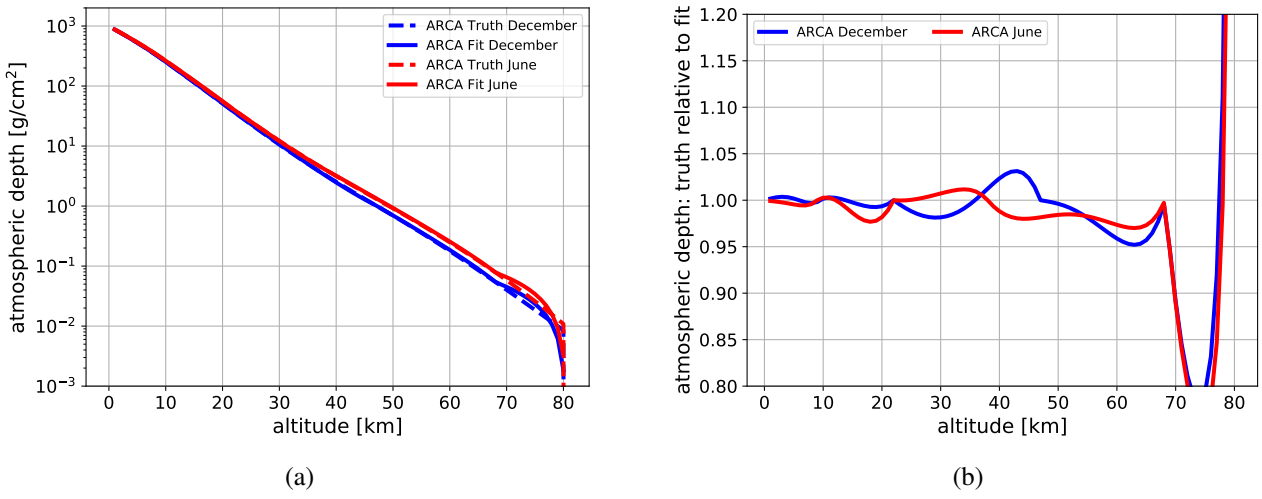

Figure A.4: Comparison of atmospheric models fitted with the Bernlohr package for ORCA

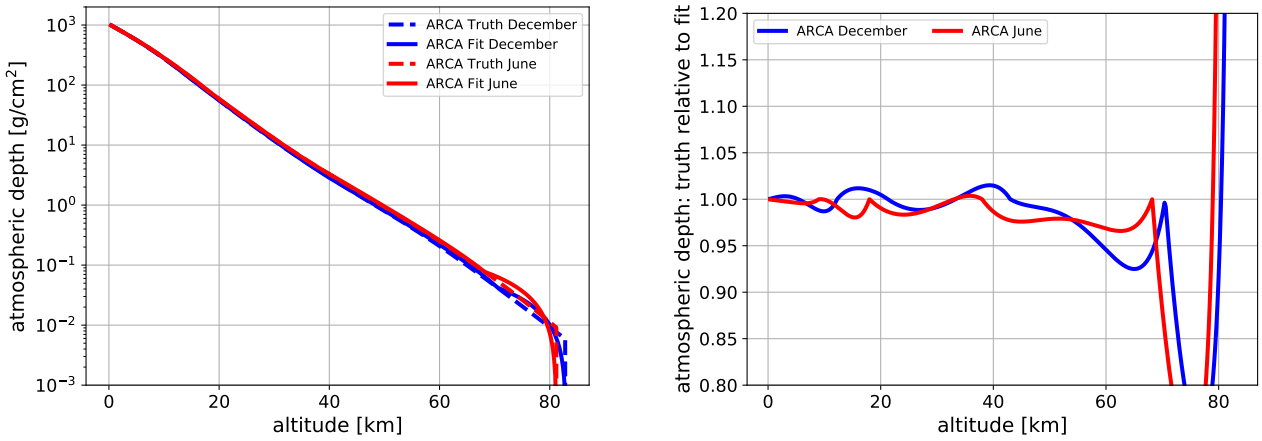

(a) (b)

Figure A.5: Comparison of atmospheric models fitted with the Bernlohr package for ARCA

Table A.6: Table of model data and fit data for the atmosphere above ARCA in June

Altitude[km]	rho(table)	rho(fit)	thick(table)	thick(fit)
0	0.00120636	0.00118322	1032.58	1032.58
1	0.00108828	0.00107128	919.152	919.949
2	0.000983839	0.000969917	816.687	817.973
3	0.000890329	0.00087815	723.993	725.646
4	0.000805702	0.000795064	640.101	642.054
5	0.00072842	0.00071984	564.222	566.371
6	0.000657353	0.000651733	495.69	497.849
7	0.000591688	0.00059007	433.935	435.81
8	0.000530854	0.000534241	378.453	379.641
9	0.00047446	0.000471304	328.786	328.786
10	0.000422242	0.000413098	284.506	284.63
11	0.000373952	0.00036208	245.209	245.927
12	0.000329211	0.000317363	210.525	212.004
13	0.000287815	0.000278168	180.114	182.27
14	0.000249717	0.000243814	153.645	156.209
15	0.000214937	0.000213703	130.787	133.366
16	0.000183575	0.000187311	111.203	113.344
17	0.000155899	0.000164178	94.5364	95.7952
18	0.000131934	0.000125038	80.4135	80.4135
19	0.000111477	0.000106867	68.4744	68.842
20	9.42038E-05	9.13361E-05	58.3872	58.9522
21	0.000079718	7.80624E-05	49.8564	50.4996
22	6.75636E-05	6.67177E-05	42.6308	43.2755
23	5.73448E-05	5.70218E-05	36.5016	37.1012
24	4.87371E-05	4.87349E-05	31.2954	31.8242
25	4.14737E-05	4.16523E-05	26.8673	27.3141
26	3.53348E-05	3.55991E-05	23.0965	23.4594
27	3.01384E-05	3.04255E-05	19.8817	20.165
28	2.57337E-05	2.60039E-05	17.1379	17.3493
29	2.19951E-05	2.22248E-05	14.7937	14.9428

Altitude[km]	rho(table)	rho(fit)	thick(table)	thick(fit)
30	1.88181E-05	1.89949E-05	12.789	12.886
31	1.61153E-05	1.62344E-05	11.0728	11.1282
32	1.38135E-05	1.38751E-05	9.60231	9.62578
33	1.18518E-05	1.18586E-05	8.34119	8.34174
34	1.01827E-05	1.01352E-05	7.25831	7.2443
35	8.7626E-06	8.66231E-06	6.32708	6.30635
36	7.55381E-06	7.40343E-06	5.52491	5.50471
37	6.52414E-06	6.3275E-06	4.83262	4.81957
38	5.64625E-06	5.21505E-06	4.234	4.234
39	0.000004897	4.61451E-06	3.71528	3.74313
40	4.25658E-06	4.08313E-06	3.2648	3.30879
41	3.70853E-06	0.000003613	2.87271	2.92447
42	3.23872E-06	3.1969E-06	2.53062	2.5844
43	2.83526E-06	2.82877E-06	2.23144	2.28349
44	2.48811E-06	0.000002503	1.96916	2.01723
45	2.18876E-06	2.21479E-06	1.73866	1.78164
46	1.9299E-06	1.95975E-06	1.53561	1.57317
47	1.70505E-06	1.73408E-06	1.35636	1.38871
48	1.5088E-06	1.53439E-06	1.19784	1.22549
49	1.33677E-06	1.3577E-06	1.05746	1.08106
50	1.18537E-06	1.20136E-06	0.933024	0.953269
51	1.05166E-06	0.000001063	0.822641	0.840192
52	9.33205E-07	9.40605E-07	0.724696	0.740136
53	0.000000828	8.3229E-07	0.637787	0.651601
54	7.34373E-07	7.36449E-07	0.560691	0.573262
55	6.50911E-07	6.51644E-07	0.492337	0.503944
56	5.76444E-07	5.76605E-07	0.431782	0.442608
57	0.00000051	5.10206E-07	0.378184	0.388335
58	4.50778E-07	4.51454E-07	0.330792	0.340312
59	0.000000398	3.99468E-07	0.28893	0.297819
60	0.000000351	3.53467E-07	0.251995	0.260219
61	3.09148E-07	3.12764E-07	0.219446	0.226949
62	0.000000272	2.76748E-07	0.190798	0.19751
63	2.38825E-07	2.4488E-07	0.16562	0.171461
64	2.09365E-07	2.16681E-07	0.143533	0.148412
65	1.83269E-07	1.91729E-07	0.124188	0.128017
66	1.6018E-07	1.69651E-07	0.107269	0.10997
67	1.39777E-07	1.50115E-07	0.0924959	0.0940017
68	1.21772E-07	1.32829E-07	0.0796165	0.0798722
69	1.05906E-07	5.9218E-08	0.0684074	0.0725104
70	9.19451E-08	5.9218E-08	0.0586688	0.0665886
71	7.96799E-08	5.9218E-08	0.050223	0.0606668
72	6.89221E-08	5.9218E-08	0.0429119	0.054745
73	5.96553E-08	5.9218E-08	0.0365856	0.0488232
74	5.14149E-08	5.9218E-08	0.0311235	0.0429014
75	4.42226E-08	5.9218E-08	0.0264214	0.0369796
76	0.000000038	5.9218E-08	0.0223821	0.0310578
77	3.25045E-08	5.9218E-08	0.0189197	0.025136
78	2.77728E-08	5.9218E-08	0.0159586	0.0192142

Altitude[km]	rho(table)	rho(fit)	thick(table)	thick(fit)
79	2.36744E-08	5.9218E-08	0.0134319	0.0132924
80	2.01327E-08	5.9218E-08	0.0112812	0.00737064
81	1.70796E-08	5.9218E-08	0.00945475	0.00144885

Table A.7: Table of model data and fit data for the atmosphere above ARCA in December

Altitude[km]	rho(table)	rho(fit)	thick(table)	thick(fit)
0	0.00123542	0.00123769	1039.24	1039.24
1	0.00111134	0.00111198	923.299	921.866
2	0.00100425	0.000999046	818.706	816.416
3	0.000909608	0.000897578	724.044	721.675
4	0.000824153	0.000806415	638.274	636.557
5	0.000745642	0.000724511	560.618	560.083
6	0.000672605	0.000650926	490.476	491.377
7	0.00060416	0.000584815	427.356	429.649
8	0.00053985	0.000525418	370.831	374.191
9	0.000479512	0.000472054	320.498	324.365
10	0.000423158	0.00042411	275.96	279.599
11	0.000370927	0.000381035	236.812	239.38
12	0.00032307	0.000342335	202.626	203.246
13	0.00027972	0.00028355	172.957	172.135
14	0.000240862	0.000239643	147.352	146.037
15	0.000206362	0.000202535	125.37	123.98
16	0.000176023	0.000171173	106.586	105.339
17	0.000149646	0.000144668	90.5973	89.584
18	0.000126941	0.000122266	77.023	76.2687
19	0.000107548	0.000103334	65.5175	65.0152
20	9.10853E-05	8.73329E-05	55.7724	55.5043
21	7.71669E-05	7.38097E-05	47.5177	47.4661
22	6.54073E-05	6.30727E-05	40.5224	40.6389
23	5.54702E-05	5.39065E-05	34.5913	34.8019
24	4.70716E-05	4.60723E-05	29.5595	29.8132
25	3.99712E-05	3.93767E-05	25.2879	25.5495
26	3.39665E-05	3.36542E-05	21.6591	21.9055
27	2.88865E-05	2.87633E-05	18.574	18.791
28	2.45867E-05	2.45832E-05	15.9491	16.1291
29	2.09455E-05	2.10105E-05	13.7137	13.8541
30	1.78604E-05	1.79571E-05	11.8083	11.9097
31	1.52447E-05	1.53474E-05	10.1827	10.2479
32	1.30256E-05	0.000013117	8.79426	8.8276
33	0.000011141	1.12108E-05	7.60722	7.6137
34	9.53757E-06	9.58152E-06	6.5914	6.57622
35	8.17409E-06	8.18906E-06	5.72122	5.68951
36	7.01539E-06	0.000006999	4.97484	4.93167
37	6.03094E-06	5.98181E-06	4.33365	4.28396
38	5.19446E-06	5.11249E-06	3.78184	3.73038
39	4.48342E-06	4.3695E-06	3.30598	3.25726
40	3.87858E-06	3.73449E-06	2.89471	2.85289

Altitude[km]	rho(table)	rho(fit)	thick(table)	thick(fit)
41	3.36358E-06	3.19176E-06	2.53841	2.50728
42	2.92454E-06	2.72791E-06	2.22895	2.21191
43	2.54969E-06	2.44667E-06	1.95946	1.95946
44	2.22909E-06	2.16281E-06	1.72412	1.72928
45	1.95431E-06	1.91189E-06	1.51804	1.5258
46	1.71812E-06	1.69008E-06	1.33706	1.34593
47	1.51405E-06	0.000001494	1.17772	1.18692
48	1.33673E-06	1.32068E-06	1.03715	1.04637
49	1.18189E-06	1.16746E-06	0.912937	0.922118
50	0.000001046	0.000001032	0.80304	0.812283
51	9.26322E-07	9.12285E-07	0.705739	0.715191
52	8.20477E-07	8.06446E-07	0.61956	0.629363
53	7.26601E-07	7.12885E-07	0.543234	0.553493
54	6.43136E-07	6.30179E-07	0.47566	0.486425
55	5.6879E-07	5.57069E-07	0.415875	0.427137
56	5.02488E-07	4.9244E-07	0.363035	0.374728
57	4.43333E-07	4.35309E-07	0.31639	0.3284
58	3.90559E-07	3.84806E-07	0.275271	0.287446
59	3.43498E-07	3.40163E-07	0.239082	0.251243
60	3.01567E-07	3.00698E-07	0.207287	0.219241
61	2.6425E-07	2.65813E-07	0.179404	0.190951
62	2.31089E-07	0.000000235	0.155	0.165943
63	2.01603E-07	2.07714E-07	0.133687	0.143837
64	1.75446E-07	1.83615E-07	0.115122	0.124295
65	1.52356E-07	1.62313E-07	0.0989865	0.107021
66	0.000000132	1.43482E-07	0.0849919	0.0917501
67	1.14157E-07	1.26836E-07	0.0728803	0.0782513
68	9.85026E-08	1.12121E-07	0.0624205	0.0663186
69	8.48205E-08	9.91133E-08	0.0534061	0.0557702
70	7.28938E-08	8.76146E-08	0.0456529	0.0464456
71	6.25248E-08	3.37628E-08	0.0389973	0.0405091
72	5.35338E-08	3.37628E-08	0.0332947	0.0371328
73	4.58268E-08	3.37628E-08	0.028413	0.0337565
74	3.91592E-08	3.37628E-08	0.0242386	0.0303803
75	3.34509E-08	3.37628E-08	0.0206723	0.027004
76	2.85692E-08	3.37628E-08	0.0176263	0.0236277
77	2.43977E-08	3.37628E-08	0.0150249	0.0202514
78	2.08351E-08	3.37628E-08	0.0128034	0.0168751
79	1.77937E-08	3.37628E-08	0.0109062	0.0134988
80	1.51977E-08	3.37628E-08	0.00928587	0.0101226
81	0.000000013	3.37628E-08	0.00790187	0.00674628
82	1.109E-08	3.37628E-08	0.00671959	0.00337
83	9.77763E-09	3.37628E-08	3.72008E-44	0

Table A.8: Table of model data and fit data for the atmosphere above ORCA in June

Altitude[km]	rho(table)	rho(fit)	thick(table)	thick(fit)
0	0.00122217	0.00114737	986.766	986.766

Altitude[km]	rho(table)	rho(fit)	thick(table)	thick(fit)
1	0.00109904	0.00103803	876.862	877.588
2	0.000992306	0.000939101	777.632	778.814
3	0.000897895	0.000849604	687.842	689.453
4	0.000812844	0.000768636	606.558	608.609
5	0.00073506	0.000695384	533.052	535.469
6	0.000663118	0.000629113	466.74	469.299
7	0.000596107	0.000569157	407.129	409.436
8	0.000533491	0.000514916	353.78	355.278
9	0.000474998	0.000460095	306.281	306.281
10	0.000420526	0.000396949	264.228	263.506
11	0.000370077	0.00034247	227.22	226.602
12	0.000323717	0.000295468	194.849	194.763
13	0.000281476	0.000254917	166.701	167.293
14	0.000243324	0.000219931	142.368	143.594
15	0.000209166	0.000189747	121.452	123.147
16	0.000178882	0.000163705	103.564	105.507
17	0.000152407	0.000141238	88.3229	90.2873
18	0.000129545	0.000121854	75.3685	77.1565
19	0.000109989	0.00010513	64.3696	65.8279
20	9.33856E-05	9.07014E-05	55.031	56.0541
21	7.93529E-05	7.82531E-05	47.0957	47.6217
22	0.000067491	6.19619E-05	40.3466	40.3466
23	5.74519E-05	5.29571E-05	34.6014	34.6124
24	4.89462E-05	4.52609E-05	29.7068	29.7116
25	4.17323E-05	3.86832E-05	25.5336	25.523
26	3.56083E-05	3.30615E-05	21.9727	21.9431
27	3.04052E-05	2.82567E-05	18.9322	18.8835
28	0.000025981	2.41502E-05	16.3341	16.2685
29	2.22163E-05	2.06405E-05	14.1125	14.0336
30	1.90106E-05	1.76409E-05	12.2114	12.1234
31	0.000016279	1.50772E-05	10.5835	10.4909
32	1.39501E-05	0.000012886	9.1885	9.09558
33	1.19644E-05	1.10133E-05	7.99206	7.90306
34	1.02773E-05	9.41277E-06	6.96433	6.88385
35	0.000008844	8.04483E-06	6.07993	6.01276
36	7.62538E-06	6.87569E-06	5.31739	5.26827
37	6.58818E-06	5.87646E-06	4.65857	4.63196
38	5.70438E-06	4.99922E-06	4.08814	4.08814
39	4.95029E-06	4.42755E-06	3.59311	3.61738
40	4.30592E-06	3.92126E-06	3.16252	3.20045
41	3.7544E-06	3.47286E-06	2.78708	2.8312
42	3.28153E-06	3.07573E-06	2.45892	2.50417
43	2.87529E-06	0.000002724	2.17139	2.21454
44	2.52557E-06	2.41253E-06	1.91884	1.95802
45	2.22383E-06	2.13665E-06	1.69645	1.73084
46	1.96273E-06	1.89232E-06	1.50018	1.52964
47	1.73578E-06	1.67594E-06	1.3266	1.35145
48	1.53758E-06	1.48429E-06	1.17285	1.19363
49	1.36373E-06	1.31456E-06	1.03647	1.05386

Altitude[km]	rho(table)	rho(fit)	thick(table)	thick(fit)
50	1.21063E-06	1.16424E-06	0.91541	0.930072
51	1.07533E-06	1.03111E-06	0.807878	0.82044
52	9.55381E-07	9.13199E-07	0.71234	0.723344
53	8.48767E-07	8.08774E-07	0.627463	0.637351
54	7.53798E-07	7.1629E-07	0.552083	0.561191
55	6.69061E-07	6.34382E-07	0.485177	0.49374
56	5.93376E-07	5.6184E-07	0.42584	0.434003
57	5.2578E-07	4.97593E-07	0.373262	0.381096
58	4.65432E-07	4.40693E-07	0.326718	0.334239
59	4.11579E-07	3.90299E-07	0.28556	0.292741
60	3.6355E-07	3.45668E-07	0.249205	0.255987
61	3.20742E-07	3.0614E-07	0.217131	0.223437
62	2.82616E-07	2.71133E-07	0.18887	0.194609
63	2.48603E-07	2.40129E-07	0.164009	0.169077
64	2.18299E-07	2.1267E-07	0.142179	0.146465
65	1.91405E-07	1.88351E-07	0.123039	0.126438
66	1.67562E-07	1.66813E-07	0.106283	0.108702
67	1.4645E-07	1.47738E-07	0.0916378	0.0929938
68	1.2778E-07	1.30844E-07	0.0788598	0.0790819
69	1.11292E-07	6.21487E-08	0.0677306	0.0715246
70	9.67531E-08	6.21487E-08	0.0580553	0.0653098
71	0.000000084	6.21487E-08	0.0496601	0.0590949
72	7.27013E-08	6.21487E-08	0.0423899	0.05288
73	0.000000063	6.21487E-08	0.0360898	0.0466652
74	5.43928E-08	6.21487E-08	0.0306505	0.0404503
75	4.68812E-08	6.21487E-08	0.0259624	0.0342354
76	4.03203E-08	6.21487E-08	0.0219304	0.0280206
77	3.45899E-08	6.21487E-08	0.0184714	0.0218057
78	2.9589E-08	6.21487E-08	0.0155125	0.0155908
79	2.52318E-08	6.21487E-08	0.0129893	0.00937596
80	2.14441E-08	6.21487E-08	0.0108449	0.0031611
80.5	2.14441E-08	6.21487E-08	3.72008E-44	0

Table A.9: Table of model data and fit data for the atmosphere above ORCA in December

Altitude[km]	rho(table)	rho(fit)	thick(table)	thick(fit)
0	0.00125156	0.00120001	988.288	988.288
1	0.00112298	0.00107813	875.99	874.489
2	0.00101354	0.000968633	774.636	772.249
3	0.000917537	0.000870253	682.883	680.392
4	0.000831003	0.000781866	599.782	597.865
5	0.000751274	0.000702455	524.655	523.72
6	0.000676695	0.00063111	456.985	457.105
7	0.00060636	0.000567012	396.349	397.257
8	0.000539898	0.000509423	342.36	343.486
9	0.000477284	0.000457683	294.631	295.177
10	0.00041869	0.00039568	252.762	252.322
11	0.000364473	0.000338768	216.315	215.674

Altitude[km]	rho(table)	rho(fit)	thick(table)	thick(fit)
12	0.000315268	0.000290042	184.788	184.296
13	0.000271377	0.000248325	157.65	157.432
14	0.000232756	0.000212607	134.375	134.431
15	0.000199137	0.000182027	114.461	114.739
16	0.000170096	0.000155846	97.4515	97.8794
17	0.000145095	0.00013343	82.942	83.4446
18	0.000123622	0.000114238	70.5798	71.086
19	0.000105219	9.78072E-05	60.0579	60.505
20	0.000089477	8.37393E-05	51.1102	51.4459
21	7.60348E-05	7.16948E-05	43.5067	43.6897
22	6.45753E-05	5.77131E-05	37.0492	37.0492
23	5.48204E-05	4.93258E-05	31.5671	31.7082
24	0.000046527	4.21574E-05	26.9144	27.1434
25	3.94837E-05	3.60307E-05	22.9661	23.242
26	3.35075E-05	3.07944E-05	19.6153	19.9076
27	2.84403E-05	2.63191E-05	16.7713	17.0578
28	2.41464E-05	2.24942E-05	14.3566	14.6221
29	2.05093E-05	1.92252E-05	12.3057	12.5404
30	1.74293E-05	1.64312E-05	10.5628	10.7613
31	1.48214E-05	1.40433E-05	9.08065	9.24067
32	1.26133E-05	1.20024E-05	7.81932	7.94105
33	0.000010743	1.02581E-05	6.74502	6.83031
34	9.15757E-06	8.76734E-06	5.82926	5.88098
35	0.000007815	7.4932E-06	5.04776	5.06962
36	0.000006679	6.40422E-06	4.37986	4.37618
37	5.71824E-06	5.47351E-06	3.80804	3.78351
38	4.90564E-06	4.67806E-06	3.31747	3.27697
39	4.21812E-06	3.9982E-06	2.89566	2.84405
40	3.63606E-06	3.41715E-06	2.53205	2.47404
41	3.14281E-06	2.92054E-06	2.21777	2.1578
42	2.7243E-06	2.49611E-06	1.94534	1.88753
43	2.36865E-06	2.13335E-06	1.70848	1.65653
44	2.06586E-06	1.82332E-06	1.50189	1.4591
45	1.80753E-06	1.55834E-06	1.32114	1.29036
46	1.58642E-06	1.33187E-06	1.1625	1.14615
47	0.000001396	1.29887E-06	1.02289	1.02289
48	0.000001231	1.14705E-06	0.899794	0.900756
49	1.08716E-06	0.000001013	0.791078	0.792894
50	9.61086E-07	8.94566E-07	0.694969	0.69764
51	8.50082E-07	0.00000079	0.609961	0.61352
52	0.000000752	6.97661E-07	0.534765	0.539232
53	6.64942E-07	6.16113E-07	0.468271	0.473628
54	5.87585E-07	5.44097E-07	0.409513	0.415692
55	5.18696E-07	4.80499E-07	0.357643	0.364528
56	4.57299E-07	4.24334E-07	0.311913	0.319345
57	4.02609E-07	3.74735E-07	0.271652	0.279443
58	3.53944E-07	3.30933E-07	0.236258	0.244205
59	3.1069E-07	2.92251E-07	0.205189	0.213085
60	2.72297E-07	2.5809E-07	0.177959	0.185604

Altitude[km]	rho(table)	rho(fit)	thick(table)	thick(fit)
61	2.38269E-07	2.27923E-07	0.154132	0.161334
62	2.08156E-07	2.01281E-07	0.133317	0.139902
63	1.81493E-07	1.77754E-07	0.115167	0.120974
64	1.57934E-07	0.000000157	0.099374	0.104259
65	1.3721E-07	1.38628E-07	0.085653	0.0894981
66	0.000000119	1.22424E-07	0.0737515	0.0764622
67	1.03071E-07	1.08114E-07	0.0634444	0.0649501
68	8.91261E-08	9.54771E-08	0.0545318	0.0547836
69	0.000000077	4.32732E-08	0.0468364	0.0494358
70	6.63478E-08	4.32732E-08	0.0402017	0.0451085
71	5.71258E-08	4.32732E-08	0.0344891	0.0407811
72	4.91218E-08	4.32732E-08	0.0295769	0.0364538
73	4.2255E-08	4.32732E-08	0.0253514	0.0321265
74	3.62945E-08	4.32732E-08	0.021722	0.0277992
75	3.11734E-08	4.32732E-08	0.0186046	0.0234719
76	2.67739E-08	4.32732E-08	0.0159272	0.0191445
77	0.000000023	4.32732E-08	0.0136278	0.0148172
78	1.9747E-08	4.32732E-08	0.0116531	0.0104899
79	0.000000017	4.32732E-08	0.00995743	0.00616257
80	1.45587E-08	4.32732E-08	0.00850156	0.00183525
80.4	1.45587E-08	4.32732E-08	3.72008E-44	0

A.4 MUPAGE

DEPTHmax	3.500	maximum depth in km (not in km.w.e.)
Zmin	0.0	minimum z in m
Zmax	920.00	maximum z in m
CANr	10000	can radius in m
EnlargedCANr	300.0	meters to add to the can radius
THETAmin	0.0	minimum zenith angle in degrees
THETAmax	85.0	maximum zenith angle in degrees
Rmin	0.0	minimum radial distribution in m
Rmax	1000.0	maximum radial distribution in m
Ethreshold	1	minimum energy of threshold in TeV
MULTmin	1	minimum multiplicity
MULTmax	100	maximum multiplicity
GEANTid	5	muon in GEANT nomenclature
density	1.025	mean value of seawater density in g cm^{-3}
AbsLength	70.0	absorption length in m
NAbsLength	3.0	number of absorption length

Table A.10: The input card for the mupage production spectified to make comparisons with CORSIKA. The numbers map the geometry of a flat detector at 920 m above sea floor.

A.5 Comparison of values characterizing atmospheric muon bundles

A.5.1 SIBYLL

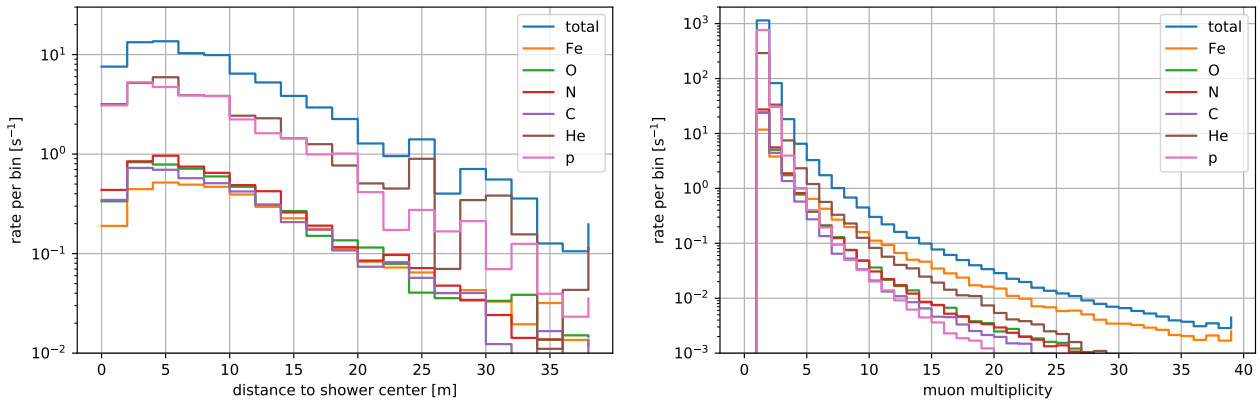

(a) (b)

Figure A.6: Composition of the atmsopheric muon flux at upper detector can level resolved in primary partiles as predicted with the GST3 cosmic-ray model and the high-energy hadronic interaction model SIBYLL

A.5.2 EPOS

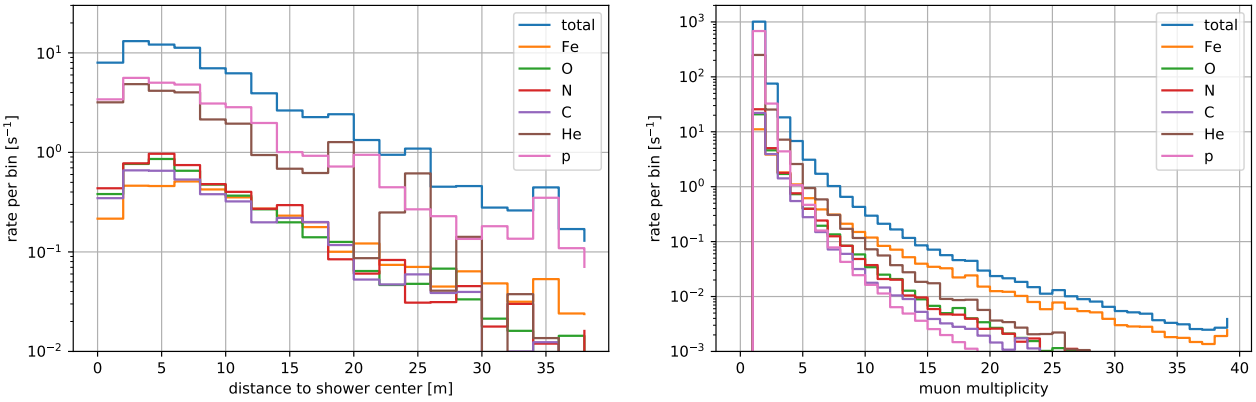

(a) (b)

Figure A.7: Composition of the atmsopheric muon flux at upper detector can level resolved in primary partiles as predicted with the GST3 cosmic-ray model and the high-energy hadronic interaction model EPOS

A.5.3 QGSJET01

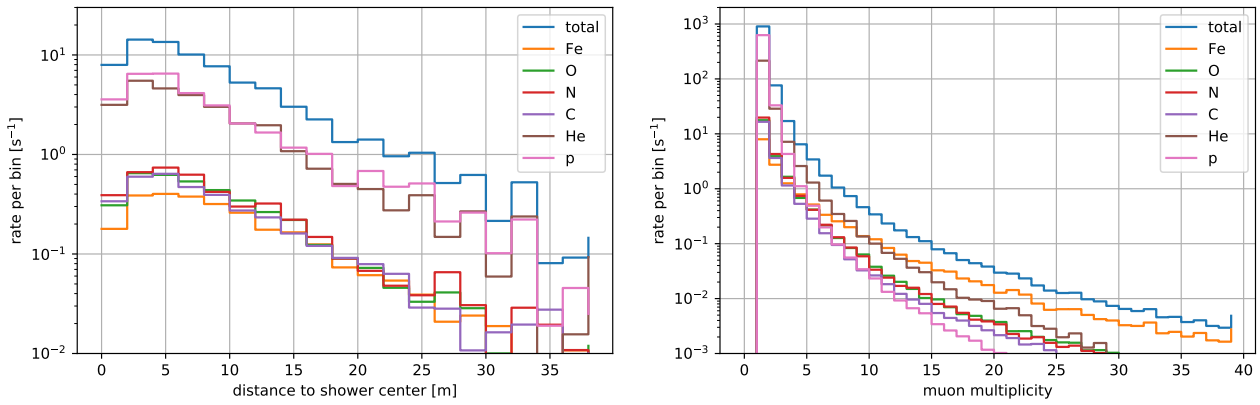

(a) (b)

Figure A.8: Composition of the atmsopheric muon flux at upper detector can level resolved in primary partiles as predicted with the GST3 cosmic-ray model and the high-energy hadronic interaction model QGSJET01

A.5.4 QGSJETII

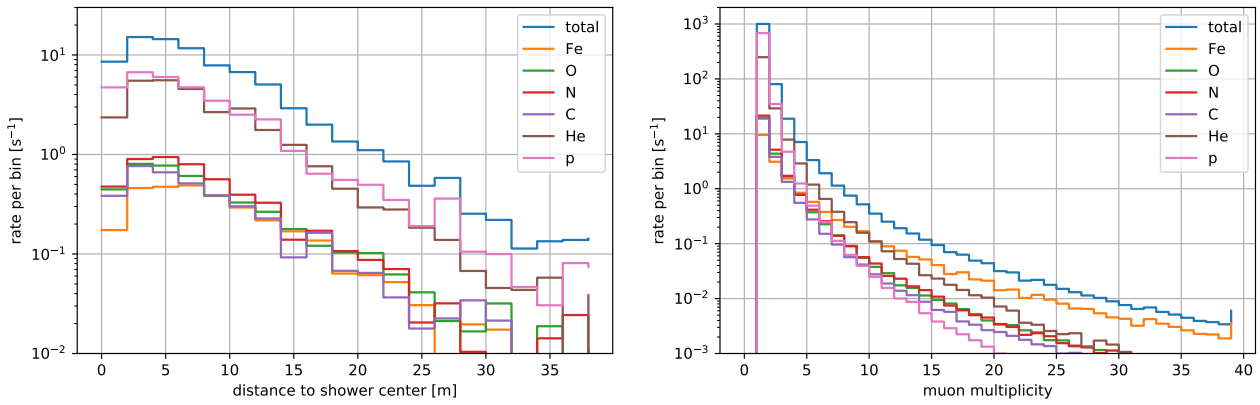

(a) (b)

Figure A.9: Composition of the atmsopheric muon flux at upper detector can level resolved in primary partiles as predicted with the GST3 cosmic-ray model and the high-energy hadronic interaction model QGSJETII

A.5.5 SIBYLL

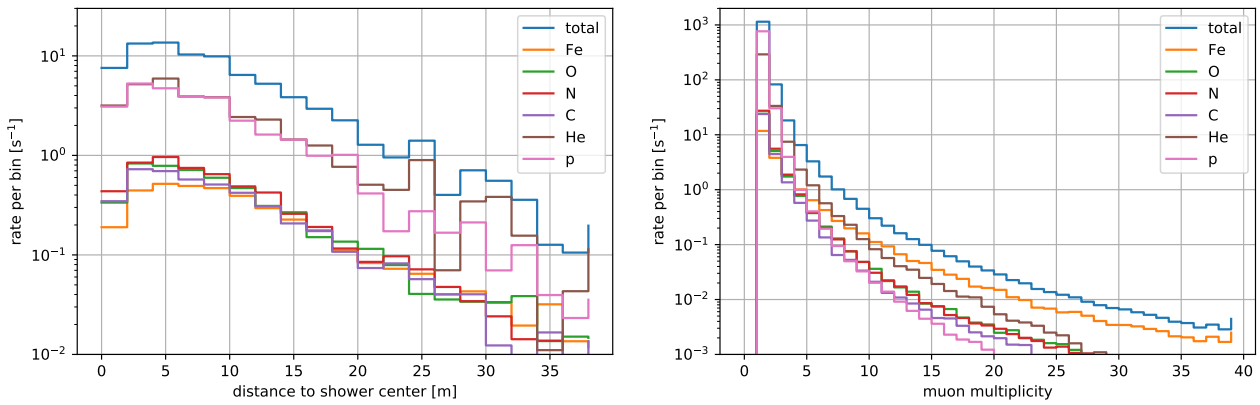

(a) (b)

Figure A.10: Composition of the atmsopheric muon flux at upper detector can level resolved in primary partiles as predicted with the GST3 cosmic-ray model and the high-energy hadronic interaction model SIBYLL

A.5.6 Comparison of hadronic interaction models

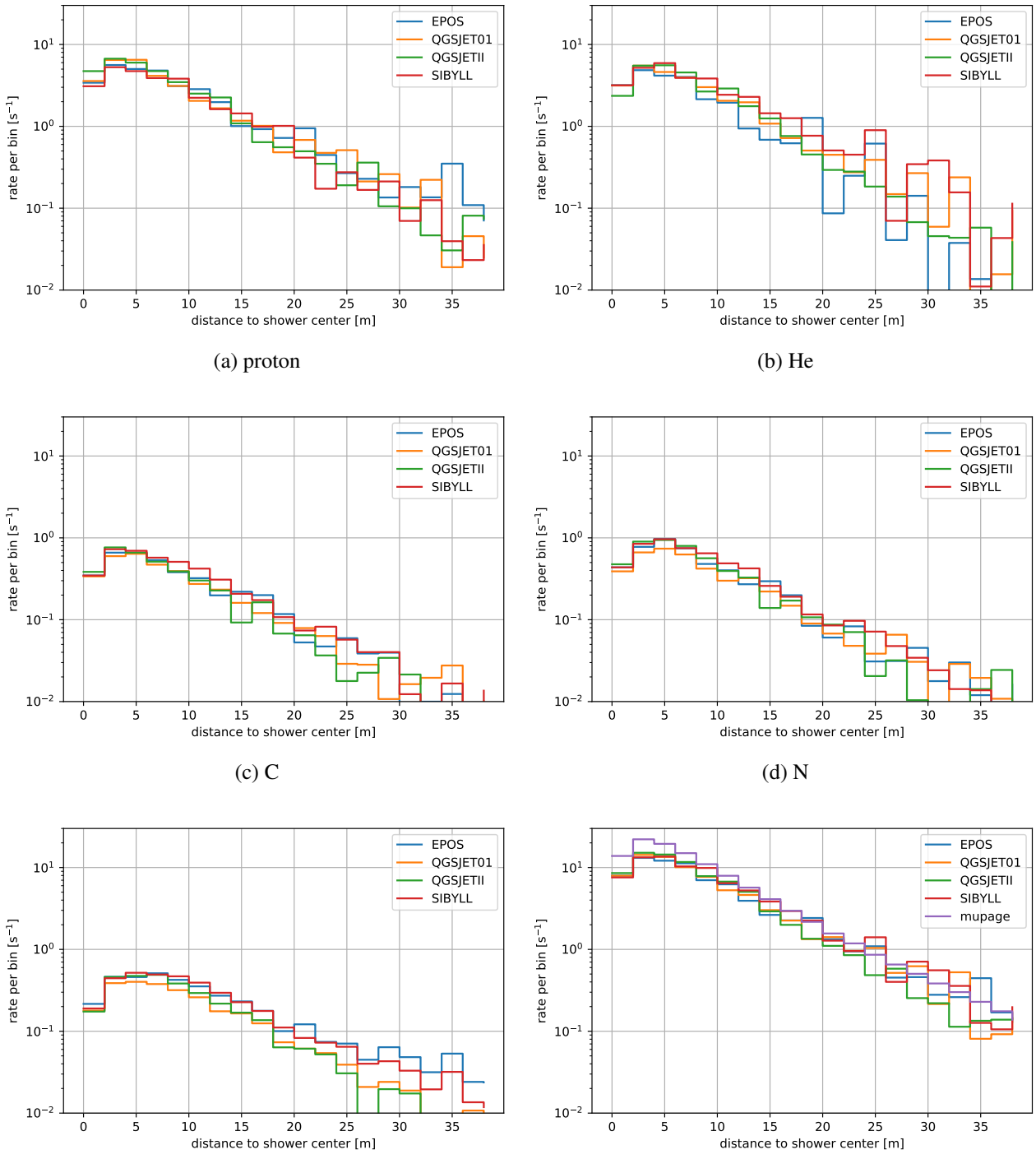

(a) proton (b) He

(c) C (d) N

(e) Fe (f) total

Figure A.11: Comparison of the event rate in the view of different cosmic-ray flux models, with respect to the lateral distance to the cascade axis

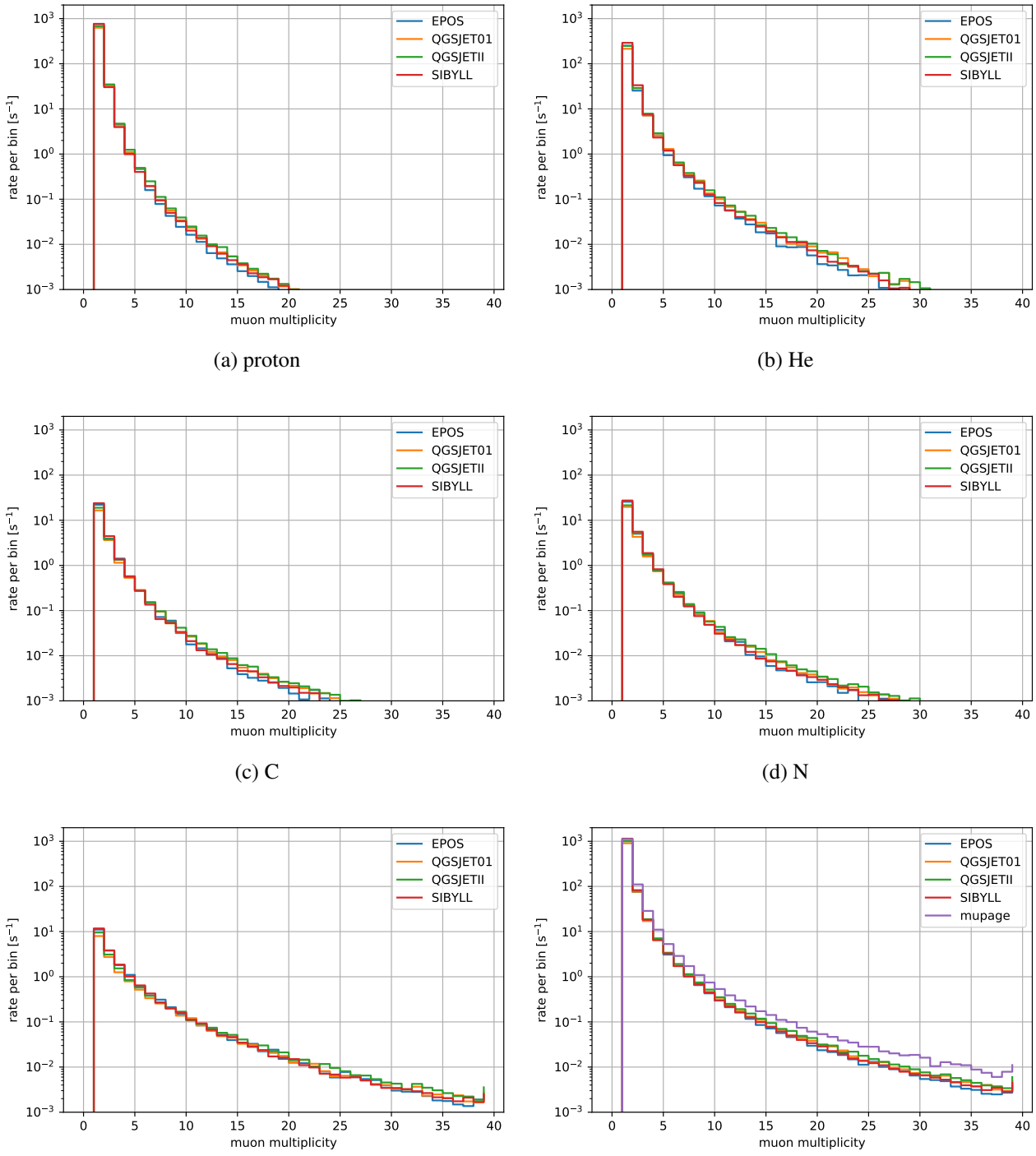

(a) proton (b) He

(c) C (d) N

(e) Fe (f) total

Figure A.12: Comparison of the event rate in the view of different cosmic-ray flux models, with respect to the muon multiplicity

A.5.7 Comparison of cosmic-ray flux models

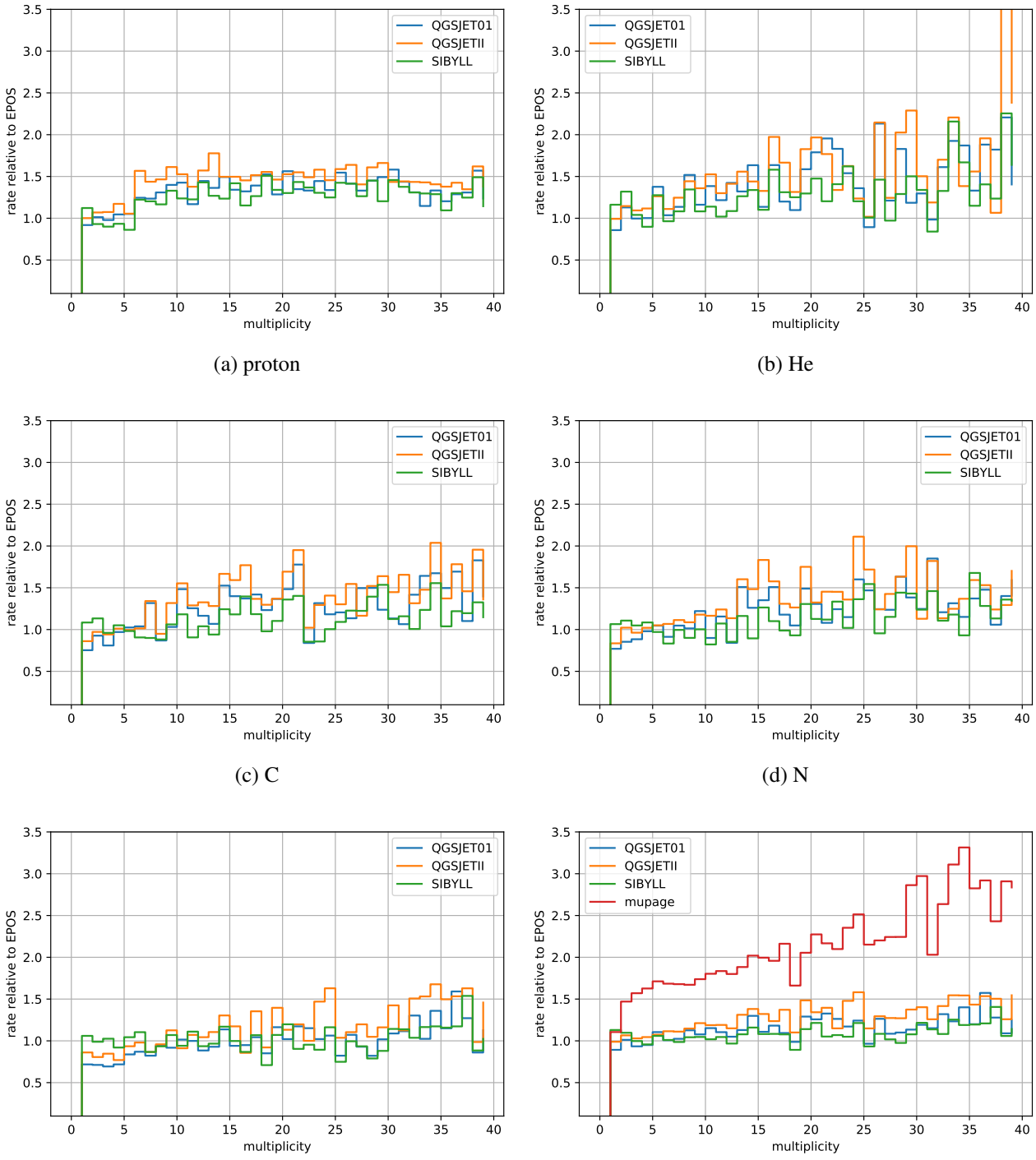

(a) proton

(b) He

(c) C

(d) N

(e) Fe

(f) total

Figure A.13: Relative comparison of the event rate in the view of different cosmic-ray flux models, with respect to the muon multiplicity

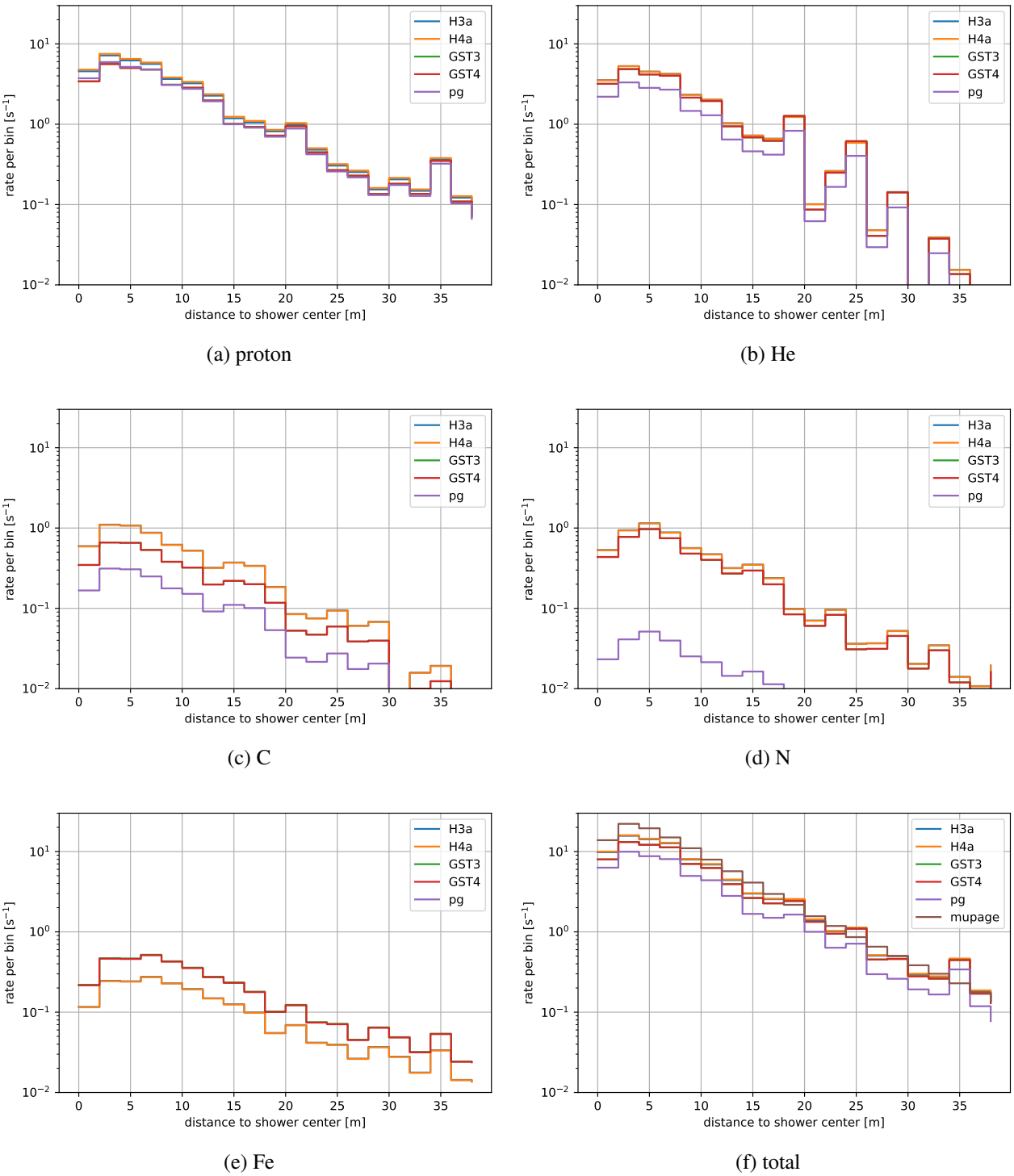

(a) proton (b) He

(c) C (d) N

(e) Fe (f) total

Figure A.14: Comparison of the event rate in the view of different cosmic-ray flux models, with respect to the lateral distance to the cascade axis

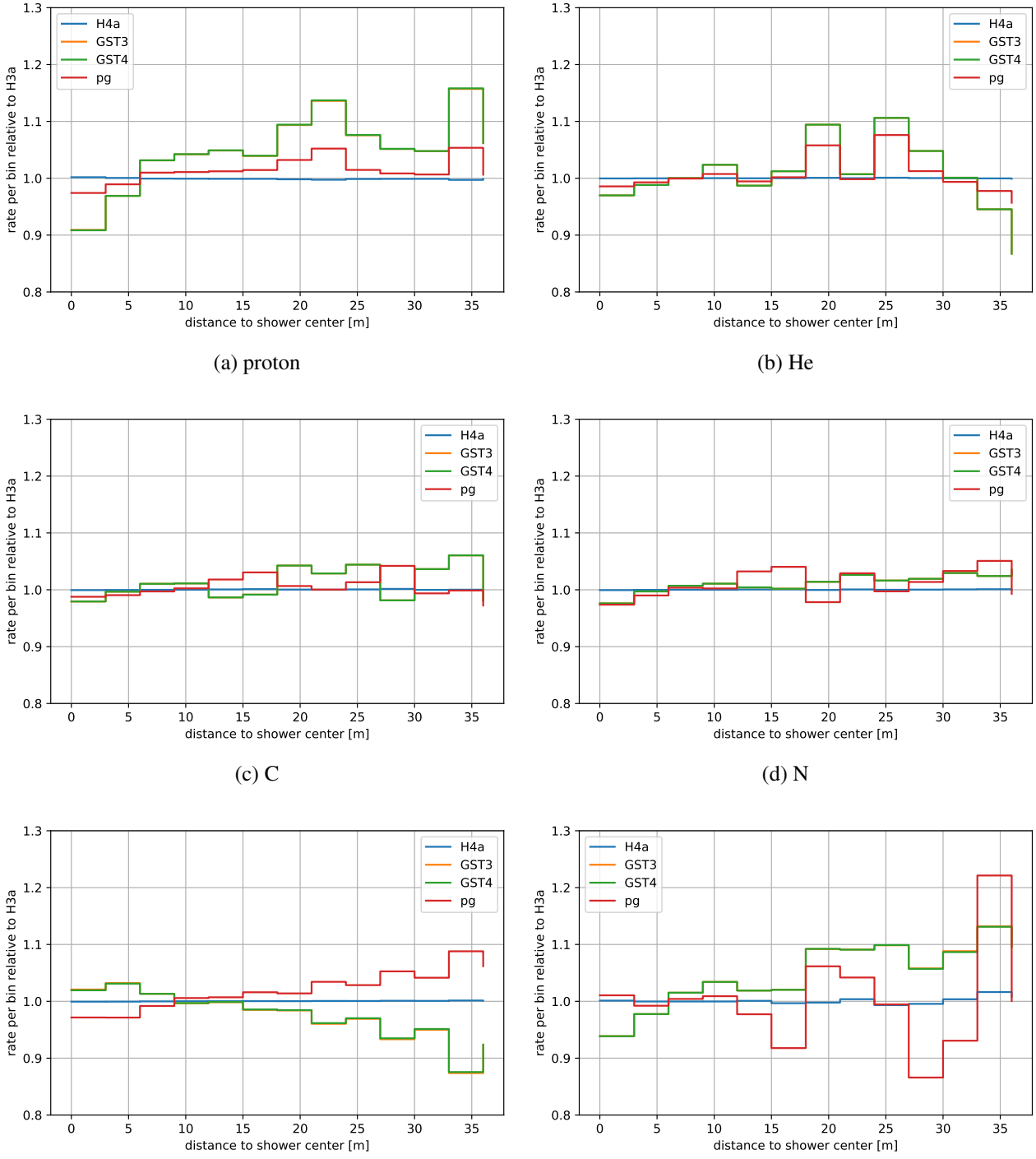

(a) proton

(b) He

(c) C

(d) N

(e) Fe

(f) total

Figure A.15: Comparison of the event rate in the view of different cosmic-ray flux models, with respect to the lateral distance to the cascade axis

Appendix B

Atmospheric self-veto

Further examples for the rejection power of the self-veto effect against the atmospheric neutrinos.

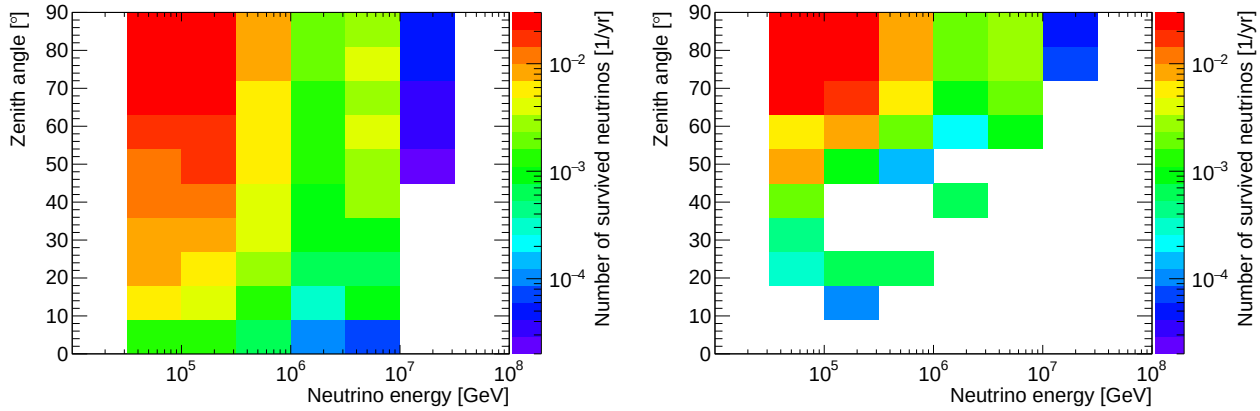

(a) without self.veto (b) with self-veto

Figure B.1: Expected event rate if $\bar{\nu}_e$-CC for diffuse analysis [97]

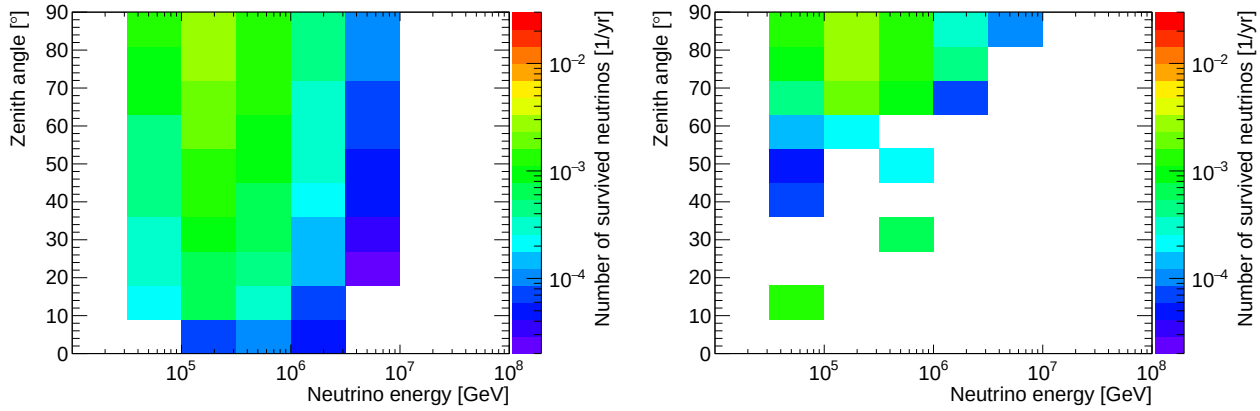

(a) without self.veto (b) with self-veto

Figure B.2: Expected event rate if $\bar{\nu}_e$-NC for diffuse analysis [97]

Appendix C

EventIdentification

C.1 Features

GoldParameter	
Slopeo1000_o100	Slope of linear fit to the cumulative time residual distribution between first and second number, where ”-” is repaced by ”o”.
Slope25_1000	
Slopeo1000_0	
Slopeo1000_o50	
Slopeo1000_o10	
Slope50_1000	
Slope0_1000	
Slopeo1000_1000	
Slope200_1000	
Slope100_1000	
Slopeo1000_o20	
Chi2o1000_0	The chi square of linear fit to the cumulative time residual distribution between first and second number, where ”-” is replaced by ”o”
Chi2100_1000	
Chi2200_1000	
Chi2o1000_o100	
Chi2o1000_1000	
Chi225_1000	
Chi250_1000	
Chi2o1000_o10	
Chi20_1000	
Chi2o1000_o50	
Chi2o1000_o20	
YIntersept0_1000	The y-intersept of linear fit to the cumulative time residual distribution between first and second number, where ”-” is replaced by ”o”
YIntersept200_1000	
YIntersept50_1000	
YIntersepto1000_o100	
YIntersepto1000_o10	
YIntersepto1000_o50	
YIntersepto1000_1000	
YIntersepto1000_0	
YIntersepto1000_o20	
YIntersept100_1000	
YIntersept25_1000	

TimeResidualMedian	Characteristic values of the time residual distribution
TimeResidualMean	
TimeResidualRMS	
TimeResidualWidth15_85	
Parameter	
GParameter	
SmallInertia	Eigenvalues of the tensor of inertia of the hit distribution as discribed in the main part
MiddleInertia	
BigInertia	
RelativeInertia	

Table C.1: Features developed in this thesis and predecessor. Each parameter is described in Chapter 6

parameter	description
NhitsAA	Number of hits used in the fit
M_estimator	Quality parameter
beta	estimated error for the direction
NhitsL0	number of L0 hits
NhitsL1	number of L1 hits
pos_z	position in z
pos_x	position in x
pos_y	position in y
dir_y	direction in y
dir_x	direction in x
dir_z	direction in z
energy	reconstructed energy

Table C.2: Features from cascade reconstruction (aashowerfit)[6]

parameter	description
beta	estimated error in the direction
n_fits	number of hits for the fit
Lambda	quality parameter
Nhits	number of hits
pos_z	position in z
pos_x	position in x
pos_y	position in y
dir_y	direction in y
dir_x	direction in x
dir_z	direction in z
energy	reconstructed energy

Table C.3: Features from second track reconstruction (reco lns)[6]

parameter	description
Energy_f	reconstructed energy in volume
Energy_can	reconstructed energy at the detector can surface
Beta0	estimated reconstruction error in the direction
Beta1	estimated reconstruction error in the direction
Lik	likelihood of the fit
Lik_reduced	reduced likelihood of the fit
pos_z	position in z
pos_x	position in x
pos_y	position in y
dir_y	direction in y
dir_x	direction in x
dir_z	direction in z
energy	reconstructed energy

Table C.4: Features from the first track reconstruction (jgandalf)[6]

Bibliography

[1] V. F. Hess. Über Beobachtungen der durchdringenden Strahlung bei sieben Freiballonfahrten. *Physikalische Zeitschrift*, 13:1084–1091, 1912.

[2] L. J. Watson et al. A bayesian analysis of the 27 highest energy cosmic rays detected by the pierre auger observatory. *Monthly Notices of the Royal Astronomical Society*, 418(1):206–213, 2011.

[3] H.E.S.S. Collaboration. Observations of the Crab nebula with HESS. *Astronomy and Astrophysics*, 457:899–915, 2006.

[4] L. Brown. The idea of the neutrino. *Physics Today*, 31(9), 1978.

[5] IceCube Collaboration. Evidence for High-Energy Extraterrestrial Neutrinos at the IceCube Detector. *Science*, 342(6161), 2013.

[6] KM3NeT Collaboration. Letter of intent for KM3NeT 2.0. *Journal of Physics G: Nuclear and Particle Physics*, 43(8):084001, 2016.

[7] IceCube Collaboration. A combined maximum-likelihood analysis of the high-energy astrophysical neutrino flux measured with icecube. *The Astrophysical Journal*, 809(1):98, 2015.

[8] C. L. Cowan, Jr. et al. Detection of the Free Neutrino: A Confirmation. *Science*, 124:103–104, 1956.

[9] G. Danby et al. Observation of high-energy neutrino reactions and the existence of two kinds of neutrinos. *Phys. Rev. Lett.*, 9:36–44, 1962.

[10] M. L. Perl et al. Evidence for anomalous lepton production in $e^+ - e^-$ annihilation. *Phys. Rev. Lett.*, 35:1489–1492, 1975.

[11] K. Kodama et al. Observation of tau neutrino interactions. *Phys. Lett.*, B504:218–224, 2001.

[12] K. A. Olive et al. Review of Particle Physics. *Chin. Phys.*, C38:090001, 2014.

[13] Super-Kamiokande Collaboration. Evidence for oscillation of atmospheric neutrinos. *Phys. Rev. Lett.*, 81:1562–1567, 1998.

[14] S. Dell'Oro et al. Neutrinoless double beta decay: 2015 review. *Adv. High Energy Phys.*, 2016:2162659, 2016.

[15] EXO Collaboration. Improved measurement of the $2\nu\beta\beta$ half-life of ^{136}xe with the exo-200 detector. *Phys. Rev. C*, 89:015502, 2014.

[16] J. K. Becker. High-energy neutrinos in the context of multimessenger physics. *Phys. Rept.*, 458:173–246, 2008.

[17] E. Fermi. On the origin of the cosmic radiation. *Phys. Rev.*, 75:1169–1174, 1949.

[18] K. Greisen. End to the cosmic-ray spectrum? *Phys. Rev. Lett.*, 16:748–750, 1966.

[19] J. Abraham et al. Observation of the suppression of the flux of cosmic rays above 4×10^{19}eV. *Phys. Rev. Lett.*, 101:061101, 2008.

[20] V. Barger et al. *The Physics of Neutrinos*. Princeton University Press, 2012.

[21] J. H. MacGibbon et al. High energy tau neutrinos. *Nuclear Physics B - Proceedings Supplements*, 110:528 – 530, 2002.

[22] C Giunti et al. *Fundamentals of Neutrino Physics and Astrophysics*. 2007.

[23] S. Choubey et al. Flavor Composition of UHE Neutrinos at Source and at Neutrino Telescopes. *Phys. Rev.*, D80:113006, 2009.

[24] IceCube Collaboration. Measurement of the ν_μ energy spectrum with IceCube-79. 2017.

[25] R. Enberg et al. Prompt neutrino fluxes from atmospheric charm. *Phys. Rev.*, D78:043005, 2008.

[26] T. K. Gaisser et al. Flux of atmospheric neutrinos. *Ann. Rev. Nucl. Part. Sci.*, 52:153–199, 2002.

[27] M. Honda et al. Improvement of low energy atmospheric neutrino flux calculation using the jam nuclear interaction model. *Phys. Rev. D*, 83:123001, Jun 2011.

[28] S. Roesler et al. The Monte Carlo event generator DPMJET-III. In *Advanced Monte Carlo for radiation physics, particle transport simulation and applications. Proceedings, Conference, MC2000, Lisbon, Portugal, October 23-26, 2000*, pages 1033–1038, 2000.

[29] IceCube Collaboration. Search for a diffuse flux of astrophysical muon neutrinos with the IceCube 59-string configuration. *Phys. Rev.*, D89(6):062007, 2014.

[30] L. Pasquali et al. Lepton fluxes from atmospheric charm. *Phys. Rev.*, D59:034020, 1999.

[31] R. Davis et al. Search for neutrinos from the sun. *Phys.Rev.Lett.*, 20:1205–1209, 1968.

[32] B. Pontecorvo. Neutrino Experiments and the Problem of Conservation of Leptonic Charge. *Sov.Phys.JETP*, 26:984–988, 1968.

[33] V. Brdar et al. Sterile Neutrinos and Flavor Ratios in IceCube. *JCAP*, 1701(01):026, 2017.

[34] M. C. Gonzalez-Garcia et al. Non-standard neutrino interactions in the Earth and the flavor of astrophysical neutrinos. *Astropart. Phys.*, 84:15–22, 2016.

[35] C. A. Argüelles et al. New Physics in Astrophysical Neutrino Flavor. *Phys. Rev. Lett.*, 115:161303, 2015.

[36] S. L. Glashow. Resonant scattering of antineutrinos. *Phys. Rev.*, 118:316–317, 1960.

[37] J. A. Formaggio et al. From eV to EeV: Neutrino cross sections across energy scales. *Rev. Mod. Phys.*, 84:1307–1341, 2012.

[38] J. D. Jackson et al. *Klassische Elektrodynamik*. de Gruyter, 2002.

[39] R. Gandhi et al. Ultrahigh-energy neutrino interactions. *Astropart.Phys.*, 5:81–110, 1996.

[40] J. G. Learned et al. Detecting tau neutrino oscillations at pev energies. *Astroparticle Physics*, 3(3):267 – 274, 1995.

[41] T. DeYoung et al. Astrophysical tau neutrino detection in kilometer-scale cherenkov detectors via muonic tau decay. *Astroparticle Physics*, 27(4):238 – 243, 2007.

[42] IceCube Collaboration. Tau neutrinos in icecube. *Journal of Physics: Conference Series*, 60(1):227, 2007.

[43] M. A. Markov. On high energy neutrino physics. In *Proceedings, 10th International Conference on High-Energy Physics (ICHEP 60): Rochester, NY, USA, 25 Aug - 1 Sep 1960*, pages 578–581, 1960.

[44] U. F. Katz et al. High-Energy Neutrino Astrophysics: Status and Perspectives. *Prog. Part. Nucl. Phys.*, 67:651–704, 2012.

[45] KM3NeT Collaboration. KM3NeT - Opens a new window on our universe. `http://www.km3net.org`, September 2013.

[46] NEMO Collaboration. Long term monitoring of the optical background in the Capo Passero deep-sea site with the NEMO tower prototype. *Eur. Phys. J.*, C76(2):68, 2016.

[47] K Melis. In-situ calibration of km3net. In *ICRC 2017*, 2017.

[48] V. Aynutdinov. The prototype string for the km3-scale Baikal neutrino telescope. *Nucl. Instrum. Meth.*, A602:227–234, 2009.

[49] IceCube Collaboration. IceCube-Gen2: A Vision for the Future of Neutrino Astronomy in Antarctica. 2014.

[50] Auger Collaboration. Improved limit to the diffuse flux of ultrahigh energy neutrinos from the Pierre Auger Observatory. *Phys. Rev.*, D91(9):092008, 2015.

[51] G. A. Askar'yan. Excess negative charge of an electron-photon cascade and its coherent radio emission. *Sov. Phys. JETP*, 14(2):441–443, 1962. [Zh. Eksp. Teor. Fiz.41,616(1961)].

[52] G. A. Askar'yan. Coherent Radio Emission from Cosmic Showers in Air and in Dense Media. *Soviet Journal of Experimental and Theoretical Physics*, 21:658, September 1965.

[53] I. Kravchenko et al. Updated results from the RICE experiment and future prospects for ultra-high energy neutrino detection at the south pole. 85(6):062004, 2012.

[54] S. W. Barwick et al. Constraints on cosmic neutrino fluxes from the anita experiment. *Phys. Rev. Lett.*, 96:171101, 2006.

[55] K. D. Hoffman. AURA: The Askaryan Underice Radio Array. *J. Phys. Conf. Ser.*, 81:012022, 2007.

[56] P. Allison et al. Performance of two Askaryan Radio Array stations and first results in the search for ultrahigh energy neutrinos. *Phys. Rev.*, D93(8):082003, 2016.

[57] S. W. Barwick et al. Design and Performance of the ARIANNA HRA-3 Neutrino Detector Systems. *IEEE Trans. Nucl. Sci.*, 62(5):2202–2215, 2015.

[58] P. Antonioli et al. A three-dimensional code for muon propagation through the rock: Music. 7:357–368, 05 1997.

[59] R. Brun et al. GEANT3 user guide, CERN data handling division DD. *EE/841*, 1985.

[60] S. Jadach et al. TAUOLA: A Library of Monte Carlo programs to simulate decays of polarized tau leptons. *Comput. Phys. Commun.*, 64:275–299, 1990.

[61] KM3NeT Collaboration. The prototype detection unit of the KM3NeT detector. *Eur. Phys. J.*, C76(2):54, 2016.

[62] G. Carminati et al. Atmospheric muons from parametric formulas: a fast generator for neutrino telescopes (MUPAGE). *Computer Physics Communications*, 179(12):915 – 923, 2008.

[63] Y. Becherini et al. A Parameterisation of single and multiple muons in the deep water or ice. *Astropart. Phys.*, 25:1–13, 2006.

[64] C. Forti et al. Simulation of atmospheric cascades and deep-underground muons. *Phys. Rev. D*, 42:3668–3689, Dec 1990.

[65] D. Heck et al. CORSIKA: A Monte Carlo code to simulate extensive air showers. 1998.

[66] S. Schönert et al. Vetoing atmospheric neutrinos in a high energy neutrino telescope. *Phys. Rev. D*, 79:043009, 2009.

[67] T. K. Gaisser et al. Generalized self-veto probability for atmospheric neutrinos. *Phys. Rev.*, D90(2):023009, 2014.

[68] J. R. Hörandel. On the knee in the energy spectrum of cosmic rays. *Astroparticle Physics*, 19(2):193 – 220, 2003.

[69] B. Wiebel-Sooth et al. Cosmic rays vii. individual element spectra: prediction and data. *Astron. Astrophys.*, 330:389, 1998.

[70] N. N. Kalmykov et al. EAS and a quark - gluon string model with jets. *Bull. Russ. Acad. Sci. Phys.*, 58:1966–1969, 1994. [Izv. Ross. Akad. Nauk Ser. Fiz.58N12,21(1994)].

[71] T. K. Gaisser. Spectrum of cosmic-ray nucleons, kaon production, and the atmospheric muon charge ratio. *Astroparticle Physics*, 35(12):801 – 806, 2012.

[72] T. K. Gaisser et al. Cosmic ray energy spectrum from measurements of air showers. *Frontiers of Physics*, 8(6):748–758, 2013.

[73] H. S. Ahn et al. Discrepant hardening observed in cosmic-ray elemental spectra. *Astrophys. J.*, 714:L89–L93, 2010.

[74] H. S. Ahn et al. Energy spectra of cosmic-ray nuclei at high energies. *Astrophys. J.*, 707:593–603, 2009.

[75] O. Adriani et al. PAMELA Measurements of Cosmic-Ray Proton and Helium Spectra. *Science*, 332:69, 2011.

[76] A. Fedynitch et al. Influence of hadronic interaction models and the cosmic ray spectrum on the high energy atmospheric muon and neutrino flux. *Phys. Rev. D*, 86:114024, 2012.

[77] ANTARES Collaboration. Antares: The first undersea neutrino telescope. *Nucl. Instrum. and Meth.*, A656(1):11 – 38, 2011.

[78] G. Giacomelli et al. The macro experiment. *Modern Physics Letters A*, 18(29):2001–2018, 2003.

[79] Auger Collaboration. The Pierre Auger Cosmic Ray Observatory. *Nucl. Instrum. Meth.*, A798:172–213, 2015.

[80] W.D. Apel et al. The kascade-grande experiment. *Nuclear Instruments and Methods in Physics Research Section A: Accelerators, Spectrometers, Detectors and Associated Equipment*, 620(2):202 – 216, 2010.

[81] Chulliat A. et al. *The US/UK World Magnetic Model for 2015-2020: Technical Report*. National Geophysical Data Center, NOAA, 2015.

[82] NAOO. International geomagnetic reference field. http://www.ngdc.noaa.gov/IAGA/vmod/igrf.html, December 2014.

[83] B. Keilhauer et al. Atmospheric Profiles at the Southern Pierre Auger Observatory and their Relevance to Air Shower Measurement. *ArXiv Astrophysics e-prints*, July 2005.

[84] J. M. Picone et al. Nrlmsise-00 empirical model of the atmosphere: Statistical comparisons and scientific issues. *Journal of Geophysical Research: Space Physics*, 107(A12):SIA 15–1–SIA 15–16, 2002. 1468.

[85] P. Abreu et al. The Rapid Atmospheric Monitoring System of the Pierre Auger Observatory. *JINST*, 7:P09001, 2012.

[86] F. Riehn et al. A new version of the event generator Sibyll. *PoS*, ICRC2015:558, 2016.

[87] B. Klose. *Meteorologie - Eine interdisziplinäre Einführung in die Physik der Atmosphäre*. Springer Berlin Heidelberg, 2016.

[88] K. Bernlohr. Simulation of Imaging Atmospheric Cherenkov Telescopes with CORSIKA and sim_telarray. *Astropart. Phys.*, 30:149–158, 2008.

[89] H. Takai et al. Tidal Frequencies in the Time Series Measurements of Atmospheric Muon Flux from Cosmic Rays. 2016.

[90] H. Fesefeldt. The Simulation of Hadronic Showers: Physics and Applications. 1985.

[91] R. Horsley et al. Charge symmetry breaking in parton distribution functions from lattice qcd. *Phys. Rev. D*, 83:051501, 2011.

[92] S. Becker et al. Direct contour deformation with arbitrary masses in the loop. *Phys. Rev. D*, 86:074009, 2012.

[93] T. Pierog et al. EPOS LHC: Test of collective hadronization with data measured at the CERN Large Hadron Collider. *Phys. Rev. C*, 92:034906, 2015.

[94] Tamás Csörgö et al. Elastic Scattering and Total Cross-Section in $p + p$ reactions measured by the LHC Experiment TOTEM at $\sqrt{s} = 7$ TeV. *Prog. Theor. Phys. Suppl.*, 193:180–183, 2012.

[95] Tanguy Pierog et al. Air Shower Simulation with New Hadronic Interaction Models in CORSIKA. In *Proceedings, 33rd International Cosmic Ray Conference (ICRC2013): Rio de Janeiro, Brazil, July 2-9, 2013*, page 0163.

[96] F. Riehn et al. Charm production in SIBYLL. *EPJ Web Conf.*, 99:12001, 2015.

[97] T. Heid et al. Self-veto approaches to reject atmospheric neutrinos in KM3NeT/ARCA. *PoS*, ICRC2015:1067, 2016.

[98] G. C. Hill et al. Unbiased cut selection for optimal upper limits in neutrino detectors: the model rejection potential technique. *Astroparticle Physics*, 19(3):393 – 402, 2003.

[99] W. Demtröder. *Experimentalphysik 1 - Mechanik und Wärme*. Springer-Verlag, Berlin Heidelberg New York, 2015.

[100] I. Alikhanov et al. Distributions for tau neutrino interactions observed through the decay $\tau \to \mu\nu_\tau\bar{\nu}_\mu$. *Phys. Lett.*, B765:272–275, 2017.

[101] S. Geisselsoeder. Rdfclassify tutorial. 2012. ANTARES-SOFT-2012-002.

[102] Klaus Geyer. *Ereignisklassifikation mit Hilfe von Neuronalen Netzen fuer das ANTARES-Neutrino Teleskop*. PhD thesis, U. Erlangen-Nuremberg (main), 2010.

[103] H. J. Kelley. Gradient theory of optimal flight paths. *Ars Journal*, 30(10):947–954, 1960.

[104] A. E. Bryson. A gradient method for optimizing multi-stage allocation processes. In *Proceedings of the Harvard Univ. Symposium on digital computers and their applications*, 1961.

[105] T. Gal et al. tamasgal/km3pipe: Km3pipe 6.8.0, 2017.

[106] F. Pedregosa et al. Scikit-learn: Machine learning in Python. *Journal of Machine Learning Research*, 12:2825–2830, 2011.

[107] A. Gelman et al. *Data Analysis Using Regression and Multilevel/Hierarchical Models*. Analytical Methods for Social Research. Cambridge University Press, 2007.

[108] S. Saarinen et al. Ill-conditioning in neural network training problems. *SIAM Journal on Scientific Computing*, 14(3):693–714, 1993.

[109] K. Pearson. On lines and planes of closest fit to systems of points in space. *Philosophical Magazine*, 2(11):559–572, 1901.

[110] O. Behnke et al. *Data Analysis in High Energy Physics: A Practical Guide to Statistical Methods*. Wiley-VCH, 1st edition, 2013.

[111] T. Calders et al. Three naive bayes approaches for discrimination-free classification. *Data Mining and Knowledge Discovery*, 21(2):277–292, 2010.

[112] J. Bergstra et al. Random search for hyper-parameter optimization. 13:281–305, 03 2012.

[113] L. Johnson. theanets v0.7.3. https://github.com/lmjohns3/theanets.

[114] Theano Development Team. Theano: A Python framework for fast computation of mathematical expressions. *arXiv e-prints*, abs/1605.02688, May 2016.

[115] Y. Bengio. Practical recommendations for gradient-based training of deep architectures. *ArXiv e-prints*, June 2012.

[116] T. P. Li et al. Analysis methods for results in gamma-ray astronomy. *Astrophys. J.*, 272:317–324, 1983.

[117] D. Stransky et al. KM3NeT/ARCA sensitivity to a diffuse flux of cosmic neutrinos. *PoS*, ICRC2015:1107, 2016.

[118] A. Aurisano et al. A Convolutional Neural Network Neutrino Event Classifier. *JINST*, 11(09):P09001, 2016.

[119] IceCube Collaboration. Observation of High-Energy Astrophysical Neutrinos in Three Years of IceCube Data. *Phys. Rev. Lett.*, 113:101101, 2014.

[120] O. Mena et al. Flavor composition of the high-energy neutrino events in icecube. *Phys. Rev. Lett.*, 113:091103, 2014.

[121] G. Pagliaroli et al. Testing nonradiative neutrino decay scenarios with icecube data. *Phys. Rev. D*, 92:113008, 2015.

[122] A. Palladino et al. What is the Flavor of the Cosmic Neutrinos Seen by IceCube? *Phys. Rev. Lett.*, 114(17):171101, 2015.

[123] S. Palomares-Ruiz et al. On the flavor composition of the high-energy neutrinos in icecube. *Nuclear and Particle Physics Proceedings*, 273:433 – 439, 2016.

[124] S. Palomares-Ruiz et al. Spectral analysis of the high-energy icecube neutrinos. *Phys. Rev. D*, 91:103008, 2015.

[125] IceCube Collaboration. Flavor ratio of astrophysical neutrinos above 35 tev in icecube. *Phys. Rev. Lett.*, 114:171102, 2015.

[126] L. Mohrmann et al. Characterization of the astrophysical neutrino flux at the icecube neutrino observatory. *Journal of Physics: Conference Series*, 718(6):062045, 2016.

[127] IceCube Collaboration. Search for astrophysical tau neutrinos in six years of high-energy starting events in IceCube. In *ICRC 2017*, 2017.

[128] S. van der Walt et al. The numpy array: A structure for efficient numerical computation. *Computing in Science Engineering*, 13(2):22–30, 2011.

[129] W. Cash. Parameter estimation in astronomy through application of the likelihood ratio. *Astro. Phys. Journal*, 228:939–947, 1979.

[130] D. Burke et al. sherpa/sherpa: Sherpa 4.9.1, 2017. https://doi.org/10.5281/zenodo.838686.

[131] J. J. More. *Levenberg–Marquardt algorithm: implementation and theory*. 1977.

[132] G. J. Feldman et al. A Unified approach to the classical statistical analysis of small signals. *Phys. Rev.*, D57:3873–3889, 1998.

[133] M. Harper et al. marcharper/python-ternary: New Features and Bug Fixes, 2017.

[134] I. N. Bronstein et al. *Taschenbuch der Mathematik*. Deutsch (Harri), 2005.

[135] S. S. Wilks. The large-sample distribution of the likelihood ratio for testing composite hypotheses. *The Annals of Mathematical Statistics*, 9(1):60–62, 1938.

[136] M. Kowalski et al. Neutrino astronomy with icecube and beyond. *Journal of Physics: Conference Series*, 888(1):012007, 2017.

[137] I. M. Shoemaker et al. Probing BSM Neutrino Physics with Flavor and Spectral Distortions: Prospects for Future High-Energy Neutrino Telescopes. *Phys. Rev.*, D93(8):085004, 2016.

[138] G. Cowan et al. Asymptotic formulae for likelihood-based tests of new physics. *Eur. Phys. J.*, C71:1554, 2011. [Erratum: Eur. Phys. J.C73,2501(2013)].

Erklärung

Hiermit bestätige ich, dass ich diese Arbeit selbstständig und nur unter Verwendung der angegebenen Hilfsmittel angefertigt habe.

Erlangen,

12.12.2017